DYNAMIC MECHANICAL PROPERTIES OF FIBRE REINFORCED PLASTICS

Kolawole Saka
Mansfield College

A dissertation submitted for the Degree of
Doctor of Philosophy in the University of Oxford

Engineering Laboratory,
Parks Road,
Oxford.

Hilary Term, 1987

DYNAMIC MECHANICAL PROPERTIES OF FIBRE REINFORCED PLASTICS

Kolawole Saka
Mansfield College, Oxford

A dissertation submitted for the degree of Doctor of Philosophy

Hilary Term 1987

ABSTRACT

A small gas gun, capable of accelerating a projectile 1m long by 25.4mm diameter to about 50 m/s, and an extended split Hopkinson bar apparatus have been designed and constructed for the tensile impact testing of fibre reinforced composite specimens at strain rates of the order of 1000/s. Elastic strain measurements derived from the Hopkinson bar analysis are checked, using strain gauges attached directly to the specimen and the validity of the elastic moduli determined under tensile impact is confirmed.

Epoxy specimens reinforced with plain-weave fabrics of either carbon or glass or with several hybrid combinations of the two in various lay-ups, giving five different weight fractions of reinforcement from all-carbon to all-glass, have been tested in tension at three strain rates, nominally, $\sim 10^{-3}$/s, ~10/s and $\sim 10^{3}$/s. The effect of both hybrid composition (volume fraction of carbon reinforced plies) and applied strain rate on the tensile modulus, the tensile strength and the strain to fracture is determined and a limited hybrid effect is observed in specimens with a carbon volume fraction in the approximate range 0.6 to 0.7 where, at all three strain rates there is an enhancement of the failure strain over that for the all-carbon plies

and an increased failure strength, most marked in the impact tests, over that predicted by the rule of mixtures. The fracture surfaces of specimens are examined by optical and scanning electron microscopy and the failure process in the hybrid composites is related to that found in the all-carbon and the all-glass specimens.

The classical laminated plate theory and the Tsai-Wu strength criterion are used to predict the stiffness and strength of the hybrid composites from the elastic and strength properties of the constituent plies. Analytical predictions are in good agreement with experimental measurements.

PREFACE

This dissertation is an account of the research carried out by the author in the Department of Engineering Science, Oxford University. The work was sponsored by the Air Force Office of Scientific Research, Air Force Systems Command, USAF, and supervised by Dr. J. Harding. No part of the dissertation has been submitted for a degree at any other University. The research described here is original, although the work of others has been drawn upon freely with due acknowledgment in the text.

For more direct contact I am immensely grateful to my supervisor for his help and advice and the kindness he has shown to me over the years. I should also like to thank Dr. C. Ruiz for instructive discussions at various stages of the work.

The computer program for data analysis was written by Dr. Ruth Thomas and Mark Taylor and Roger Stone respectively gave considerable technical support and advice while John Mooney was particularly helpful with photographic work. To all these individuals I am very thankful. Financial support from the Polytechnic, Ibadan, Nigeria and also from the USAF is gratefully acknowledged. It was under the former's Staff Development Programme that I was able to come to Oxford. Finally I should like to express my appreciation to Karen Smart and Lynn Riches who worked all hours of day and night in order that this thesis should be typed in time.

To my family

CONTENTS

CHAPTER 1

INTRODUCTION

CHAPTER 2

TESTING EQUIPMENT AND TECHNIQUES

CHAPTER 3

THE ANALYTICAL PREDICTION OF STIFFNESS AND STRENGTH OF INTERLAMINATED FABRIC-REINFORCED HYBRID COMPOSITES

CHAPTER 4

EXPERIMENTAL RESULTS

CHAPTER 5

COMPARISON OF ANALYTICAL PREDICTIONS AND EXPERIMENTAL RESULTS

CHAPTER 6

DISCUSSION

CHAPTER 1 - INTRODUCTION

1.1 Why Reinforced Plastics?

Basic structural design requirements may be said to be largely responsible for the current level of materials research. Structures including age-long ones like shells, clubs and armour must fulfil such diverse requirements as high strength, high stiffness, toughness and low density if they are to be safe, efficient and cost effective. Indeed the search for materials with these attributes has always been the subject of research.

Primitive engineering structures were based on wood which was readily available and could easily be shaped. The use of thick sections provided the required stiffness and strength. When steels became available, the use of wood as a structural material was de-emphasized and means were found for economically shaping these new materials of greater stiffness and strength. It was also possible to obtain increased strengths in steels by manipulating the microstructures through conventional metallurgy. However, the same does not apply to stiffness. Stiffness epitomized by the elastic modulus is structure insensitive and the development of strong aluminium and titanium alloys did not result in any significant improvement (see Fig. 1.1 from [1]); the specific stiffness (ratio of elastic modulus to specific gravity) of metals being fairly constant. And so the search for structurally efficient materials continued. But the clues were all there.

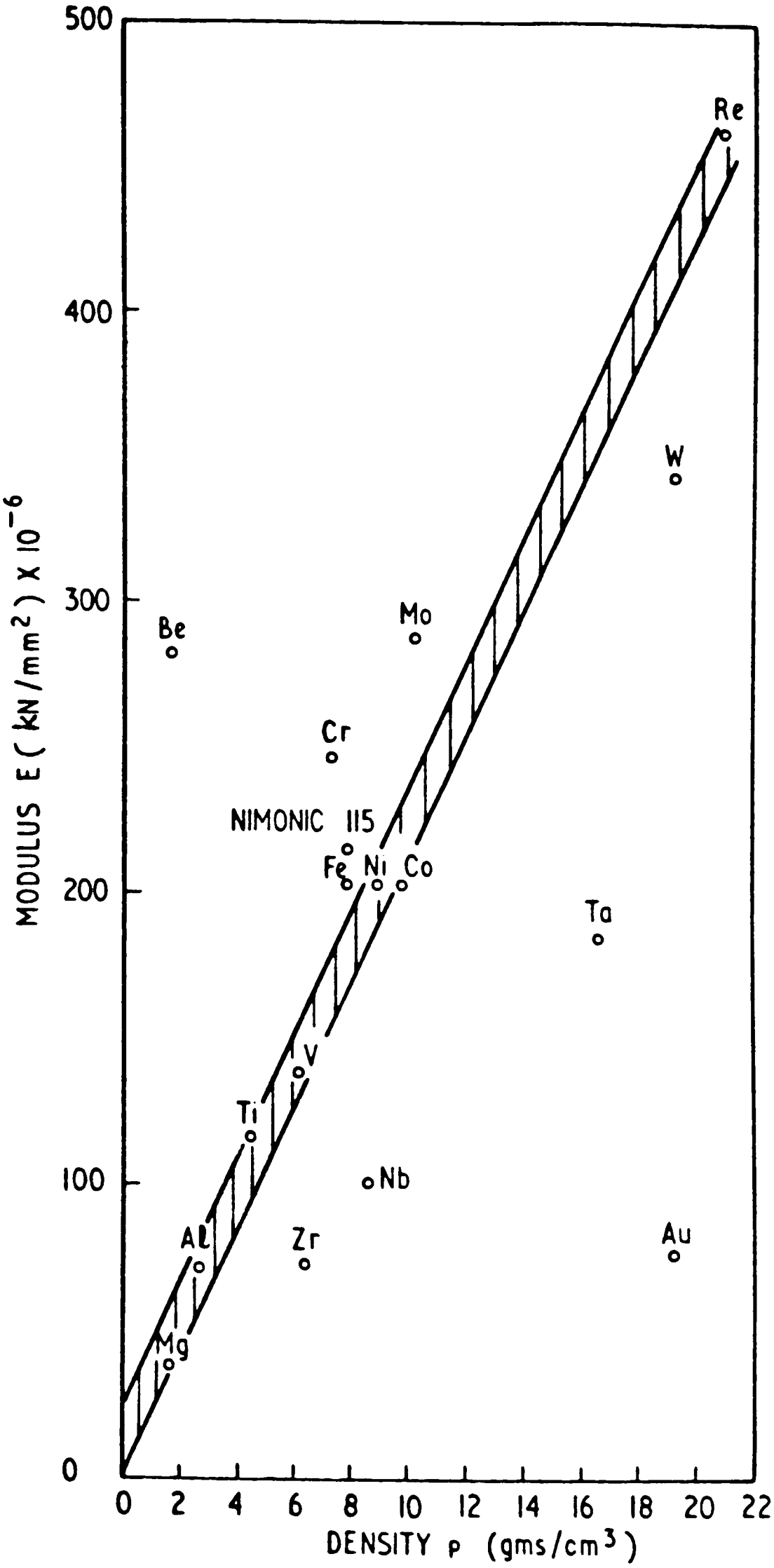

MODULUS AGAINST DENSITY FOR METALS
(after Hancock and Hokenhull [1])

The Egyptian bricks of ancient civilization invariably contained some straw [2] which not only assisted the evaporation of moisture from the interior but resulted in an even distribution of cracks; while stiff collagen fibres embedded in a weaker matrix results in the strong, stiff composite tissues in the body [3]. Indeed many naturally occurring materials derive their superb properties from a combination of two or more components which can be distinguished readily when examined in an optical or electron microscopes. It is curious, therefore, that the first breed of fibre reinforced plastics [FRP] did not surface until the early 1940's [4]. Perhaps, as Cottrell [5] observed, "we have been slow to learn from nature".

1.2 Stress Transfer Mechanism - Efficacy of Continuous Fibres

The main objective of a fibre/resin composite is to combine the merits of its constituents while simultaneously mitigating their less desirable characteristics. The matrix on its own, is a weak low modulus material having a relatively high coefficient of thermal expansion. The fibre on the other hand is highly susceptible to surface damage which impairs its excellent stiffness and strength. Suitably combined, the result is a material of considerable stiffness and strength coupled with a comparatively low coefficient of thermal expansion. In the process, however, a non-nominal third phase (the fibre/matrix interface) is introduced. This phase is significant in that it sometimes dominates the entire spectrum of the material response - a pointer, perhaps, to the complexity of FRP.

To illuminate the mechanism of mechancial property enhancement accruing from the union of fibre and resin we consider the idealised reinforced plastic schematically illustrated in Fig. 1.2. Here, a single fibre of diameter d, and breaking stress σ_f, is partially embedded in a polymeric matrix. Under the applied tensile stress, sliding friction develops at the fibre-matrix interface resulting in the building-up of tensile stress from the fibre end contained by the resin. This indeed is the process of load transfer by the resin to short fibres. For the embedded length l, and an interfacial shear strength τ, the force equilibrium equation is

$$\pi d l \tau = \frac{\pi d^2}{4} \sigma_f$$

or

$$\frac{l}{d} = \frac{\sigma_f}{4\tau} \qquad (1.1)$$

where $\frac{l}{d}$ is the fibre aspect ratio. It is clear from equation (1.1) that for $\frac{l}{d} > \frac{\sigma_f}{4\tau}$, the fibre will break rather than pull out. If, however, $\frac{l}{d} < \frac{\sigma_f}{4\tau}$ the reinforcement may be pulled out of the resin. It follows, therefore, that a stress equal to the breaking stress of the fibre can be transferred to it by the matrix if and only if the fibre aspect ratio exceeds that given by equation (1.1). In a real composite, the fibre is wholly embedded in the resin and stress is transferred to the former from both ends, in which case the critical fibre aspect ratio is given by

$$\left(\frac{l}{d}\right)_c = \frac{\sigma_f}{2\tau} \qquad (1.2)$$

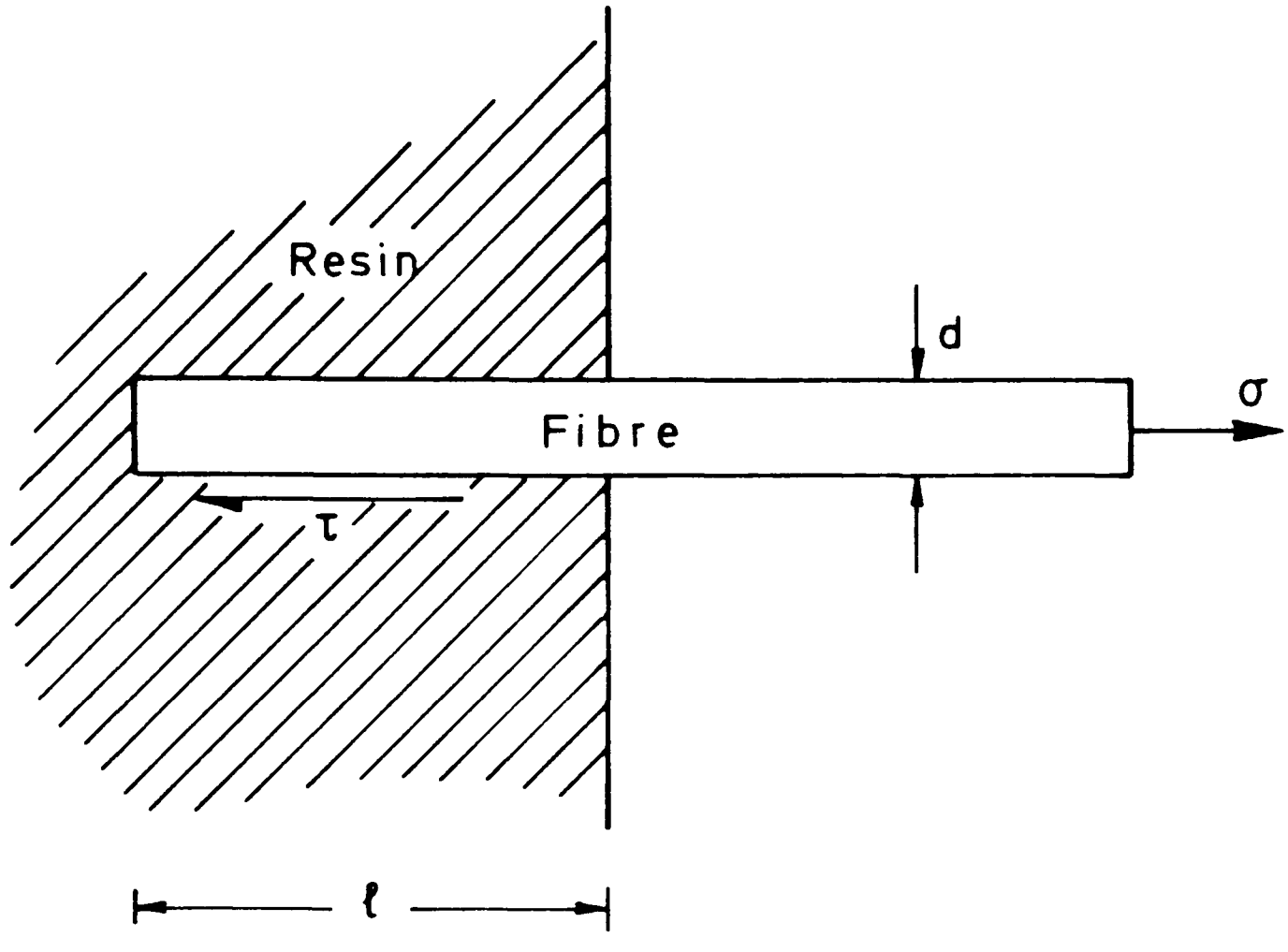

Fig. 1.2 Idealised FRP material under applied tensile stress

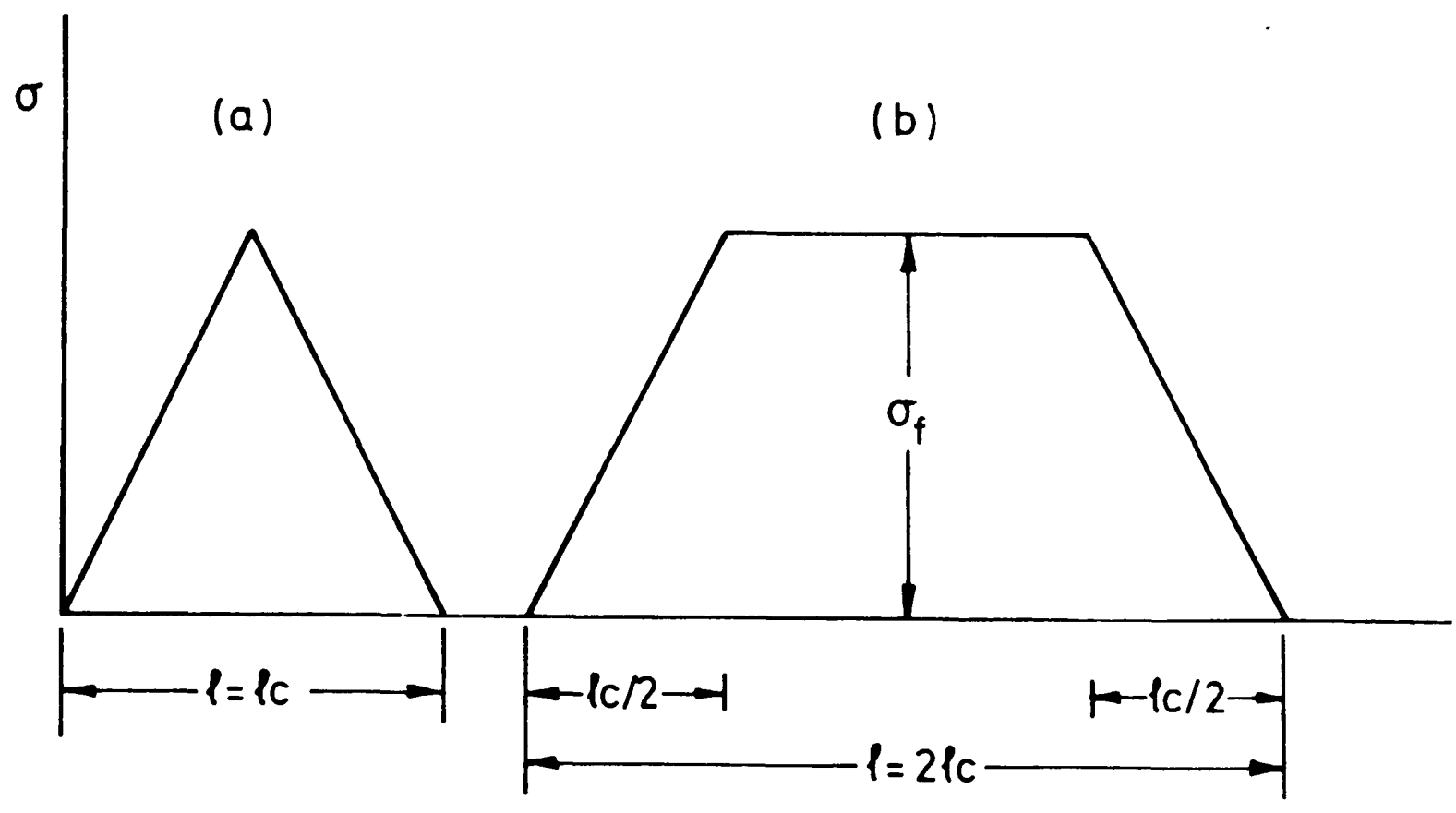

Fig. 1.3 Variations of fibre tensile stress for (a) $\ell = \ell_c$ and (b) $\ell = 2\ell_c$

Alternatively equation (1.2) may be written as

$$l_c = \frac{r\,\sigma_f}{\tau} \qquad (1.3)$$

where r is the fibre radius and l_c, the critical stress transfer length.

For advanced composites (i.e. polymeric materials reinforced with glass, carbon or Kevlar fibres), the critical stress transfer length is only a fraction of a millimetre.

Precise distribution of stresses (shear and tensile) along the fibre in discontinuous fibre/resin composites has been the subject of theoretical work and was reviewed by Kelly [6] and Holister and Thomas [7]. It is usual, however, to assume a linear build-up of tensile stress (as in the preceding example) from the fibre ends. Based upon this assumption, the variations of tensile stress along the fibre for $l = l_c$ and $l = 2l_c$ (see Figs. 1.3(a) and (b)) are obtained. It is obvious that only by using fibres much longer than the critical stress transfer length can the full strengthening potential of the reinforcement be utilised. In general the mean stress, σ_A, carried by the fibre is given by

$$\sigma_A = \sigma_f \quad \frac{l - l_{c/2}}{l}$$

or

$$\sigma_A = \sigma_f \quad (l - {}^{l_c}/_{2l}) \qquad (1.4)$$

For the special case of continuous fibres, $l_c = 0$ and

$$\sigma_A = \sigma_f \qquad (1.5)$$

Putting $l = 10l_c$ in equation (1.4) we obtain $\sigma_A = 0.95\sigma_f$. In other words, a short fibre composite whose fibre length is ten times the critical stress transfer length is able to attain 95% of the reinforcement of a continuous fibre composite, though matrix creep may be a problem at high stresses [8].

From the foregoing, we may also add that a continuous fibre/resin composite will exhibit a higher modulus than the equivalent short fibre composite when both are strained by the same amount, and the advantage of continuous over discontinuous FRP in terms of strength and modulus enhancement may be appreciated. Current emphasis on polymeric materials reinforced with continuous fibres especially in engineering applications is most probably related to this observation. In the above discussion, we have tacitly assumed that the failure strain of the fibre is less than the matrix failure strain. When the converse holds, failure is initiated at the matrix failure strain and the subsequent behaviour of the composite depends, at least partially, on the relative proportions of the constituents. A typical value of fibre content (by volume) in commercial FRP is 60%.

1.3 Fibres, Matrices and the Interface

The main components of a fibre/resin composite are the reinforcing fibre, the matrix and the fibre/matrix interface, but undesirable

elements like voids and inclusions, especially the former, cannot be neglected. A note on the measurement of void content appears in Chapter 2 and selected properties of FRP components are given at the end of this section.

1.3.1 Fibres

The principal role of fibres in FRP is to improve the specific mechanical properties. Ideally, therefore, prospective reinforcements will possess a high density of covalent bonds and be related to the lighter atoms like Boron, Hydrogen, Nitrogen, Carbon, Silicon, Oxygen, etc [9]. Such reinforcements have in fact been developed using appropriate production methods. Examples are carbon and boron fibres. However, other considerations like cost, toughness and ease of fabrication have extended the list of candidate materials so that in addition to carbon and boron fibres, glass fibre is widely used and metallic and natural fibres have been explored [10,11]. None the less, the reinforcements which are commonly used today and are likely to dominate the FRP scene for the next decade are glass, carbon and Kevlar [12]. Further discussion in this section is therefore limited to these fibres.

Glass Fibre.

This is the commonest and cheapest man-made reinforcing fibre and has been used in various forms for more than forty years. Four grades of the material have been identified [13]. These are: A (high alkali), C

(chemical), E (electrical) and S (high strength). Only the last two are of particular interest in composite work. E-glass is a borosilicate material originally developed for electrical applications but was found to be adaptable and highly effective in a great variety of processes and products ranging from decorative to structural. S-glass is a silica alumina magnesia mixture which may be preferred to E-glass in situations demanding higher strength and stiffness if the higher cost can be justified. It exhibits superior strength retention at elevated temperatures and has a high fatigue limit [14].

Continuous glass fibre manufacture employs marbles as raw material. These are fed into an electrically heated crucible otherwise known as a "bushing". At the base of the bushing are several holes (usually about 200) through which filaments are drawn at high speed and a filament diameter as small as ~5μm may be attained. A sizing is applied to the filaments just before they are gathered into a strand. The strand is then wound on to a forming cake until the desired weight is reached, when the winder is stopped and the cake removed. The cake is subsequently dried or cured (depending on the sizing) and the strand processed into roving of typically 1 or 12 strands. A review of glass fibre manufacture is contained in reference [15]. Glass is very much a supercooled liquid and as such is amorphous. The properties of the fibre are isotropic.

Carbon Fibre.

The first application of carbon fibre dates back to the latter part of the nineteenth century when Thomas Edison employed a carbonisation

process to produce the carbon fibre that was used as filament material in incandescent lamps. Despite this early record of its application, the versatility of the element (carbon) has only recently been exploited. In the effort to obtain a strong, stiff, thermally stable material for use in aerospace structures, interest fell on derivatives of graphite. Graphite, a common crystal form of carbon possesses a sheet structure in which one carbon atom is covalently bonded to three others in the plane of the sheet. The sheets are stacked in the ABAB manner with van der Waals bonds between them. Consequently, the graphite crystal is anisotropic. Observed values of intraplanar and interplanar moduli are 1000 and 35 GPa respectively [16]. To produce a carbon fibre with a high axial modulus, therefore, the sheets must be oriented parallel to the fibre axis. Indeed, all carbon fibre production processes utilize this idea. The various methods employed in carbon fibre manufacture make use of some polymeric material (the precursor) which is oxidised and carbonised under controlled conditions to obtain a fibre with the desired properties. Typical precursors are polyacrylonitrile (PAN), cellulose and pitch. The PAN based carbon fibre developed at the R.A.E. Farnborough in the early 1960s constitutes the majority of commercially available carbon fibres [17]. An outline of the production process for the PAN based fibre is given below:

(i) Oxidise under tension at 220^{o}C to crosslink and maintain molecular orientation within the fibre.

(ii) Carbonise at 1000^{o}C - no tension.

(iii) Post-treat at temperatures up to 2500°C to promote the desired structure. Optimum strength and modulus are obtained at 1500 and 2500°C respectively.

The completed fibre is usually surface treated to improve adhesion to organic matrices. Fibre diameter is typically 7-8 μm and designations are Type I (the stiffest), Type II (the strongest) and Type III (the cheapest).

Kevlar Fibre.

The enormous modulus and ultimate stress (300 and 18 GPa respectively) of macromolecules based on bond strength analysis [9] indicate a high potential for stiffness and strength in polymeric materials, but as normally prepared, the molecules are coiled or randomly oriented and the materials are weak and of very low modulus. However, exceptional properties may be obtained if the chains are stretched during their conversion into fibre. Encouraging results have been obtained with linear polyethylene using such processes as drawing and extrusion [18]. Fibrillar crystals may also be grown from flowing solutions. None the less, these techniques are not suitable for high melting point polymers such as aromatic polyamides (aramids) [19], even though the real hope in organic fibres as reinforcements lies in these materials. Low melting point polymers (e.g. polyethylene) are not generally useful because of the dramatic decrease in tensile properties at elevated temperatures and the propensity to creep.

A very significant development took place at the Laboratory of E.I. du Pont de Nemours in the USA where aromatic polyamide fibre (Kevlar) was successfully produced. A discussion of the underlying principles and the method of production has been given by Magat [19]. The essential stages in the manufacture of Kevlar are as follows:

(i) Preparation of a concentrated solution of the polymer in strong mineral acid such as oleum. This solution is crystalline and contains highly ordered domains of extended polymer chains.

(ii) The solution is filtered and passed through spinnerets into a neutralising bath.

(iii) Finally, the spun fibres are washed, dried and heated in nitrogen at temperatures up to 550^{o}C under tension.

The end-product is a yellowish fibre with a range of moduli from ~60 to ~130 GPa and strengths up to 3.0 GPa.

Two types of Kevlar are available, Kevlar 29 and Kevlar 49. Kevlar 29 has roughly half the modulus and twice the elongation of Kevlar 49. The diameter of the two types of fibre is approximately 12μm.

1.3.2 Matrices

"Bundles of fibres are, in themselves, of relatively little use to an engineer, no matter how strong or rigid the individuals in the population may be, and it is only the presence of a matrix or binder that

enables us to make use of them" [20]. However, binding capability is only one of several conflicting requirements of the ideal resin matrix. Other requirements include the ability to infiltrate among individual fibres, form a chemical or in certain cases, a frictional bond and solidify quickly at as low a temperature and pressure as possible. Additionally, the matrix must protect the filaments from mechanical damage and be resistant to chemical attack and the influence of moisture. Thermosetting resins are said to conveniently fulfil most of the above requirements [21], which is why they are dominant in composite manufacture. None the less, thermosetting resins have several weak points including: a short pot-life, elaborate cure operations and poor resistance to creep and impact. Consequently, thermoplastic polymers are being actively studied for use as matrix materials. Polyetheretherketone (PEEK) is probably the most promising in this respect and a case for its use in high performance composites was admirably made by Belbin [22]. A review of recent effort in thermoplastic matrix development has been given by Cogswell and Leach [23]. Of the thermosets, polyester resins have the longest history of application in composite work, having been developed for use with glass fibres. They exhibit good physical and chemical properties and are relatively cheap. However, for composites based on continuous carbon and aramid fibres, epoxy resins are to be preferred. The use of epoxy resins results in better properties but they are rather expensive and may present curing problems. Information on commercially available resins and their applications in composite fabrication may be found in reference [24].

1.1.3 Interface

The incorporation of fibres in a resin followed by a cure at room and/or elevated temperature results in the adherence of the resin to the fibres. And it is the degree of coupling between the two constituents that identifies the interface. Despite the general agreement that the interface exerts considerable influence on composite mechanical properties, it is most probably the least understood of the main components of a reinforced plastic. And the use of inprecise phrases like "interfacial strength" or "interfacial bond strength" often adds to the confusion.

Consider a composite lamina composed of aligned, unidirectional fibres in a resin matrix. An increasing tensile load is applied in the fibre direction until the composite fails. Prior to ultimate failure, several events might occur. The matrix might have cracked and fibres broken. An examination of the fracture surface may reveal some fibres that have pulled out of the matrix - their average length depending on the interfacial shear strength of the composite. In compression parallel to the fibres, the matrix will tend to support the fibres against premature buckling. What support is available will again depend on the interfacial shear strength. However, the application of a tensile load in a direction normal to the fibres presents a slightly different situation. The failure strength of the composite now depends on the interfacial tensile strength. It is assumed that the strength of the bulk resin is greater than the tensile strength of the fibre/resin interface. The foregoing examples are somewhat idealised as the

thickness of a composite lamina may be of the order of 0.12 mm and the specimen is not amenable to such mechanical tests. None the less, similar observations have been made on tests with practical composite specimens [25,26]. Also, structural elements are frequently subjected to complex stressing for which unidirectionally reinforced configurations are unsuitable. The usual approach in such cases is to base the structure on several bonded laminae, each containing a single layer of reinforcement (unidirectional or multidirectional e.g. woven) with various orientations such that the structure can resist load in several directions. This introduces another type of interface - that between any two adjacent laminae; and is characterised by the interlaminar shear strength. The ease with which the laminate deplies (delaminates) under any loading situation depends on the interlaminar shear strength.

Because of its significance in relation to composite properties attempts have been made to quantify the interfacial properties of composite materials. Techniques for measurement of interfacial tensile and shear strengths are based on single fibre tests [27] while the simplest and most popular method for measuring the interlaminar shear strength is the short beam shear test. Although these are not true measurements of interfacial properties they are informative in showing the effect of resin properties and fibre finishes on resistance to decohesion [28]. It is also significant that the various properties of the interface follow the same trend [29,30]. Information on fibre finishes for interfacial property enhancement are available from most handbooks on composite materials.

1.4 Desirability of Impact-Loading Design Data

From what has been said, it is readily appreciated that FRP are complex materials whose mechanical behaviour may be no less complex. However, the weight-saving advantage of reinforced plastics over more conventional structural materials (see Fig. 1.4) and the possibility of tailoring the materials to specific design requirements are among the attributes that commend them to many areas of industrial activity.

Notable aerospace applications of CFRP include [33] the truss structure of the Applications Technology Satellite (ATS) - Model F, whose orbital distance from the earth is approximately 22000 miles (~ 35400 km). Temperatures of between -250°F (-157°C) and + 250°F (121°C) are encountered in outer space and the satellite's accuracy depends on the position of the Earth Viewing Module, with respect to the antenna, being maintained within very close tolerances. The high specific strength of CFRP coupled with its low coefficient of thermal expansion (along the fibres) satisfies this requirement.

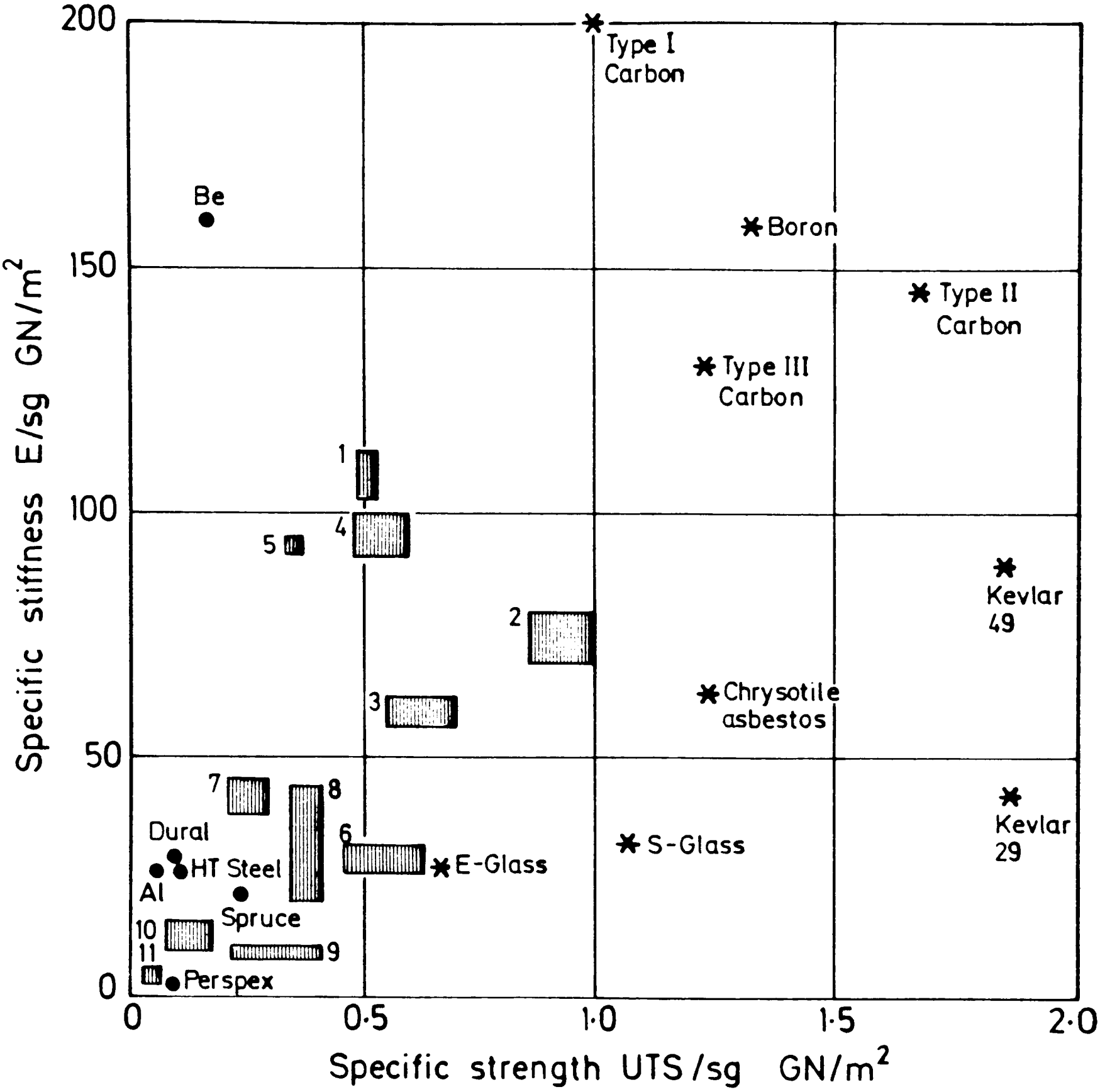

Composite properties

Fibre properties

Bulk material properties

1 Aligned Type 1 carbon/epoxy
2 Aligned Type II carbon/epoxy
3 Aligned Type III carbon/epoxy
4 Aligned Boron/epoxy
5 Aligned Boron/Aluminium
6 Aligned Glass/resin
7 Aligned Asbestos/Plastics
8 Woven Type II Carbon/epoxy
9 Woven Glass/Polyester
10 Random Asbestos/Plastics
11 Random Glass/Polyester (chopped strand mat)

Fig. 1.4 Specific properties of engineering materials. (after Green and Phillips [31])

Table 1.1 Quasi-static room temperature properties of some FRP constituents

Material	Ultimate Tensile Strength MPa	Tensile Modulus GPa	Strain at break in tension %
E-Glass	1700	70	2-3 **
S-Glass	2600	80	-
Carbon I	2000	400	0.5 **
Carbon II	3000	260	1.0 **
Carbon III	2200	230	-
Kevlar 49	2700	130	2.1 ***
Kevlar 29	2700	60	4.0 ***
Epoxide	55.0 - 120.0*	2.0 - 5.0*	1.5 - 8.5*
Unsaturated Polyester	42.0 - 90.0*	1.2 - 4.0*	2.0 - 6.0*

Unless otherwise indicated data are from Green and Phillips [31]

* after Hancox [4]

** after Powell [32]

*** Anon

Composites based on glass or Kevlar fibres are now widely used in marine environment. Their performance is trouble-free and maintenance costs low. They are also resistant to boring organisms and are easy to repair [34].

Successful applications of FRP to date owe much to basic design data that have been made available. Unfortunately, these data are predominantly of the quasi-static loading, room temperature type. FRP are frequently subjected to other types of loading, especially impact. Impact problems can be most serious in the aerospace field. The closing speed of the damaging agent varies from less than 1 m/s for dropped tools and careless handling, through stones, birds and hail, up to engine debris, small arms fire and missile fragments at several hundred m/s [35]. In applications to protective armour, composites are subjected to particularly high velocity impacts. These impact loadings are of short duration, of the order of 100μs and a strain rate of a few hundred per second [36]. The design of vehicles for improved impact response, in particular the low speed 5 mph (8 km/h) no-damage behaviour and higher speed 30 mph (48 km/h) survival requirements necessitate knowledge of material behaviour at strain rates commensurate with these speeds [37].

The CFRP compressor blade of Rolls Royce RB 211 engine [38] failed under bird impact. This experience is in contrast to another incident [39] in which a 74ft (~22.6 m) glass/polyester composite trawler was accidentally crushed between the quayside and a 26000 ton (~26440 tonne) tanker - her hull was compressed by 9 ins (~22.9 cm) amidships. Although the superstructure and deck were extensively damaged, the hull returned

to its original dimensions. After redecking the boat returned to service with no repairs of any kind to the hull. Much as one may learn from incidents like these, a far less expensive approach to studying the impact response of composites is through the use of proven experimental techniques from which fundamental information may be obtained. Such information is indeed scarce. In the remaining sections of this Chapter, we examine some of the various attempts that have been made to fill this gap, the extent to which they succeeded and state the additional contribution we intend to make through the present work.

1.5 Developing Techniques for Impact Test on Composites

The poor impact resistance of advanced composites especially CFRP and the marked reduction in the quasi-static mechanical properties found for many FRP following micro-damage resulting from a prior sub-critical impact has made clear the need for a full characterisation of the behaviour of such materials under dynamic loading conditions. Early work in the 1970's [40-43] often adopted Charpy or Izod test configurations. These tests have the advantages of being easily and rapidly performed, and are very widely quoted. They are, however, to be criticised on many grounds, including: a complex specimen geometry, combined stress system comprising bending and shear, and the attendant problem of correlating the impact energies which they measure with service performance. For this reason, many manufacturers prefer to rely upon component testing, despite the high cost of this approach [44]. An innovation to the Charpy

set-up is the instrumentation of the tup from which load-time and energy-time records may be obtained. Even with this modification, several problems remain. Among these is the accuracy of the load measuring system under impact conditions. The load on the specimen is sensed via strain gauges mounted on the sides of the impacting tup. Since the gauges are some finite distance from the point of contact and the tup is part of a more rigid structure consisting of the pendulum and the mounting mechanism, wave reflections and interactions from the various free and fixed boundaries are often superimposed on the signals recorded with the strain gauges [45]. For brittle reinforced plastics, the test duration under impact loading is especially short and the question arises as to how important wave reflections might be in the interpretation of the experimental data. Additionally, the energy contribution from the impacting machine stiffness and vibration must be considered [46]. A recent analysis [47] of the Charpy set-up concluded that a rigorous specification of the dynamic characteristics of the machine is required if the test is used for the determination of material properties rather than just for quality control.

Examples of other technological impact tests which like the Charpy or Izod may not provide fundamental information on material response but are at the same time useful in simulating in-service impact conditions are the 'ball-gun' [48] and 'drop-weight' [49] impact tests. The drop-weight impact test primary data is rather sensitive to noise and it is usually difficult to avoid distortions arising from processing [50].

The failure of the foregoing techniques to provide basic design data has led to the demand for more suitable tests from which dynamic mechanical properties may be obtained in tension, compression and in shear. Problems associated with the development of such tests together with some of the attempts that have been made to fulfil this demand are considered in Section 1.6.

1.6 Review of Work Already Done

1.6.1 Difficulties of Testing Under Impact

A common feature in all impact tests is the occurrence of wave propagation in the testing machine, the design of which must be such that wave propagation effects are accounted for in the analysis of the experimental data. In impact tests on composite materials, other difficulties arise - the degree depending on the type of test i.e. shear, compression or tension. In dynamic shear tests, a major problem is the development of a simple test specimen that gives repeatable results. The thin-walled tubular test-piece is generally accepted as being suitable for shear property measurement in isotropic metals but may be difficult to make in composite materials. More serious problems are encountered in dynamic compression especially when short cylindrical specimens are used. In uniaxial compression, frictional end effects may induce a multiaxial stress state in the specimen and are likely to modify material response. Any misalignment of the specimen to the axis of loading will cause significant bending stresses resulting in premature failure of the

specimen. Dynamic tension testing of FRP is probably the most difficult to accomplish. Reinforced plastics may be highly anisotropic. The longitudinal tensile strength/interlaminar shear strength ratio of unidirectionally reinforced CFRP may be as high as 60:1 [51]. This poses a serious problem with specimen design and gripping [51,52]. Naturally, in this test, a tensile failure in the gauge length is desired but the specimen tends to fail by shear in the vicinity of the grips. A specimen that satisfies the tensile failure requirement may not attain a uniform state of stress during the course of the test. In addition to all these, the specimen must be large enough compared with the scale of the reinforcement of the composite for it to be representative of the material as a whole. The impedance mismatch in the grip regions must also be minimised. Clearly, specimen design and gripping must be a matter of compromise.

Unlike metallic materials, the strains to failure of reinforced plastics are small (~ 1% for commercial CFRP) and the testing technique must facilitate the accurate measurement of strain.

1.6.2 Split Hopkinson Bar Type Tests.

For metallic materials, tests at the highest rates of loading are frequently performed using the split Hopkinson bar (SHB) technique. In recent years, however, this technique has been adopted in tests on other materials including composites [53-55]. Information on the principle and application of the SHB system may be found in references [56] and [57].

Compression tests:

Until relatively recently, attempts to adapt the SHB technique to composite material testing were limited to compression tests on short cylindrical specimens. One such attempt was by Sierakowski and his co-workers [58] who studied the dynamic response of steel wire reinforced epoxy over a strain rate range of 10^{-5} to 10^{3} s^{-1}. Although specimen faces were carefully ground and lubricated, different failure modes were observed at quasi-static and impact loading rates. This observation has been attributed, partly, to the "multiaxial states of stress induced in the short cylindrical specimens by the Hopkinson bar" [59]. Support for the observed change in fracture behaviour with strain rate, however, comes from work on woven glass reinforced epoxy [60] where longitudinal cracking predominates in dynamic compression as opposed to shear fracture at quasi-static loading rate.

Compression tests have also been conducted on epoxy based CFRP [55] with various fibre orientations with respect to the applied load. In longitudinal impact (i.e. parallel to the fibres) on unidirectionally reinforced specimens, a dependence of deformation behaviour on specimen length was observed. This difference in behaviour between long and short specimens was attributed to dissimilar boundary conditions.

Evidence that frictional end effects may not be significant in woven glass reinforced composites comes from a series of tests on similar cylindrical woven glass/epoxy specimens of different length to diameter ratios, from 1 to 2.5 [61]. In tests at both a quasi-static rate of

$\sim 10^{-3}$ s^{-1} and an impact rate of $\sim 10^{3}$ s^{-1}, the compressive strength appeared unaffected by the specimen geometry.

Shear tests:

Probably because of lack of general agreement on a simple specimen design for characterising FRP in shear, the SHB technique has not until recently been used for this purpose.

The punch-loading Hopkinson bar developed in the early 1970's has been used to investigate the dynamic shear response of various woven roving GFRP laminates [62]. Although primarily a technological impact test, it offers the advantages of a simple stress system and specimen geometry over comparable impact tests. An increase in through-thickness shear strength with punch speed was observed in tests on GFRP laminates.

In an attempt to obtain more basic information on the dynamic shear response of composites, tubular glass/epoxy specimens were tested in a torsional Hopkinson bar machine at shear strain rates ranging from 100 to 600 s^{-1} [63]. A strong dependence of yield torque on strain rate was observed. In contrast, the failure torque was relatively unaffected by variations in strain rate. However, in view of the specimen configuration, these conclusions must be treated with caution.

More recently, dynamic tests were conducted on woven graphite/epoxy laminates in interlaminar and transverse shear [64]. The SHB used is

similar to the compression version of the apparatus but incorporates a double shear fixture. Shear strain rates of up to 18 x 10^3 s^{-1} were attained in these tests. Considerable scatter was observed in the interlaminar shear tests but the shear strength remained fairly constant as the strain rate was varied from ~ 10^4 to ~1.8 x 10^4 s^{-1}. Delamination in the interlaminar shear tests, at all strain rates, was ascribed to fibre/matrix interfacial failure with little matrix adhering to the fibres; indicating, according to the authors, an insignificant effect of increasing strain rate on deformation mechanisms.

In transverse shear, the shear strength decreased with increasing strain rate and delamination density was correspondingly greater. The technique suffers from the small amount of material involved in the deformation process especially in interlaminar shear.

Tension tests:

The difficulties of testing FRP under impact tension were discussed in section 1.6.1. In spite of the scale of the problem, several attempts have been made to develop a tensile impact test for composite materials based on the SHB principle. Probably the first successful attempt to design this type of machine was that due to Kawata et al [65]. In their bar-block set-up, a cylindrical specimen threaded at both ends connects a long output bar to the loading block which is impacted by a rotating hammer. Strain gauges on the output bar monitor the tensile stress wave transmitted through the specimen and from which the output stress and

velocity may be obtained. The velocity of the input end of the specimen is assumed to be that of the loading block and is measured by an electro-optical device.

This apparatus has been used to study the tensile impact behaviour of GFRP and CFRP, and significant effect of strain rate on GFRP properties was reported; these properties increased as the strain rate was increased. No such effect was observed in CFRP specimens where properties at quasi-static and impact loading rates were hardly distinguishable.

However, certain aspects of the experimental technique give rise to some doubt as to the validity of the results obtained in these tests. In particular, the absence of an independent check of the specimen strain as obtained from the Hopkinson bar analysis is unsatisfactory. The use of a cylindrical as opposed to strip specimens is unorthodox and makes comparison with other similar work difficult. Failure to remove all play from the screw fixing to the output bar and loading block may result in uneven loading and spurious wave reflections. Accurately coaxial impact is required on the impact block to minimize bending stresses in the specimen.

A second design of impact tension test for composite materials [66,67] based on the standard version of the SHB first introduced in 1960 [68] largely circumvents the aforementioned weaknesses of the design of reference [65] and is the precursor of the present work. Although the apparatus is discussed in more detail in Chapter 2, some information on

the modification to the original design [68] is useful at this stage. In the modified version, a thin strip specimen of standard design [51] is fixed into slots in two elastic loading bars. The instrumented input bar screws into a yoke of similar material and the loading bar assembly is inserted in the existing weighbar tube. The length of the Hopkinson bar assembly, and by implication, the maximum test duration is therefore limited by the length of the tube. A compression stress wave is generated by physical impact on top of the tube and is subsequently reflected as a tension wave at its free end; this is transmitted to the input bar. Strain gauges on the input bar provide information from which the stress and particle velocity at the input end of the specimen are obtained, while the stress wave transmitted through the specimen is monitored by gauges on the output bar, and the output stress and particle velocity may thus be derived.

The equipment has been used to perform tests on unidirectionally reinforced carbon fibre/epoxy composites [66] where the elastic modulus and fracture strength were found to be fairly constant as the strain rate was increased from $\sim 10^{-4}$ to $\sim 10^{3}$ s^{-1}. A tensile failure in the centre of the parallel gauge region of the specimen with little damage to either side of the fracture surface was observed at all rates of loading. Within the constraints of the existing tube, the technique is either limited to specimens failing within 30 μs (e.g. unidirectionally reinforced CFRP) or requires a very careful determination of the input velocity from a separate test. This is one of the limitations of this set-up. In tests on higher strain to failure composites [67], therefore, the near-linear response obtained in a CFRP specimen test was used to

determine the input velocity. This is said to give a more accurate result than the standard 'elastic' test approach [68].

Unlike the tests on CFRP, tests on woven glass/epoxy composites showed a significant increase in strength, modulus and fracture strain at impact rates of strain over those observed under quasi-static loading. The change in failure mode from limited damage at low rates of loading to widespread damage under dynamic loading conditions is assumed to account for the increase in energy absorption in GFRP at impact rates of strain.

1.6.3 Other High Rate Tests

Either for experimental simplicity or to avoid difficulties intrinsic in the SHB technique, other impact test configurations are sometimes used.

The dynamic stress-strain response of a unidirectionally reinforced glass/polymer composite was investigated by a wave propagation technique [69] in which a rigid mass impacted the free end of a 1m by 10 mm diameter rod material. Wave propagation records from strain gauges suitably positioned along the specimen were used in conjunction with a model of the material mechanical behaviour to construct the dynamic stress strain curve in compression. However, the need for separate experiments to determine some constants in the model renders the technique of limited value for the rapid evaluation of FRP.

More fundamental information may be obtained from a drop weight impact test when an instrumented load cell is used and provision is made for the measurement of specimen strain. Nevertheless, the technique is bedevilled by stress wave reflections in the load cell and the rate of deformation is therefore very limited. This technique has been used in tension tests on E-glass fibre bundles and matrix resins [70] as well as GFRP [70,71]. The maximum strain rates attained in the tests were 30 s^{-1} [70] and 4 s^{-1} [71] and in both cases, strain measurements were made by bonding gauges onto the specimen. This method of strain measurement is very accurate up to the point at which the gauges fail but is unsatisfactory for materials which exhibit surface damage prior to failure.

Attempts have been made to use hydraulically operated machines for high strain rate testing of composites. The technique may be adequate in the medium rate range but is unsuitable for tests at high rates of deformation. Thus Daniel and Liber [59] successfully conducted tension tests on various composite materials using an electro hydraulic machine up to a maximum strain rate of 27 s^{-1}, but an attempt by Davies and Magee [37] to use a similar machine, in similar tests, at rates in excess of 80 s^{-1} met with difficulties. According to these authors, "ringing occurs due to the reflection of elastic stress waves in the sample and the test machine, and is manifest in the stress-strain curve".

A technique proposed by Daniel et al [36] overcomes some of the difficulties inherent in the SHB method. Here, the specimen, in the form of a thin ring, is loaded by an internal pressure pulse. In theory, the

specimen is stressed uniformly at all times so stress wave reflections do not arise and problems associated with end effects and the fixing of the specimen to the loading bars are eliminated. Nevertheless several major disadvantages remain [67]. The specimen experiences a continuously decreasing strain rate throughout the test. The state of stress in the ring specimen is far from simple including, as well as membrane stresses, a pressure induced radial stress at the inside face and shear stresses resulting from any variation in the dynamic load along the axial direction. Also the practical difficulty of making the specimens and actually performing the tests limits its value as a technique for the rapid evaluation of a large number of materials, particularly composite materials.

From the above examples it may be concluded that there is no real alternative to the SHB system for characterising composite materials at impact rates of strain.

1.7 Strain Rate Effects in FRP

Before discussing the effects of strain rate on FRP, it is helpful to consider the individual rate dependencies of the components i.e. the reinforcing fibre, the matrix and the interface.

1.7.1 Fibres

That little information is available on the response of fibres at high rates of strain is a direct consequence of the experimental difficulties involved in performing such tests. Possibly the only successful attempt to date is due to Rotem and Lifshitz [70] who conducted tension tests on E-glass fibre bundles at moderate rates of ~5 to ~30 s^{-1}. A drop weight impact machine was employed in these tests. An increase in fracture strength of ~200% was observed over similar tests performed in an Instron machine at a strain rate of ~10^{-6} s^{-1}. In the absence of similar data for carbon or Kevlar fibres it is generally assumed that they do not show any significant rate dependence either of strength or fracture strain [72].

1.7.2 Matrix

Most studies of the effect of strain rate on polymeric resins have been conducted in compression [73-75]. These results show that polymeric resins exhibit considerable increase in fracture strength at higher loading rates.

In tension, more recent work [76] on epoxy resin specimens shows a less pronounced but still significant effect of strain rate on fracture strength. A clear picture on the trend followed by the fracture strain is still to emerge.

1.7.3 Interface

In the absence of a generally acceptable technique for measuring interfacial properties, it is only realistic to talk of their relative strengths (i.e. weak or strong). This is easily inferred from failed composite specimens and may be supplemented by optical or electron microscopy.

If we are to believe the result of Werner and Dharan [64] who used the SHB technique to measure the interlaminar shear strength of woven carbon/epoxy laminates and obtained no rate effect up to a shear strain rate of 1800 s^{-1}, then the interfacial properties of the woven carbon/epoxy laminate are strain rate insensitive. This follows from the observation that interfacial properties follow the same trend [29,30]. No similar tests have been performed on glass or Kevlar based composites. However, it has been suggested [77] that in brittle/brittle systems (i.e. brittle fibre/brittle matrix composites) the energy contribution comes mainly from the frictional work required to pull broken fibres from the matrix after the latter has cracked. The increased energy absorbed by woven-glass/polyester composite specimens [78] at high rates of loading may be associated with increased fibre pull-out suggesting a reduction in the interfacial shear strength at high strain rates.

1.7.4 Strain Rate Effects in FRP

The components just considered often interact in an unpredictable manner and their rate dependencies are therefore not additive. The reinforcement geometry is particularly important as it contributes significantly to the level of interaction between the various constituents of the composite.

For example, the mechanical properties of unidirectionally reinforced specimens in the direction of the fibres under tensile loading largely depend on the fibres which are much stronger and stiffer than the matrix. That rate effects have been observed in unidirectional GFRP [70,71,79] and not in unidirectional CFRP [66] is directly related to this.

Matrix properties, however, may be important in unidirectionally reinforced specimens under compressive loading where the shear modulus of the matrix should be great enough to support the fibre against buckling failure [72].

In woven reinforced composites, there is greater interaction between fibre and matrix, and resin cracking at fibre crossovers which are regions of stress concentration will lead to debonding. This allows the crimp to straighten out along the stress direction and so give apparently better properties [80].

1.8 Reasons for Present Work

The results of work reported in reference [67] may be summed up as follows:

Glass fibre reinforced materials show a markedly increased modulus, strength, strain to failure and ability to absorb energy under impact loading whereas this is not true for CFRP.

In general terms, this marked difference between the impact response of glass/epoxy composites and carbon/epoxy composites has been known for some time [41] and has led to the introduction of hybrid composites where the high 'toughness' of GFRP at impact rates is combined with the high stiffness of CFRP at all rates in an attempt to optimise the overall mechanical behaviour. Most studies of the impact response of hybrid composites, however, have employed Charpy type tests [81,82]. The inadequacy of Charpy type tests has already been stated [see section 1.5]. Although the bar-block impact tester of Kawata et al [65] was recently used for tests on hybrid composites [83] this work is qualitative, and the uncertainties in the technique as stated in section 1.6.2 leave its results open to question. The technique employed by reference [67] avoids many of these limitations and should therefore, allow a more fundamental study to be made of the impact response of hybrid composites. This then is the main objective of the present work. Nevertheless, two outstanding problems relating to the technique used in reference [67] must first be resolved. These are:

(i) The physical dimensions of the apparatus limits the technique to specimens that fail within ~30 μs or requires very careful determination of the input velocity.

(ii) In tests on commercially-produced (high volume fraction) unidirectionally reinforced GFRP with similar specimen design as for the CFRP, failure always occurred in shear within the specimen at the resin/fibre interface nearest to the slots in the loading bars.

The first problem may be resolved by extending the dimensions of the existing apparatus i.e. using longer loading bars and a weighbar tube to match. Because of space restriction in the test area a horizontal loading set-up has to be adopted, the impact being applied through a projectile accelerated by a compressed gas gun. A new gas gun will therefore be constructed.

The shear failure observed in commercially-produced unidirectionally reinforced GFRP may be due to its high tensile strength/shear strength ratio. We therefore propose to use materials that are based on woven reinforcement. Although such materials are not as strong as unidirectionally reinforced composites, they are widely used and have several advantages.

Of the woven reinforcements, the plain weave is the oldest and most common textile weave. Its construction is stable and provides porosity and minimum slippage [14]. Materials to be used in this investigation

will therefore be based on this reinforcement. A schematic of the plain weave fabric is shown in Fig. 1.5.

It is also hoped to model the linear-elastic stress-strain behaviour of laminated carbon/glass hybrid composites under impact loading from the elastic and strength properties of the constituent plies. Fracture mechanisms in impacted specimens are to be studied by optical and electron microscopy.

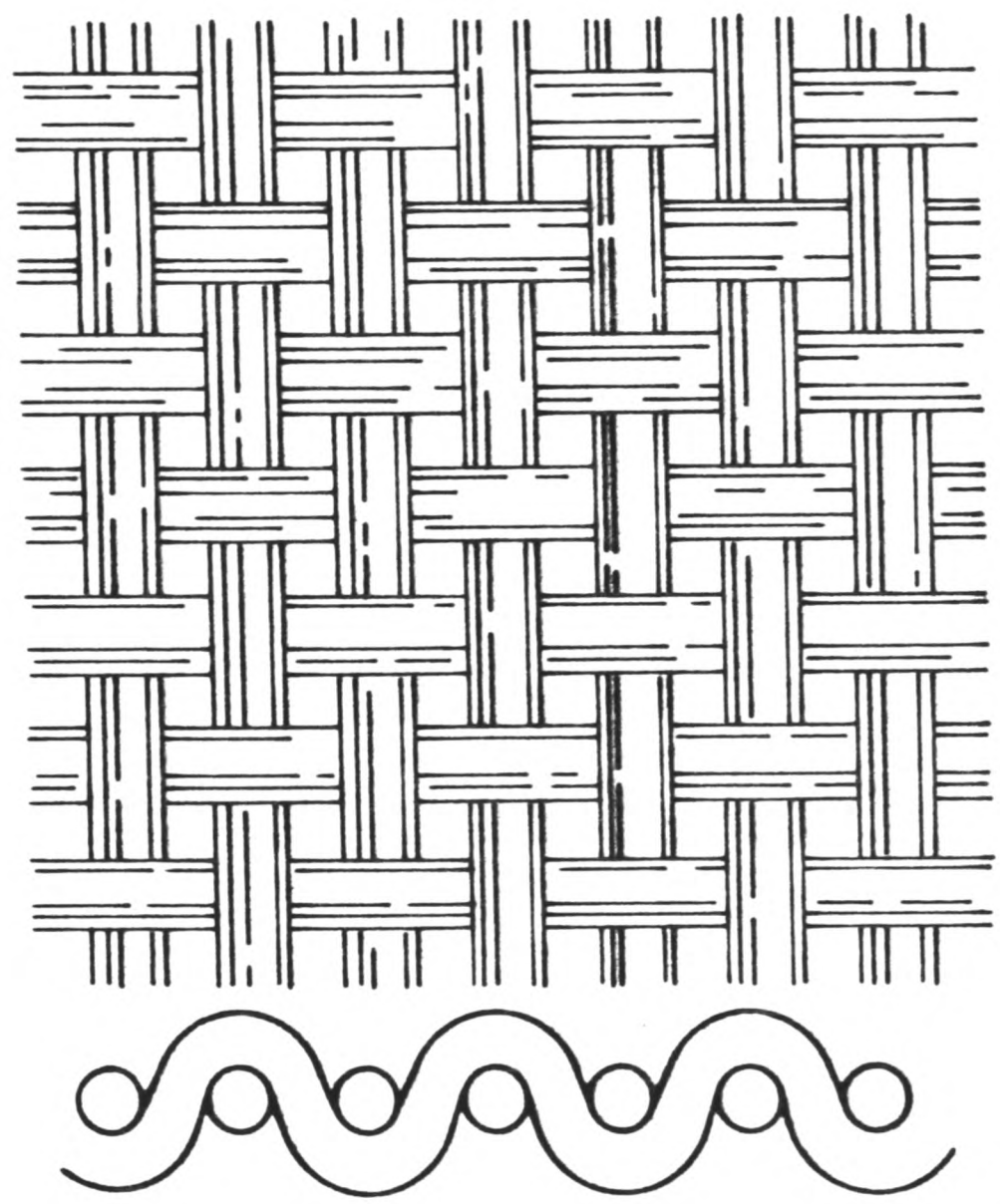

Fig.1.5 A two-dimensional plain weave fabric.

CHAPTER 2

TESTING EQUIPMENT AND TECHNIQUES

2.1 Introduction

The experimental programme was conceived with the following objectives in mind:

(i) to provide fundamental data on the room temperature tensile stress-strain response of hybrid composites based on carbon and glass, and their constituent plies over a range of strain rates from quasi-static (~ 10^{-3}/s) to impact (~ 10^{3}/s),

(ii) to explore the possibility of analytically predicting the elastic moduli and strengths of plain-woven carbon-glass/epoxy hybrid composites at a given strain rate from the elastic and strength properties of the constituent plies at that rate of loading,

(iii) to identify the mechanisms of fracture and energy absorption under tensile impact loading in the above materials.

The first two of these objectives called for the use of various testing equipment such as the tensile Hopkinson-bar machine at the

highest rate of loading, a hydraulically-operated loading system for the intermediate rate of deformation (~ 10/s) and the screw-driven Instron tester for quasi-static tests. The prediction of hybrid composite strength also required measurement of the compressive strengths of the all-carbon and the all-glass composites. For this purpose a special gripping attachment was incorporated in the Instron machine while a new impact compression rig was constructed.

Detailed descriptions of high and medium rate test equipment have been given in previous publications [84,85]. The emphasis, here therefore, is on modifications that suited them for testing composite materials. The design and operation of the Instron machine is well known and will not be discussed. The third aspect of the experimental programme is addressed in Chapter 4.

2.2 Gas Gun and Tensile Impact Apparatus

The tensile impact tester used previously for work on composite materials [67] is shown in Fig. 2.1. It is a modification of the "standard" tensile Hopkinson-bar apparatus originally developed in 1960 for testing metal specimens [68]. The introduction of an instrumented input bar eliminated the need for a complementary "elastic" test and greatly improved the accuracy of strain measurement in the elastic region but limited the maximum duration of test for which the full dynamic analysis is possible so that complete stress-strain curves could only be obtained for specimens fracturing within ~ 30μs. For the low modulus,

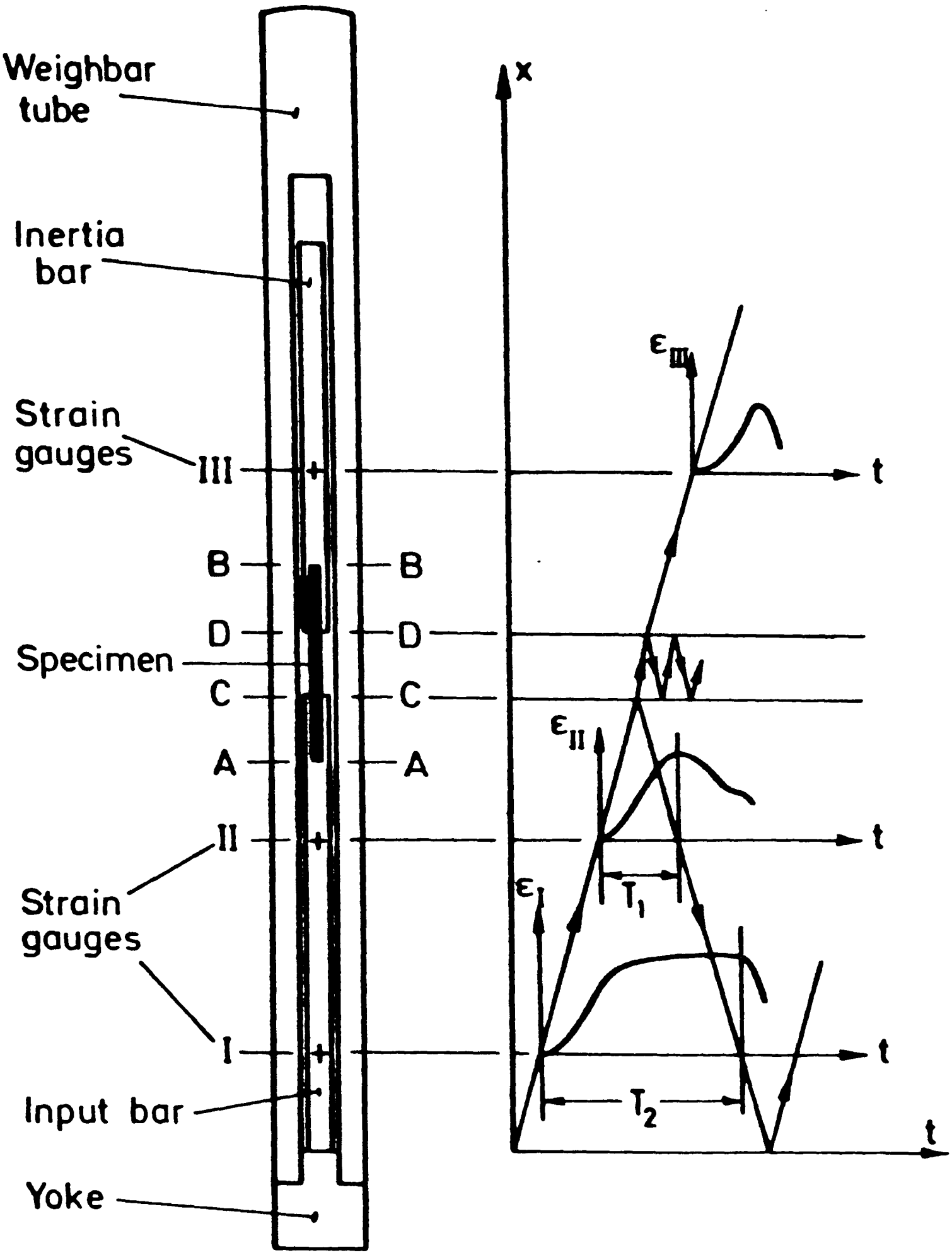

Fig.2.1 SCHEMATIC ARRANGEMENT AND LAGRANGE (x,t) DIAGRAM FOR TENSILE HOPKINSON-BAR

high strain to failure GFRP, therefore, it was necessary to revert to the standard technique before a complete stress-strain curve could be obtained. Although this problem might be solved by increasing the physical dimensions of the impact machine the use of a falling weight as the energy reservoir as had been the practice up till then, and the associated limitation of available space militated against this course of action. It is necessary, therefore, to use a different technique for applying the impact load and for this purpose it was decided to build a new gas gun. It then became possible to construct an extended version of the modified tensile Hopkinson-bar operating on exactly the same principles as before but allowing a full analysis to be performed at times up to 150 μs.

2.2.1 Gas Gun

In Hopkinson-bar systems, a convenient means of applying the load is through the impact of a projectile accelerated by a compressed gas gun. For an idealised gas gun, the projectile velocity at the muzzle depends on the reservoir pressure, barrel bore, projectile mass and barrel length. These parameters are interdependent and may be chosen to suit the particular test requirement. In the case under consideration, the form of the gas gun was dictated by the test configuration and requirements. For instance, the indirect generation of the tensile wave via the compressive impact of a missile on the rear of the weighbar and the need for adequate test duration for fibre/resin composites called for a fairly long projectile of about the same diameter as the weighbar.

This in turn influenced the choice of the barrel. Furthermore, the maximum impact velocity must be compatible with the following demands:

(i) the input bar must always operate below its dynamic yield strength,

(ii) failure must be avoided in the Hopkinson-bar apparatus itself, the weakest point being at the yoke/input bar connection see Fig. 2.1,

(iii) the incident pulse corresponding to the maximum impact velocity must be sufficient to induce failure in the strongest of the materials to be tested,

(iv) strain rates of the order of 10^3/s must be attainable.

Information from previous work [66] in which a falling weight was used and a knowledge of the dynamic properties of the input bar material [72] indicated that a maximum impact velocity of 50 m/s might be suitable.

The design of the gas gun and firing system is shown schematically in Fig. 2.2 and a photograph of the gun is given in Fig. 2.3. Essentially, it consists of the reservoir and a barrel. The reservoir is a 267 x 227.5 x 267 mm steel block with longitudinal and transverse bores of diameters 38.5 mm and 75 mm respectively. Two 267 mm square, 50mm thick cover plates with locating spigots and o-ring seals, seal the

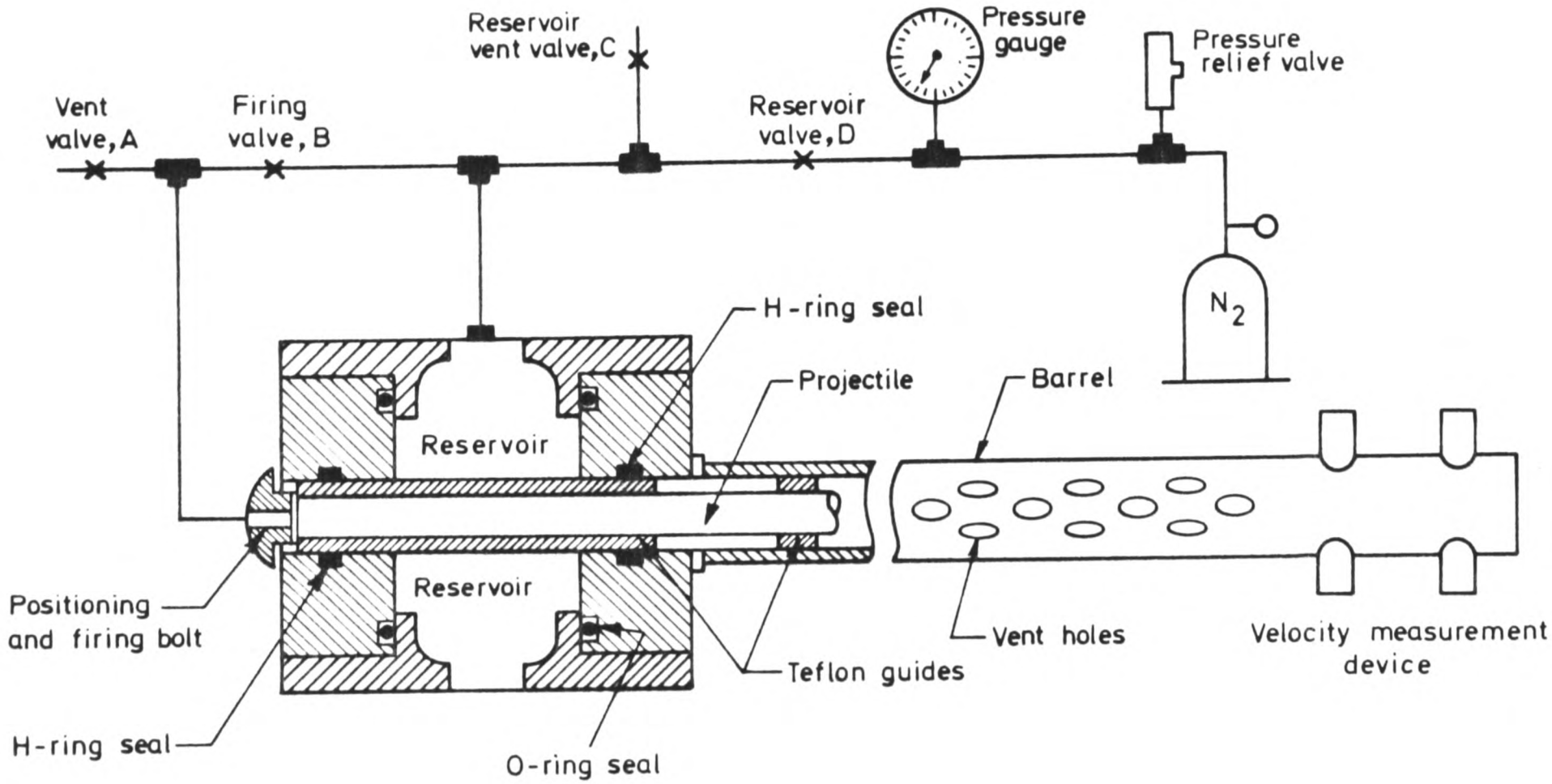

Fig. 2.2 Schematic arrangement for gas gun.

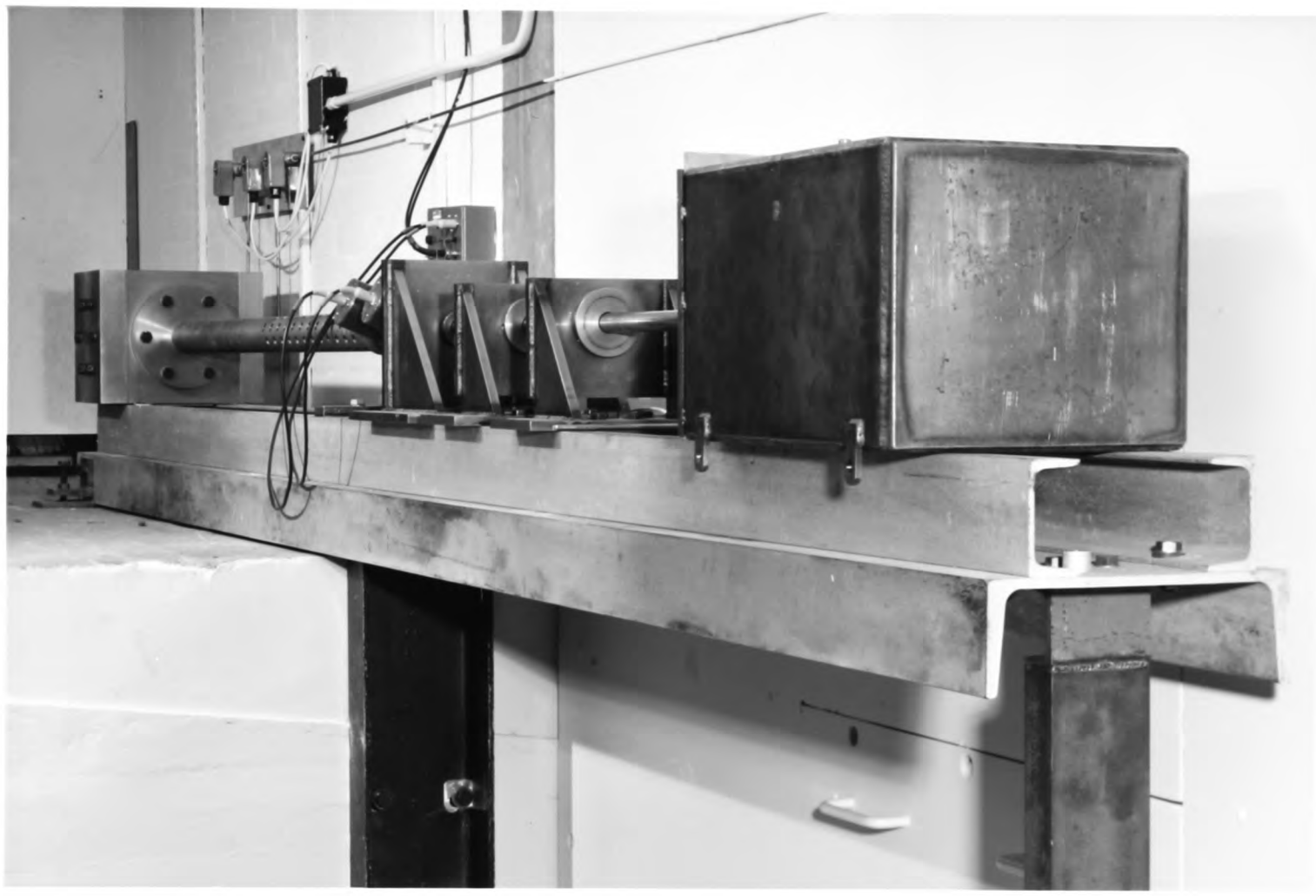

Fig. 2.3 GENERAL VIEW OF GAS-GUN

transverse bore when bolted onto the block. One plate carries a centrally located 1/4" (6.35 mm) BSP tapped hole for admitting nitrogen gas into the reservoir. A mild steel tube 1.755 m long, 38.5 mm internal diameter and 11 mm thick constitutes the barrel. Its last 1 m is vented for use as a guide and the threaded breech end screws into a circular flange of 206 mm outside diameter. The flange is bolted to the block as shown in Fig. 2.2. The projectile, an alloy steel bar 1 m long by 25.4mm diameter is carried on teflon guides separated by 4 mm thick 25.4 mm internal diameter length of rubber tube, the guides being a sliding fit in the barrel. The entire gun assembly is mounted on steel channels which also carry the Hopkinson-bar apparatus, thus allowing alignment of the gun with respect to it. Valves A and C (see Fig. 2.2) are normally open while B and D are normally closed - all are operated electromagnetically. The projectile is loaded into the tube and seals the reservoir at the H-ring pressure seals. Valves C and D are respectively closed and opened in that order and the reservoir is filled with nitrogen to a predetermined pressure. Valve D and then A are closed. Impact is initiated by opening valve B which increases the pressure behind the projectile to that of the reservoir, causing it to move down the barrel until its back end clears the first H-ring whereupon the whole mass of the gas in the reservoir becomes available to accelerate it. Towards the muzzle end, two photocells, 150 mm apart, are used to check the projectile velocity just before impact with the test equipment occurs.

In an emergency, the gas supply is shut off and the reservoir pressure is relieved by opening the vent valves, beginning with valve A.

A calibration curve relating the projectile velocity to reservoir pressure is given in Fig. 2.4.

2.2.2 Input/Output Bars and Tubular Weighbar

From the Lagrange diagram of Fig. 2.1 it can be seen that the interval over which the wave analysis in the input bar can be carried out cannot conveniently exceed $(T_2 - T_1)$. Current requirement is for a machine that is adequate for the testing of advanced composites without recourse to an elastic test which reduces the accuracy of strain measurements. In terms of the critical time interval $(T_2 - T_1)$ the demand of the 45^o woven glass/epoxy composite is likely to be the stiffest. Previous work has shown that an interval of 110 μs may be appropriate [67]. The corresponding distance between the strain gauges at stations I and II is given by

$$d = \frac{1}{2} (T_2 - T_1) C_i \qquad (2.1)$$

where C_i is the longitudinal wave velocity in the input bar. Using the experimentally determined value of C_i = 5106 m/s, therefore, a minimum value of d ~ 281 mm is obtained. Some allowance is made for a possible variation in fracture strain and this distance is set at 362 mm which gives $(T_2 - T_1) \simeq 142$ μs on an input bar of length 451 mm. Thus at a constant strain rate of 1000/s a failure strain of over 14% may be reached, well beyond that expected for most FRP materials. Similarly the

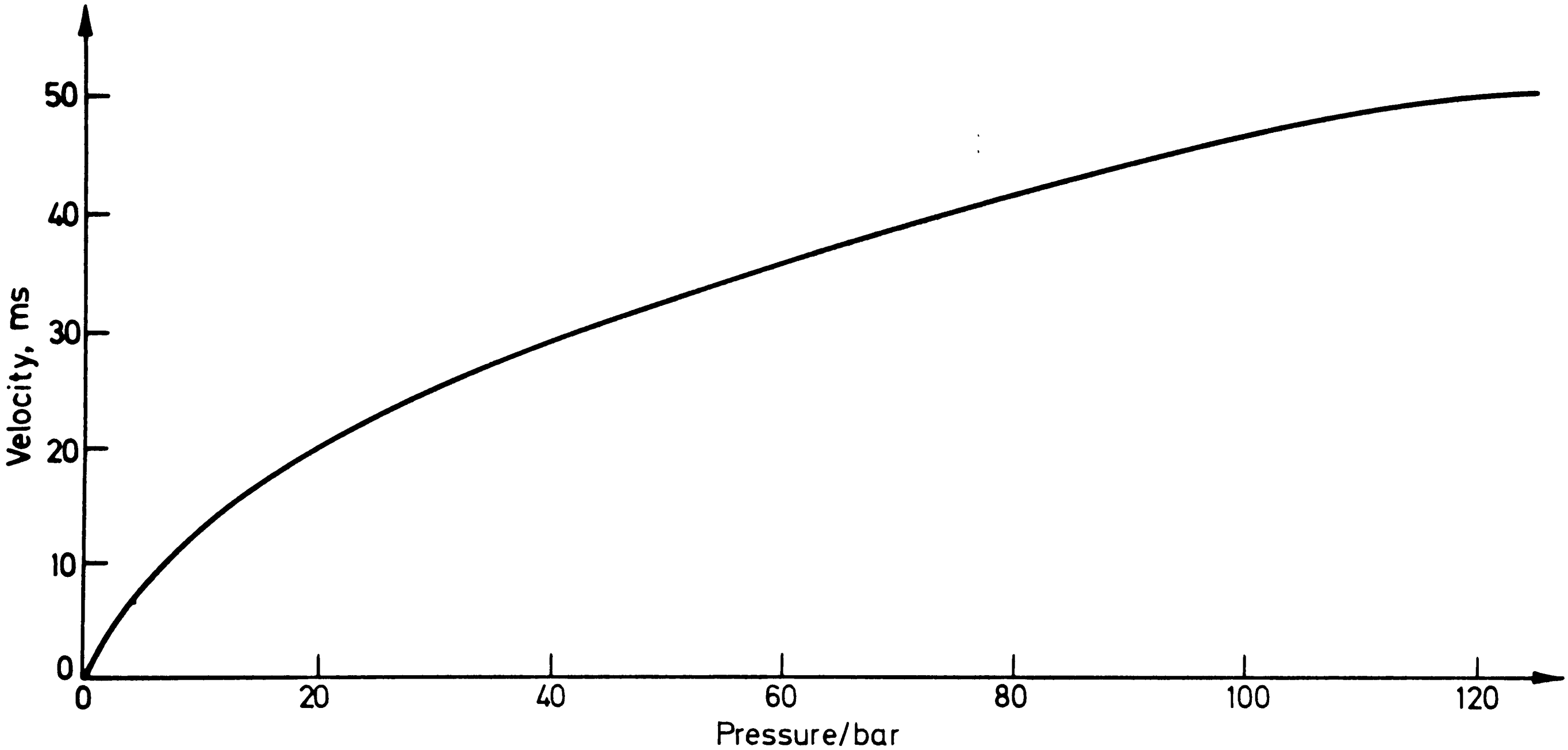

Fig. 2.4 Pressure-velocity calibration for gas gun.

length of the inertia bar was increased to 422 mm and the output signal may be analysed for periods in excess of 150 μs.

A matching weighbar tube was required and was constructed from 27 mm diameter centreless ground annealed I.M.I. 318 titanium alloy bar, bored to a diameter of 3/8" (9.525 mm) $\begin{cases} +\ 0.001 \text{ in} & (0.025 \text{ mm}) \\ +\ 0.003 \text{ in} & (0.076 \text{ mm}) \end{cases}$ along its full length of ~ 0.91 m with a clearance of 9/16" (14.288 mm) at one end. An accurately straight bore is required since on this depends the alignment of the loading bars. The impact end of the weighbar tube is closed with a solid bar of the same material, the impact head, against which the projectile impinges. At the further end a yoke, also of annealed I.M.I. 318 titanium alloy bar, connects the weighbar tube with the input loading bar, reflecting the compressive loading wave in the former as a tensile loading wave in the latter. This system differs from those used previously only in its much greater length.

2.2.3 Output Bar Catching Device.

Following fracture of the specimen the output bar becomes free of restraint and may rebound from the top end of the hole in the weighbar tube, see Fig. 2.1, so that the two broken halves of the specimen suffer a subsequent compression impact, damaging the original tensile fracture surface. In previous work various devices have been used to prevent the output bar from a possible rebound. Two common methods are illustrated in Figs. 2.5(a) and (b), and may be used jointly. In one case, a ring of soft solder is suitably positioned on the inertia bar and is rammed into

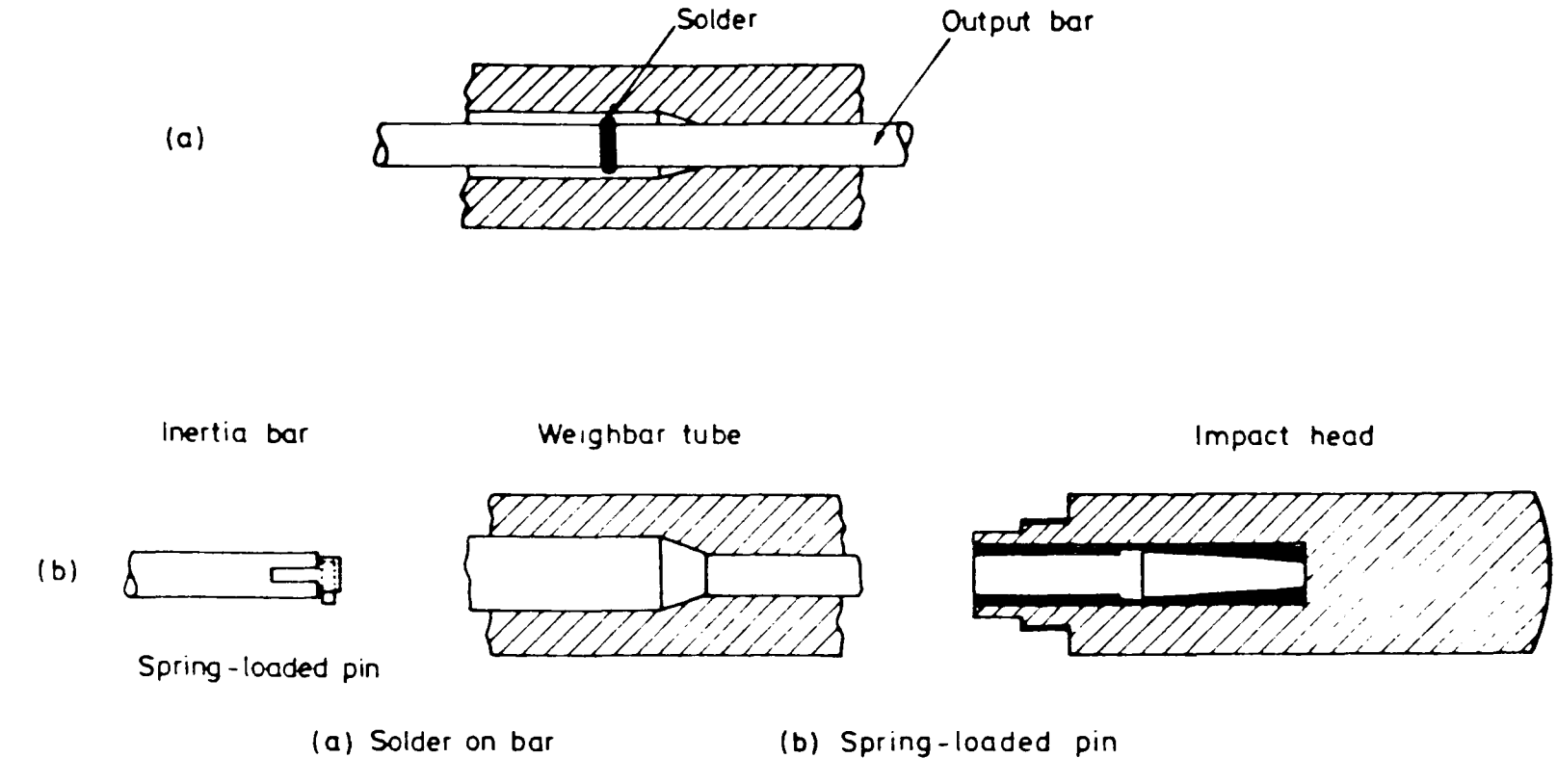

Fig. 2.5 Previous methods used to catch inertia bar
(a) Solder on bar, (b) Spring-loaded pin

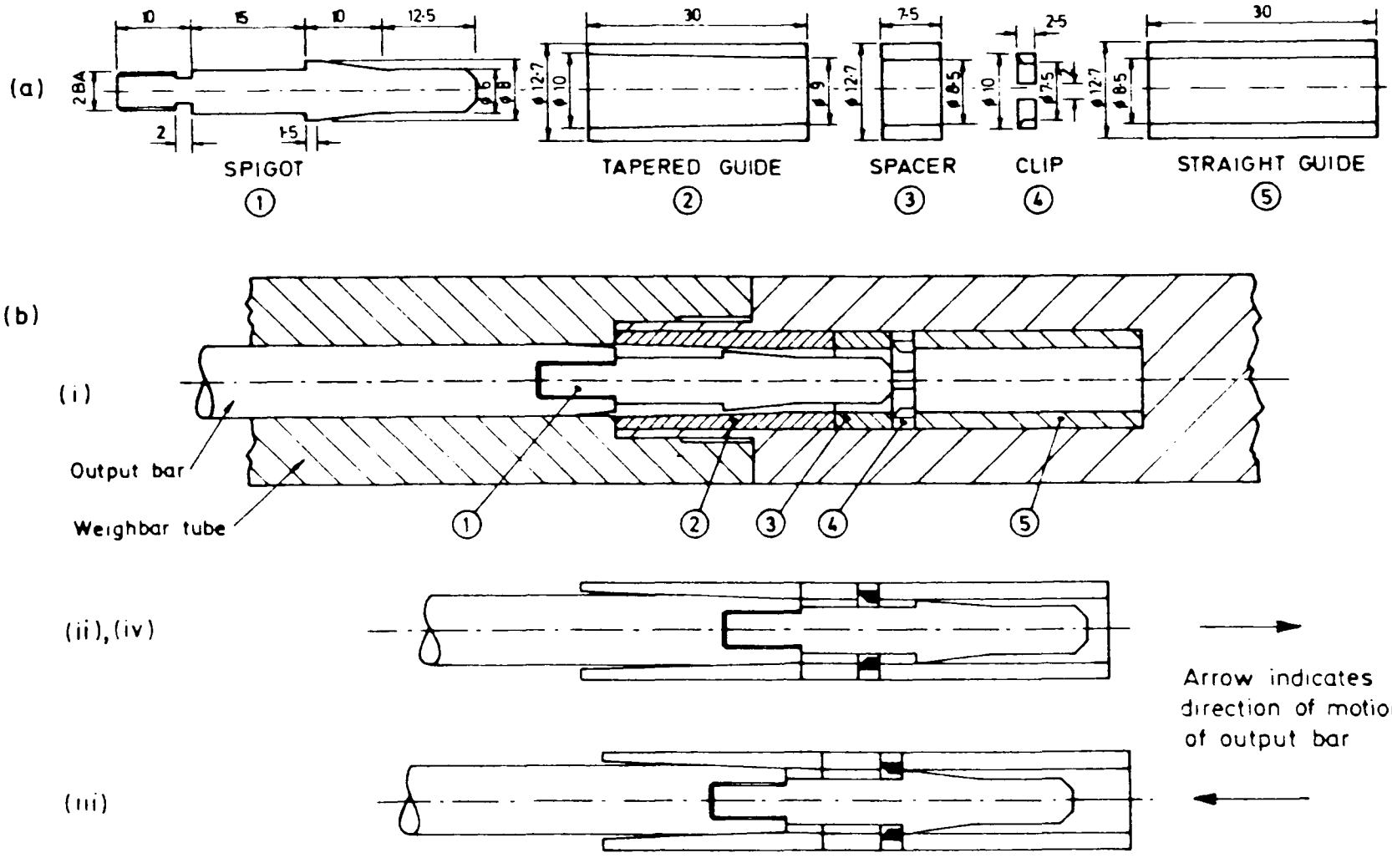

Fig 2.6 New output bar catching device All dimensions in mm.

the taper in the weighbar tube after fracture of the specimen. The success of this approach depends on just the right amount of solder being used so that it is able to absorb practically the whole of the kinetic energy of the moving bar through plastic deformation without causing rebound. The other arresting mechanism is a spring-loaded pin in the end of the inertia bar which when released locks in the impact head. Both techniques have met with limited success but neither is 100% reliable. In present work a knowledge of the operating fracture mechanism is sought through optical and scanning electron examination of fracture surfaces. The catching of the output bar is therefore critical. A new device therefore, has been specially developed. It comprises a spigot, two guides, a spacer and a spring clip. These are shown as items (1) to (5) in Fig. 2.6(a). Except for the 10 mm outside diameter clip all components were machined from Carr's 552 bar stock (EN 30B), oil quenched from 825^{o}C and tempered at 475^{o}C for 1 hour. The spring clip is in silver steel and was similarly tempered after being oil quenched from 770^{o}C. An assembly of the device within the weighbar tube prior to a test is indicated in Fig. 2.6(b)(i). The sequence of events following specimen failure in a test at a typical impact velocity of 11 m/s is depicted in Figs. 2.6(b)(ii) to (iv) and is self explanatory. A recurrence of stage (ii) (also shown as (iv)) depends on the initial kinetic energy of the output bar.

After several tests, some damage may be visible in the spring clip. Further usage may then be detrimental. However, experience has shown that a clip would normally survive a minimum of six tests and does not require considerable machining.

2.3 Materials and Specimen Design

2.3.1 Materials

Four laminated composite plates, each 0.3 m square and of 2 mm nominal thickness, were supplied by Fothergill and Harvey Ltd. All laminates were hand laid up using the Ciba-Geigy XD 927 epoxy resin system, with 100 parts by weight of resin to 36 parts by weight of hardener, and a cure schedule of 24 hours at room temperature followed by 16 hours at 100^{o}C. Two plates were, (i) all carbon to an actual thickness of 3.4 mm and containing 12 woven mats (plies) with, overall, a 50% fibre content by weight, and (ii) all glass to an actual thickness of 1.75 mm and containing 14 plies, also with overall, a 50% fibre content by weight.

All fabrics were of plain weave construction. The carbon fibre fabric was woven from Toray 3000 filament fibre tows, type T300 - 3000A, and had a weight of 189 g/m^2 and an approximate thickness of 0.28 mm. The fibres were supplied with a surface treatment suitable for use with epoxy resin. Unfortunately this fabric has a relatively coarse weave geometry, with only 47 ends and picks per 10 cm. Previous work [78] has shown that more reliable results are obtained at impact rates when the scale of the reinforcement geometry is relatively fine in comparison with the overall specimen dimensions. However, to obtain a finer weave would have required the use of 1000 filament fibre tows and the production of specially woven fabrics which would have been extremely expensive. The glass fabric was woven from continuous E-glass fibres, designation 11 x

2EC5, and had a weight of 96 g/m^2 and an approximate thickness of 0.08 mm. With 252 ends and 173 picks per 10 cm the weave was much finer than for the carbon fabric. The fibre finish, type 205, was suitable for use with both epoxy and polyester resins.

The remaining two plates of hybrid construction, either alternating layers of carbon and glass or two layers of glass interlaminated with a single layer of carbon. In each case the overall fabric weight fraction was 50%.

Determination of void contents.

Voids are an inherent feature of fibre-reinforced plastics and may be caused by a number of effects including entrapment of air and the release of volatiles from the resin during fabrication. Their presence in fibre/resin composites influences such properties as the interlaminar shear strength, fatigue resistance, susceptibility to water penetration and weathering and may be responsible for any observed variation in fracture strength [86,87]. Unfortunately there exists no technique that is generally accepted for measuring void content.

Most of the available methods are either limited to some class of composite materials or are unsuitable for assessing material quality simply and quickly. Recently, however, two simple techniques were proposed by Purslow [88] and are said to be adequate for the assessment of material quality for both development and production purposes. One of these, the 'optical comparison technique' is especially simple and was

adopted in this investigation. Here, a sample which ideally should be of the total thickness of the material is prepared for optical examination using standard procedures [89]. The void content is then estimated from a micrograph which is representative of the cross-section as a whole. Samples were cut from composite plates through the plate thickness in a direction normal to the fibres. These were then prepared for optical examination in the usual way [89]. The area of section examined as a representative region varied with plate thickness but was not less than the recommended value of 15 mm^2 even in the relatively thin all-glass sample. Micrographs in Figs. 2.7 and 2.8 show typical void distributions in the materials. A 10 x 10 grid was superimposed on each micrograph and the area of each void was assessed as a percentage of that of the small square or squares within which it fell. Hence estimates were obtained of the total void content. The estimates obtained for the all-glass, the all-carbon and the two hybrid laminates are listed in table 2.1 below.

Table 2.1 Estimates of void contents in the materials

MATERIAL	VOID CONTENT
ALL GLASS	1.0% < V < 2.0%
ALL CARBON	2.0% < V < 5.0%
C/G TYPE 1	2.0% < V < 5.0%
C/G TYPE 2	2.0% < V < 5.0%

(a)

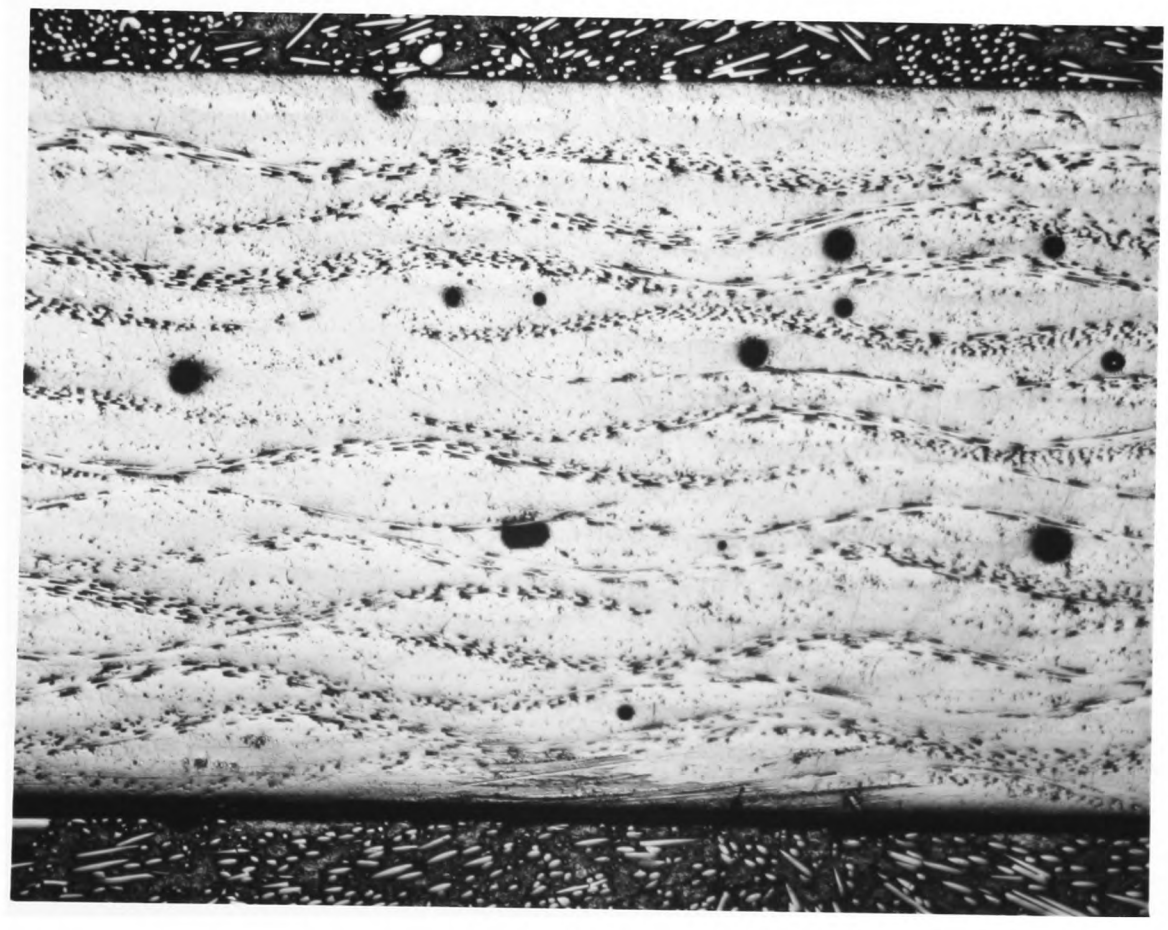

(b)

Fig. 2.7 Void Distribution in (a) all-carbon and (b) all-glass laminates

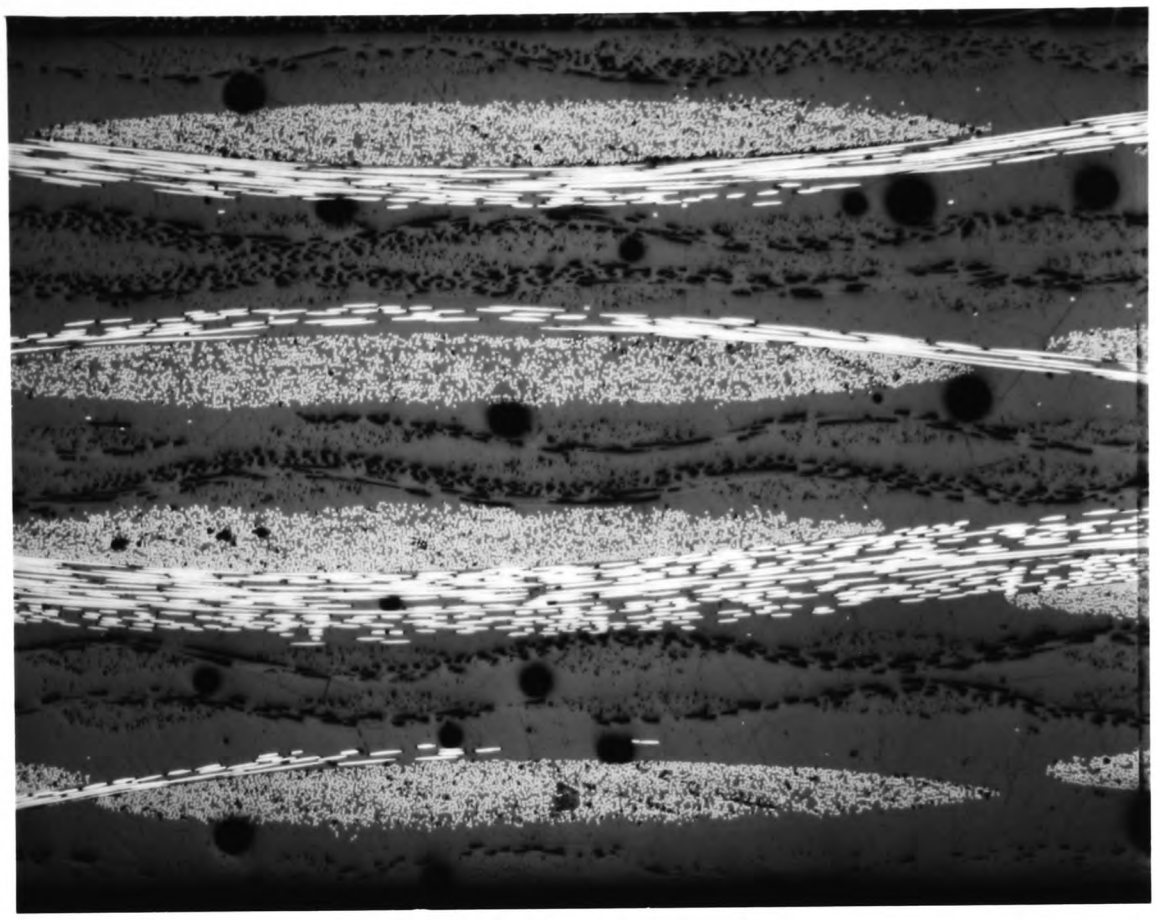

(a)

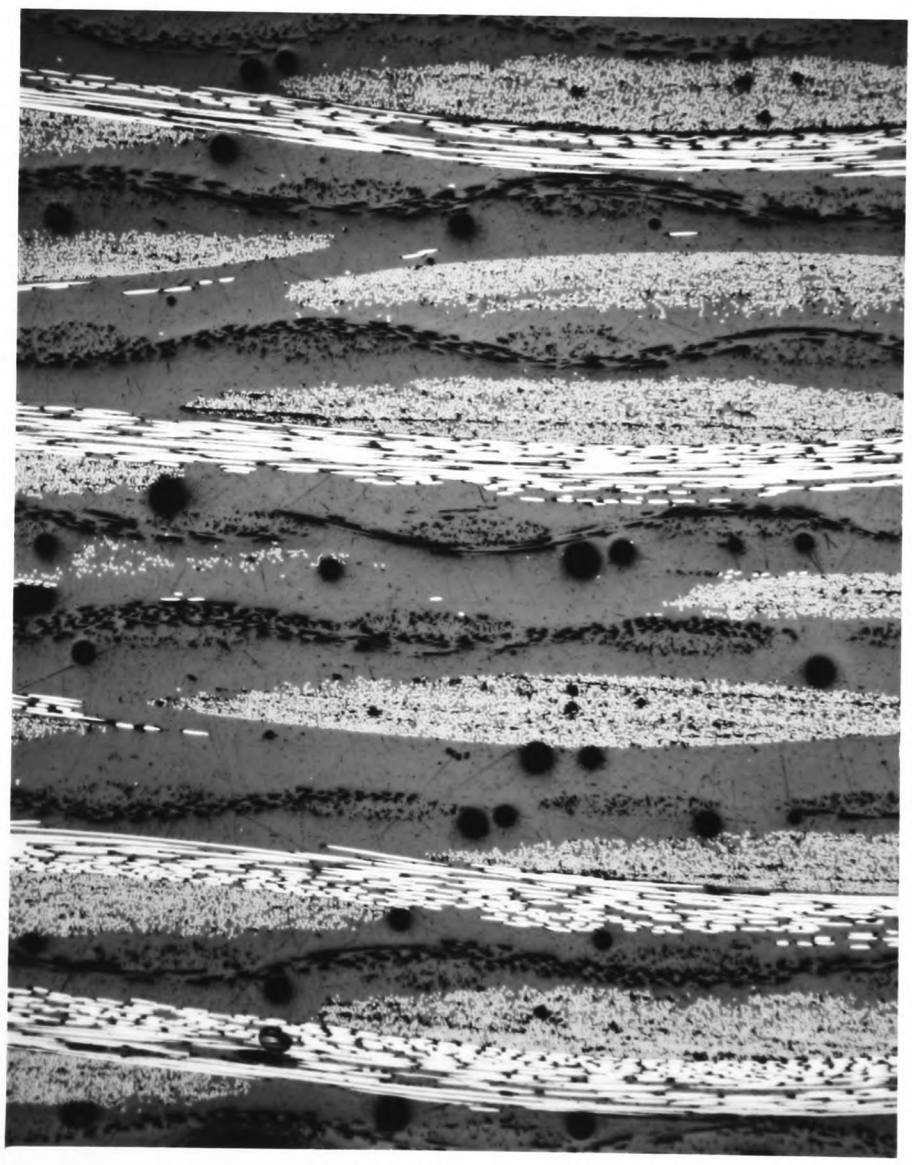

(b)

Fig. 2.8 Void distribution in (a) carbon glass type 1 and carbon glass type 2 hybrid laminates (b) λ

2.3.2 Specimen Design

Thin strip specimens, 9.5 mm wide and waisted in the thickness direction as recommended for the quasi-static testing of unidirectionally-reinforced CFRP specimens [51], were found in earlier work [66, 67, 78] to give satisfactory results under tensile impact loading. Specimens of this geometry, therefore, were used in the present investigation.

Specimens were cut from the laminates to the standard dimensions, for the various carbon/glass hybrids, given in Fig. 2.9. The specimen thickness in the parallel gauge section and in the thicker grip sections varied with the reinforcement configurations as shown in Fig. 2.9 for three different carbon to glass hybrid weight fractions and for the all glass and the all carbon specimen configurations. The thickness in the grip sections is approximately twice that in the gauge section. Specimens were cut by hand using specially designed jigs and were carefully surface finished. These were stored in a desiccator until required for fixing into the slots in the loading bars using Chemlok 304 high strength adhesive. The use of longer loading bars accentuated the problem of aligning the bars and the specimen during the glueing-in process. It also meant that the bar/specimen assembly was less rigid and therefore more fragile especially when a low modulus, low fibre volume fraction specimen was to be tested. To overcome these difficulties, a special jig (see Fig. 2.10) was made. The loading bar/specimen assembly remained in the jig until the glue was given the recommended cure

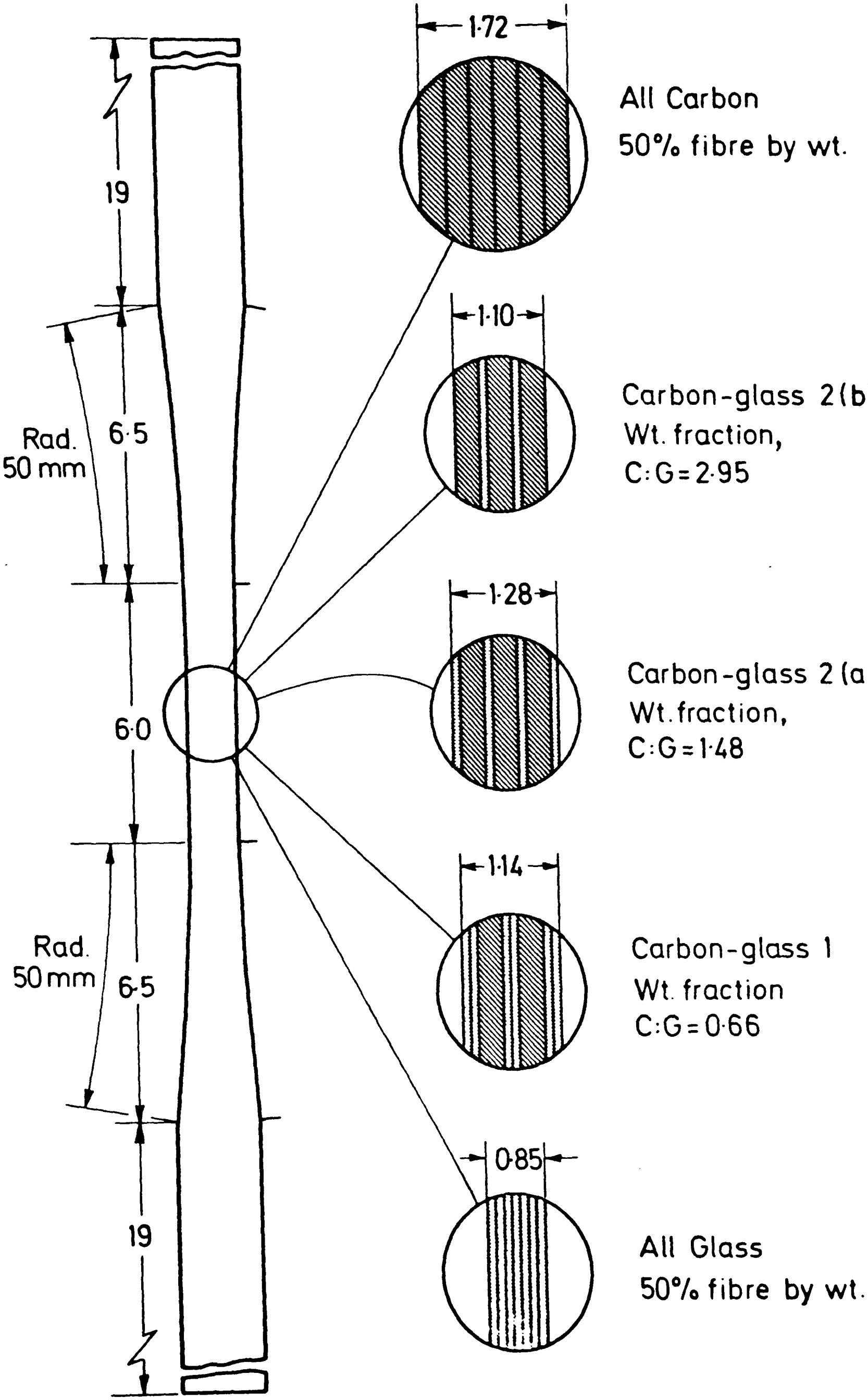

Fig.2.9 SPECIMEN DESIGN AND HYBRID LAY-UP
(all dimensions in millimeters)

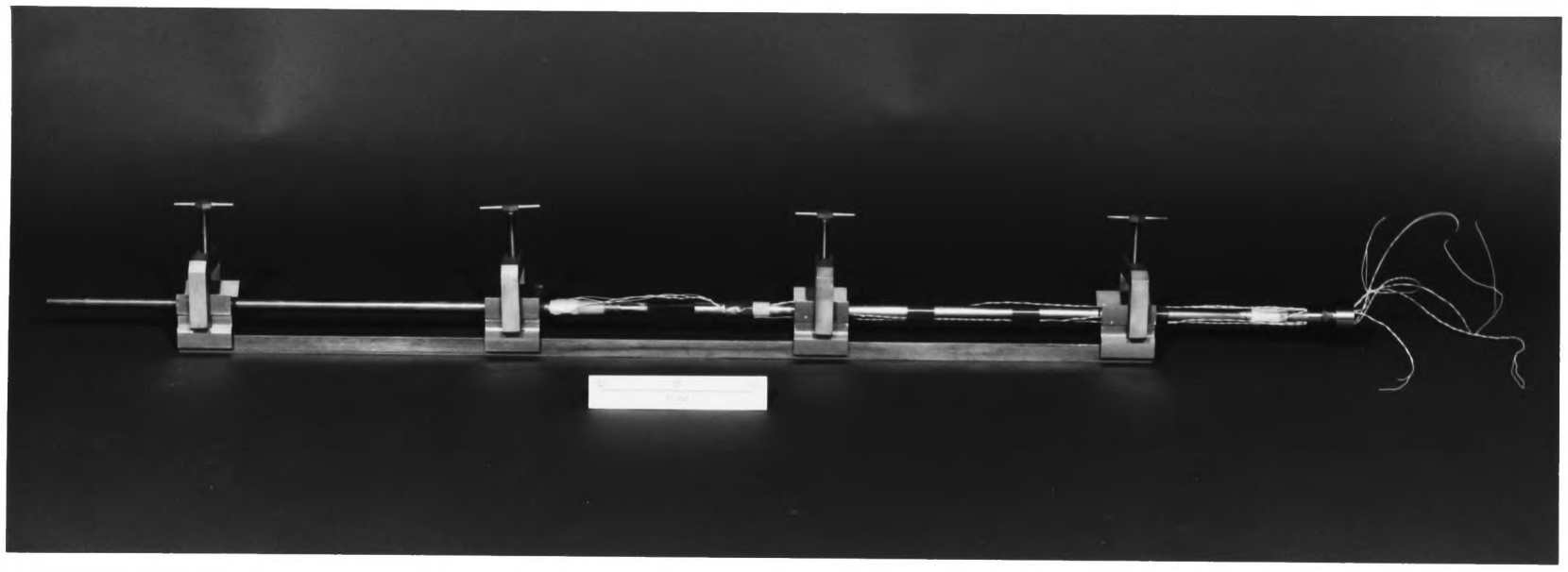

Fig. 2.10 Jig for fixing specimen into the slots in the loading bars

schedule. Care was also taken to avoid damaging the specimen while the Hopkinson bar assembly was being inserted into the weighbar tube.

2.4 Calibration of Loading Bars.

At each gauge station in Fig. 2.1, four electrical resistance strain gauges temperature compensated for the loading bar material were attached at 90^{o} intervals see Fig. 2.11(a) and wired in opposite pairs to maximise the sensitivity of strain measurement. Care was taken to preclude any magnetostrictive signals that might be caused by changes in magnetic flux around the bar. The gauges were wired into a purpose built bridge circuit with a stabilized bridge voltage of 5 volts. In order to monitor the specimen elastic strain independently of the Hopkinson-bar analysis two Techni-Measure type FLA3, 120 Ω, electrical resistance strain gauges, having an active gauge region 3 mm long by 1.9 mm wide were bonded centrally, one on each face of the specimen using the recommended cyanoacrylate adhesive. These gauges have preattached leadwires thus eliminating the risk of damaging the specimen through the use of high temperature soldering iron. It is also known that all commercially available strain gauge adhesives are compatible with epoxy matrix composite materials [90]. Specimen gauges were set in a conventional bridge circuit using the same purpose-built box as for the bar gauges. It was necessary to establish a relationship between the output voltage of each monitoring system and the corresponding applied stress or strain. All measuring systems were therefore calibrated. For the loading bars each set of strain gauges and the associated bridge circuit was

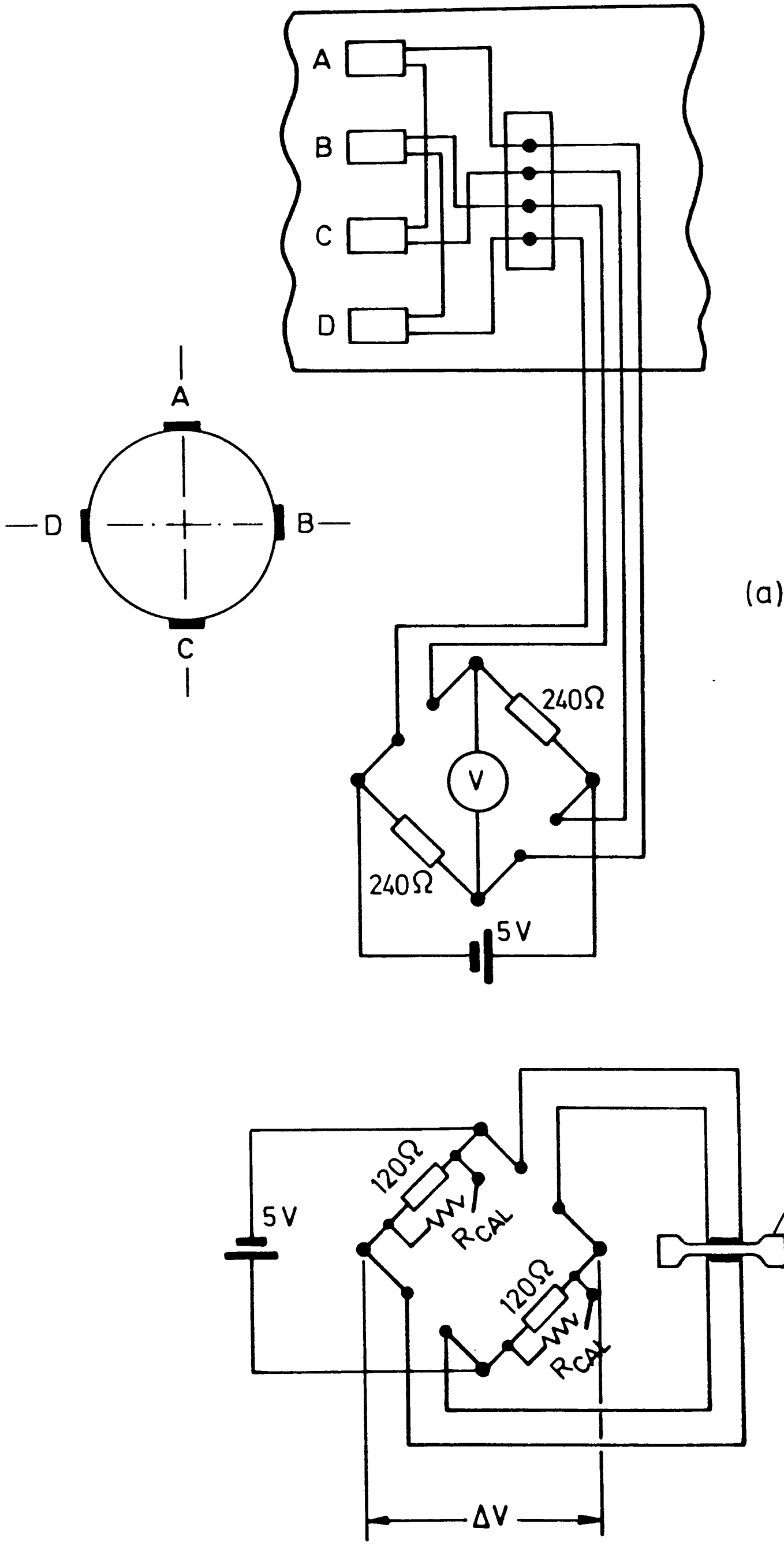

Fig. 2.11 Strain gauge systems for (a) Loading bars and (b) Specimen

calibrated by loading the bar statically in tension in an Instron testing machine and measuring the output from the bridge on a microvoltmeter. This technique makes the usual assumption for metals that the static and dynamic Young's moduli are identical. Typical values for the input and output bar gauges are 643.24 μV/kN (gauge station I), 617.65 μV/kN (gauge station II), and 642.12 μV/kN (gauge station III).

The specimen strain gauge circuit was calibrated by simulating a change in the gauge resistance see Fig. 2.11(b) and noting the resulting output voltage from the bridge. A typical calibration value is 0.019% strain per mV, obtained from the linear plot of the simulated resistance change versus the bridge output voltage assuming the manufacturers quoted gauge factor. As a result of slight variations in the acoustic velocities of supposedly identical loading bar materials supplied by manufacturers in the past, it was thought useful to check these values for the latest set of bars. For this purpose, a freshly machined bar of known length was suspended at its mid-point and set in longitudinal vibration by an electrical oscillator via a transducer in contact with one end of the bar. The frequency of vibration was indicated by a counter and the output from a pickup at the other end of the bar was displayed on an oscilloscope. The frequencies producing resonance were noted and the wave velocity was obtained from the fundamental frequency. If the fundamental frequency is f, then for a rod of length L suspended at its mid-point, the wave velocity $c=f\lambda$, where $\lambda = 2L$. The density of the bar was obtained in the usual manner. The dynamic Young's modulus E may then be obtained from the relationship $E = \rho c^2$ where ρ is the density of the bar. Using the values for E, the strain-time signals from gauges

on the loading bars may be converted to equivalent stress-time traces. The variations of the input and the output velocities with time may also be derived. Typical values of acoustic velocities are:

Input bar (IMI 318 titanium alloy), C = 5106 m/s;

Output bar (phosphor bronze), C = 3627 m/s

2.5 Electronic Recording Equipment

Strain gauges at stations I and II on the input bar, see Fig. 2.1, monitor the incident and reflected stress waves on the input side of the specimen while strain gauges at station III on the output, or inertia bar, side monitor the stress wave transmitted through the specimen. A typical set of signals from the three strain gauge stations and from the specimen strain gauges are shown in Fig. 2.12 for a test on type 2b carbon/glass hybrid specimen for which details are given in Fig. 2.9. The specimen gauges are likely to fail at the limit of linear-elastic response of the composite or at the point where the surface damage of the specimen becomes excessive. This can often cause an electrical 'pick-up' signal which appears as a spike on the traces derived from the strain gauges at stations I and II on the input bar, as has happened in the test of Fig. 2.12. In this case the spike on the gauge I trace lies outside the region involved in the analysis. This is not true for the gauge II trace, however, so the Hopkinson-bar analysis for strain and strain-rate has to take account of this effect. Up to this point however, as shown in Fig. 2.13, very close agreement is obtained between the strain time

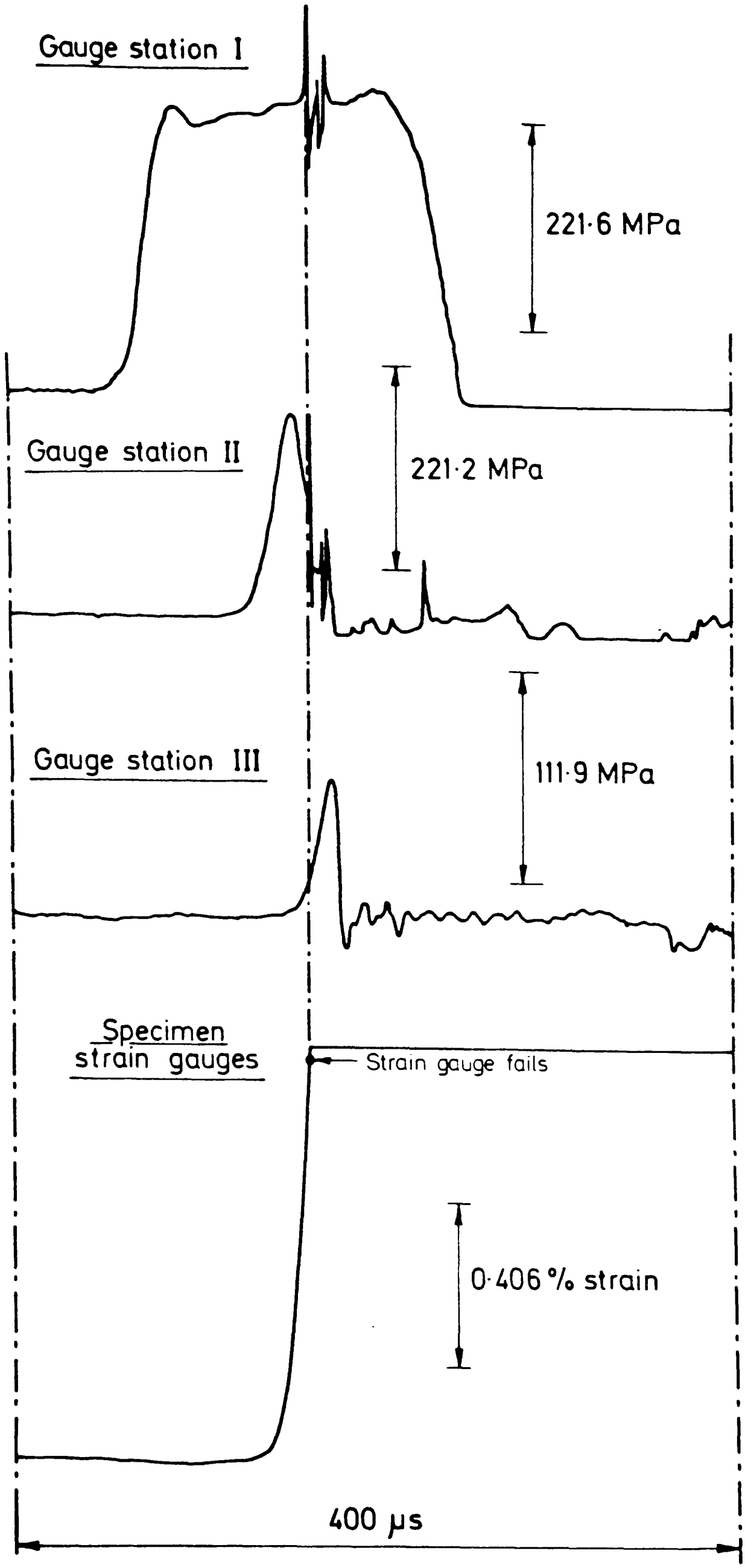

Fig.2.12 STRAIN-GAUGE SIGNALS FOR A TEST ON A TYPE 2b HYBRID SPECIMEN

curves derived from the strain gauges fixed to the specimen, and from the Hopkinson-bar analysis to be described in section 2.6.1 which gives an average strain over the full length of the specimen between the loading bars. This close agreement encourages confidence in the validity of the Hopkinson-bar analysis in the region of elastic deformation.

In the early part of the experimental programme, the strain gauge signals were stored in type DL 922 dual-channel transient recorders and were subsequently displayed on an oscilloscope and plotted on graph paper for manual calculation using an X-Y chart recorder. The transient recorders were triggered externally using a delay unit and a trigger signal obtained when contact was made at the impact surface between the projectile and the weighbar tube impact head. A block diagram of the electronic recording system is shown in Fig. 2.14 and additional information on the electronic instrumentation is given in Appendix 1. Subsequently, the experimental data was processed on a Rainbow micro-computer as discussed in section 2.6.3.

2.6 Analysis of Impact Test Data

2.6.1 Standard Analysis

In previous work [66] on unidirectionally-reinforced CFRP specimens using the experimental configuration of Fig. 2.1, the strain-time signals from gauge stations, I, II and III, when subjected to the standard Hopkinson-bar analysis, gave the results shown in Fig. 2.15.

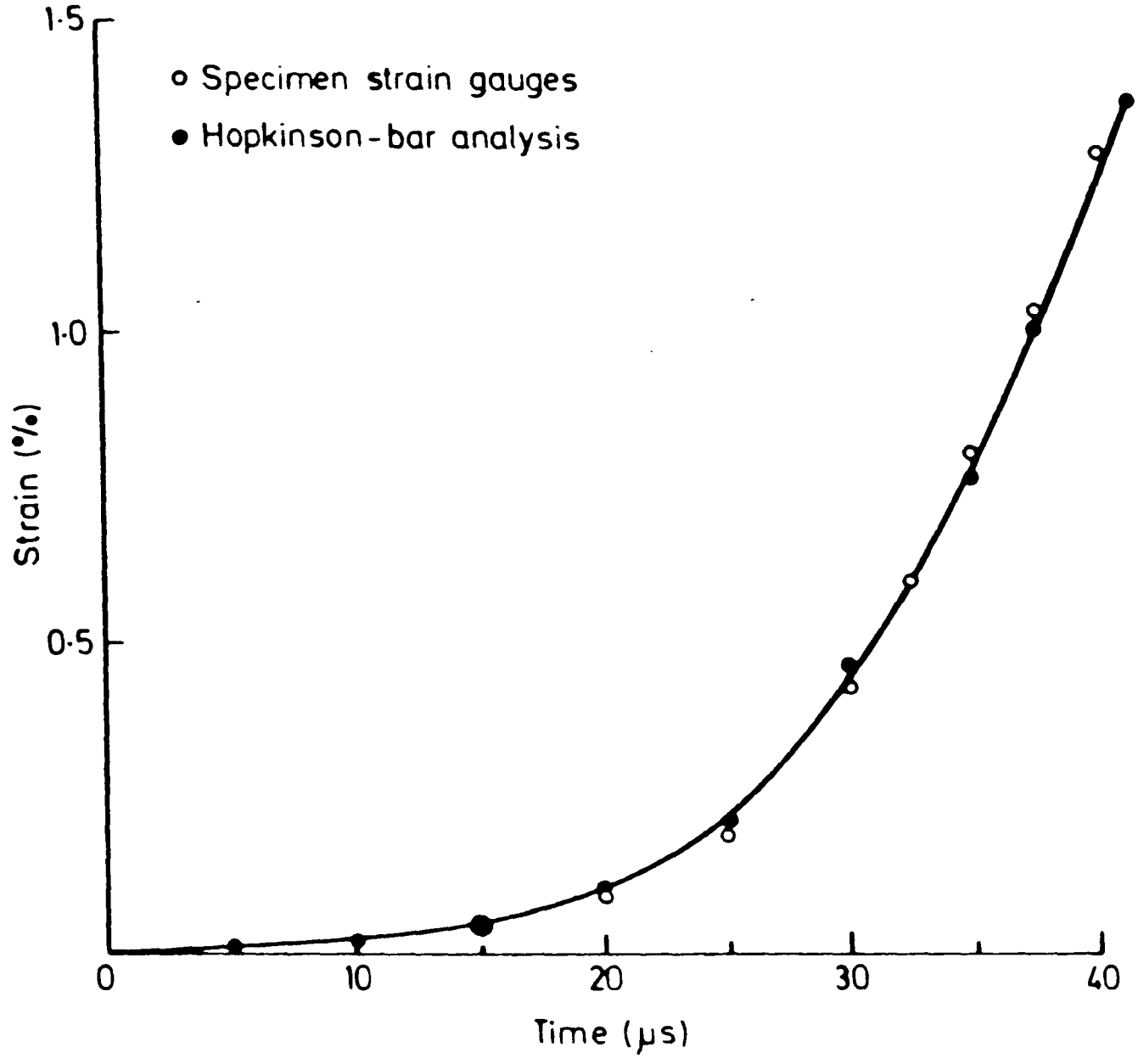

Fig.2.13 COMPARISON OF STRAIN-TIME CURVES FROM SPECIMEN STRAIN GAUGES AND HOPKINSON-BAR ANALYSIS

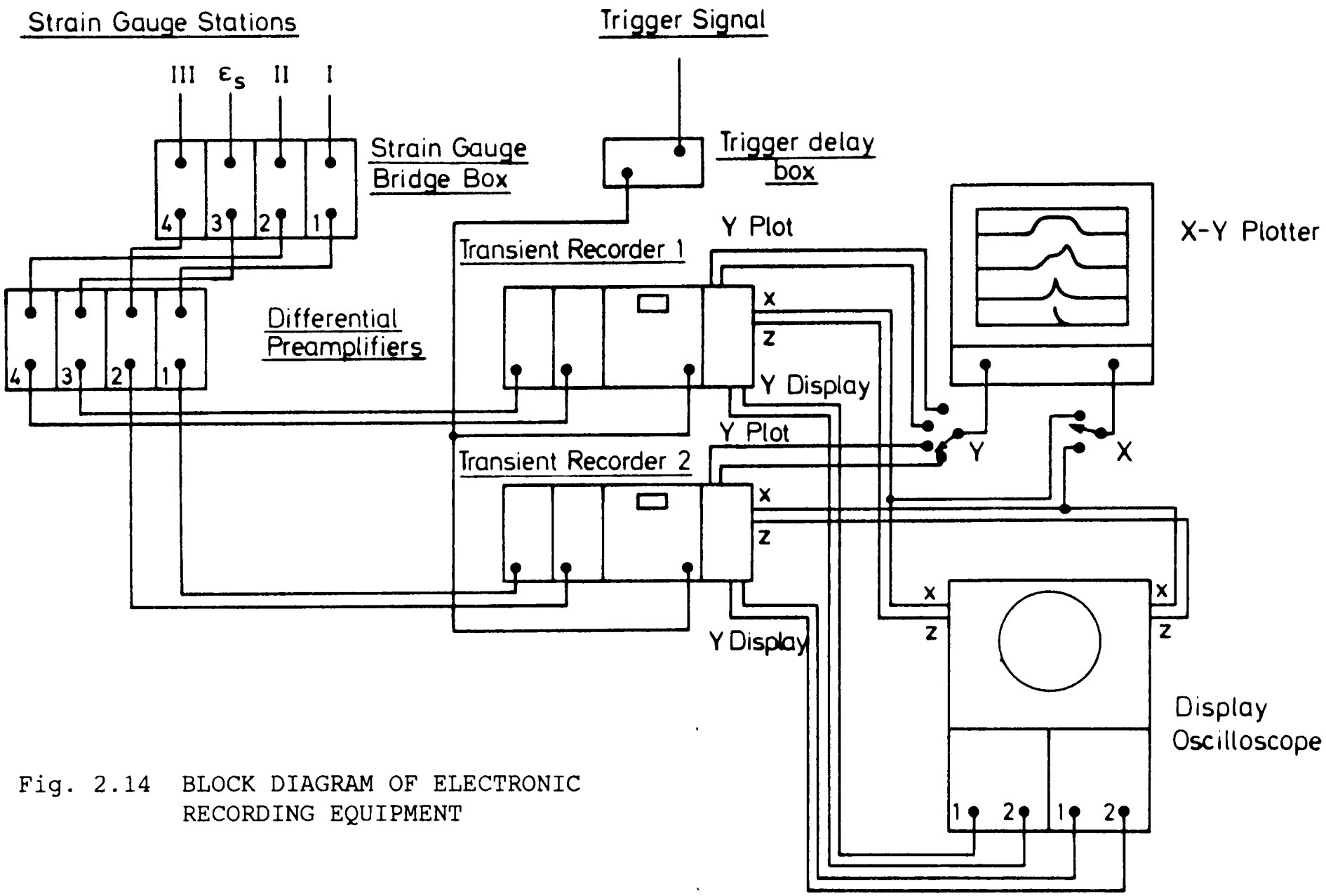

Fig. 2.14 BLOCK DIAGRAM OF ELECTRONIC RECORDING EQUIPMENT

Exceptionally good agreement was obtained between the stress levels, σ_{cc} and $E\varepsilon_{III}$, determined at the input and output ends of the specimen. Some allowance was made in this calculation for the modified wave speed in the grip regions of the loading bars, AA-CC and BB-DD in Fig. 2.1, due to the presence of the composite but the change in impedance in these regions compared with that in the loading bars alone was so small, for this particular test material, that wave reflections at sections AA and BB were ignored. The almost identical profiles for the strain-time signals from gauge stations I and II at times up to T_1, see Fig. 2.15, was further justification for this procedure.

In the present tests, however, using glass fibres and a woven reinforcement geometry where the expected specimen modulus is significantly lower and, in some cases, the thickness of the specimen in the grip region considerably greater, a more marked change in the impedance across the sections at AA and BB might be expected. The worst case is likely to be for a woven glass reinforced epoxy composite tested in the 45^{o} orientation where previous work suggests a modulus under impact loading of about 18 GPa, compared with about 140 GPa for the unidirectionally reinforced CFRP, and where the specimen thickness in the grip region was 3.4 mm, compared with 2 mm for the previous CFRP tests. The corresponding impedance mismatch at AA could be expected to result in a reflected wave equal in magnitude to about 20% of the incident wave, while at BB a transmitted wave some 20% greater than the incident wave might be anticipated. No evidence for such reflections, however, was apparent when comparing the rising profiles of the signals from gauge stations I and II in the test of Fig. 2.16. As shown in Fig. 2.17 these

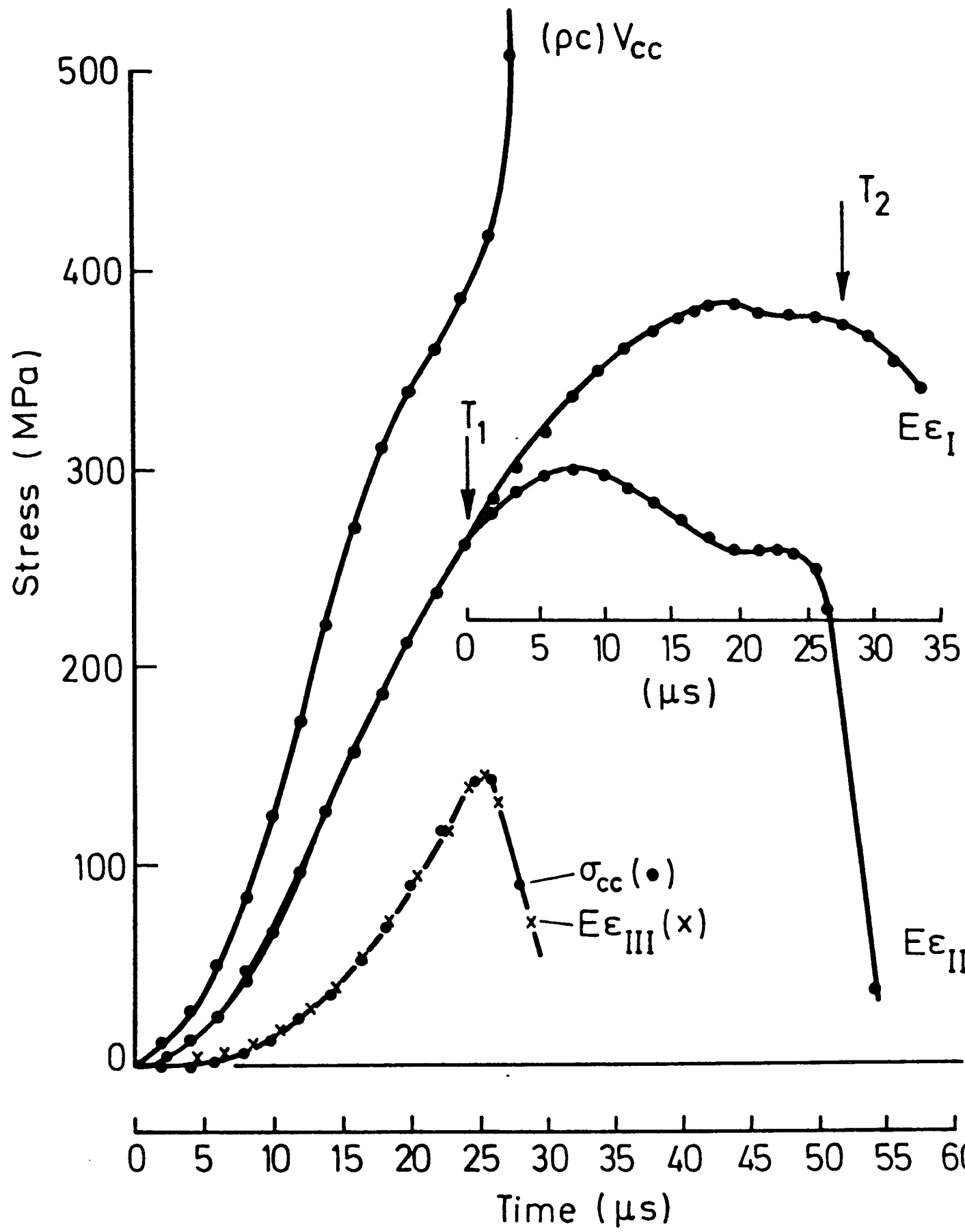

ig.2.15 HOPKINSON-BAR ANALYSIS FOR UNIDIRECTIONALLY-REINFORCED CFRP SPECIMEN

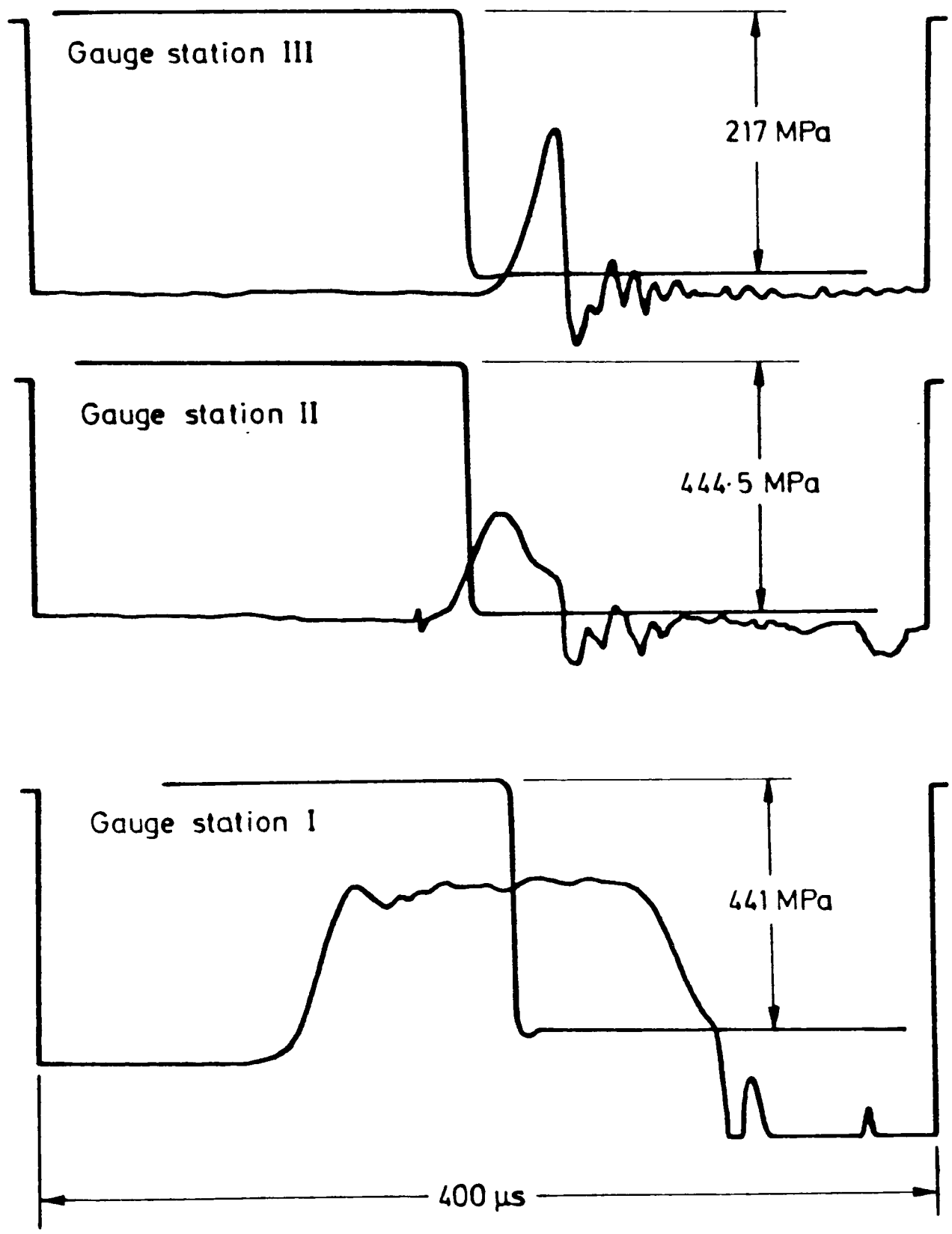

Fig. 2.16 STRAIN-GAUGE SIGNALS FOR CALIBRATION TEST ON GFRP SPECIMEN

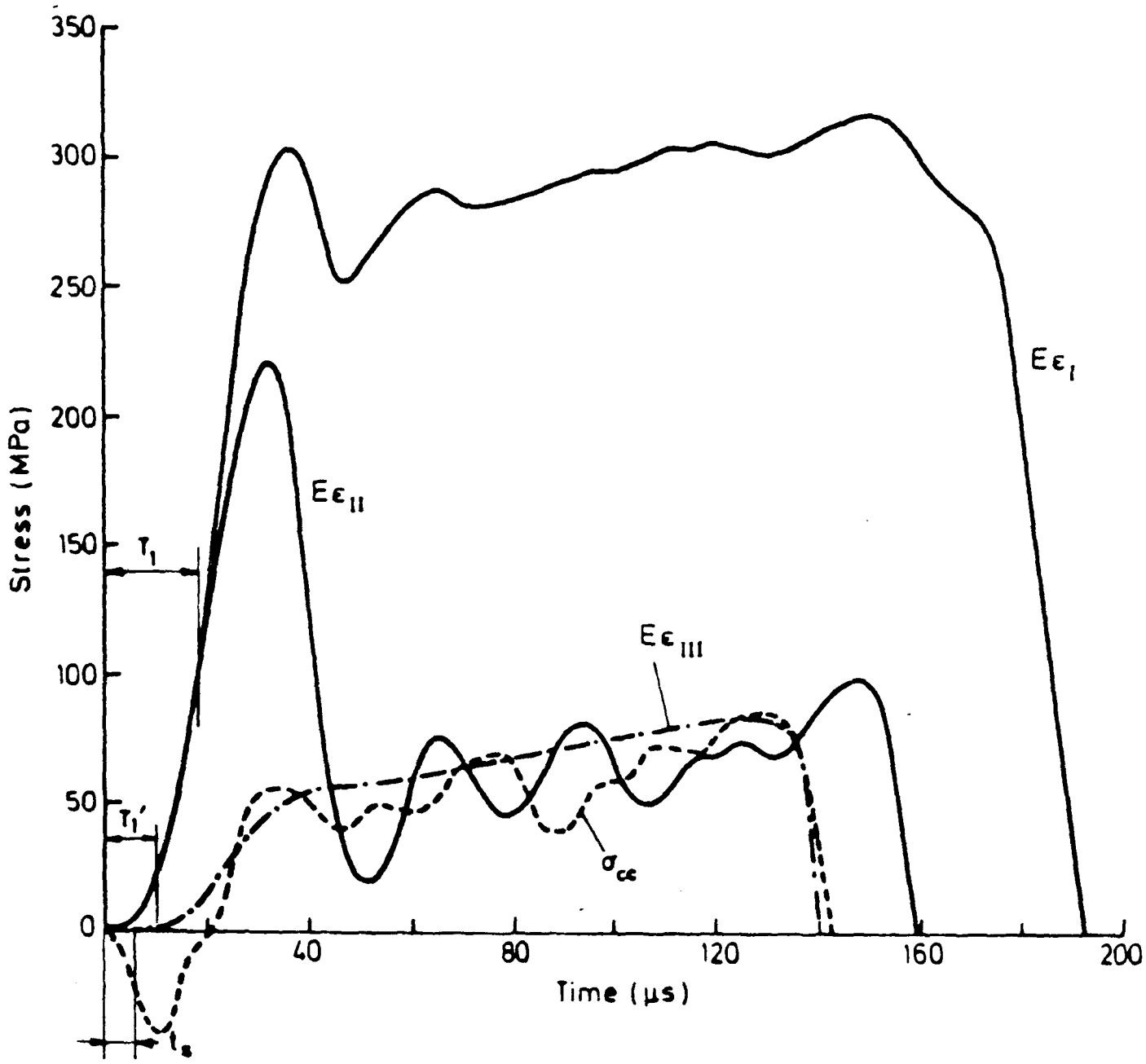

Fig. 2.17 HOPKINSON-BAR ANALYSIS FOR CALIBRATION TEST ON WOVEN GFRP SPECIMEN OF Fig. 2.16

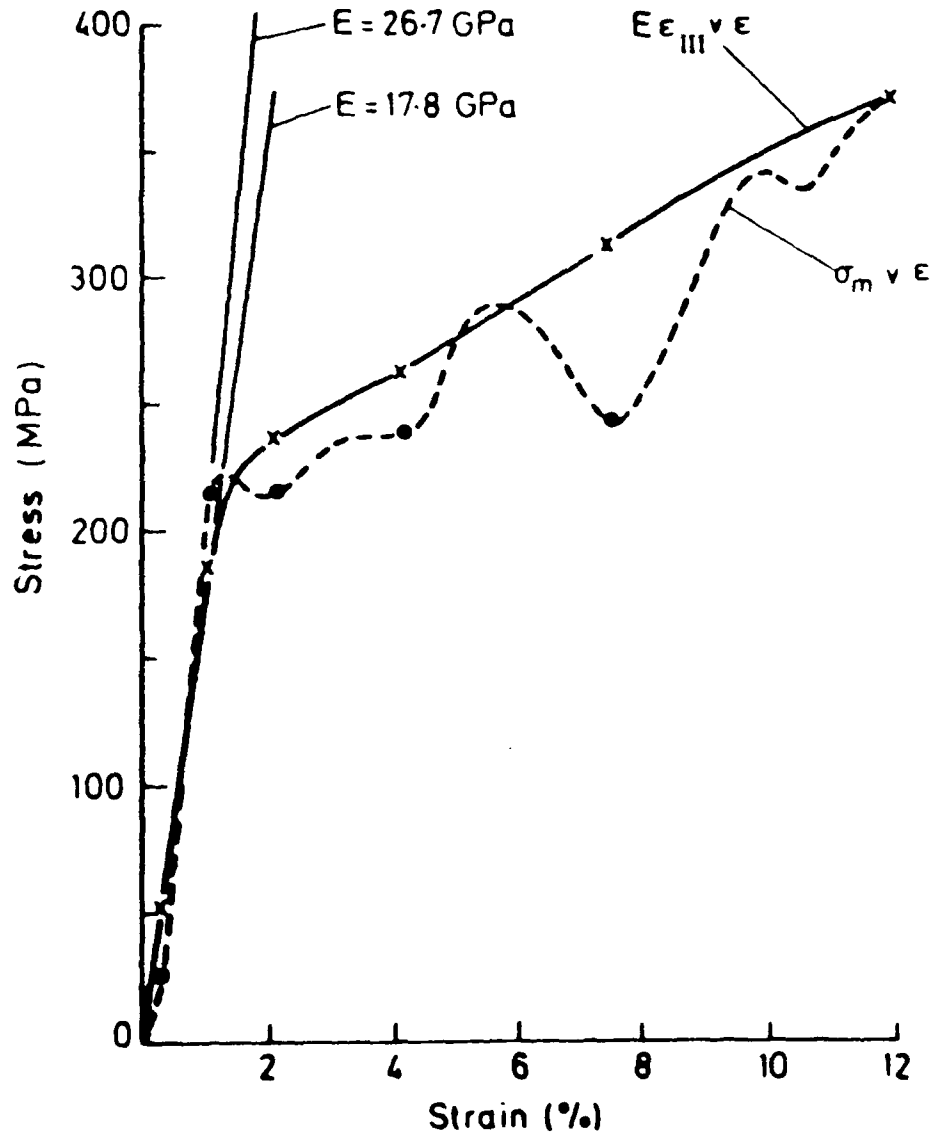

Fig. 2.18 STRESS-STRAIN CURVES FOR CALIBRATION TEST, IGNORING WAVE REFLECTIONS IN SPECIMEN GRIP REGIONS

(x - based on output bar signal; ● - based on specimen 'mean' stress)

remain coincident for times $\leq T_1$. While this is still on the steeply rising part of the curve, where a small difference in magnitude might be difficult to detect, reflections from section AA would be expected to show up as a divergence between the rising profiles at even earlier times, i.e., at about T_1' rather than T_1.

Assuming that these reflections, if present, are small enough to be ignored, the stress variation at the input end of the specimen, σ_{cc}, is calculated from $E\varepsilon_I$ and $E\varepsilon_{II}$ in the normal way and is shown as the dotted curve in Fig. 2.17. It is compared with the stress at the output end of the specimen, $E\varepsilon_{III}$, shown chain-dotted in Fig. 2.17 where t_s is the estimated transit time for a stress wave across the specimen, i.e., from CC to DD (see Fig. 2.1).

Although in general form the stress variations at the input and the output ends of the specimen are similar, the almost exact agreement found previously, see Fig. 2.15, is not reproduced here. The present results show as good a correlation as would normally be expected in tensile impact testing where the input stress, σ_{cc}, can only be determined with limited accuracy as the small difference between a large incident and a large reflected wave. For this reason, it is usual to base specimen stress measurements on the directly determined output stress levels, $E\varepsilon_{III}$. It may perhaps be noted that in the earlier work on unidirectionally-reinforced CFRP the specimens were much stronger and the reflected wave correspondingly much smaller, allowing a more accurate determination of σ_{cc}. Also the divergence between $E\varepsilon_I$ and $E\varepsilon_{II}$ at $t = T_1$

occurred at a later time, close to the end of the rising profile of $E\varepsilon_{II}$, further improving the accuracy of the wave analysis.

The effect of relating the specimen stress entirely to the output signal, $E\varepsilon_{III}$, rather than to the mean of both the output and the input stresses, i.e., σ_m given by

$$\sigma_m = \frac{1}{2} (\sigma_{cc} + E\varepsilon_{III})$$

is shown in Fig. 2.18, where the two resulting stress-strain curves are compared. That based on $E\varepsilon_{III}$ agrees very closely with previous results for the same material [67] at a similar strain rate, about 900/s in the present tests. While there is little difficulty in discounting the dashed curve, based on σ_m, at strains greater than about 2%, because of the difficulties involved in accurately determining σ_{cc}, and hence σ_m, a problem still remains regarding the confidence with which the initial modulus value can be determined. This is particularly important for composite specimens where fracture at strains as low as 2 to 3% is not unusual and the only significant parameters to be measured are the fracture strength and the modulus, both of which may well be rate dependent. In the present tests a modulus of 17.8 GPa, based on $E\varepsilon_{III}$, at an average strain rate of 890/s compares with a previous measurement [67] of 18.3 GPa at about 1120/s. However, if the mean stress, σ_m, is used, an apparent modulus of 26.7 GPa is obtained. Since measurements made during the initial stages of stress wave loading are likely to be particularly sensitive to any reflections in the grip regions it was decided to repeat the analysis of Fig. 2.17, making allowance for such

reflections so as to assess, in particular, what effect they might have on the resulting value of the modulus.

2.6.2 Data Analysis Including Stress-Wave Reflections in Grip Regions.

Details of the analysis for the effect of reflections at AA and BB (see Fig. 2.1) are given in Appendix 2. The dynamic modulus of the composite had to be assumed and was estimated from the results of previous work. An approximate value is adequate as the calculation is not sensitive to small differences in modulus.

The results of this analysis are shown in Figs. 2.19a and 2.19b, where are compared, respectively, the stress at the input end of the specimen, σ_{cc}', after allowance for reflected waves at AA, with that previously calculated, σ_{cc}, and the stress at the output end of the specimen, σ_{DD}', after allowance for reflections at BB, with that previously assumed, $E\varepsilon_{III}$. The only significant difference in each case is, as suspected, in the rising profile, the rate of stress increase with time being slightly reduced. As shown in the corresponding dynamic stress-strain curves, given in Fig. 2.20, this results in a slight decrease in the dynamic modulus from 17.8 to 16.6 GPa, for the curve based on the output stress, σ_{DD}, while for the curve based on $\sigma_m = \frac{1}{2}(\sigma_{cc}' + \sigma_{DD})$ the modulus remained unaltered, within the accuracy with which it can be determined, at about 26.7 GPa. It is concluded that the marginal differences resulting from allowing for the reflections in the grip regions do not justify the complications of the analysis involved.

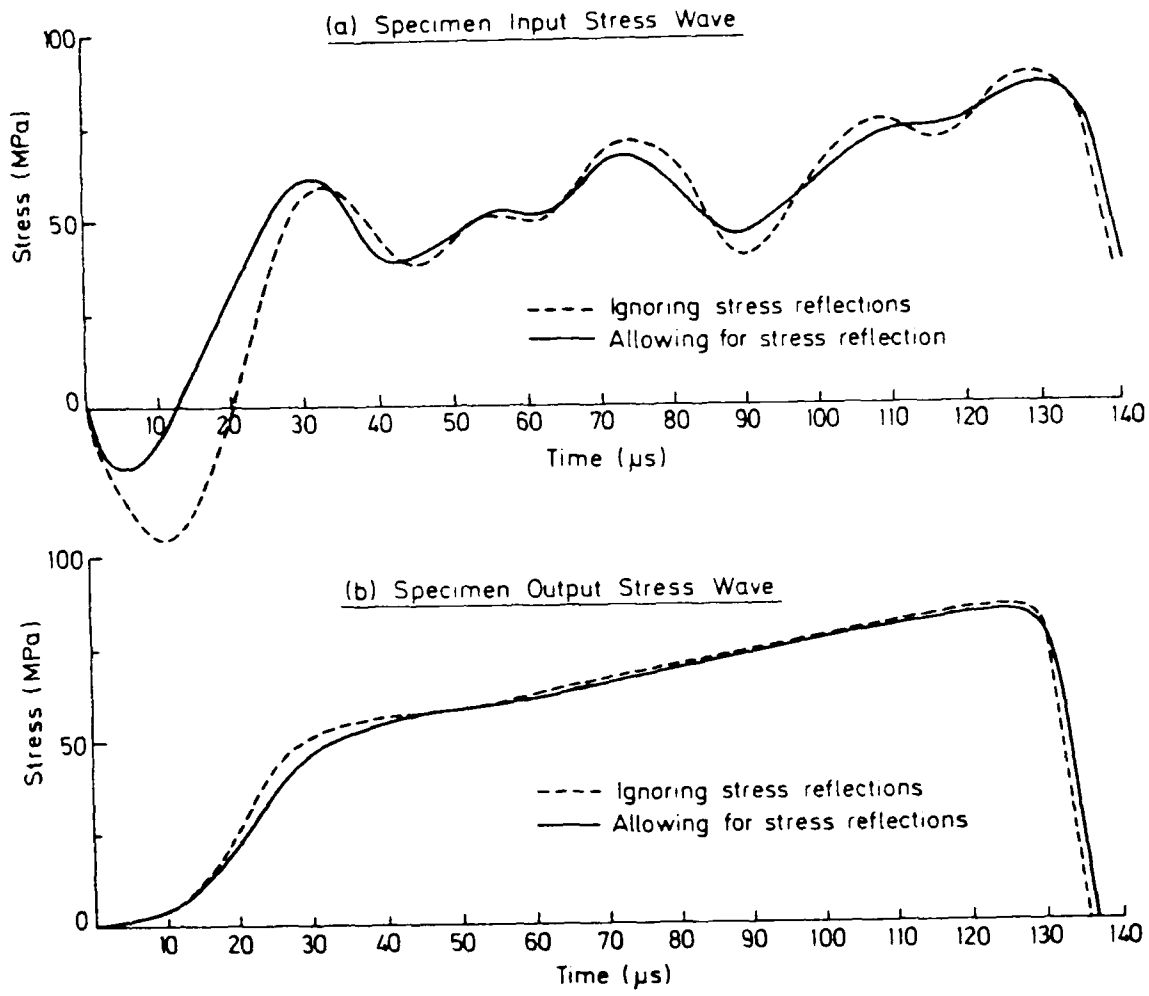

Fig. 2.19 EFFECT OF CORRECTING FOR STRESS WAVE REFLECTIONS IN SPECIMEN GRIP REGIONS

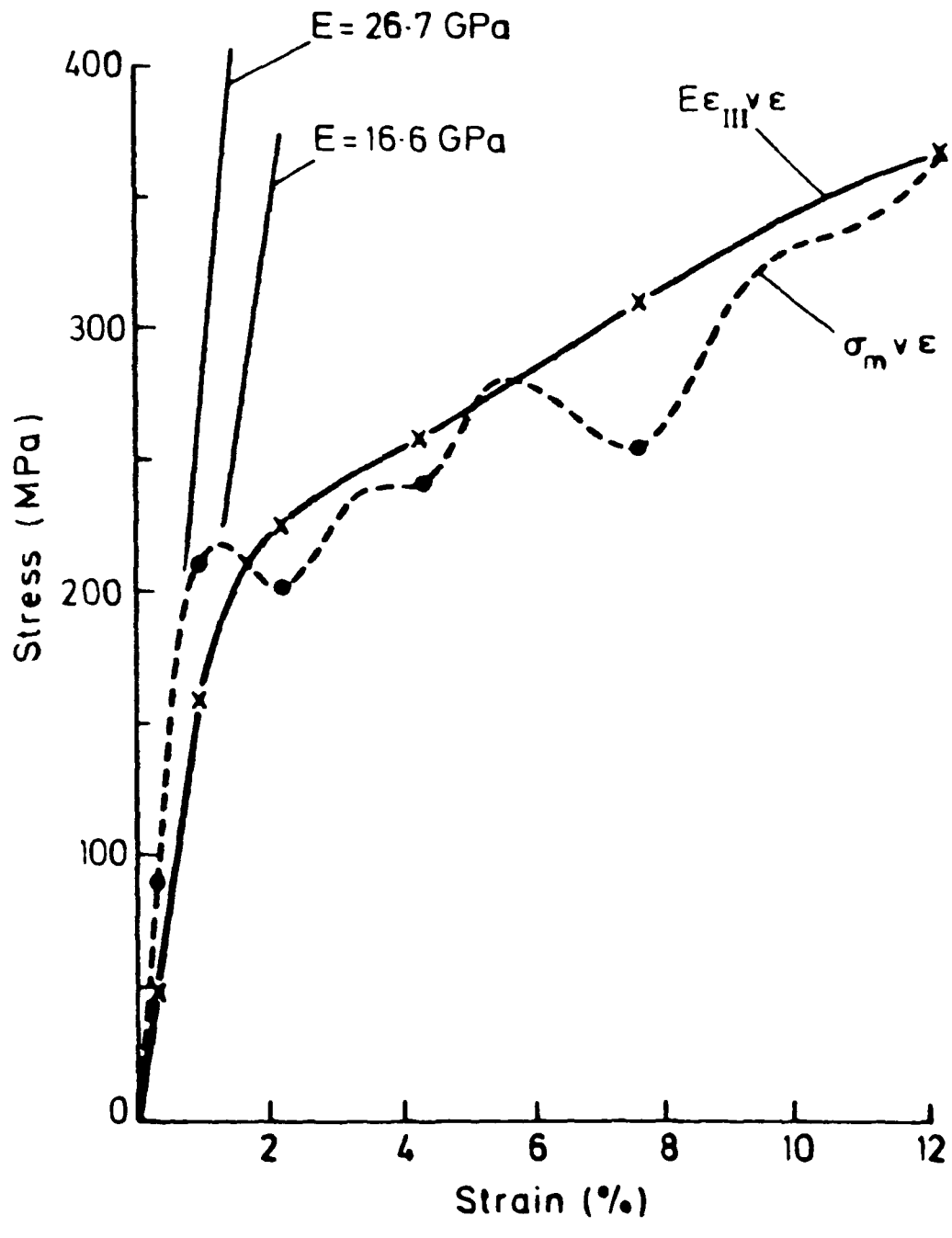

Fig. 2.20 STRESS-STRAIN CURVES FOR CALIBRATION TEST, INCLUDING CORRECTION FOR STRESS WAVE REFLECTIONS IN SPECIMEN GRIP REGIONS

(x - based on output bar signal; ● - based on specimen 'mean' stress)

2.6.3 Computer Analysis of Impact Test Data

The various strain gauge signals were stored in two Datalabs type DL922 (later 912) transient recorders and then input to the microcomputer for processing. The operator chooses the time zero for gauge I trace from which the computer calculates, in terms of the densities and Young's moduli of the loading bars and the specimen, the corresponding time zero's for gauge traces II and III and the time T_1, defined in Fig. 2.1, for the reflected wave first to reach gauge station II. The signals from gauge stations I and II are then computed as stress-time traces, after subtracting the calculated time delay between them. The resulting curves may be compared on the chart recorder, a typical example being given in Fig. 2.21 for a test on type 1 carbon/glass hybrid specimen. In this test a 'pick-up' spike, see section 2.5 above, appeared on the signal from gauge station II. The two computed curves should be coincident at times $< T_1$ and should only begin to diverge when the time exceeds T_1. If necessary the operator can choose to override the computer's calculated time delay between gauge stations I and II in order to improve the initial coincidence of the two curves. This has not been done in Fig. 2.21. From the two curves of Fig. 2.21, the computer then calculates the stress and particle velocity at the input end of the specimen, and compares the resulting stress curve with that for the output end of the specimen. This is calculated from the signal derived from the gauges at station III, again after subtracting the computer calculated time delay to the start of the trace. The two curves shown in Fig. 2.22 are obtained. If the 'pick-up' spike is discounted close agreement between the two stress-time curves is apparent, confirming that stress

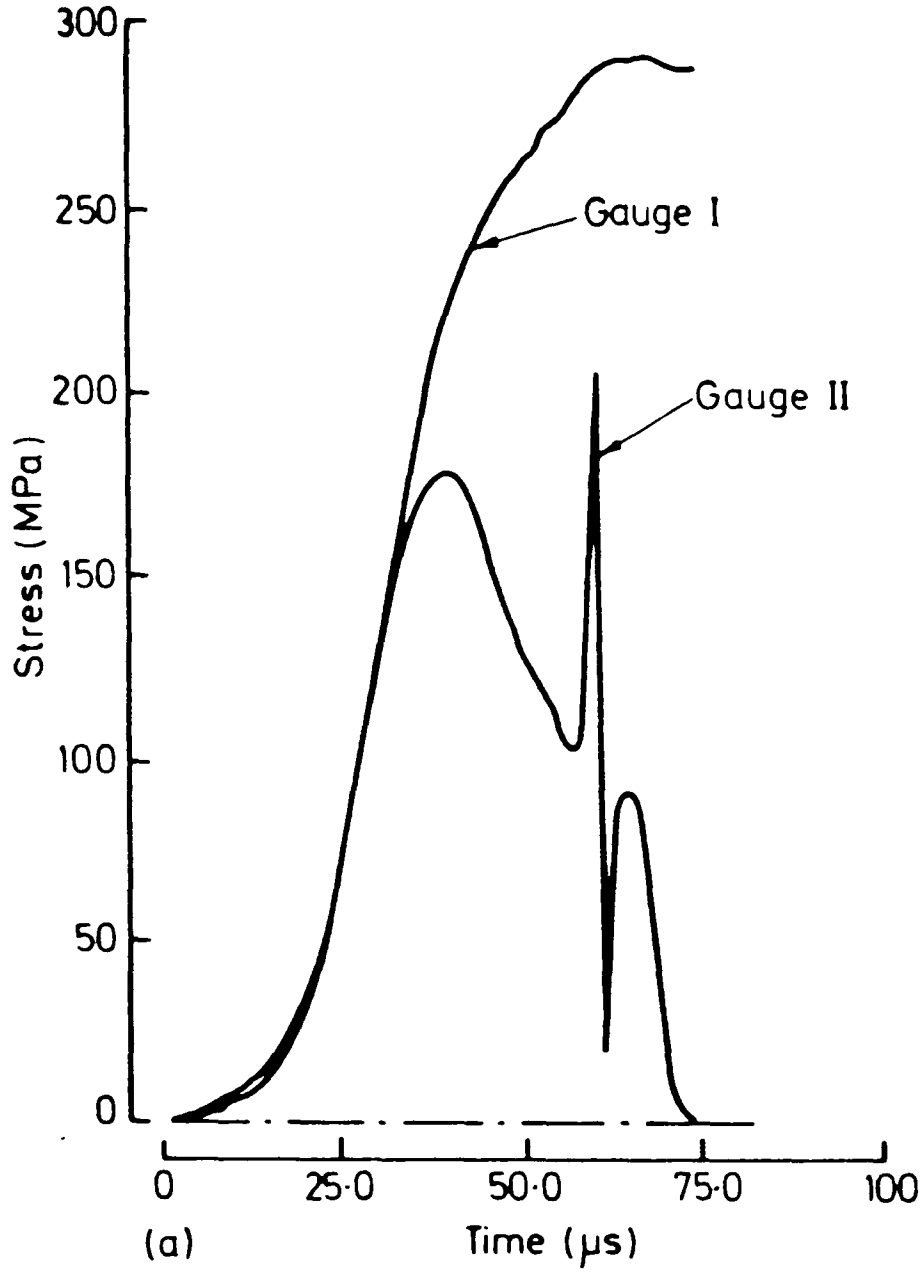

Fig.2.21 COMPUTER ANALYSIS OF INPUT BAR TRACES FOR A TEST ON A TYPE I HYBRID SPECIMEN

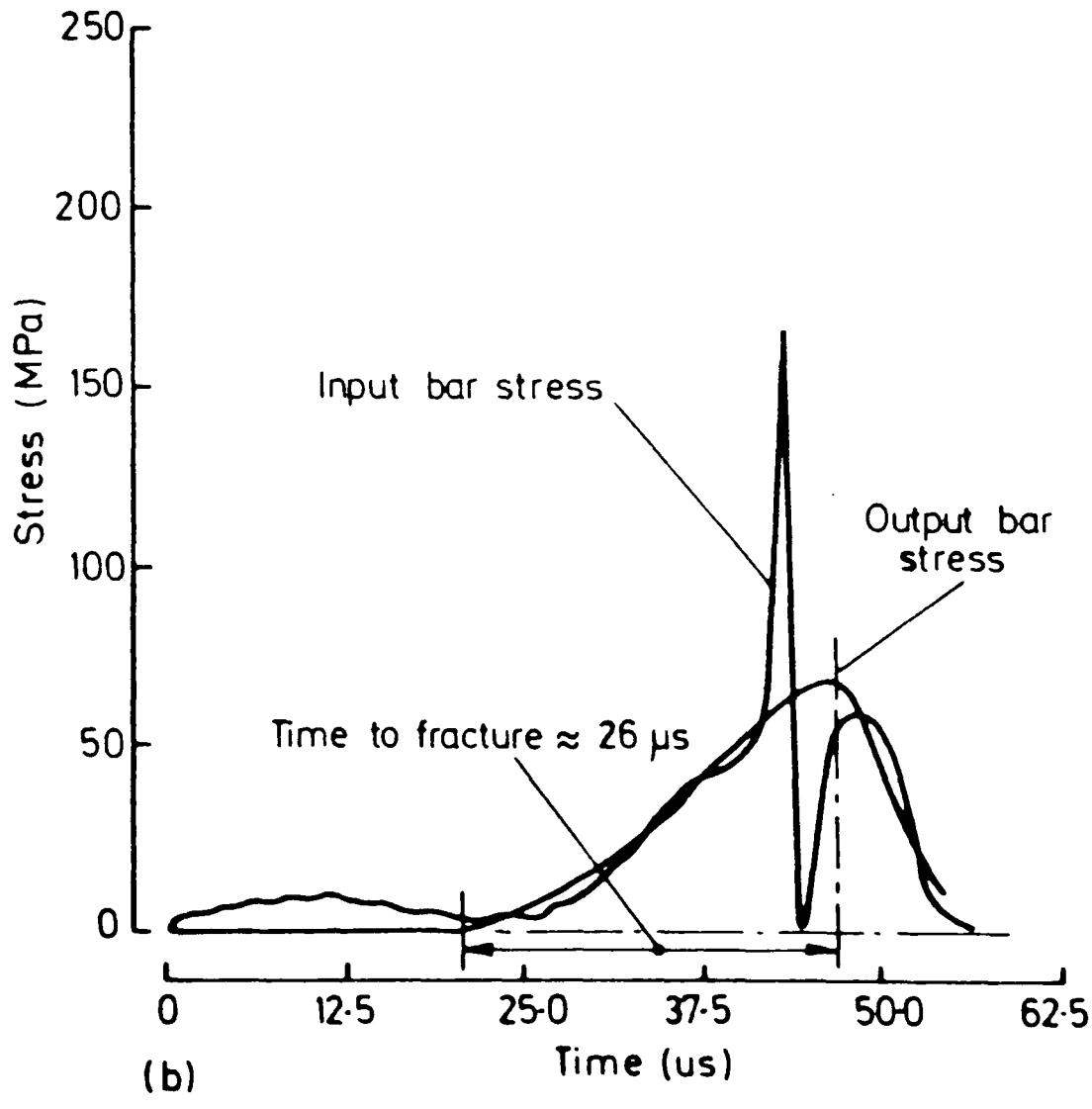

Fig.2.22 COMPUTED STRESS IN LOADING BARS EITHER SIDE OF SPECIMEN FOR TEST OF Fig.2.21

equilibrium across the specimen has been achieved during the course of the test. Again the operator can choose to override the computer's calculated time delay to the start of trace III if this will improve the agreement between the computed curves of Fig. 2.22. No such adjustment was required in the test of Fig. 2.22.

The computed stress-strain and strain rate-strain curves for this test are shown in Fig. 2.23. The pick-up spike has no noticeable effect on the stress strain curve but is the cause of the apparent perturbation on the strain rate-strain curve at a strain of about 1.3%. Discounting this perturbation, it is clear that, although the strain rate increases continuously throughout the test, it lies between 800 and 1200/s over the most significant region, i.e. where damage is developing and fracture is propagating. To allow comparison between different tests an average strain rate may be defined as the fracture strain divided by the time to fracture, where the fracture point is taken to coincide with the maximum stress. In the test of Fig. 2.23, this gives an average strain rate of ~640/s. This definition, therefore, is likely to give a value of average strain rate somewhat less than the controlling strain rate during fracture of the composite. Since a microcomputer is used to process the experimental data, it is possible to eliminate the effect of the pick-up spike, by suitably editing the gauge II data file. A schematic representation of the computer program for the above analysis is given in Fig. 2.24.

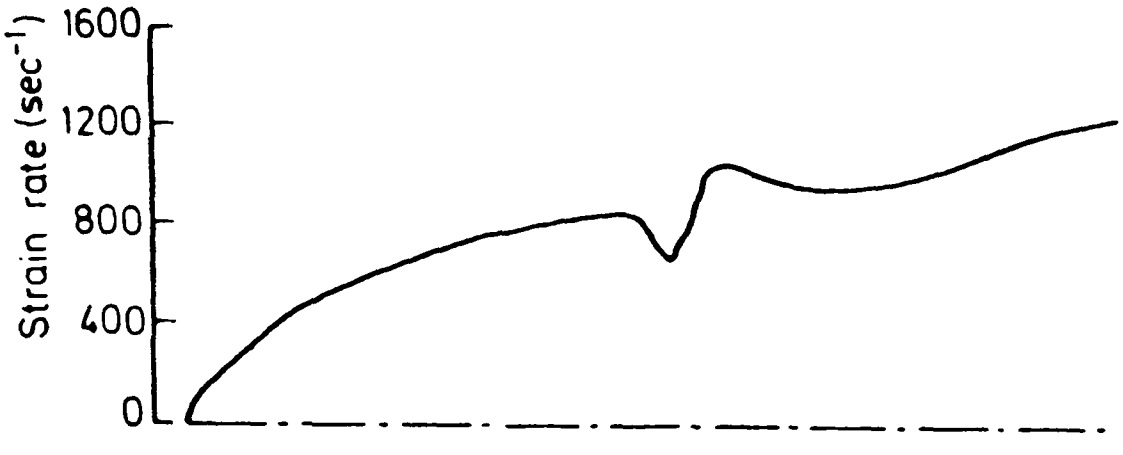

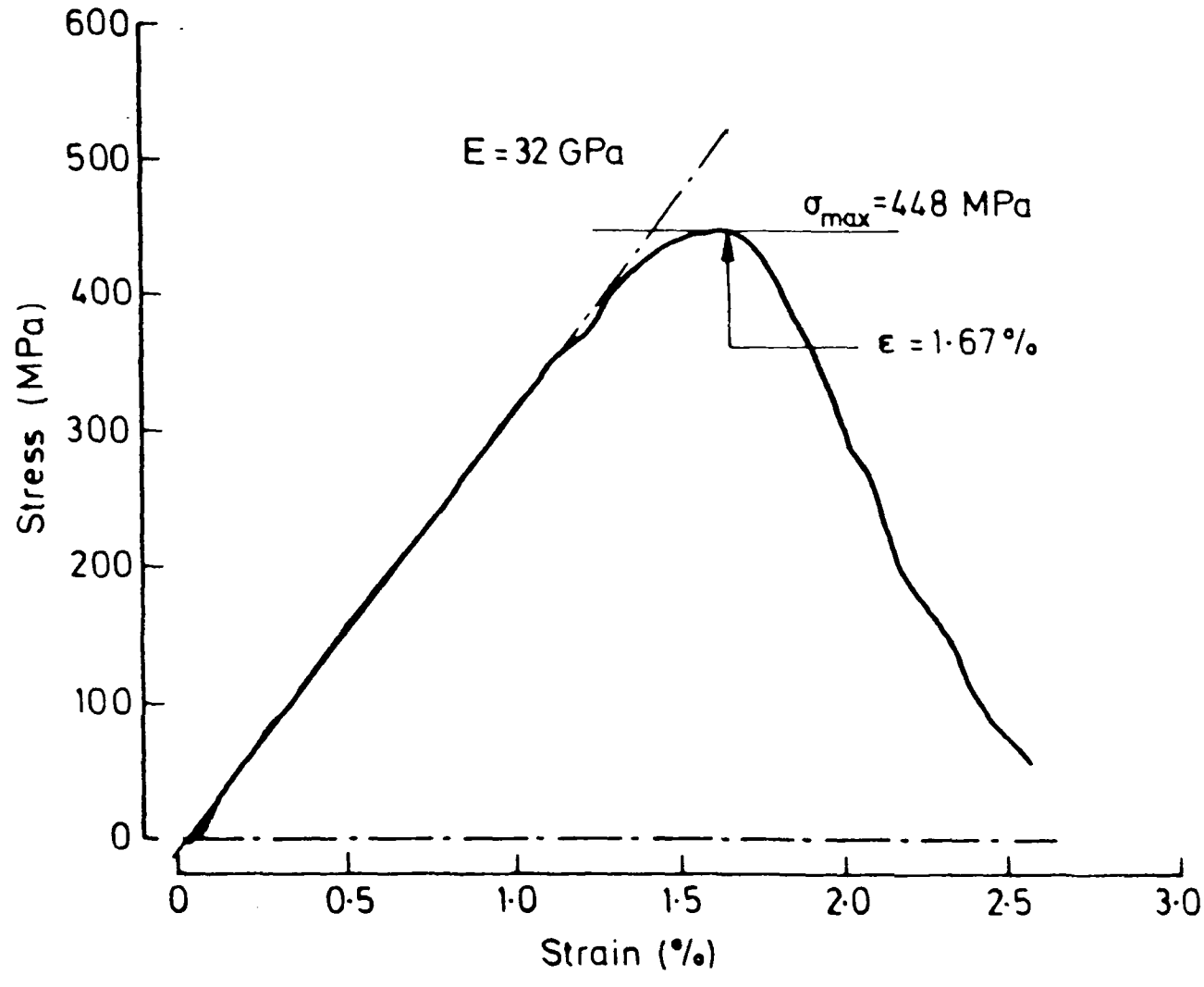

Fig.2.23 COMPUTED STRESS-STRAIN AND STRAIN RATE-STRAIN CURVES FOR TEST OF Fig.2.21

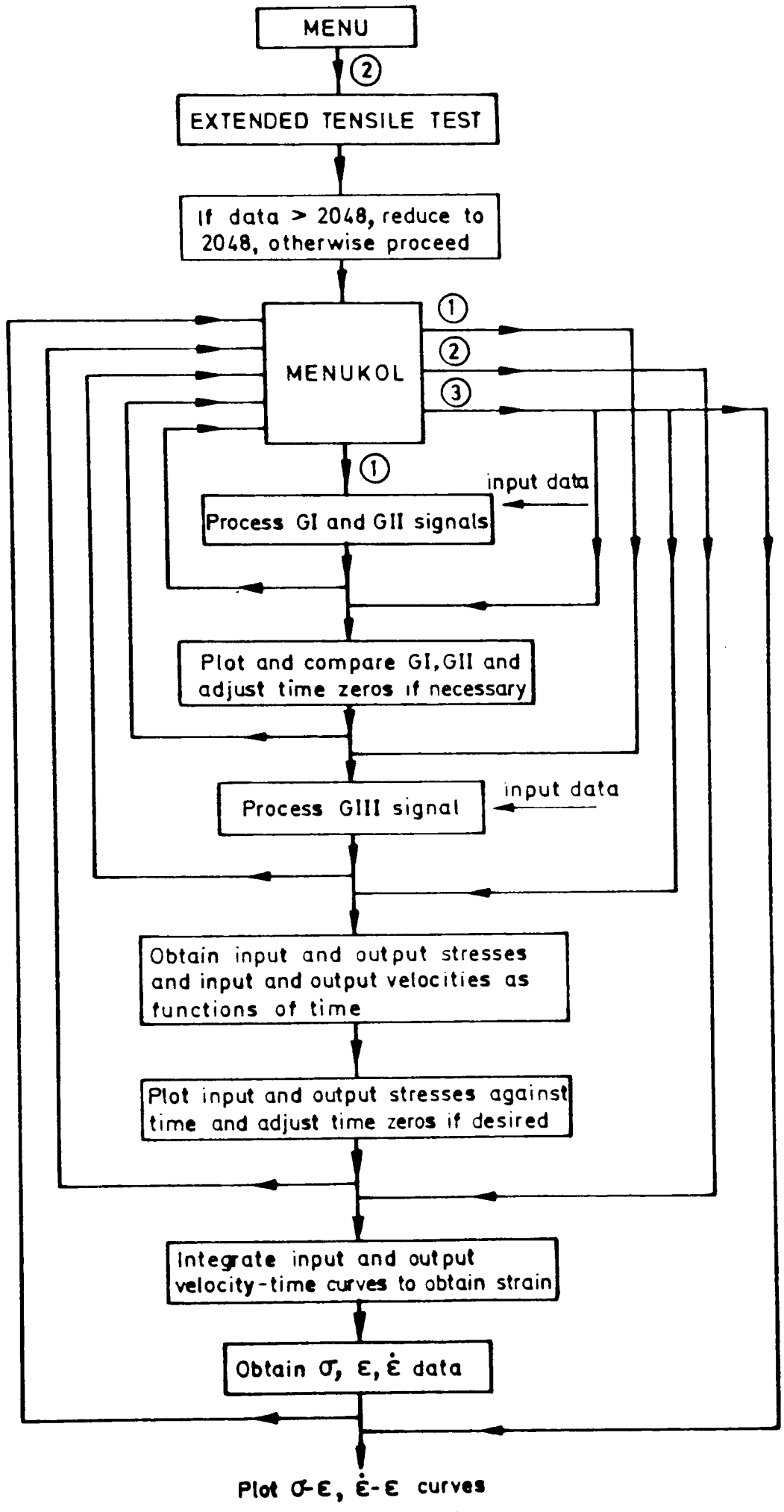

Fig. 2.24 Schematic representation of computer program for analysis of tensile impact test data.

2.7 Modification to the Gas Gun Loading System.

Although satisfactory results were obtained from the impact tests on composite specimens using the experimental arrangement depicted in Fig. 2.1, one obvious disadvantage in this set-up is the inaccessibility of the specimen during the course of the experiment. Also the process of inserting the loading bar/specimen assembly into the weighbar tube, given the increased lengths of the bars, was rather tricky, and could lead to damage to the specimen. For these reasons, and in view of the longer-term intention to conduct tensile impact tests on composite materials at temperatures other than ambient it was decided to modify the existing gas-gun loading equipment. A schematic diagram of the modified loading system is shown in Fig. 2.25 and photographs of the new gun and the test assembly are given in Figs. 2.26 and 2.27.

In the new arrangement the projectile is cylindrical in form and slides freely on the loading bar which extends through the back of the gun to the test assembly. When the projectile impacts the loading block, which is attached to the right-hand end of the loading bar, a tensile wave is set up which travels back along the loading bar to the test assembly. This consists of the input bar, the specimen and the output bar, exactly as before. Only a few tests has been performed so far with the new set-up and it is clear from the results that some improvement is needed in the design of the loading block and of its fixing to the loading bar in order to reduce the large stress fluctuations see Fig. 2.28, which appear on the initial part of the tensile loading wave making an accurate determination of the input stress relatively more difficult.

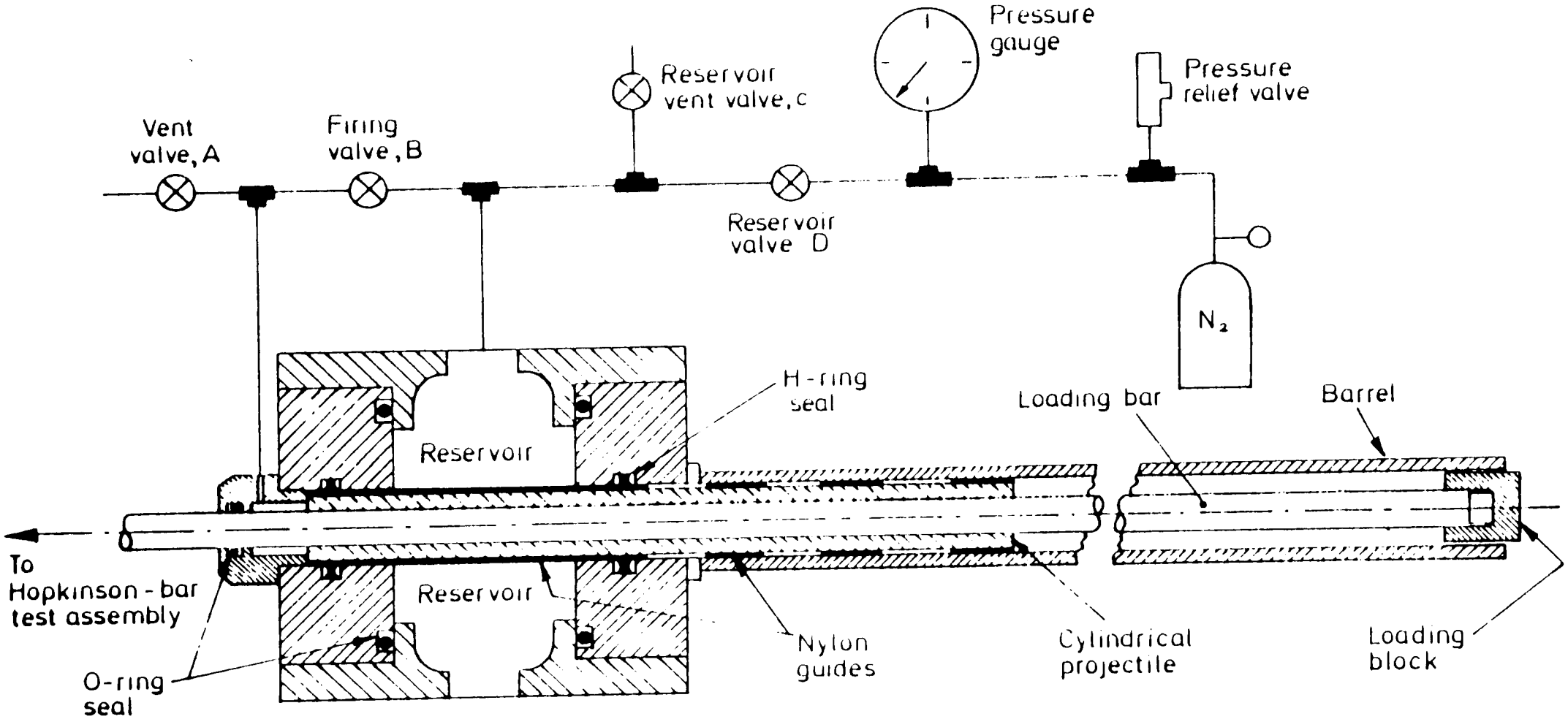

Fig.2.25 SCHEMATIC DIAGRAM OF MODIFIED GAS-GUN

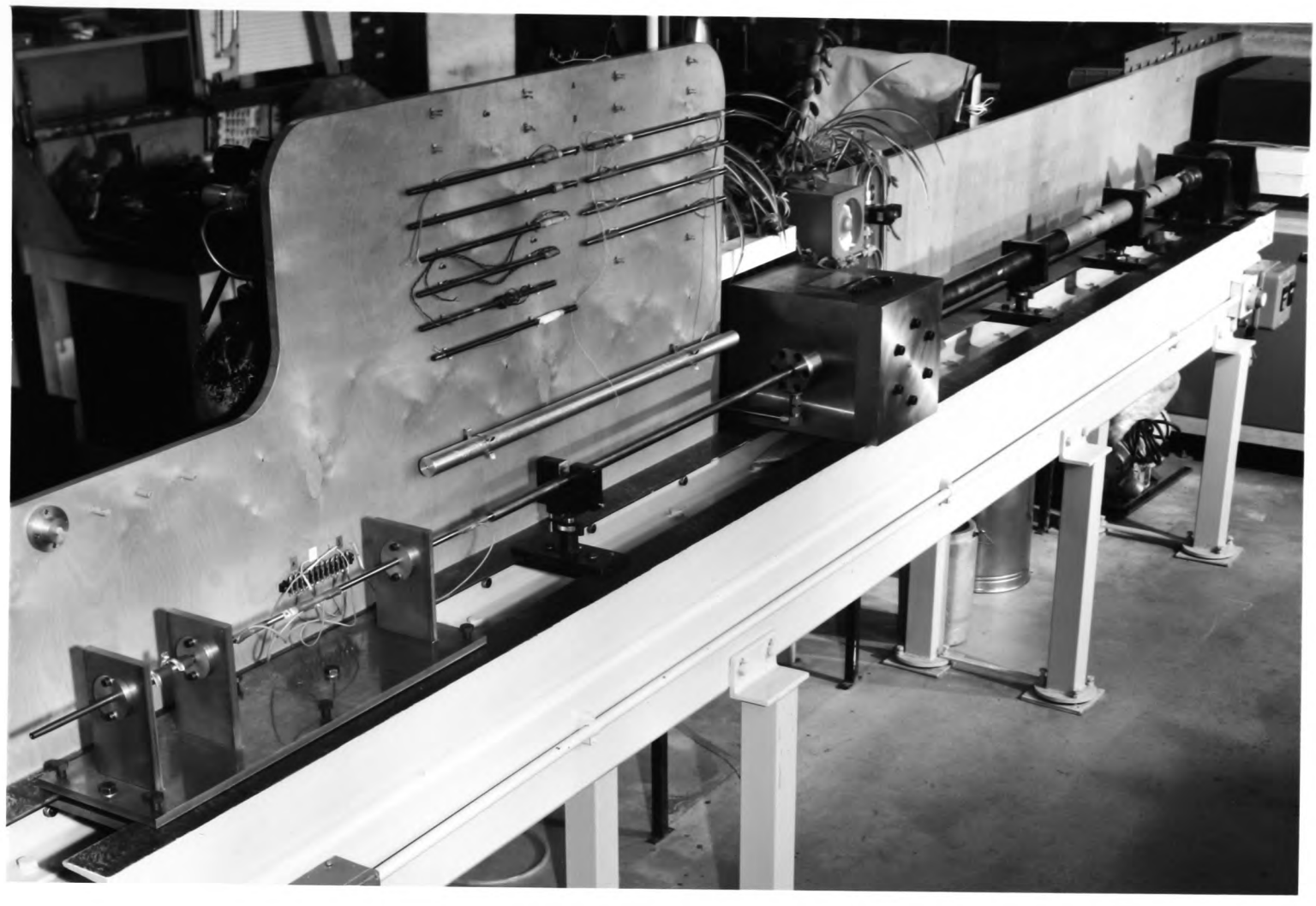

Fig. 2.26 GENERAL VIEW OF MODIFIED GAS-GUN

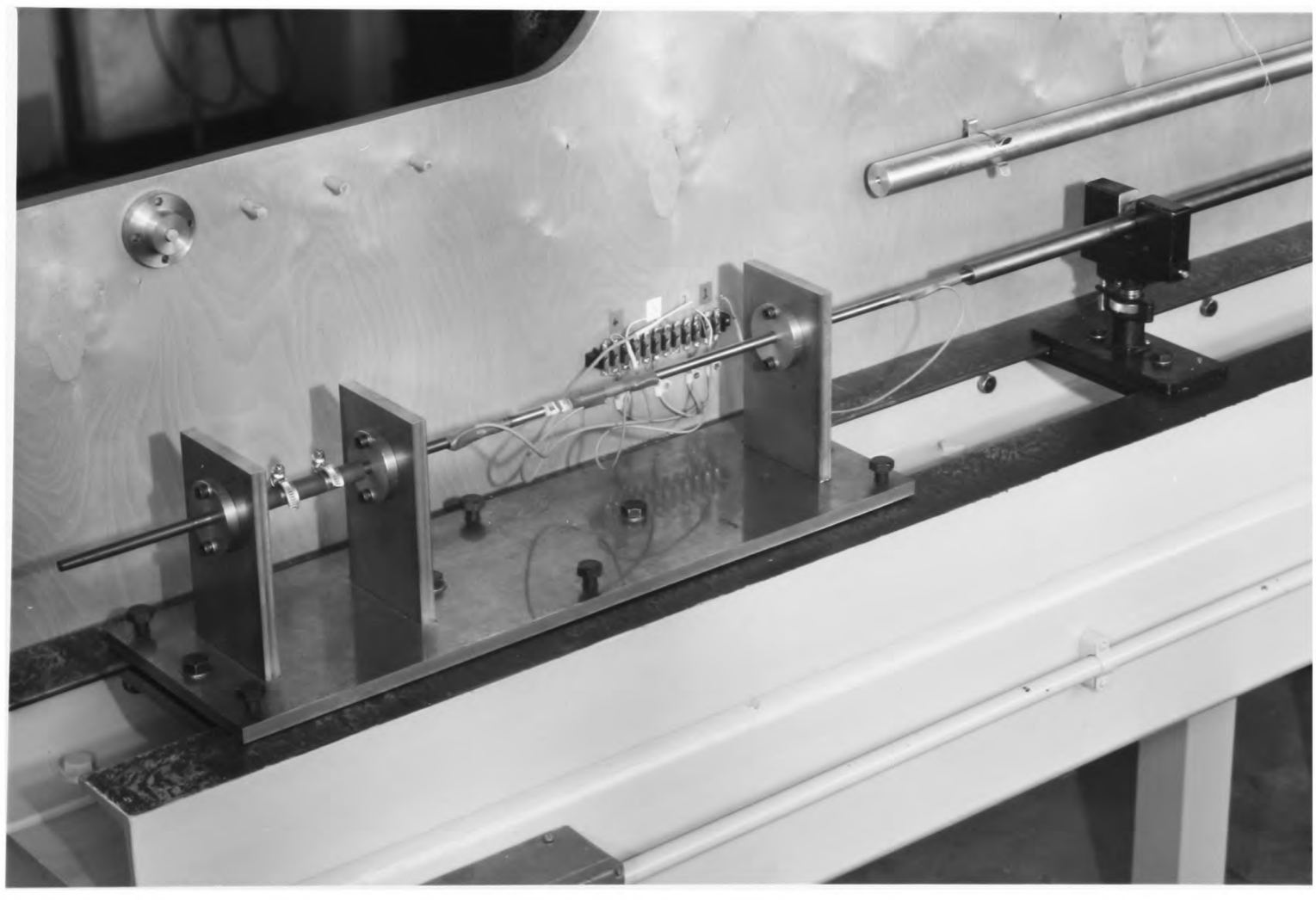

Fig. 2.27 HOPKINSON-BAR TEST ASSEMBLY FOR MODIFIED GAS-GUN

Fig.2.28 RAW DATA FOR IMPACT TEST ON AN ALL-CARBON SPECIMEN

(Input bar strain gauge signals)

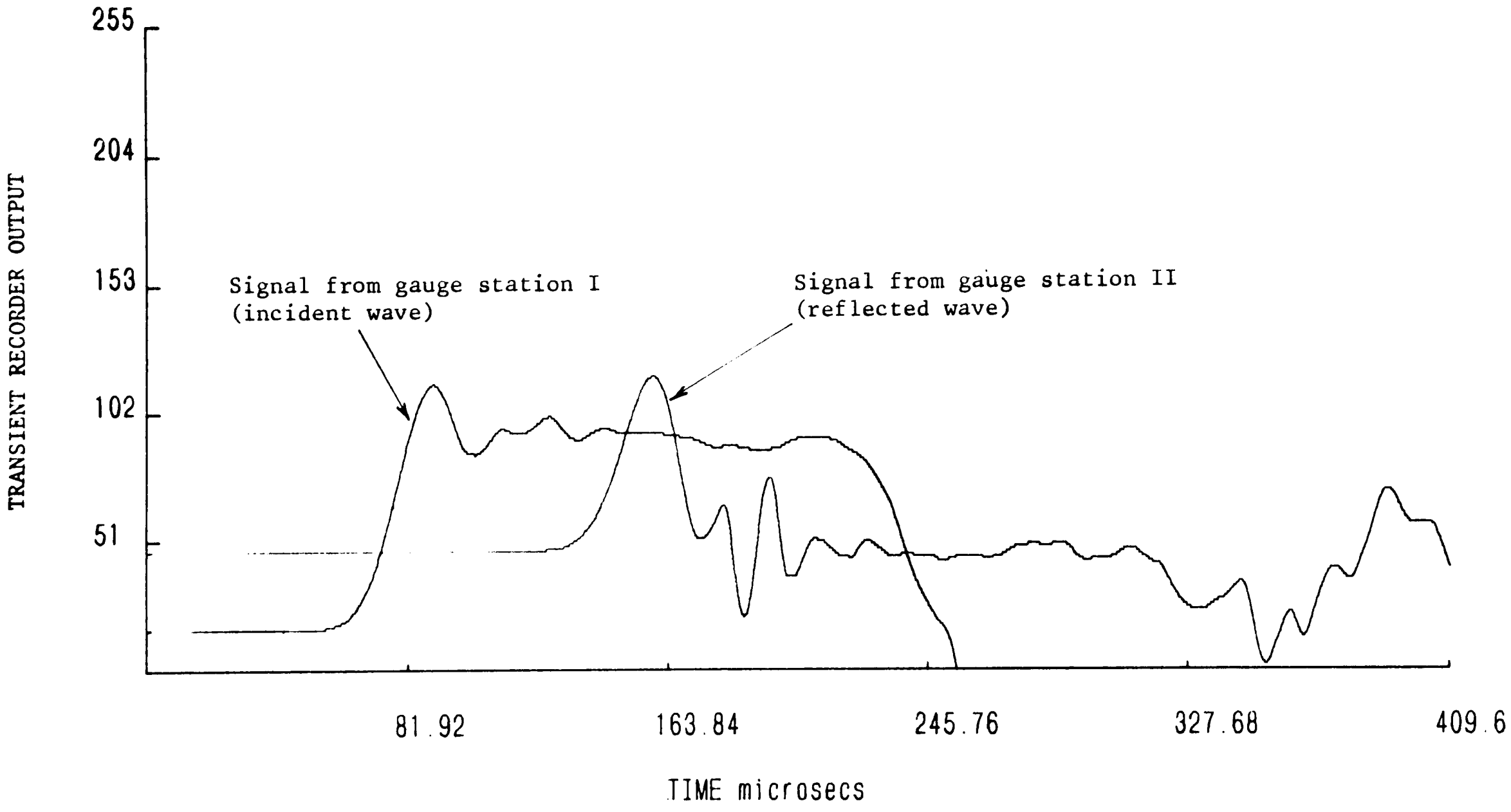

2.8 Hydraulic Testing Machine.

For the medium rate tests (~10/s) the hydraulic machine developed by Cooper and Campbell [85] was used. This equipment was developed to study strain rate effects in a variety of materials including composites [91] and is shown schematically in Fig. 2.29. It may be used for both tension and compression tests. For tension testing, valves V_1, V_2 and V_3 are opened and the oil pressure in the reservoir R and above and below piston P, i.e. in regions U and L, is raised to the required level. A sudden release of pressure from region L, through valves V_6 and D (the dump valve) results in the downward motion of piston P and hence of the moving crosshead Y, which is an integral part of the piston. The flow rate, and, for a given cylinder pressure and specimen, the strain rate, is controlled by the choice of one of six orifices in valve V_6. The largest orifice was used in all tests and the cylinder pressure was 2000 psi (13.8 MPa).

When strip as opposed to cylindrical composite specimens are to be tested, the gripping technique is modified from that shown in Fig. 2.29, where S is the specimen. In this investigation special grips were used to attach the test-piece to the strain-gauged load cell at one end and to the moving crosshead at the other, see Fig. 2.30. A pair of linear variable differential transformers (LVDT's) attached to the grips either side of the specimen measure the velocity at which the specimen deforms. Their integrated output is proportional, therefore, to the displacement across the specimen. Strain gauges attached to the specimen parallel

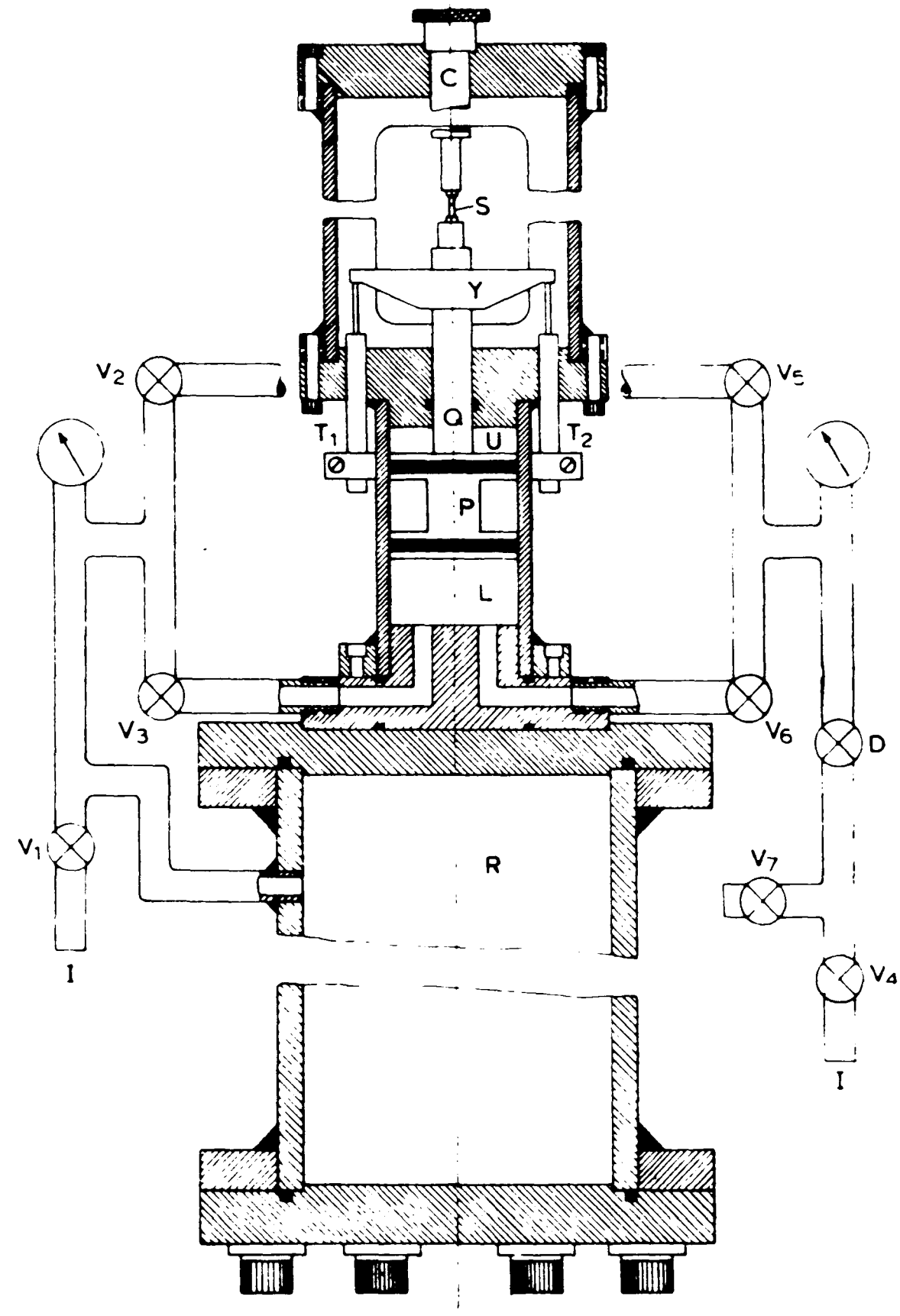

Fig.2.29 SCHEMATIC ARRANGEMENT OF INTERMEDIATE RATE HYDRAULICALLY-OPERATED LOADING MACHINE

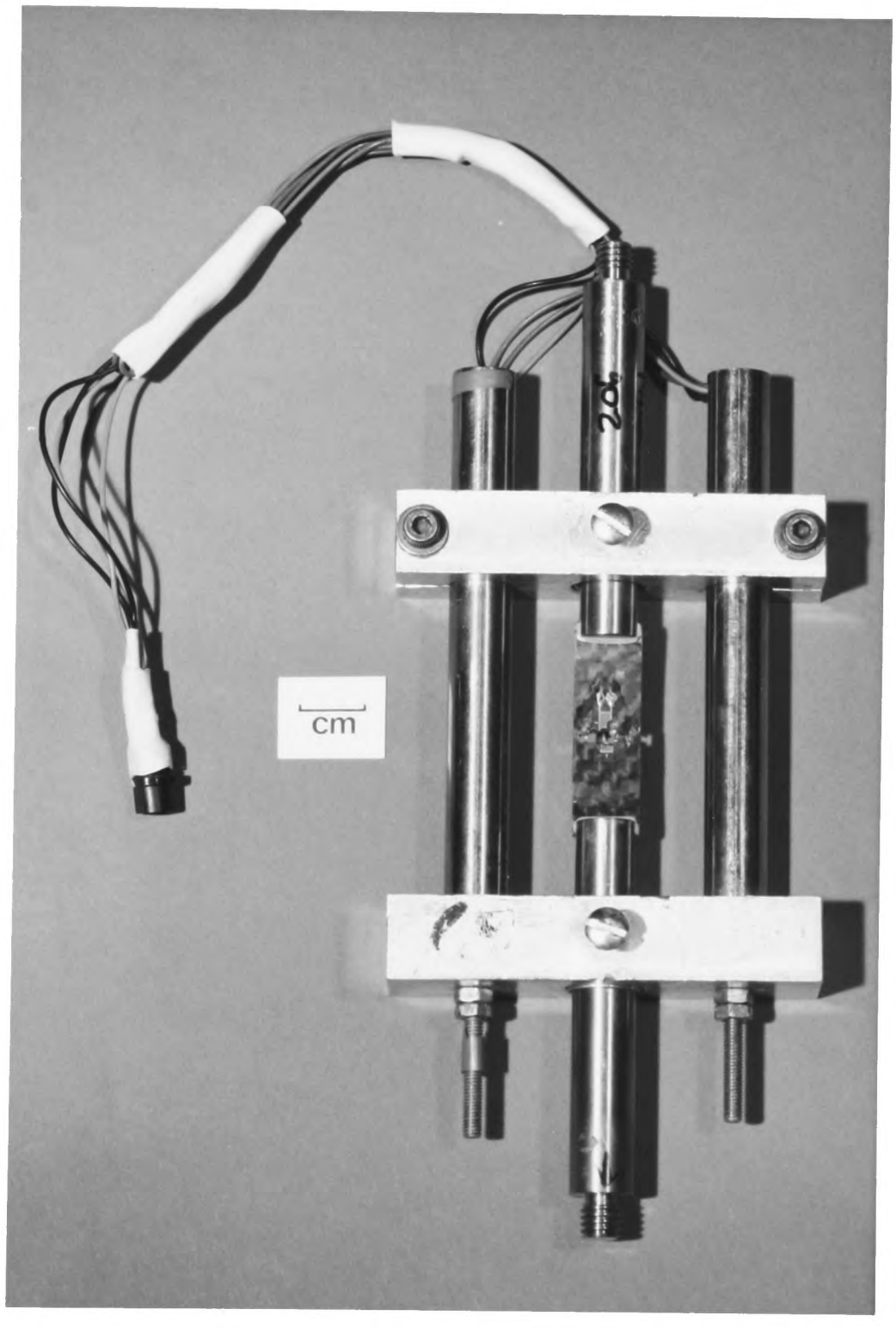

Fig. 2.30 SPECIMEN AND TEST ASSEMBLY FOR INTERMEDIATE RATE LOADING

gauge section provide a check of the strain, and hence of the tensile modulus, while the deformation is elastic.

Output signals from the load cell strain gauges, channel I, the LVDT's, channel II, and the specimen strain gauges, channel III, were stored in two Datalabs type 902 dual-channel transient recorders and subsequently could be plotted on an X-Y chart recorder or input to the microcomputer for processing. Typical raw data, as plotted on the chart recorder, for a test on type 1 hybrid specimen, are shown in Figs. 2.31a, b and c. The same data, after processing in the computer, were again plotted on the chart recorder and are shown in Figs. 2.32a, b and c. The full stress-strain curve for the specimen was obtained by cross-plotting the results from channel I against those from channel II. The tensile modulus was checked from a plot of channel I against channel III. The two curves obtained in this way are compared in Fig. 2.33. In this particular test the specimen fractured towards one end of the parallel section leaving the specimen strain gauges undamaged until separation of the specimen into two halves caused a breakage of the gauge leads. As a result the channel I/channel III plot shows a clear linear-elastic response, corresponding to a modulus of ~31GPa, over a stress range up to ~400 MPa. The channel I/channel II plot initially follows the same linear-elastic response, corresponding to a modulus in close agreement with that from specimen gauges, but then, at a stress of ~300 MPa, diverges from this and deforms anelastically up to failure at a strain close to 2%.

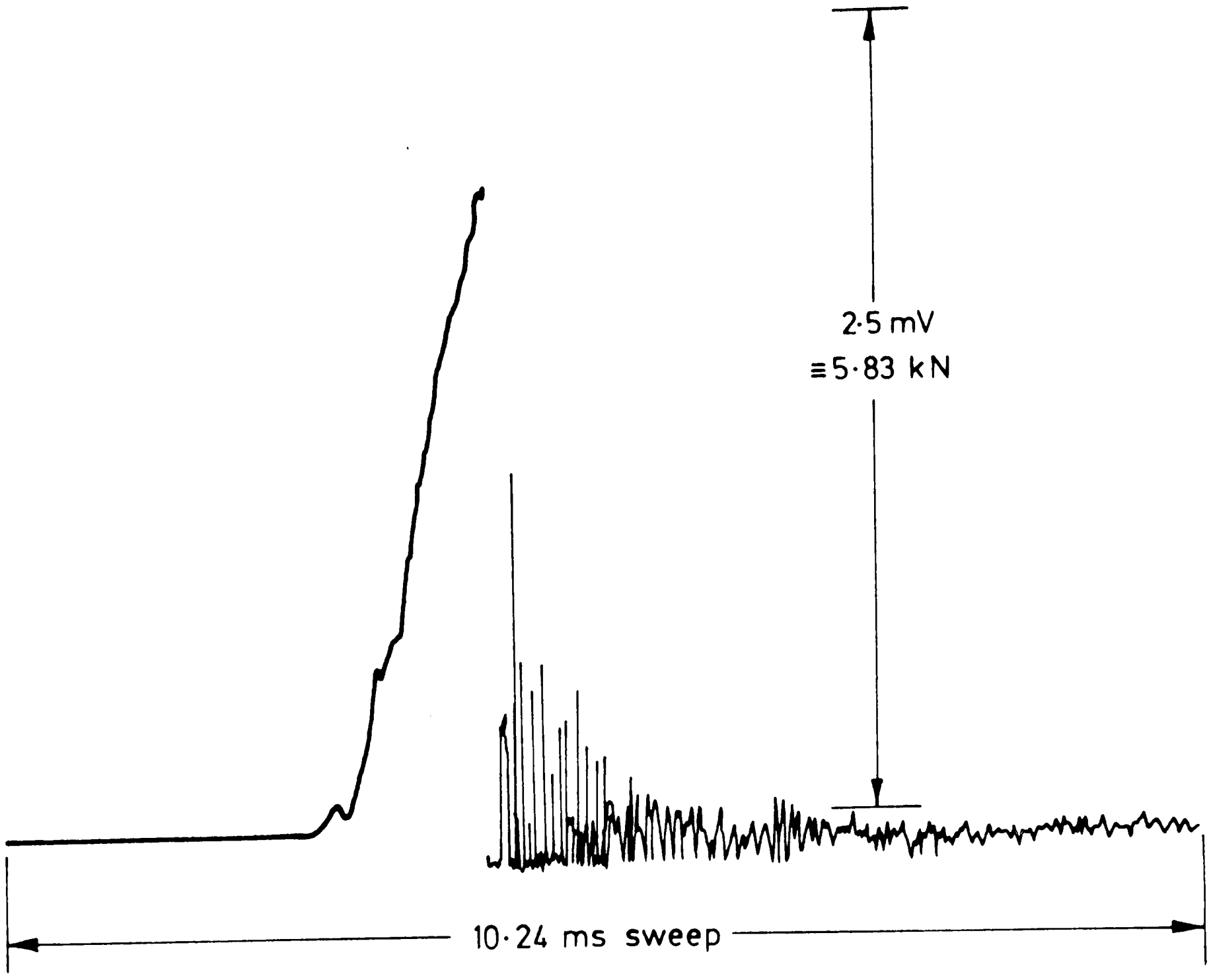

Fig.2.31 TEST RECORDS FROM HYDRAULICALLY-OPERATED LOADING MACHINE FOR TEST ON A TYPE I HYBRID SPECIMEN

a) Channel I, load-time signal

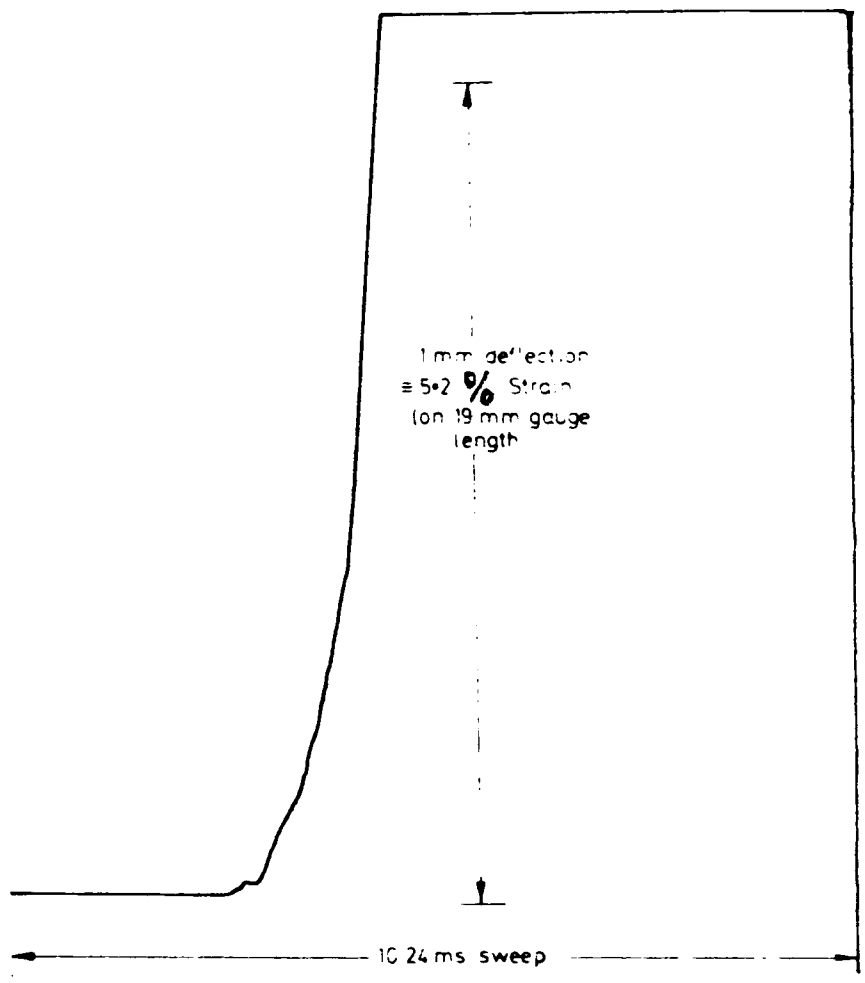

b) Channel II, displacement-time signal

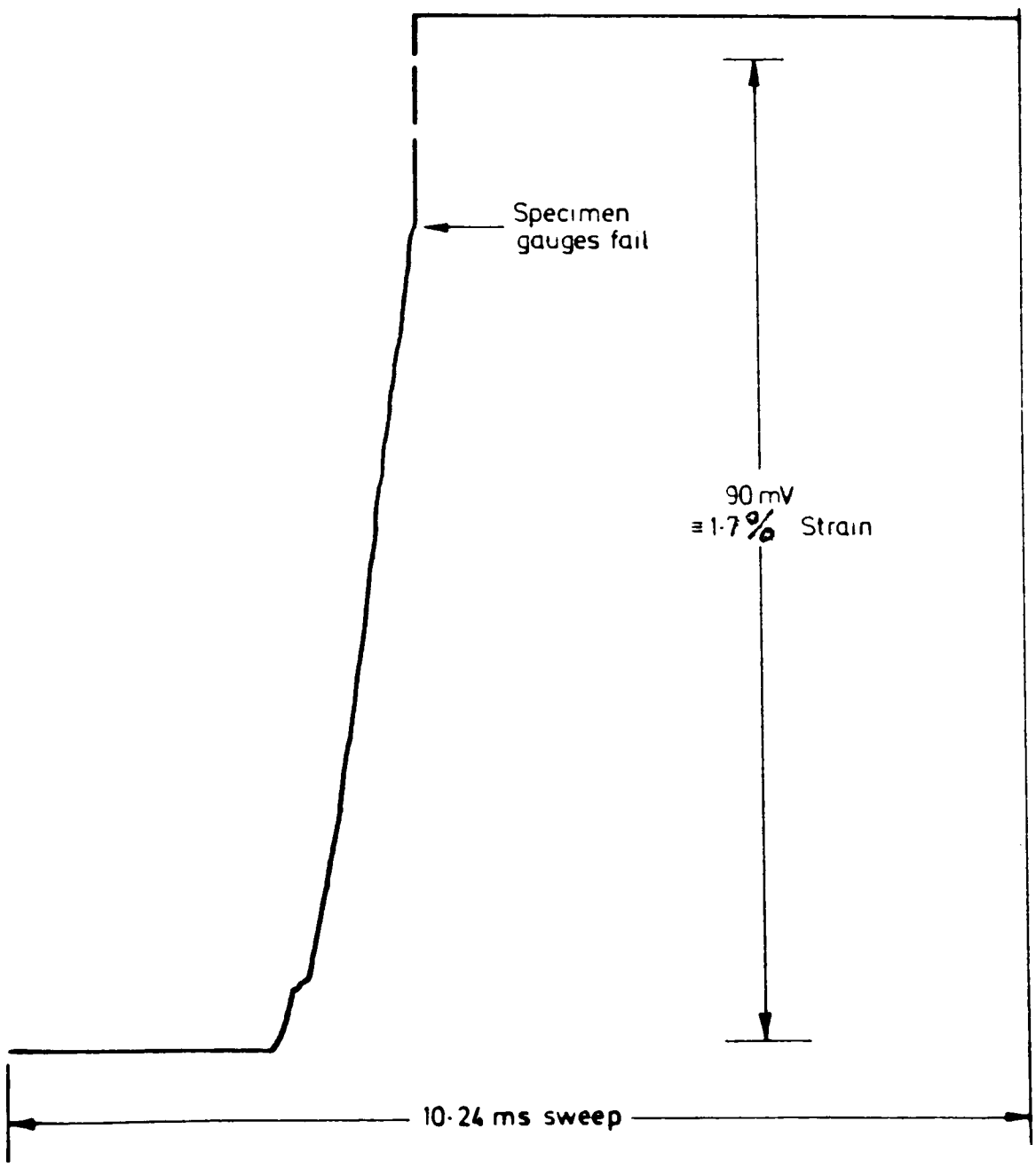

c) Channel III, specimen strain-time signal

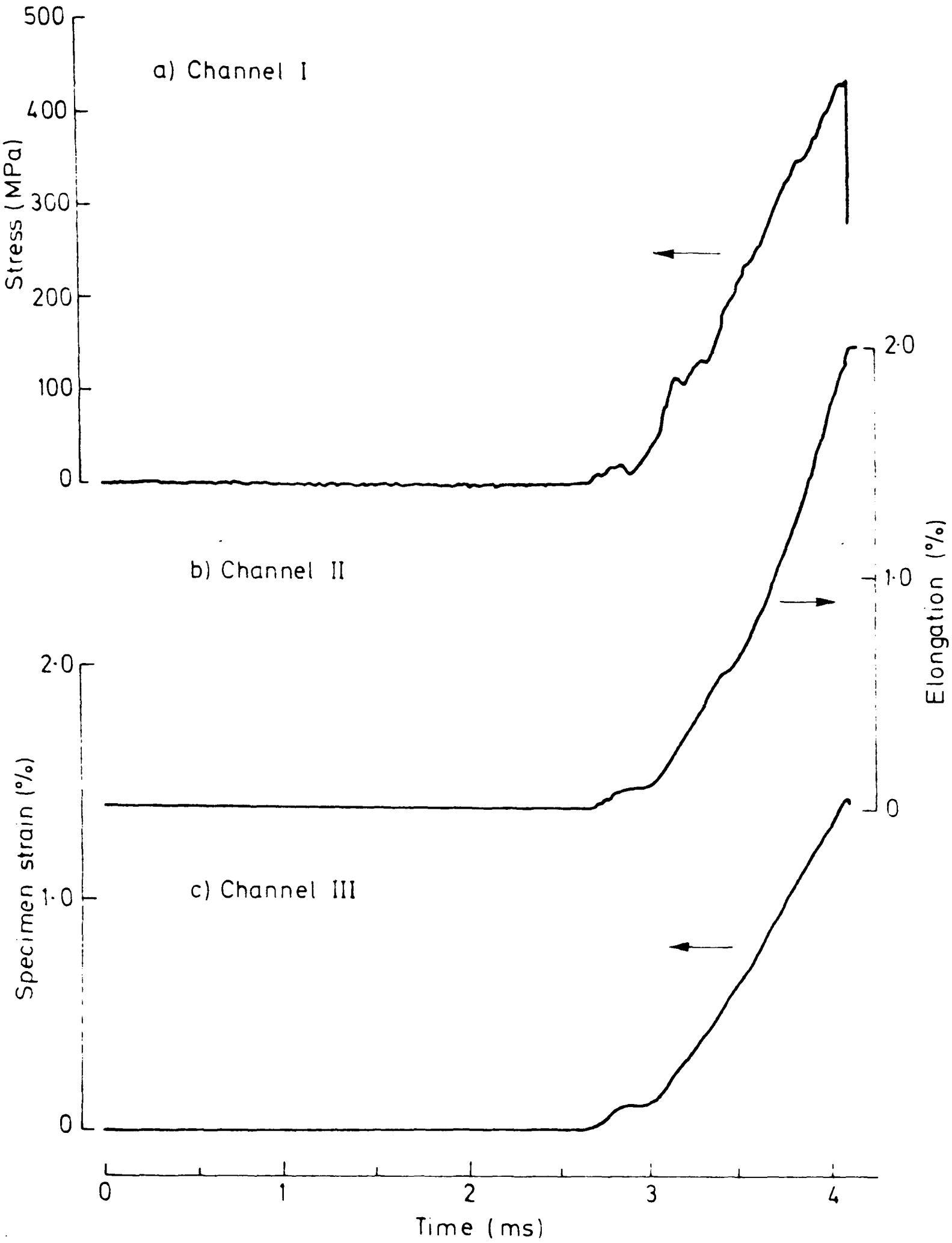

Fig. 2.32 TEST RECORDS OF Fig.2.31 AFTER PROCESSING IN THE MICROCOMPUTER

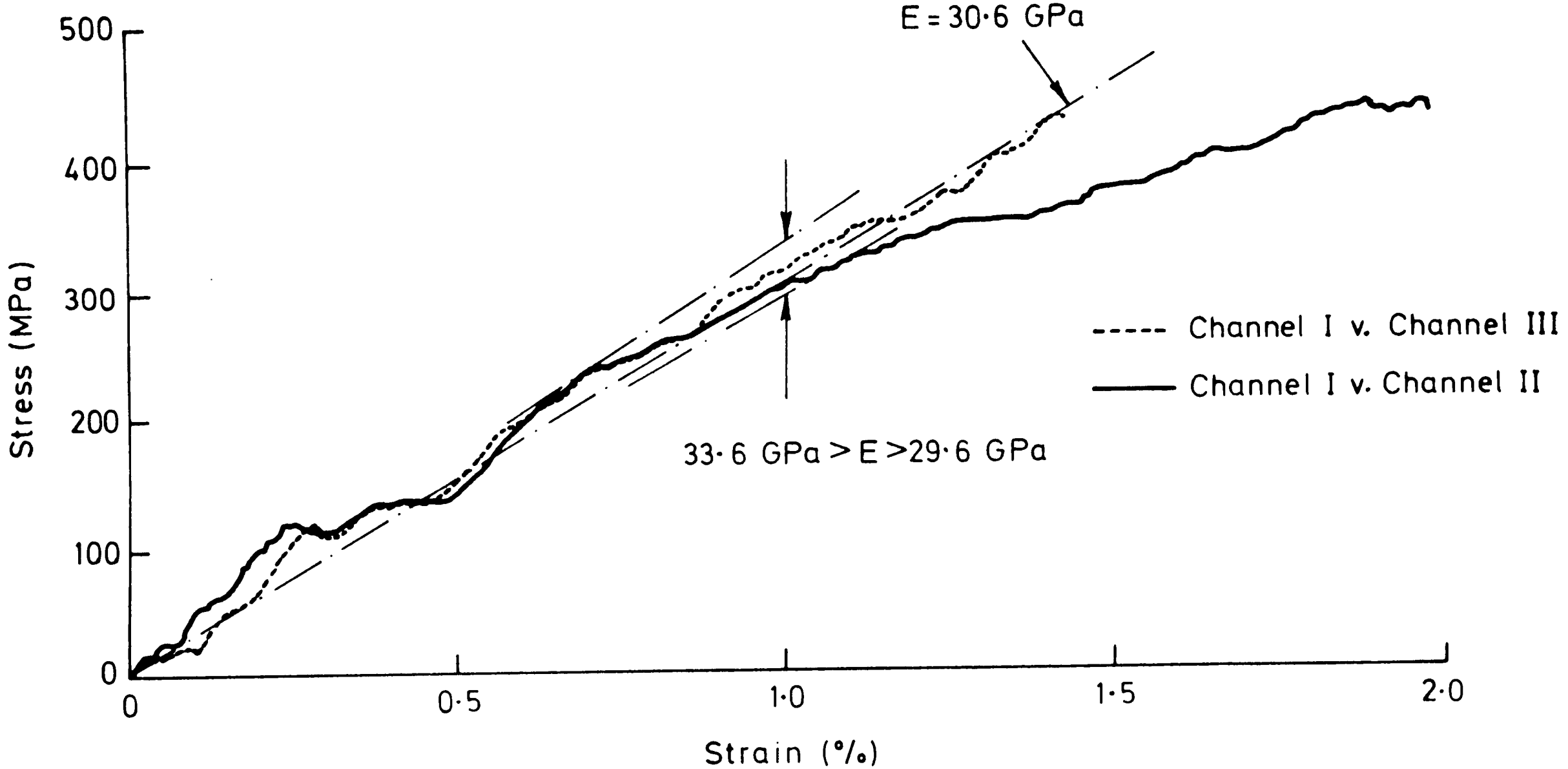

Fig.2.33 COMPUTED STRESS-STRAIN CURVES FOR TEST OF Fig.2.31

2.9 Instron Testing Machine

The principles of operation of this machine is well known and will not be discussed. For the quasi-static tests the same load cell, specimen grips and displacement measurement technique, employing the integrated output from two velocity transducers, as described for the intermediate rate tests, were again used, the only difference being that the load is applied more slowly using the Instron testing machine. Again strain gauges attached to the specimen parallel gauge section provide a check of the strain, and hence the tensile modulus, while the deformation is elastic. Output signals from the load cell strain gauges, the velocity transducers and the specimen strain gauges were stored in two dual-channel DL 902 transient recorders and were subsequently processed on a microcomputer to obtain two stress strain curves derived from the load cell signal and either the velocity transducers or the specimen strain gauges. Two such curves for a test on an all-carbon specimen are compared in Fig. 2.34 from which it is apparent that the velocity transducers overestimate the specimen strain, presumably because they also measure the deflection in the grips, and the specimen strain gauges fail well before final failure of the specimen. To obtain a corrected stress-strain curve for the test, therefore, the strain measured from the velocity transducers was reduced to give a stress-strain curve with an initial slope in agreement with that from the specimen strain gauges. In tests on all-glass specimens, for which the initial tensile modulus is less than half that for the all-carbon specimens, the velocity transducers were found to underestimate the true specimen strain, see Fig. 2.35 and the required correction is in the opposite direction. This

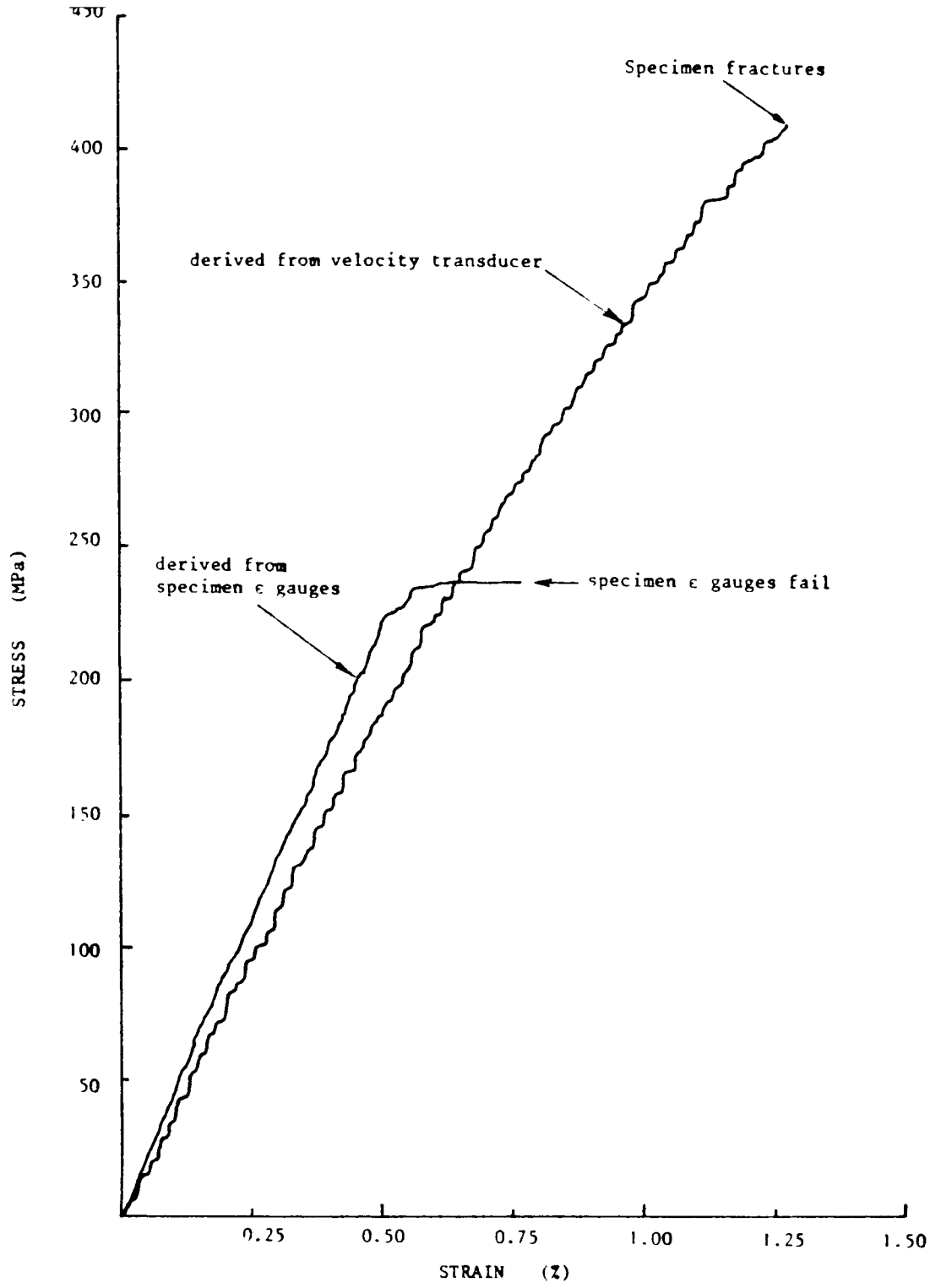

Fig.2.34 QUASI-STATIC STRESS-STRAIN CURVES FOR AN ALL-CARBON SPECIMEN

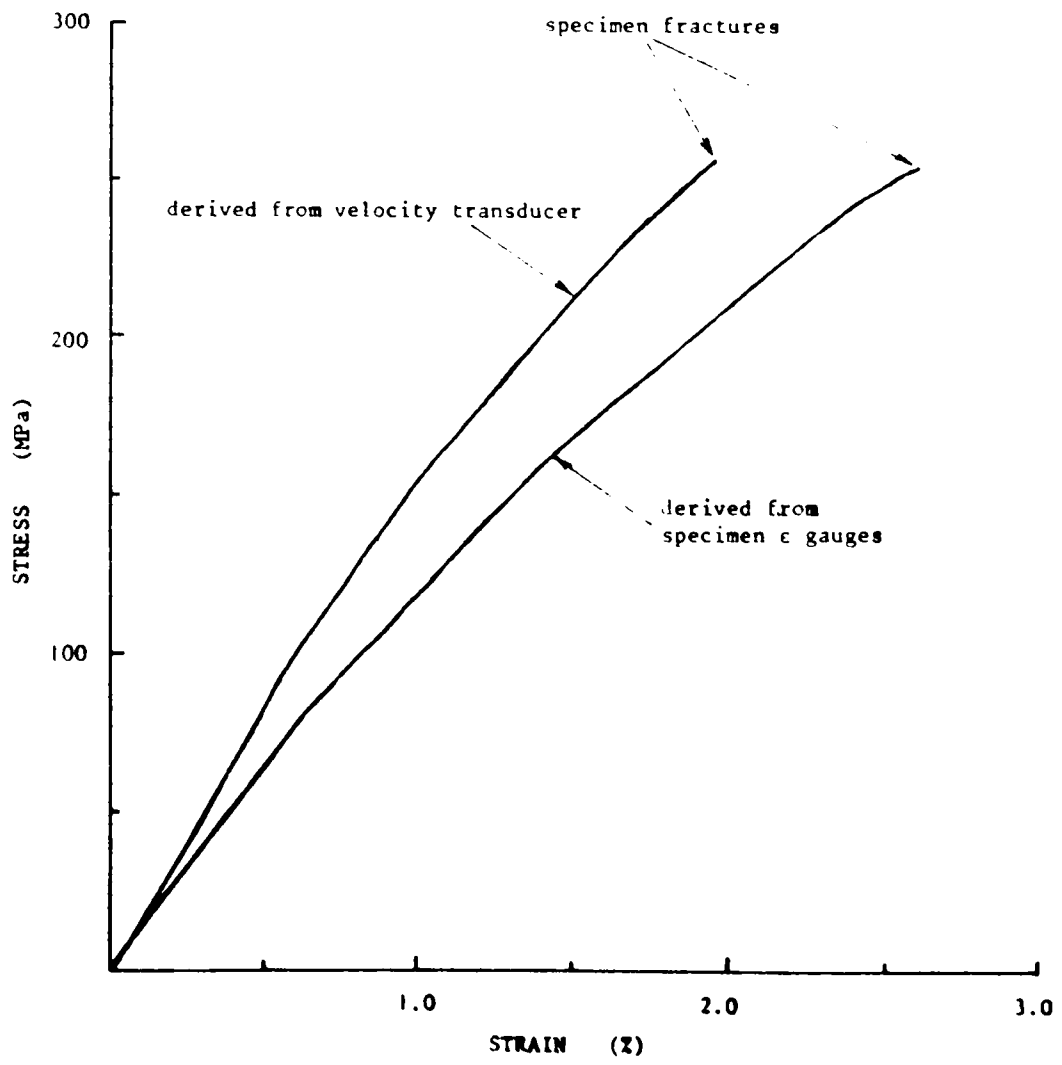

Fig.2.35 QUASI-STATIC STRESS-STRAIN CURVES FOR AN ALL-GLASS SPECIMEN

is presumably because, the specimen grips make a much less significant contribution to the overall displacement measured by the velocity transducers in tests on the more flexible all-glass specimens.

2.10 Determination of Stiffness Matrices.

The analytical prediction of the elastic modulus of a hybrid composite laminate requires a knowledge of the elastic properties of its constituent plies. It will be shown in Chapter 3 that the stiffness matrix of a woven fabric reinforced lamina is in general given by:

$$Q_{ij} = \frac{1}{\psi} \begin{bmatrix} E_L & \nu_{LT}E_T & 0 \\ \nu_{LT}E_T & E_T & 0 \\ 0 & 0 & \psi G_{LT} \end{bmatrix} \qquad (2.2)$$

where $\psi = 1 - \nu_{LT}\nu_{TL}$. Only four of the engineering constants are independent; i.e. the elastic moduli in the warp and weft directions E_L, E_T; the in-plane shear modulus, G_{LT} and the major Poisson's ratio ν_{LT}. E_L, E_T and ν_{LT} are usually derived from the results of two tension tests in the warp and weft directions. There is controversy [92-94], however, on what constitutes a simple and reliable technique for measuring the in-plane shear modulus of a composite material. Recent evidence [95,96] suggests that the 45^o off-axis tension test is quite adequate for evaluating this parameter. For this configuration(see Fig. 2.36)Rosen [97] has shown that the in-plane shear modulus takes the form

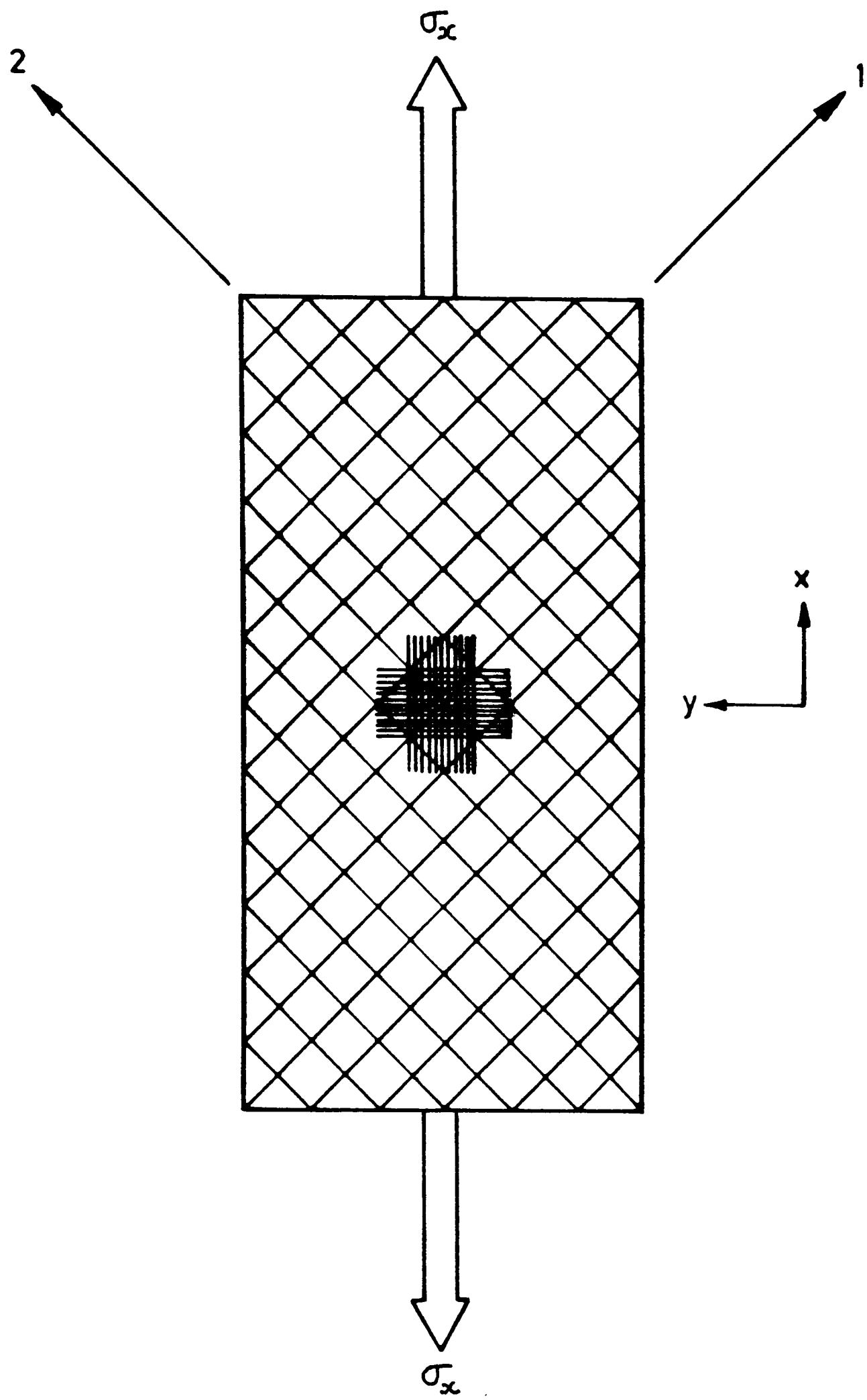

Fig. 2.36 Specimen configuration for measurement of in-plane shear modulus (after Rosen [97])

$$G_{LT} = \frac{\sigma_x}{2\,(\varepsilon_x - \varepsilon_y)} \qquad (2.3)$$

The plain-woven fabric reinforced-plastic laminate with a tensile load applied at 45^o to the fibre axes is analogous to the $[\pm 45^o]_s$ specimen material of Rosen. This method, therefore, is applicable in the present work. Additionally, the in-plane shear modulus determined in this way is easily checked against that obtained from the 'three tension tests' approach which is based on the orthotropic transformation equation

$$\frac{1}{\bar{E}_\theta} = \frac{1}{\bar{E}_L}\,\mathrm{Cos}^4\theta + \left[\frac{1}{G_{LT}} - \frac{2\nu_{LT}}{E_L}\right]\mathrm{Sin}^2\theta\,\mathrm{Cos}^2\theta + \frac{1}{\bar{E}_T}\,\sin^4\theta \qquad (2.4)$$

where θ is the angle between the warp tows and the applied tension. For $\theta = 45^o$, equation (2.4) may be written

$$G_{LT} = \left[\frac{4}{\bar{E}_{45}} - \left(\frac{1}{\bar{E}_L} + \frac{1}{\bar{E}_T} - \frac{2\nu_{LT}}{E_L}\right)\right]^{-1} \qquad (2.5)$$

Since E_L, E_T and ν_{LT} and known and E_{45} may be obtained from the test of Fig. 2.36, an alternative G_{LT} is obtained by substitution in equation (2.5). These two approaches, therefore, were employed in this investigation.

2.10.1 Quasi-Static Stiffness Matrix.

For the acquistion of quasi-static stress-strain data, the specimen design of Fig. 2.9 was adopted. In determining the quasi-static

stiffness matrix, however, although the same experimental set-up was employed, the test specimens were parallel sided coupons taken from the all-glass or all-carbon laminates and with the loading axis in either the warp or the weft directions or at 45^{o} to both warp and weft directions. Strain gauge rosettes were attached to either side of the specimens, as shown schematically in Fig. 2.37, and a digital microvoltmeter was used to measure the strain gauge outputs as each specimen was loaded and unloaded several times within the elastic range. Finally each specimen was loaded through to failure, usually by pull-out of the specimen from the grips, the various load cell, velocity transducer and specimen strain gauge signals being stored in transient recorders in the usual way. Raw data from one such test on an unwaisted all-carbon specimen loaded in the warp (L) direction is shown in Fig. 2.38a, b and c, for the load cell, the velocity transducer and the two specimen strain gauge directions respectively, each curve being a direct plot of the corresponding data file as stored in the microcomputer. The derived variation of stress with strain in the loading direction determined from the specimen strain gauges is shown in Fig. 2.39 the slope of which gives for the modulus in the warp direction a value of 47.6 GPa. By comparing the specimen strain gauge signals for the two orthogonal directions, longitudinal and transverse, see Fig. 2.40, a Poisson's ratio, ν_{LT}, of 0.119 is obtained.

2.10.2 Dynamic Stiffness Matrix.

The procedure for determining the stiffness matrix under dynamic loading was similar to that under quasi-static loading, specimen design

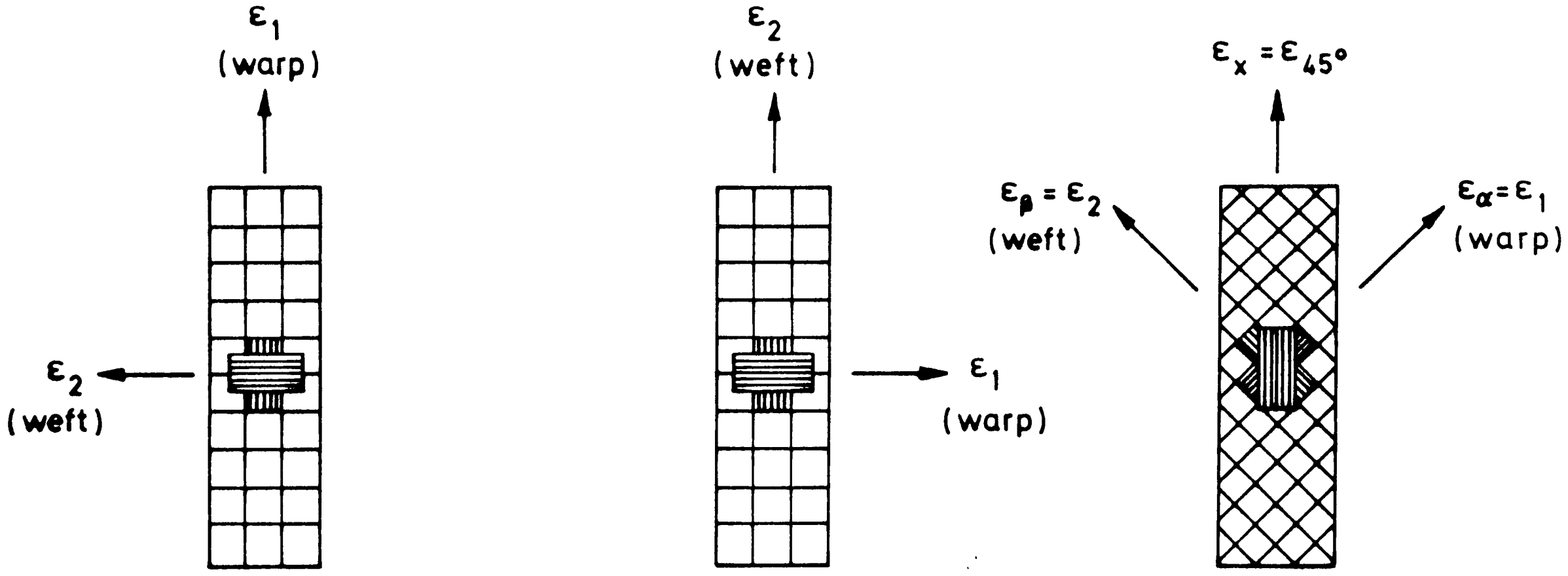

Fig. 2.37 Test specimens for stiffness matrix determination

Fig.2.36 RAW DATA FOR ELASTIC TEST ON AN ALL-CARBON SPECIMEN LOADED IN THE WARP (L) DIRECTION

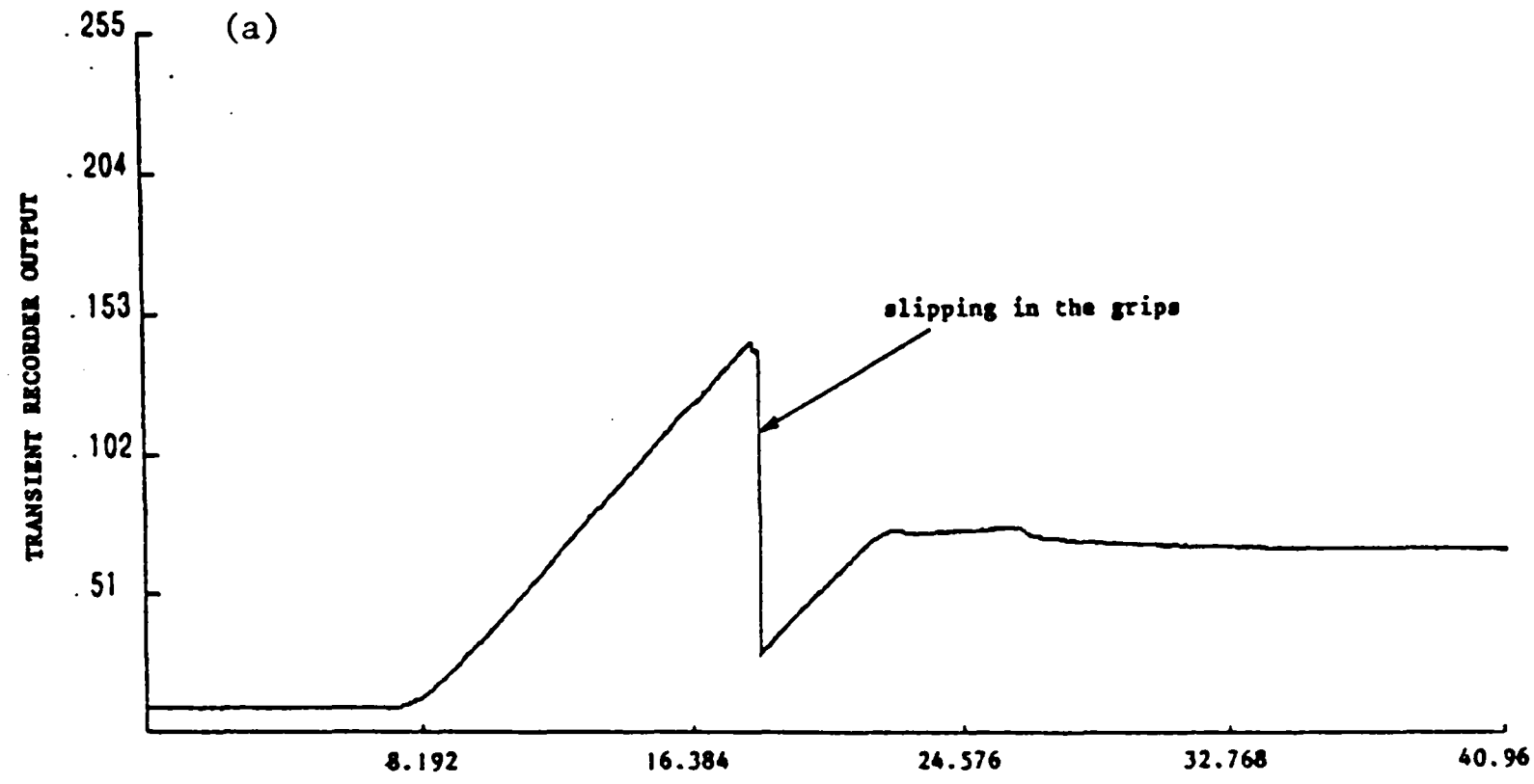

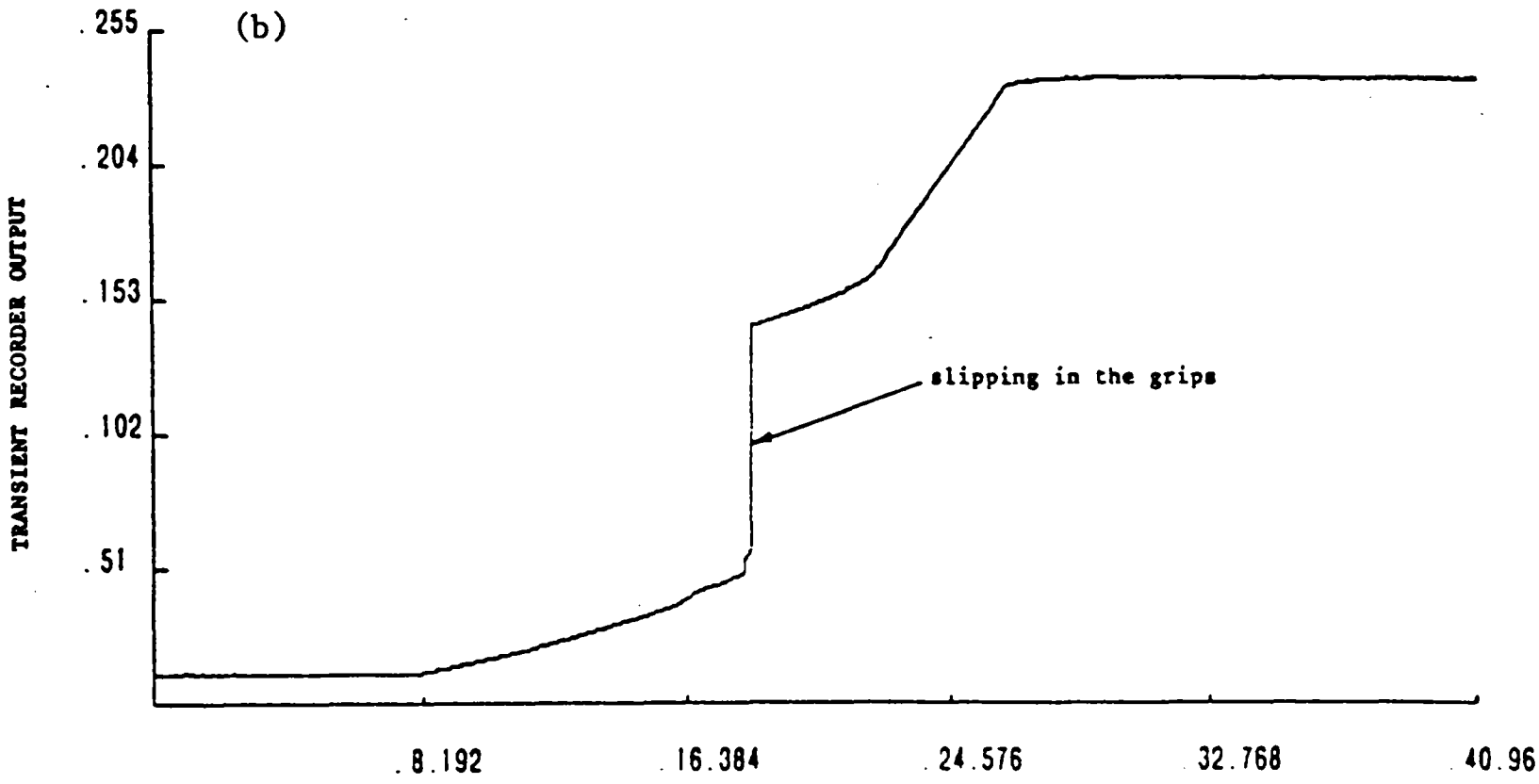

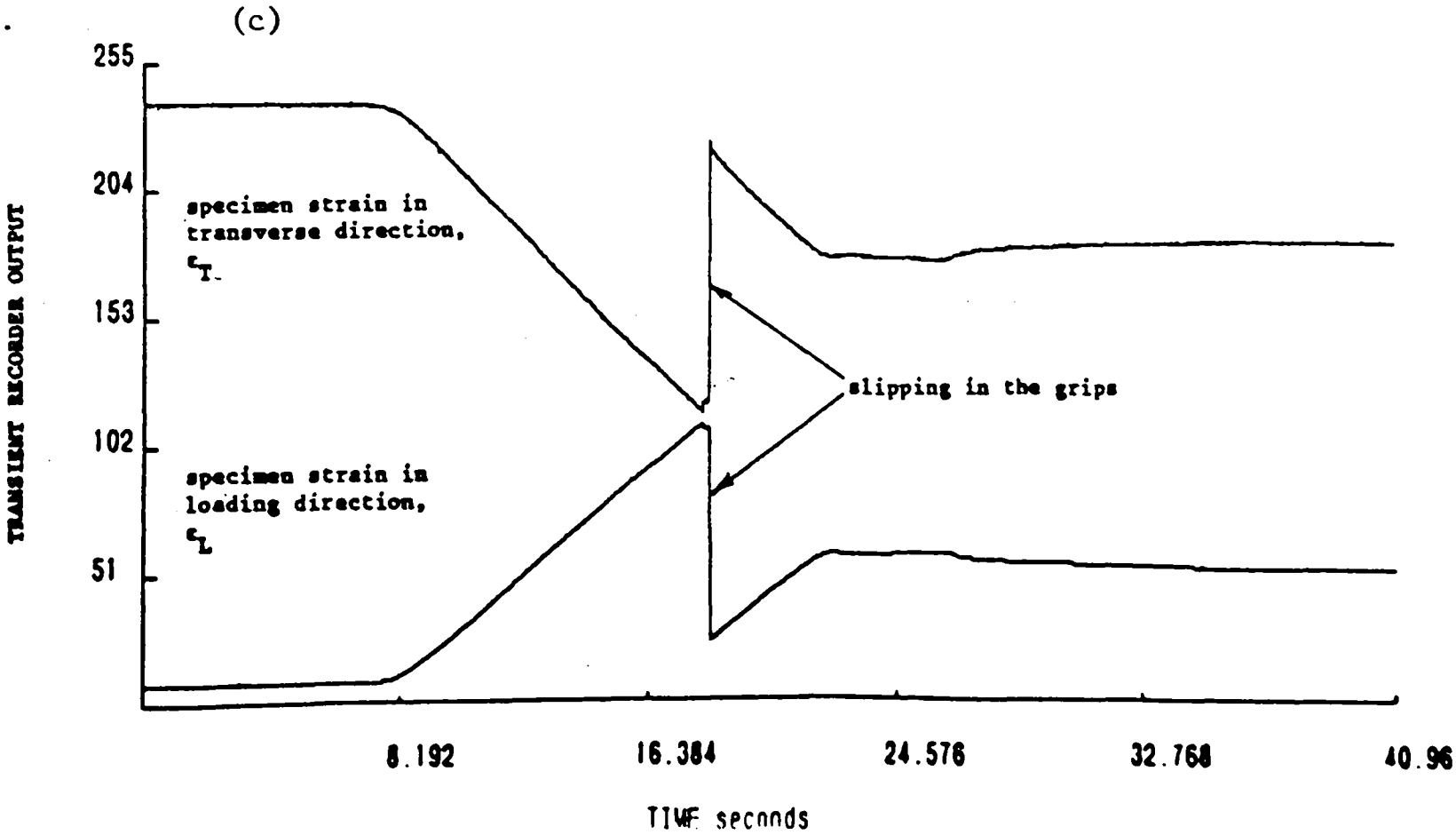

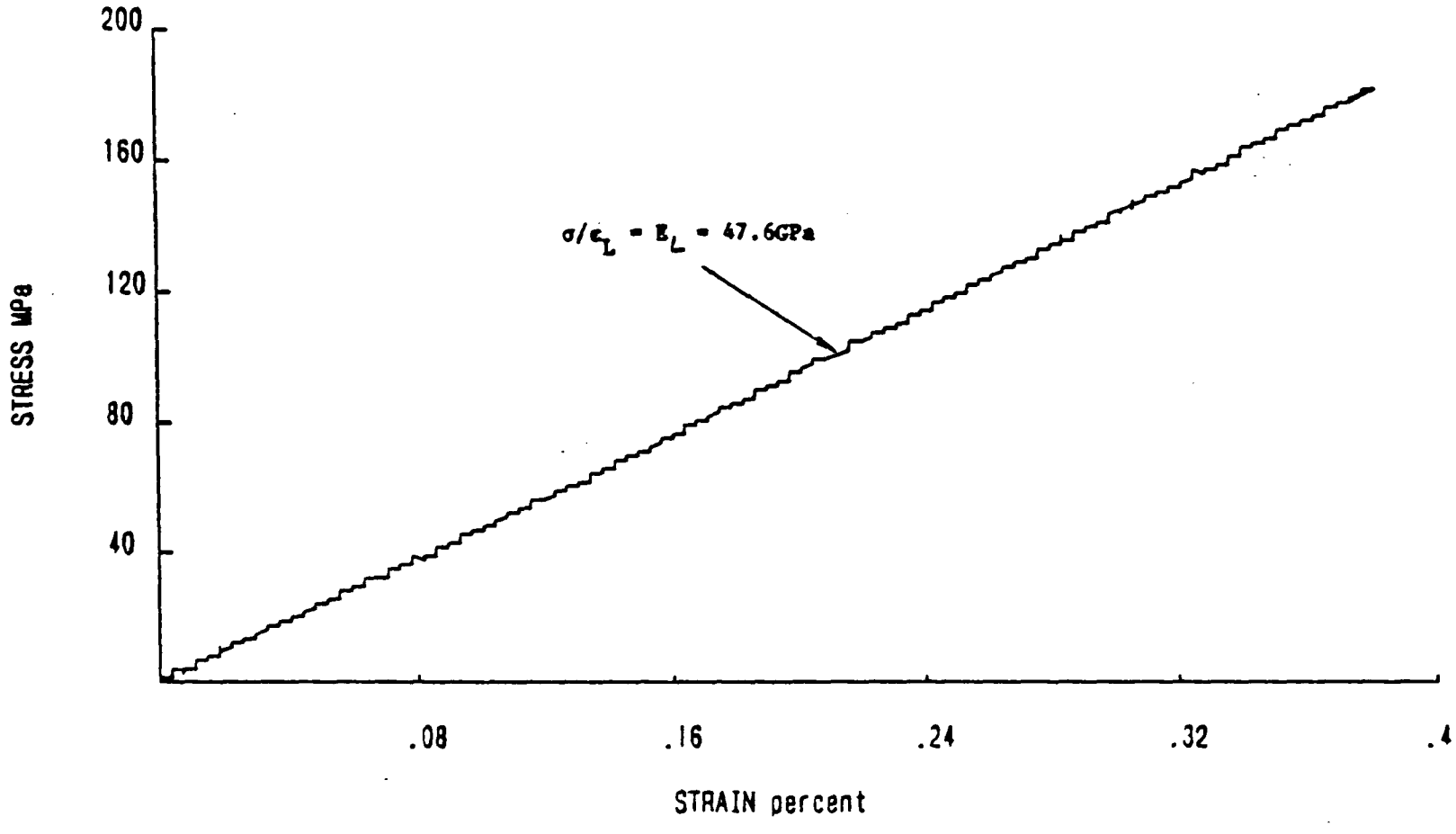

Fig.2.40 TRANSVERSE STRAIN (ϵ_T) v. LONGITUDINAL STRAIN (ϵ_L) FOR TEST OF Fig.2.38

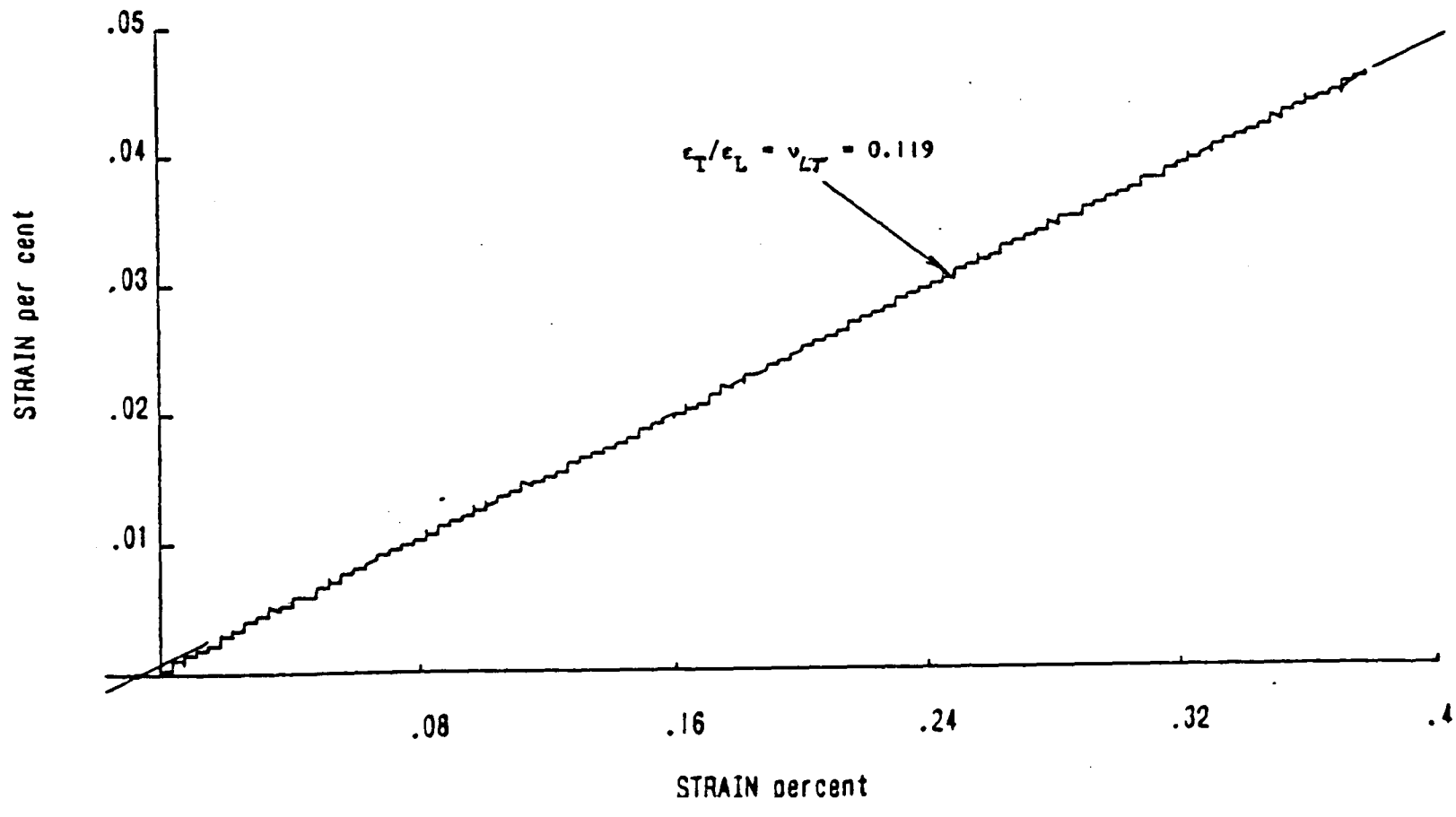

and instrumentation being identical in both cases. The modified impact loading system was used and strain gauge signals (six for the 45° off-axis tension tests) were stored in transient recorders and processed in the micro-computer as usual. All results are averages of three tests. The variation of stress as obtained from the output bar signal, with the strain in the loading direction for an all-carbon specimen cut in the warp direction is shown in Fig. 2.41. This gives a dynamic modulus of 59.4 GPa. A crossplot of the strain gauge signals for the warp and weft directions is given in Fig. 2.42. The Poisson's ratio in this case is 0.065.

2.10.3 Effect of Transverse Sensitivity.

The strain measurements in sections 2.10.1 and 2.10.2 were not corrected for transverse sensitivity even though this effect might be expected. Transverse sensitivity relates to the behaviour of a strain gauge in responding to strains which are perpendicular to the primary sensing axis of the gauge and is a consequence of such factors as gauge alloy, gauge backing and several manufacturing variables [90]. In general, errors in strain indication resulting from this effect are quite small since the transverse sensitivity itself is small [98]. However, except for a material with a Poisson's ratio of 0.285 under uniaxial stress for which the transverse sensitivity is zero, it is useful to check the degree of error. The transverse sensitivity coefficients, K, for the 90 and 45° strain gauge rosettes used in the present investigation were given by the manufacturers as +1.5 and +0.8%

Fig.2.41 STRESS (σ) v. LONGITUDINAL STRAIN (ε_L) FOR IMPACT TEST ON AN ALL-CARBON SPECIMEN LOADED IN THE WARP DIRECTION

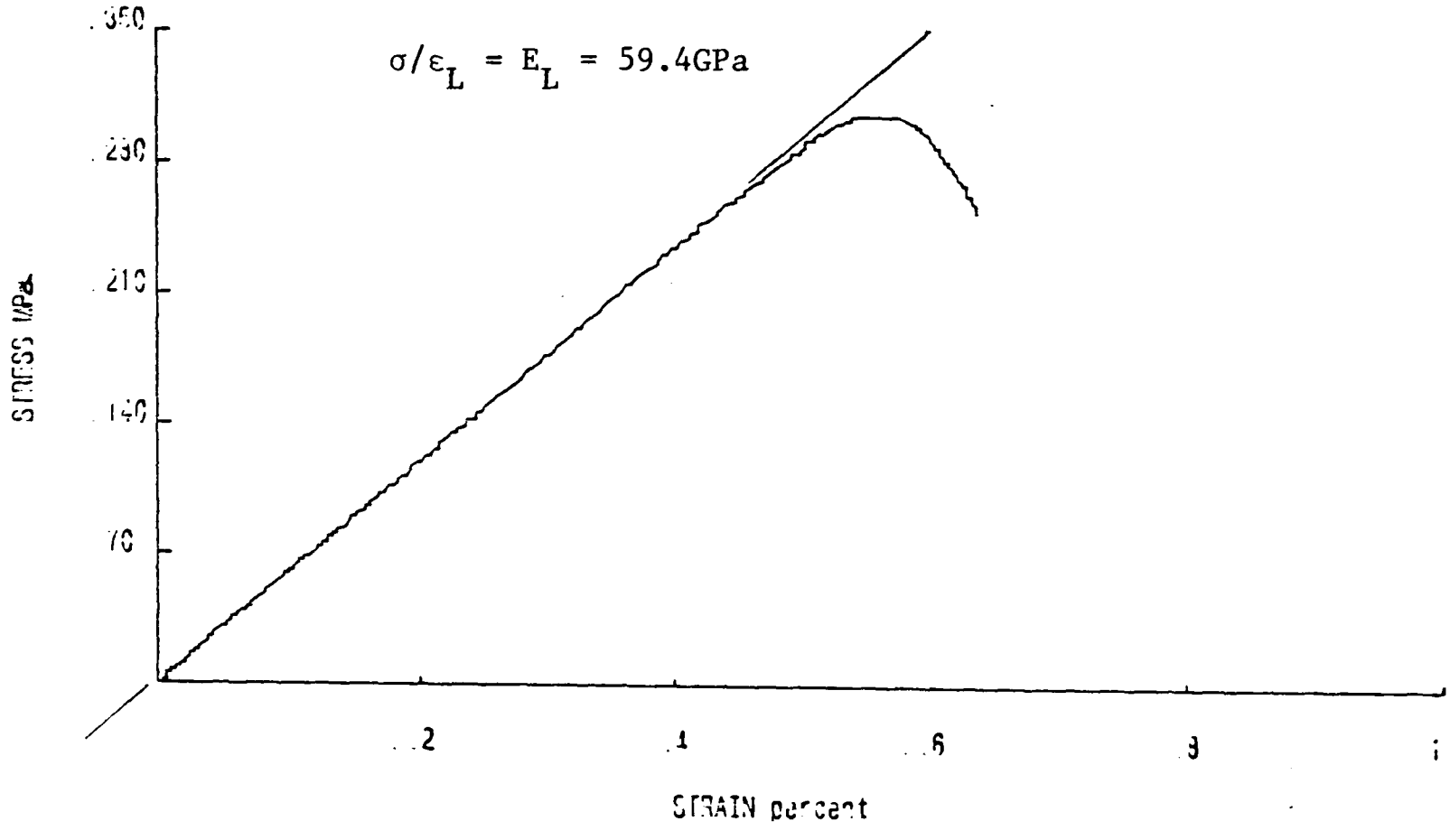

Fig.2.42 TRANSVERSE STRAIN (ε_T) v. LONGITUDINAL STRAIN (ε_L) FOR TEST OF Fig.2.41

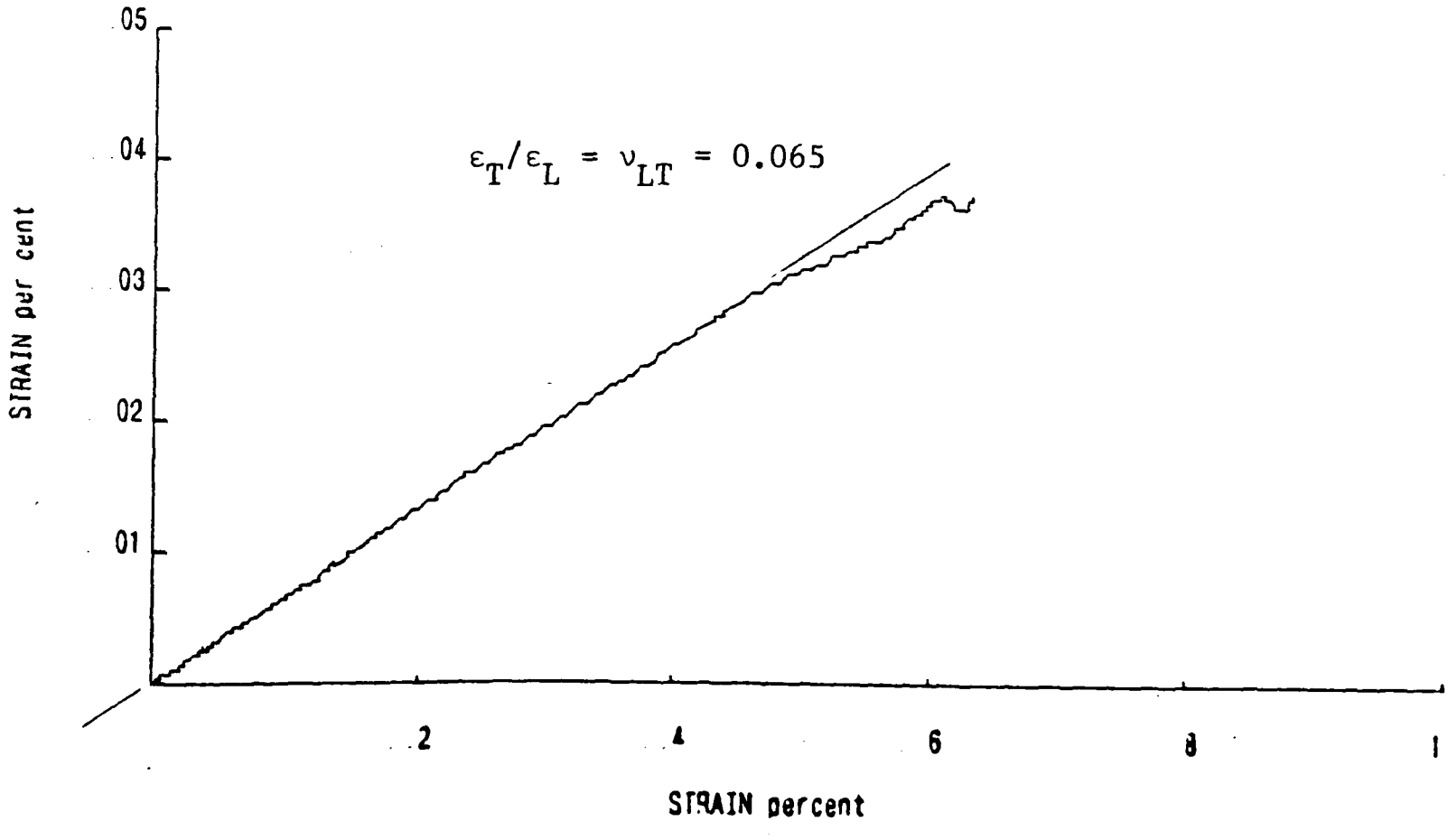

respectively, and in the absence of any information to the contrary it was assumed that the individual gauge elements in a rosette have the same K-value.

Substitution into the appropriate forms of standard correction equations [98] yielded errors of ~0.2 and ~9% in the experimental values of longitudinal and transverse strains respectively, although in impact tests on parallel sided CFRP specimens cut in the warp direction the error in transverse strain measurements was significantly greater at about 20%. The effects of these observations on the predicted properties of hybrid specimens will be discussed in Chapter 5.

2.11 Measurement of Compressive Strengths

Fundamental to the problem of acquiring reliable data on any material is the use of suitable specimens. This is especially true of compression tests on FRP materials where the stress-strain response and the failure mode may depend on the specimen configuration [55,58]. A recent survey [99] of test specimens used for the evaluation of the compressive strength of CFRP concluded that the optimum test-piece was that evolved by the RAE [51] as it gave consistent results. This design is particularly suited to the present work where conventional cylindrical specimens could not be prepared from available laminates. Specimens of identical dimensions to those tested in tension were therefore used in the compression tests.

2.11.1 Quasi-Static Compressive Strengths

As stated above, specimen design was identical to that adopted for the acquisition of tensile stress-strain data. A special fitting (see Fig. 2.43) designed to provide a satisfactory load transfer from the machine to the specimen and reduce the tendency of the latter to buckle under load was incorporated in the Instron tester. Three tests on specimens from each of the warp and the weft directions of the all-carbon and the all-glass laminates were conducted. The maximum load and hence the compressive strength was obtained from the output of the strain-gauged load cell (see Fig. 2.44). A typical compressive failure in a CFRP specimen is shown in Fig. 2.45. The compressive strength in each case was less than the corresponding tensile strength.

2.11.2 Dynamic Compressive Strengths

The test configuration for impact compression followed the standard SHB arrangement originally used by Kolsky [100] and shown schematically in Fig. 2.46. A small capacity gun operated from airline pressure already existed in the department and was used to accelerate a 12.5 mm diameter by 330 mm long projectile which impinged on the input bar. The maximum compressive load in a test was determined from the output bar strain gauge signal. One such trace for an all-glass specimen is shown in Fig. 2.47.

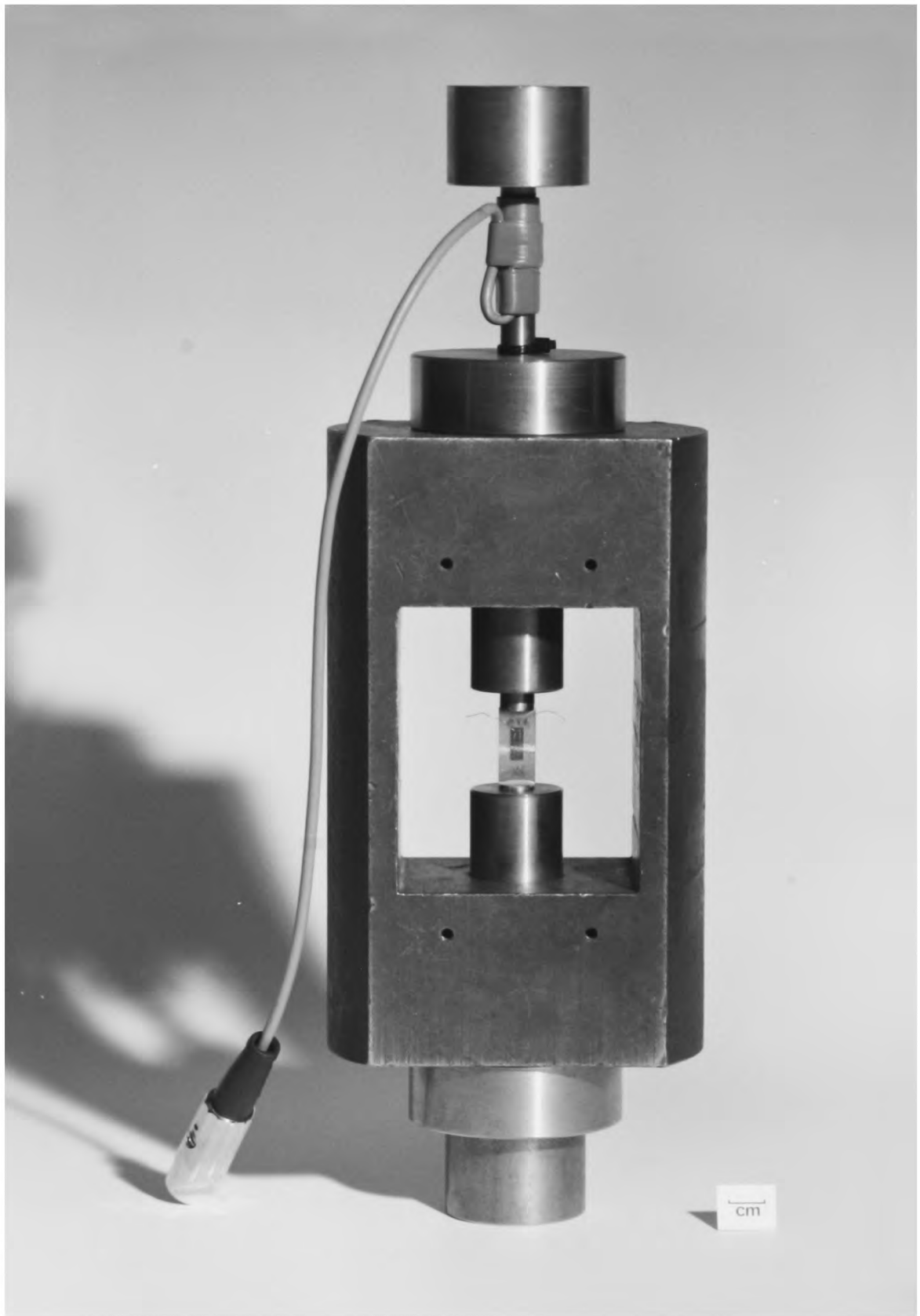

Fig.2.43 LOADING RIG FOR QUASI-STATIC COMPRESSION TESTS

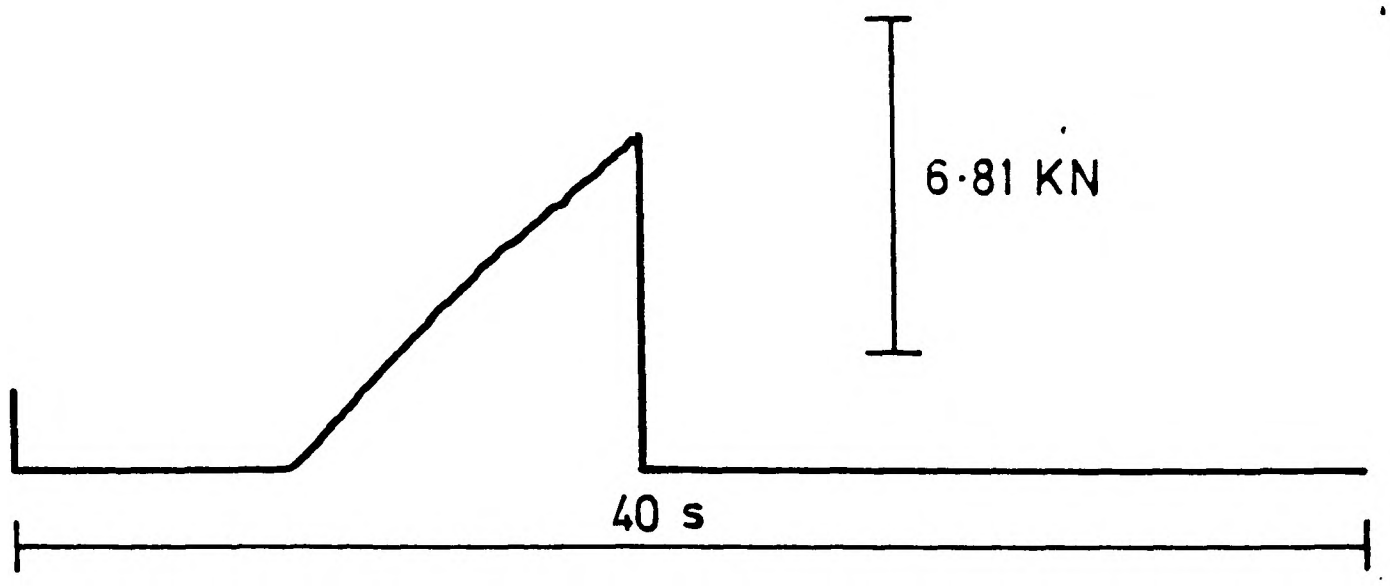

Fig. 2.44 Load-time trace for a quasi-static compression test on an all-carbon specimen loaded in the weft direction

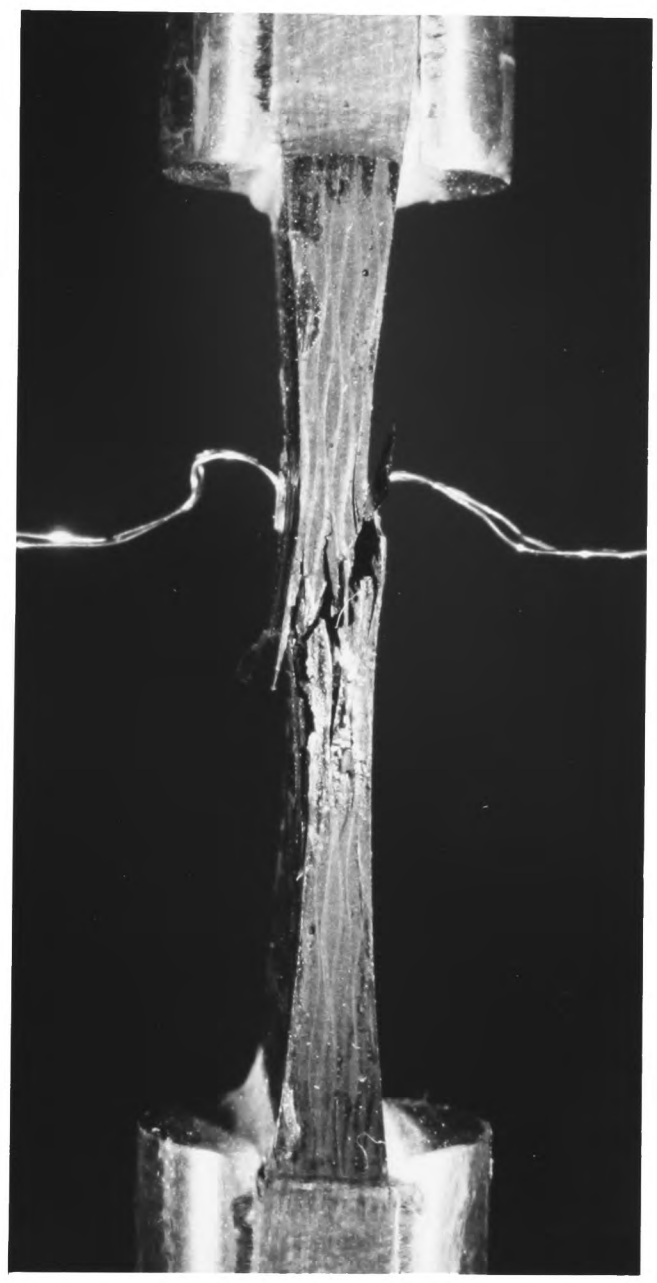

Fig. 2.45 TYPICAL COMPRESSIVE FAILURE IN AN ALL-CARBON SPECIMEN UNDER QUASI-STATIC LOADING

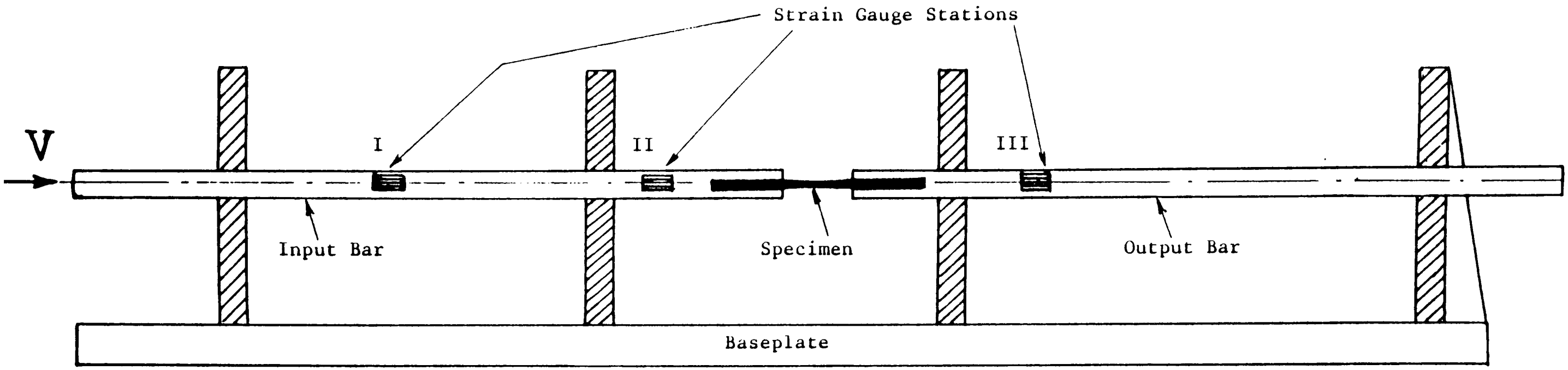

Fig. 2.46 TEST RIG FOR IMPACT COMPRESSION TESTS

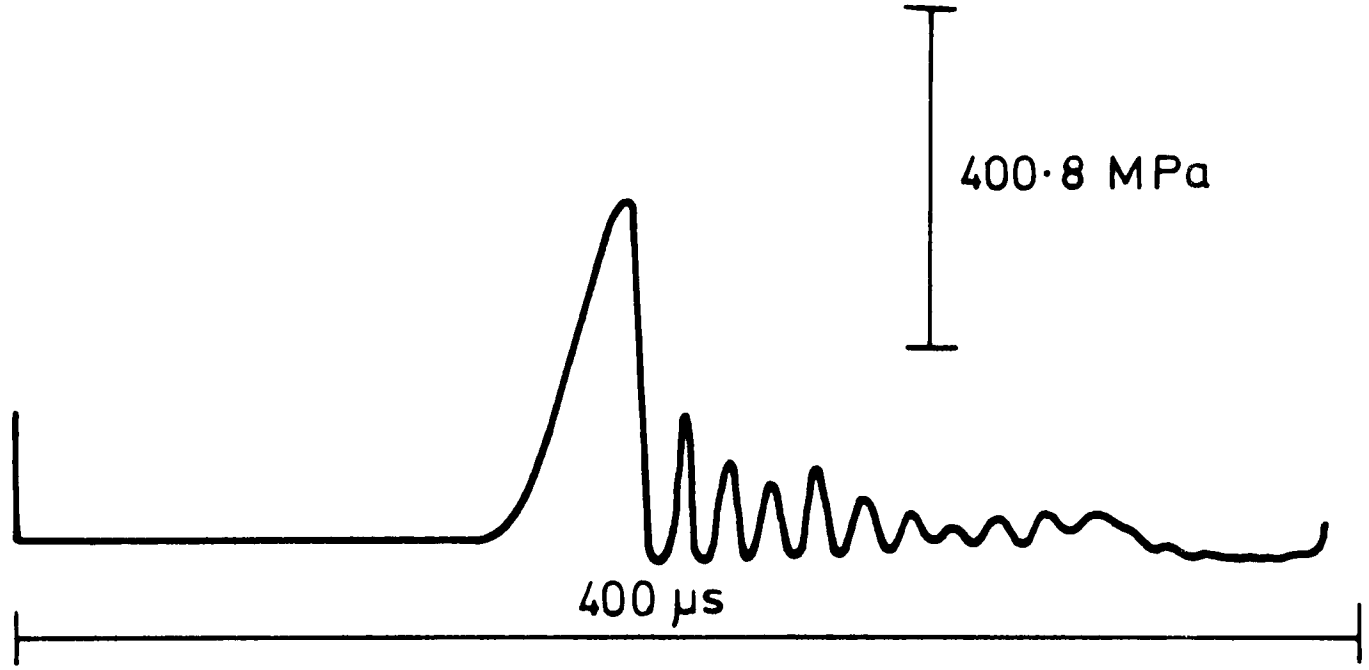

Fig. 2.47 Output bar strain-gauge signal for a typical impact compression test on an all-glass specimen loaded in the weft direction

CHAPTER 3

THE ANALYTICAL PREDICTION OF STIFFNESS AND STRENGTH OF INTERLAMINATED FABRIC-REINFORCED HYBRID COMPOSITES

3.1 Introduction

The classical theory of laminated anisotropic plates based on the Poisson-Kirchhoff assumptions has been considered by a number of investigators [101-104] and verified for laminates of the glass/epoxy [105] and carbon/epoxy [106] types. Application to hybrid laminates, especially those with fabric reinforcement, has been neglected however [107]. Hybridisation offers the opportunity of an expanded range of properties and a possible reduction in cost while, in spite of the disadvantage of reduced properties due to the presence of crimps, fabric reinforcements possess the attractions of ease of handling, which lends itself to automation and a consequent reduction in labour, the ability to conform to complex shapes and more isotropic in-plane properties than those of unidirectional material [108]. Analytical consideration of the response of fabric-reinforced hybrid composites is therefore desirable.

In this chapter expressions are derived for the various elastic moduli of laminated hybrid composites in terms of the properties of the constituent plies and lamination parameters. These expressions, together with the Tsai-Wu strength criterion [109], are used to predict the linear-elastic stress-strain response of the hybrid composites. These

predicted results may then be checked against the experimentally observed stress-strain behaviour once the various elastic and strength properties of the constituent plies at any given strain rate have been determined.

3.2 Anisotropic Elasticity and Laminate Theory

The generalised form of Hooke's law [110] may be expressed mathematically as

$$\sigma_{ij} = C_{ijkl}\varepsilon_{kl} \quad (i,j,k,l = 1,2,3) \tag{3.1}$$

where σ_{ij} is the second rank stress tensor, ε_{kl} is the second rank strain tensor and C_{ijkl} is the fourth rank stiffness tensor; the 1,2, and 3 directions form a right-handed orthogonal coordinate system. From equation (3.1), it is seen that each component of stress is related to nine components of strain tensor and the number of elastic constants (stiffnesses) is 81.

A consideration of the symmetry of stress reduces the number of elastic constants to 54 i.e.

$$\sigma_{ij} = \sigma_{ji} \tag{3.2}$$

Consequently $$C_{ijkl} = C_{jikl} \tag{3.3}$$

Because of the symmetry of the strain tensor, we may also write

$$\varepsilon_{kl} = \varepsilon_{lk} \tag{3.4}$$

$$C_{ijkl} = C_{ijlk} \tag{3.5}$$

Only 36 of the elastic constants are now independent. To reduce the number of constants still further, we resort to thermodynamic considerations. For this purpose, it is assumed that a strain energy density function

$$U = U(\varepsilon_{ij}) \tag{3.6}$$

exists (see, for example Love [111]) such that

$$\frac{\partial U}{\partial \varepsilon_{ij}} = \sigma_{ij} \tag{3.7}$$

and from equation (3.1),

$$\frac{\partial U}{\partial \varepsilon_{ij}} = C_{ijkl}\ \varepsilon_{kl} \tag{3.8}$$

Differentiating equation (3.8) with respect to ε_{kl}, we get

$$\frac{\partial^2 U}{\partial \varepsilon_{kl} \partial \varepsilon_{ij}} = C_{ijkl} \tag{3.9}$$

Similarly

$$\frac{\partial^2 U}{\partial \varepsilon_{ij} \partial \varepsilon_{kl}} = C_{klij} \tag{3.10}$$

so that, as the order of partial differentiation is immaterial,

$$C_{ijkl} = C_{klij} \tag{3.11}$$

and we are left with 21 independent elastic constants for the generally anisotropic linear-elastic material.

The macroscopic nature of the structure of materials results in the existence of symmetry in their elastic properties with respect to certain planes or axes. Hence some constants will vanish while others may be algebraically related. Of particular interest to us in the present work are orthotropic materials, i.e. those that exhibit symmetry in their elastic properties with respect to two orthogonal planes.

To identify a particular symmetry we invoke the condition that the coefficients C_{ijkl} remain invariant under the transformation of coordinates which describe the symmetry. The transformation law for a fourth rank tensor is

$$C'_{ijkl} = a_{im}a_{jn}a_{ko}a_{lp}C_{mnop} \tag{3.12}$$

where C'_{ijkl} is the stiffness tensor in the transformed (X'_i) axes, C_{mnop} is the stiffness tensor in the original (X_i) system of axes and a_{im}, a_{jn}, a_{ko}, a_{lp} are direction cosines.

Taking x_1x_2 and x_2x_3 as the planes of symmetry of the orthotropic material and applying the invariance condition under the coordinate transformations of Fig. 3.1, the following results are obtained:

$$C_{1113} = C_{1123} = C_{1213} = C_{1223} = C_{2213} = C_{2223} = C_{3313} = C_{3323} = 0 \qquad (3.13)$$

for the transformation of Fig. 3.1 (a),

and
$$C_{1112} = C_{2212} = C_{2313} = C_{3312} = 0 \qquad (3.14)$$

for that indicated in Fig. 3.1.(b). A three dimensional orthotropic material therefore possesses nine independent elastic constants, and it is usual to describe these constants by the following array:

$$C_{ijkl} = \begin{bmatrix} C_{1111} & C_{1122} & C_{1133} & 0 & 0 & 0 \\ C_{1122} & C_{2222} & C_{2233} & 0 & 0 & 0 \\ C_{1133} & C_{2233} & C_{3333} & 0 & 0 & 0 \\ 0 & 0 & 0 & C_{2323} & 0 & 0 \\ 0 & 0 & 0 & 0 & C_{1313} & 0 \\ 0 & 0 & 0 & 0 & 0 & C_{1212} \end{bmatrix} \qquad (3.15)$$

A careful examination of equation (3.15) reveals the futility of identifying the elastic constants of the orthotropic material by four subscripts. The subscripts may be contracted as follows:

11 ≡ 1	23 ≡ 4
22 ≡ 2	13 ≡ 5
33 ≡ 3	12 ≡ 6

so that equation (3.1) may be written as

(a)

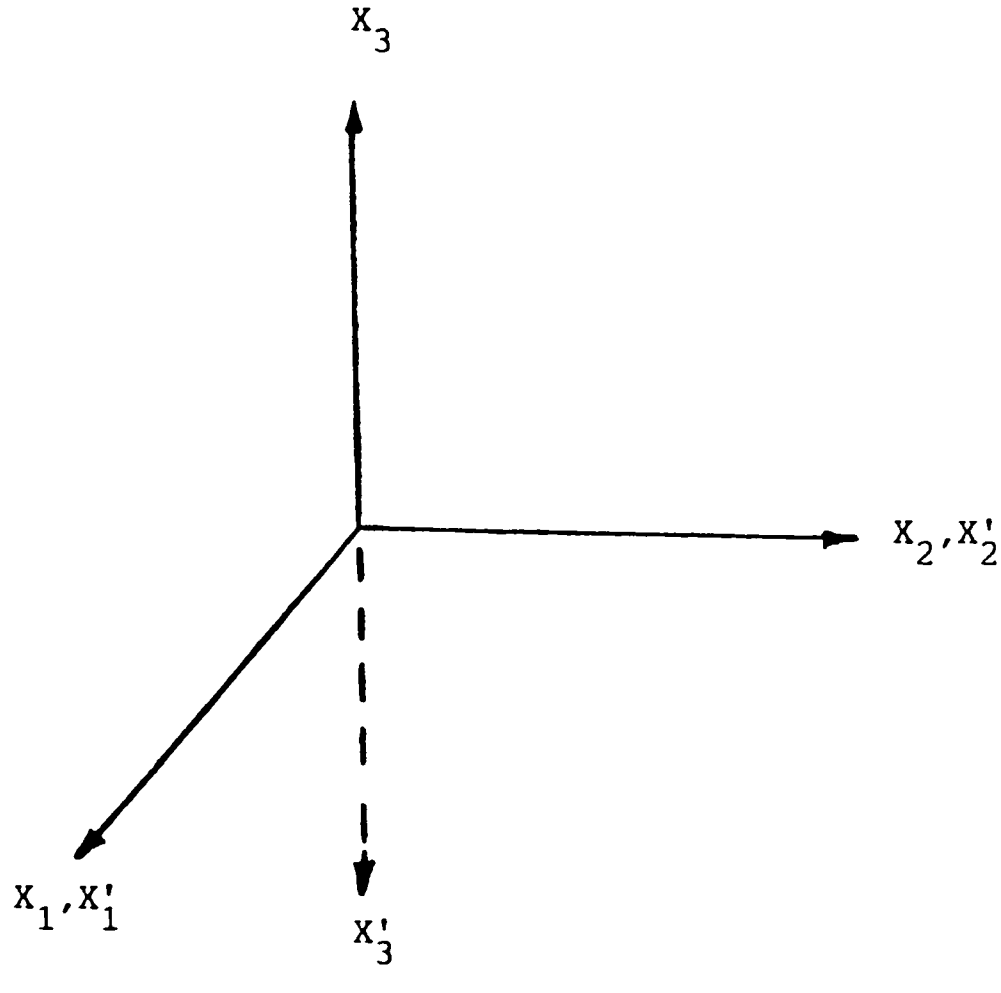

(b)

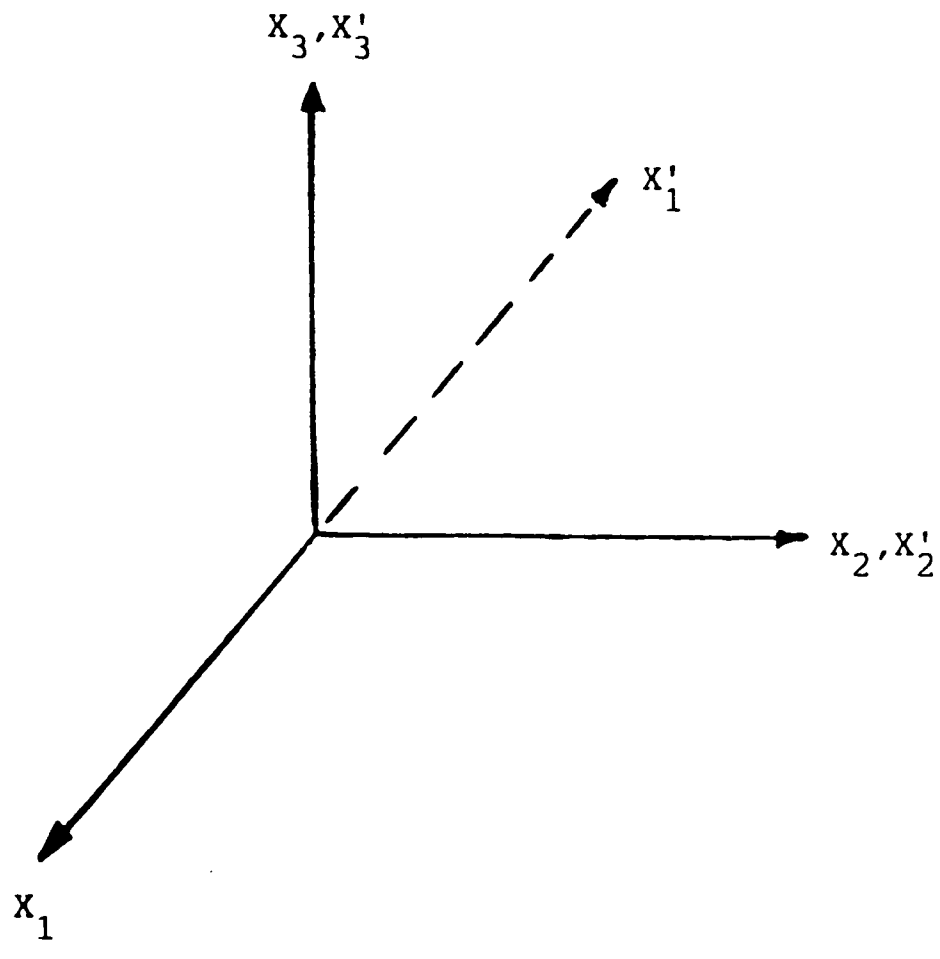

Fig. 3.1 Transformation of coordinate axes with (a) X_1X_2 as a plane of symmetry, and (b) X_2X_3 as a plane of symmetry

$$\sigma_i = Q_{ij}\ \varepsilon_j \quad (i,j = 1,2,3 \ldots 6) \tag{3.16}$$

where σ_i are the stress components, Q_{ij} is the stiffness matrix and ε_j are the engineering strain components. It is worth noting that an engineering shear strain is twice its corresponding tensor shear strain. Hence

$$\begin{aligned} \varepsilon_4 &= 2\varepsilon_{23} = \gamma_{23} \\ \varepsilon_5 &= 2\varepsilon_{13} = \gamma_{13} \\ \varepsilon_6 &= 2\varepsilon_{12} = \gamma_{12} \end{aligned} \tag{3.17}$$

γ_{23}, γ_{13} and γ_{12} are the engineering shear strains using the more familiar notation. We now write equation (3.16) in full.

$$\begin{Bmatrix} \sigma_1 \\ \sigma_2 \\ \sigma_3 \\ \sigma_4 = \tau_{23} \\ \sigma_5 = \tau_{13} \\ \sigma_6 = \tau_{12} \end{Bmatrix} = \begin{bmatrix} Q_{11} & Q_{12} & Q_{13} & 0 & 0 & 0 \\ Q_{12} & Q_{22} & Q_{23} & 0 & 0 & 0 \\ Q_{13} & Q_{23} & Q_{33} & 0 & 0 & 0 \\ 0 & 0 & 0 & Q_{44} & 0 & 0 \\ 0 & 0 & 0 & 0 & Q_{55} & 0 \\ 0 & 0 & 0 & 0 & 0 & Q_{66} \end{bmatrix} \begin{Bmatrix} \varepsilon_1 \\ \varepsilon_2 \\ \varepsilon_3 \\ \varepsilon_4 = \gamma_{23} \\ \varepsilon_5 = \gamma_{13} \\ \varepsilon_6 = \gamma_{12} \end{Bmatrix} \tag{3.18}$$

For the two-dimensional orthotropic plate, the stress-strain relations become

$$\begin{Bmatrix} \sigma_1 \\ \sigma_2 \\ \tau_{12} \end{Bmatrix} = \begin{bmatrix} Q_{11} & Q_{12} & 0 \\ Q_{12} & Q_{22} & 0 \\ 0 & 0 & Q_{66} \end{bmatrix} \begin{Bmatrix} \varepsilon_1 \\ \varepsilon_2 \\ \gamma_{12} \end{Bmatrix} \qquad (3.19)$$

The stiffness matrix of a woven fabric reinforced composite lamina which is assumed to be orthotropic is obtained by inspection, from equation (3.19) as:

$$Q_{ij} = \begin{bmatrix} Q_{11} & Q_{12} & 0 \\ Q_{12} & Q_{22} & 0 \\ 0 & 0 & Q_{66} \end{bmatrix} \qquad (3.20)$$

Its components are related to the engineering constants as follows (see, for example, Jones [112]:

$$Q_{11} = \frac{E_L}{\psi}$$

$$Q_{22} = \frac{E_T}{\psi}$$

$$Q_{12} = \frac{\nu_{LT}E_T}{\psi} = \frac{\nu_{TL}E_L}{\psi} \qquad (3.21)$$

$$Q_{66} = G_{LT}$$

where $\psi = 1 - \nu_{LT}\nu_{TL}$ and E_L, E_T, ν_{LT} and G_{LT} have the same meanings as before (Chap. 2, section 2.10); ν_{TL} is the minor Poisson's ratio. From the third of equations (3.21) we see that

$$\nu_{LT} E_T = \nu_{TL} E_L \qquad (3.22)$$

and only four of the five engineering constants are independent.

If the lay-up of the plies in a composite laminate is such that there is no relative orientation between the plies, i.e. the principal material directions of each ply, given by the 'local' or lamina L-T coordinate system, are coincident with a common set of reference axes, given by the 'global' or laminate x-y coordinate system, we may write

$$\left[\bar{Q} \right] = \left[Q \right] \qquad (3.23)$$

where the $\left[\bar{Q} \right]$ matrix is similar to the $\left[Q \right]$ matrix of equation (3.19) but relates engineering strains to the stresses referred to an abritrary set of axes, e.g. the x-y axes in Fig. 3.2. Hence the $\left[\bar{Q} \right]$ matrix is defined by the equation:

$$\begin{Bmatrix} \sigma_x \\ \sigma_y \\ \tau_{xy} \end{Bmatrix} = \begin{bmatrix} \bar{Q}_{11} & \bar{Q}_{12} & \bar{Q}_{16} \\ \bar{Q}_{12} & \bar{Q}_{22} & \bar{Q}_{26} \\ \bar{Q}_{16} & \bar{Q}_{26} & \bar{Q}_{66} \end{bmatrix} \begin{Bmatrix} \varepsilon_x \\ \varepsilon_y \\ \gamma_{xy} \end{Bmatrix} \qquad (3.24)$$

In general the relations between the elements of the $\left[\bar{Q} \right]$ matrix and the $\left[Q \right]$ matrix are those given in equations (3.25) below:

$$\bar{Q}_{11} = Q_{11}\, m^4 + Q_{22}\, n^4 + 2(Q_{12} + 2Q_{66})\, m^2 n^2$$

$$\bar{Q}_{22} = Q_{11}\, n^4 + Q_{22}\, m^4 + 2(Q_{12} + 2Q_{66})\, m^2 n^2$$

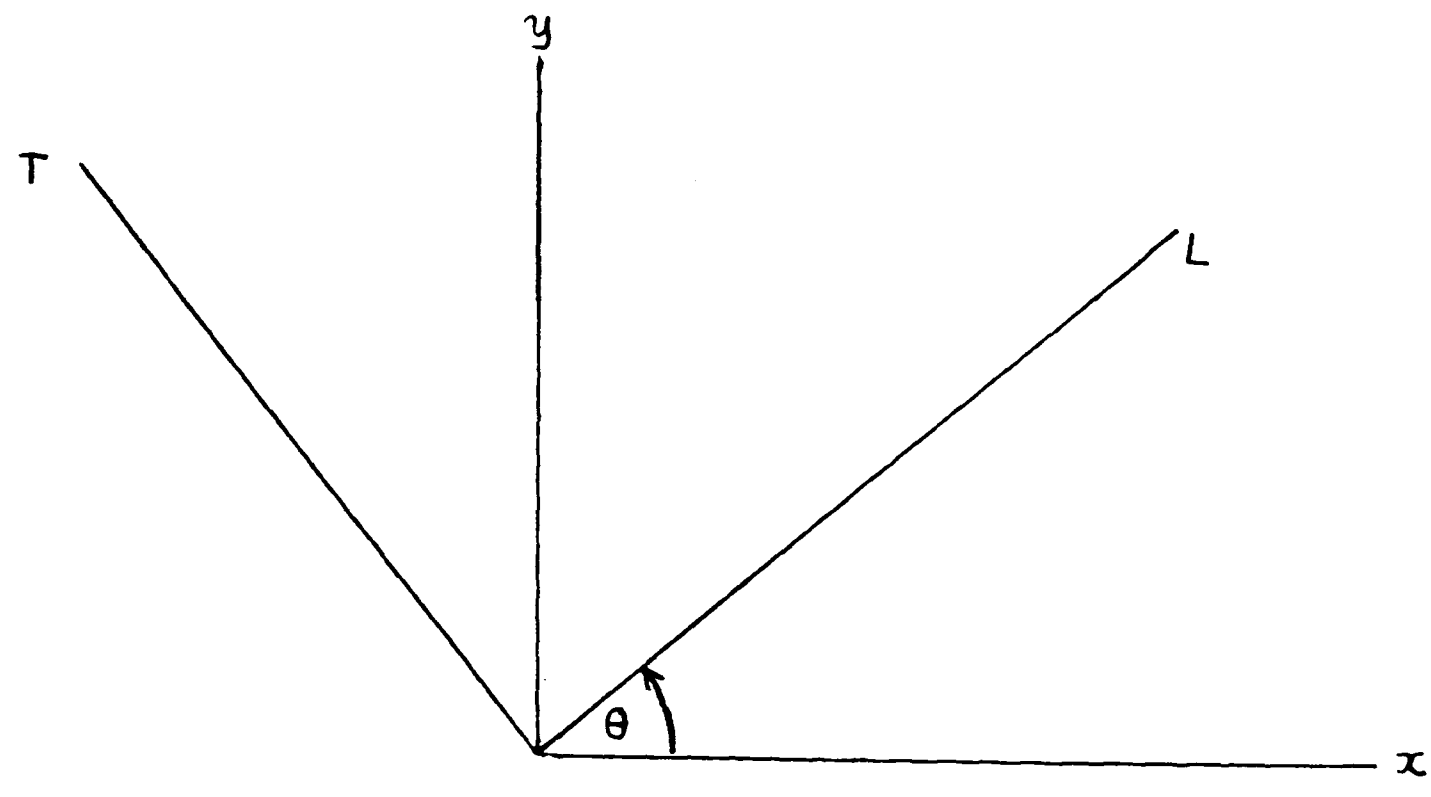

Fig. 3.2 Lamina (L-T) and Laminate (x-y) coordinate systems with θ positive.

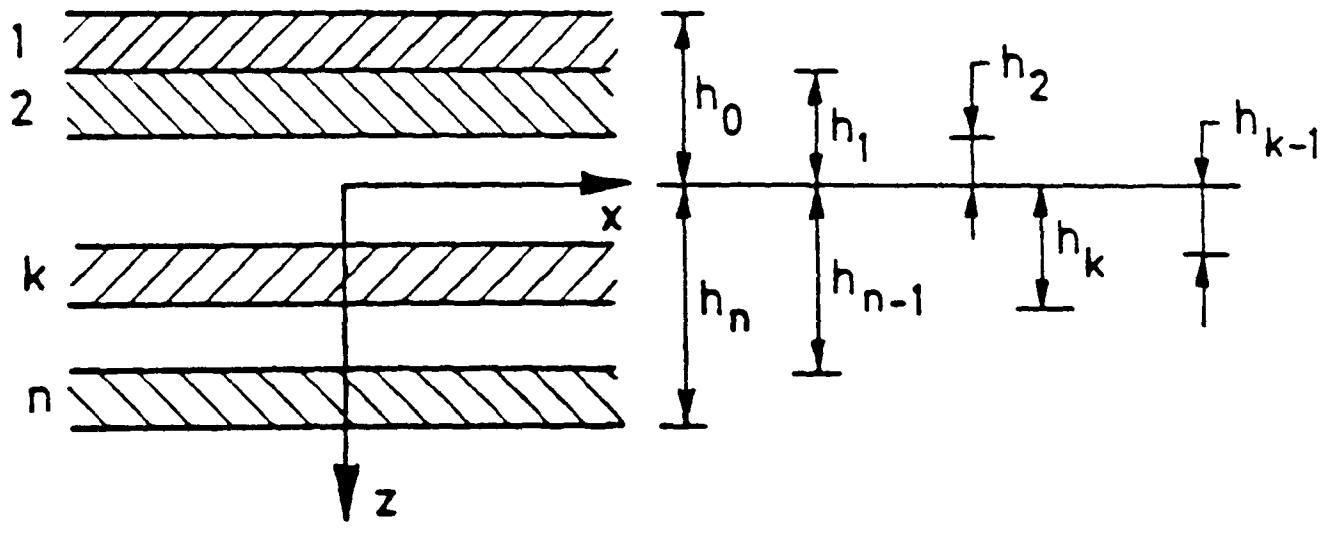

Fig. 3.3 Schematic of a composite laminate composed of n plies

(3.25)

$$\bar{Q}_{12} = (Q_{11} + Q_{22} - 4Q_{66})\, m^2n^2 + Q_{12}\,(m^4 + n^4)$$

$$\bar{Q}_{66} = (Q_{11} + Q_{22} - 2Q_{12} - 2Q_{66})\, m^2n^2 + Q_{66}\,(m^4 + n^4)$$

$$\bar{Q}_{16} = (Q_{11} - Q_{12} - 2Q_{66})\, m^3n - (Q_{22} - Q_{12} - 2Q_{66})mn^3$$

$$\bar{Q}_{26} = (Q_{11} - Q_{12} - 2Q_{66})\, mn^3 - (Q_{22} - Q_{12} - 2Q_{66})m^3n$$

where $m = \cos\theta$, $n = \sin\theta$, and θ is shown positive in Fig. 3.2. It is important to note that the stress-strain relations referred to the L-T axes are given in matrix form by equation (3.19). When tensor, as opposed to engineering, strains are used, the stiffness matrix of equation (3.19) must be modified in the following manner:

$$\begin{Bmatrix} \sigma_L \\ \sigma_T \\ \tau_{LT} \end{Bmatrix} = \begin{bmatrix} Q_{11} & Q_{12} & 0 \\ Q_{12} & Q_{22} & 0 \\ 0 & 0 & 2Q_{66} \end{bmatrix} \begin{Bmatrix} \varepsilon_L \\ \varepsilon_T \\ \frac{1}{2}\gamma_{LT} \end{Bmatrix} \tag{3.26}$$

The constitutive equation for laminated two-dimensional orthotropic composite materials may be written as [113].

$$\left\{\begin{array}{c} N \\ \hline M \end{array}\right\} = \left[\begin{array}{c|c} A & B \\ \hline B & D \end{array}\right] \left\{\begin{array}{c} \varepsilon^o \\ \hline \chi \end{array}\right\} \tag{3.27}$$

where N are the resultant tractions, M the resultant moments, ε^o are the midplane strains, χ the plate curvatures and A,B and D the extensional

stiffness matrix, the coupling stiffness matrix and the bending stiffness matrix respectively. The definitions of these matrices are as follows:

$$A_{ij} = \sum_{K=1}^{n} (\bar{Q}_{ij})_k (h_k - h_{k-1})$$

$$B_{ij} = \frac{1}{2} \sum_{K=1}^{n} (\bar{Q}_{ij})_k (h_k^2 - h_{k-1}^2) \qquad (3.28)$$

$$D_{ij} = \frac{1}{3} \sum_{K=1}^{n} (\bar{Q}_{ij})_k (h_k^3 - h_{k-1}^3)$$

where $(\bar{Q})_k$ is the $\left[\bar{Q} \right]$ matrix of the K^{th} layer of the laminate and h_k and h_{k-1} are defined in Fig. 3.3 for a laminate composed of n layers. For a symmetrically stacked laminate, the coupling stiffness matrix is zero so from equation (3.27) we have

$$N = A \, \varepsilon^o \qquad (3.29)$$

or

$$\left\{ \varepsilon_j^o \right\} = \left[A_{ij}^{-1} \right] \left\{ N_i \right\} \qquad (3.30)$$

where, using equation (3.23), A_{ij} may be written as

$$A_{ij} = \sum_{k=1}^{n} (Q_{ij})_k (h_k - h_{k-1}) \qquad (3.31)$$

for a laminated, symmetrically-stacked, composite material with no relative orientation between the principal material directions of the plies.

3.3 Review of Anisotropic Failure Strength Theories.

Much of the early work on failure criteria for anisotropic materials was concerned with the development of empirical expressions, such as those of Jacoby, Howe and Hankinson, discussed by Norris [114]. In recent years, however, it has become much more common to base strength theories for anisotropic materials on generalisations of the well-known yield criteria for isotropic metals due to Tresca and von Mises. The inspiration for this new approach derived from the classic work of Hill [115] in 1948. He proposed a generalisation of the von Mises criterion in the form

$$F(\sigma_y - \sigma_z)^2 + G(\sigma_z - \sigma_x)^2 + H(\sigma_x - \sigma_y)^2 + 2L\tau_{yz}^2 + 2M\tau_{zx}^2 + 2N\tau_{xy}^2 = 1 \qquad (3.32)$$

where F,G,H,L,M and N are the anisotropic parameters and x,y and z are the reference axes. For the plane stress condition, i.e. with $\sigma_z = 0$, this reduces to

$$(G+H)\sigma_x^2 + (F+H)\sigma_y^2 - 2H\sigma_x\sigma_y + 2N\tau_{xy}^2 = 1 \qquad (3.33)$$

Since it is assumed in Hill's theory that the axes of anisotropy (1,2,3) are coincident with the reference axes (x,y,z), this may also be written

$$(G+H)\sigma_1^2 + (F+H)\sigma_2^2 - 2H\sigma_1\sigma_2 + 2N\tau_{12}^2 = 1 \qquad (3.34)$$

where the axes of anisotropy do not necessarily coincide with those of principal stress. Also implicit in this criterion is the assumption that the yield strength in tension is equal to that in compression. These two requirements, however, present difficulties when the criterion is used for composite materials.

Several attempts have been made to overcome this inadequacy in Hill's criterion. Azzi and Tsai [116] used a stress transformation technique to allow for cases where the axes of anisotropy may not be coincident with the reference axes. Except for higher values of the angle between the two sets of axes, good agreement was observed between theory and experiment for the unidirectionally-reinforced glass/epoxy composite used in their investigation. The material was asssumed to be transversely isotropic.

Marin [117] proposed a 'generalised theory of strength' which allowed for differences between the tensile and compressive strengths of anisotropic materials. His criterion has the form

$$(\sigma_1 - a)^2 + (\sigma_2 - b)^2 + (\sigma_3 - c)^2 + q\,[(\sigma_1 - a)(\sigma_2 - b) + (\sigma_2 - b)(\sigma_3 - c) + (\sigma_3 - c)(\sigma_1 - a)] = \text{constant} \qquad (3.35)$$

where a,b and c are experimentally determinable constants and σ_1, σ_2 and σ_3 are principal stresses. The usefulness of Marin's criterion is limited, however, by the requirement that the axes of principal stress and of material symmetry (i.e. the axes of anisotropy) should be coincident which is not generally the case for anisotropic materials.

In another attempt to allow for differing strengths in tension and compression Hoffman [118] suggested an expression in which linear terms are added to Hill's formulation to give

$$C_1(\sigma_y - \sigma_z)^2 + C_2(\sigma_z - \sigma_x)^2 + C_3(\sigma_x - \sigma_y)^2 + C_4\sigma_x + C_5\sigma_y + C_6\sigma_z + C_7\tau_{yz}^2 + C_8\tau_{zx}^2 = C_9\tau_{xy}^2 = 1 \qquad (3.36)$$

where $C_1 \ldots . C_9$ are material parameters which must be determined experimentally. Although the theory can account for widely differing tensile and compressive strengths in various directions it suffers from the large number of parameters involved, even under plane stress, while experimental verification has been limited to uniaxial tension and compression tests on variously oriented specimens.

Based on the very general assumption that a strength theory has to be of the form

$$f(\sigma_1, \sigma_2, \sigma_3) = 0 \qquad (3.37)$$

where σ_1, σ_2 and σ_3 are principal stresses, Zakharov [119] proposed a criterion which in plane stress reduces to

$$K_{11}\,\sigma_1^2 + K_{22}\,\sigma_2^2 + 2K_{12}\,\sigma_1\sigma_2 + 2K_{14}\,\sigma_1 + 2K_{24}\,\sigma_2 = \text{constant} \qquad (3.38)$$

where K_{11}, K_{22}, K_{12}, K_{14} and K_{24} are constants to be determined by experiment. Experimental verification of this criterion has been limited to tests on resin-impregnated laminated paper and cloth cylinders. An

equally general approach was followed by Gol'denblat and Kopnov [120]. They contended that many of the earlier theories were essentially empirical and that to base failure criteria on such propositions as a maximum shear stress or a critical total strain energy, for example, implied single-valued relations between the ultimate strengths in tension and shear for different materials which, in general, are not observed in practice. After listing a set of fundamental conditions that must be met by a generalised theory of strength, they proposed the expression

$$(F_i\sigma_i)^{\alpha} + (F_{ij}\sigma_i\sigma_j)^{\beta} + (F_{ijk}\,\sigma_i\sigma_j\sigma_k)^{\gamma} + \ldots. = 1 \qquad (3.39)$$

which they claimed satisfied these requirements. F_i, F_{ij} and F_{ijk} etc. are strength tensors, α,β and γ etc. are material constants and $i,j,k = 1,2, \ldots.6$. Clearly equation (3.39) may be taken to contain as many terms as is desired. Thus Huang and Kirmser [121], in an investigation on textolite and GFRP, adopted the first three terms. It is more usual, however, to take only the first two terms and to assume specific values for α and β such that the Gol'denblat-Kopnov criterion becomes

$$F_i\sigma_i + (F_{ij}\sigma_i\sigma_j)^{1/2} = 1 \qquad (3.40)$$

This has been found to give satisfactory results for a variety of orthotropic materials [120,122].

An operationally simple strength criterion, essentially similar to that of Gol'denblat and Kopnov, has been proposed by Tsai and Wu [109]. This has the form

$$F_i\sigma_i + F_{ij}\sigma_i\sigma_j = 1 \qquad (3.41)$$

where F_i and F_{ij} are as defined above. Since this criterion obeys tensor transformation rules it is especially suitable for engineering applications. In proposing this form Tsai and Wu point out the awkwardness of the $\pm$ ve sign indeterminancy associated with the square root in equation (3.40). Although this may be overcome by a simple rearrangement the resulting additional term adds no more generality than the linear and quadratic approximation of equation (3.41). The equivalence of equations (3.40) and (3.41) in practice is supported by the work of Owen and Rice [123] who obtained indistinguishable results when the two criteria were applied to the biaxial strength of fabric reinforced composites under both static and fatigue loading. It is also significant that in a review of multiaxial strength criteria for composite materials, Sendeckj [124] concluded that the Gol'denblat-Kopnov and Tsai-Wu formulations gave the best fit to experimental data.

In its two-dimensional form the Tsai-Wu criterion may be written

$$F_{11}\sigma_1^2 + F_{22}\sigma_2^2 + 2F_{12}\sigma_1\sigma_2 + F_{66}\sigma_6^2 + F_1\sigma_1 + F_2\sigma_2 + F_6\sigma_6 = 1 \qquad (3.42)$$

where $F_{11} = \frac{1}{XX'}$; $F_{22} = \frac{1}{YY'}$; $F_{66} = \frac{1}{SS'}$

$$F_1 = \frac{1}{X} - \frac{1}{X'} \; ; \quad F_2 = \frac{1}{Y} - \frac{1}{Y'} \; ; \quad F_6 = \frac{1}{S} - \frac{1}{S'} \qquad (3.43)$$

X,X′ and Y,Y′ are the tensile and compressive strengths in the longitudinal and transverse directions respectively and S,S′ and the in-plane shear strengths. The interaction stress coefficient, F_{12}, is especially difficult to obtain experimentally and has attracted comments from various workers, in particular Narayanaswami and Adelman [125] and Liu [126]. A biaxial stress system is required for its evaluation but the parameter is said to be sensitive to small errors in measured stresses in this state of stress [127]. Simplifying assumptions, therefore, have often been made to arrive at suitable alternative expressions. A very commonly used relation, given by Tsai and Hahn [128], is

$$F_{12} = -\frac{1}{2}\ (F_{11}F_{22})^{1/2} \qquad (3.44)$$

This approximation has been extensively tested and verified under general loading and its use is currently accepted for a variety of composite materials [128,129].

Combining equation (3.44) with previous equations (3.42) and (3.43) gives for the Tsai-Wu criterion in two dimensions the expression

$$\frac{\sigma_1^2}{XX'} + \frac{\sigma_2^2}{YY'} - \frac{\sigma_1\sigma_2}{(XYX'Y')}1/2 + \frac{\sigma_6^2}{SS'} + \frac{\sigma_1(X'-X)}{XX'} + \frac{\sigma_1(Y'-Y)}{YY'} + \frac{\sigma_6(S'-S)}{SS'} = 1 \qquad (3.45)$$

3.4 Application to Hybrid Laminates

3.4.1 Elastic Stress Distribution

We consider an 'interlaminated' symmetric composite with two different plain-weave fabrics (designated a and b) as reinforcement. The lay-up is such that there is no relative orientation between the principal material directions of the plies. Additionally, the principal material directions are coincident with a common set of reference axes. Of the n plies in the laminate, m are made from type b fabric and h_a and h_b are the thicknesses of the constituent plies.

From equations (3.20) and (3.31) the extensional stiffness matrix A_{ij} is given by

$$A_{ij} = (n-m)h_a \begin{bmatrix} Q_{11} & Q_{12} & 0 \\ Q_{12} & Q_{22} & 0 \\ 0 & 0 & Q_{66} \end{bmatrix}_a + mh_b \begin{bmatrix} Q_{11} & Q_{12} & 0 \\ Q_{12} & Q_{22} & 0 \\ 0 & 0 & Q_{66} \end{bmatrix}_b \qquad (3.46)$$

which may be written as

$$A_{ij} = (n-m)h_a \begin{bmatrix} (1+\alpha\beta)(Q_{11})_a & (1+\alpha\lambda)(Q_{12})_a & 0 \\ (1+\alpha\lambda)(Q_{12})_a & (1+\alpha\mu)(Q_{22})_a & 0 \\ 0 & 0 & (1+\alpha\eta)(Q_{66})_a \end{bmatrix} \qquad (3.47)$$

where $\alpha = \frac{m}{(n-m)} \cdot \frac{h_b}{h_a}$; $\beta = \frac{(Q_{11})_b}{(Q_{11})_a}$; $\lambda = \frac{(Q_{12})_b}{(Q_{12})_a}$; $\mu = \frac{(Q_{22})_b}{(Q_{22})_a}$

$$\eta = \frac{(Q_{66})_b}{(Q_{66})_a} .$$

and the inverse of the extensional stiffness matrix is therefore

$$A_{ij}^{-1} = \frac{1}{\phi(n-m)\, h_a} \begin{bmatrix} (1 + \alpha\mu)(Q_{22})_a & -(1 + \alpha\lambda)(Q_{12})_a & 0 \\ -(1 + \alpha\lambda)(Q_{12})_a & (1 + \alpha\beta)(Q_{11})_a & 0 \\ 0 & 0 & \dfrac{\phi}{(1 + \alpha\eta)(Q_{66})_a} \end{bmatrix} \tag{3.48}$$

where $\phi = \left\{(1 + \alpha\beta)(1 + \alpha\mu)(Q_{11})_a(Q_{22})_a - (1 + \alpha\lambda)^2(Q_{12}^2)_a \right\}$

For uniaxial tension with the load applied in the x-direction, equation (3.30) may be written as

$$\begin{Bmatrix} \varepsilon_x^o \\ \varepsilon_y^o \\ \gamma_{xy}^o \end{Bmatrix} = \left[A_{ij}^{-1} \right] \begin{Bmatrix} N_x \\ 0 \\ 0 \end{Bmatrix} \tag{3.49}$$

$$= \frac{1}{\phi(n-m)h_a} \begin{Bmatrix} (1 + \alpha\mu)(Q_{22})_a & N_x \\ -(1 + \alpha\lambda)(Q_{12})_a & N_x \\ 0 \end{Bmatrix} \tag{3.50}$$

From the stress-strain relations of equation (3.19) the stress distribution in the laminate is obtained as follows

$$\begin{Bmatrix} \sigma_x \\ \sigma_y \\ \tau_{xy} \end{Bmatrix}_a = \frac{1}{\phi(n-m)h_a} \begin{Bmatrix} \left[(1+\alpha\mu)(Q_{11})_a(Q_{22})_a - (1+\alpha\lambda)(Q_{12}^2)_a\right] N_x \\ \alpha(\mu-\lambda)(Q_{12})_a\,(Q_{22})_a\; N_x \\ 0 \end{Bmatrix} \tag{3.51}$$

$$\begin{Bmatrix} \sigma_x \\ \sigma_y \\ \tau_{xy} \end{Bmatrix}_b = \frac{1}{\phi(n-m)h_a} \begin{Bmatrix} \left[(1+\alpha\mu)(Q_{22})_a(Q_{11})_b - (1+\alpha\lambda)(Q_{12})_a(Q_{12})_b\right] N_x \\ \left[(1+\alpha\mu)(Q_{22})_a(Q_{12})_b - (1+\alpha\lambda)(Q_{12})_a(Q_{22})_b\right] N_x \\ 0 \end{Bmatrix} \tag{3.52}$$

3.4.2 Prediction of Failure

It follows from equations (3.51) and (3.52) above that in our special case τ_{xy} (ie. σ_6 in equation (3.45) is zero so that the Tsai-Wu) criterion reduces to

$$\frac{\sigma_1^2}{XX'} + \frac{\sigma_2^2}{YY'} - \frac{\sigma_1\sigma_2}{(XYX'Y')^{1/2}} + \frac{\sigma_1(X'-X)}{XX'} + \frac{\sigma_2(Y'-Y)}{YY'} = 1 \tag{3.53}$$

For a given tensile loading, i.e. traction N_x, the state of stress in each ply, i.e. σ_x, σ_y ($\equiv \sigma_1, \sigma_2$) for both a and b plies, may be determined from equations (3.51) and (3.52). Each ply is then subjected to a failure strength test, i.e. the approprite values of stress are substituted into equation (3.53) for the case under consideration. As N_x is increased the first ply to fail is identified and the corresponding

critical traction, N_x^*, is obtained. The overall laminate stress in the direction of the applied load when the first ply fails is given by

$$\sigma_x^* = \frac{N_x^*}{[\, mh_b + (n-m)h_a]} \tag{3.54}$$

and the corresponding strain, from equation (3.50), by

$$\varepsilon_x^* = \frac{(1 + \alpha\mu)(Q_{22})_a \, N_x^*}{\phi(n-m)h_a} \tag{3.55}$$

Assuming linear-elastic response up to first-ply failure (FPF) the hybrid longitudinal modulus is given by the ratio of σ_x^* to ε_x^*, i.e. by

$$E_x^* = \frac{\phi}{(1 + \alpha)(1 + \alpha\mu)(Q_{22})_a} \tag{3.56}$$

For our carbon/glass hybrid composite specimens, the elastic modulus as given by equation (3.56) depends only on α i.e. the volumetric ratio of the constituent plies. The classical laminated plate theory as applied here therefore boils down to the rule of mixtures. However, the rule of mixtures 'per se' gives no indication of the stress distribution in a hybrid composite specimen under load and may not be used in conjunction with a multi-axial strength theory to predict the ultimate strength. The laminated plate approach overcomes this difficulty.

Equations (3.54), (3.55) and (3.56) relate to FPF. If general failure follows, rather than coincides with, FPF, and is preceded by progressive damage, a realistic form of the stress-strain plot for a given laminate may only be predicted by a repeated application of the above procedure, resulting in several discontinuities in the 'flow' curve. A difficulty arises, however, in knowing how to deal with the already damaged or failed plies. This is because of the complicated nature of the damage process in composites and the difficulty of quantifying its effect on strength. Current practice with uni-directionally reinforced composites is to assume some damage function in describing the subsequent behaviour of the degraded composite [130-132]. Alternatively the damaged ply is eliminated altogether. It is also possible, of course, that some damage may precede FPF which could invalidate the linear-elastic assumption on which equation (3.56) is based. Such damage is usually associated with transverse cracking. Tsai and Azzi [130], for example, in work on glass/epoxy cross-ply laminates, assumed transverse cracking to be the predominant damage mechanism prior to FPF. Following FPF they accommodated the observed damage by taking all components of the stiffness matrix not associated with the fibre directions to be vanishingly small. The resulting matrix is then employed in subsequent analysis. Good agreement was obtained between theory and experiment.

If analyses with laminates based on unidirectionally-reinforced plies are seen to be so complex, the situation with fabric reinforced composites is even more daunting due to the additional complication of the warp/weft interaction on the resin. The work of Kimpara et al.[133]

addressed the 'knee' phenomenon, i.e. the reduced stiffness after FPF, in woven-roving composites. Using a combination of acousitc emission and finite element techniques, the authors identified the resin rich region between the fibres of the weft rovings as highly strained and thus constituting a source of weft yielding and accumulated resin cracking. Ishikawa and Chou [107] have systematically developed some models for predicting the stress-strain response of fabric composites. Idealised configurations are assumed for the warp and weft tows and the laminated plate theory is applied. Although good agreement has been reported between theory and experiment, the paucity of experimental data used to verify the models leaves open the question as to their validity for general application to woven fabric laminates [see, for example, Ishikawa et al.[134]].

Carbon/glass hybrid composites of sufficient glass content normally show some discontinuity in their quasi-static, room temperature, tensile stress-strain response [135,136]. Although this phenomenon may be delayed or inhibited by factors such as the thickness of the region reinforced with the low elongation phase [136,137] and the rate of loading, the requirement in this investigation, of relating the properties of the various hybrid specimens to those of the constitutents at any given strain-rate suggests that the damage quantification approach might be helpful. Beyond the FPF, therefore, the stiffness matrix of the carbon phase is modified in accordance with its fracture behaviour as observed in the SEM. The resulting stiffness matrix of the degraded hybrid composite and the appropriate forms of equations (3.54) (3.55) and

(3.56) may then be employed to obtain the ultimate strength and the reduced stiffness of the hybrid specimen.

It should be noted that thermal interaction caused by differential thermal expansion or contraction between constituent layers is ignored in the above anlaysis. However, other investigators, [105,129,131], in work on laminates composed of unidirectionally reinforced plies, have made a similar assumption and it is likely to be even more justified for fabric reinforced composites [138].

CHAPTER 4

EXPERIMENTAL RESULTS

4.1 Introduction

The experimental results are presented under three main headings. These are:

(i) Nominal tensile stress-strain response of the all-carbon, the all-glass and carbon/glass hybrid specimens (see Fig. 2.9) at each of three strain rates, nominally 10^{-3}/s, 10/s and 10^{3}/s.

(ii) Elastic properties and compressive strengths of the all-glass and the all-carbon composite specimens at quasi-static and impact loading rates.

(iii) Optical and SEM studies of the fracture surfaces of various specimens obtained from tests the results of which are presented in (i) above.

Polymeric materials reinforced with plain weave fabrics often exhibit identical properties in both warp and weft directions [see, for example, Hancox [4] and Curtis and Bishop [108]]. Since a plain weave fabric was used in both types of reinforcing ply it was assumed that the properties in the warp and weft directions would be the same. Subsequently, however, experimental measurements indicated that, at least for the glass reinforcing

plies, this was not the case. A distinction, therefore, had to be made between specimens cut in the warp or weft directions.

For the all-glass and the all-carbon materials, stress-strain curves are presented for specimens loaded in the principal material directions at quasi-static and impact loading rates.

4.2 Stress-Strain Curves

4.2.1 Impact Tests

Using the extended tensile impact machine and the compressed gas gun described in section 2.2 it was possible to test to failure the five types of specimen at strain rates of the order of 1000/s without recourse to a supplementary elastic or similar tests. In all tests a tensile failure was obtained with fracture across the central parallel gauge region of the specimen, as shown in Fig. 4.1, for a test on a type 2a carbon/glass hybrid specimen.

All hybrid specimens were cut with the loading axis in the weft direction. For type 2b specimens stress-strain curves for three tests are compared in Fig. 4.2. The strain rate applied to the specimen increases during the course of the test, reaching a relatively steady value of ~900/s before fracture occurs. The scatter in the measured values of tensile modulus, 38.8 GPa < E < 39.8 GPa, tensile strength, 514 MPa < σ_{TS} < 530 MPa, and strain to fracture, 1.48% < ε_f < 1.55%, is relatively small and the

Fig.4.1 TENSILE FAILURE MODE IN AN IMPACTED TYPE 2a CARBON/GLASS HYBRID SPECIMEN

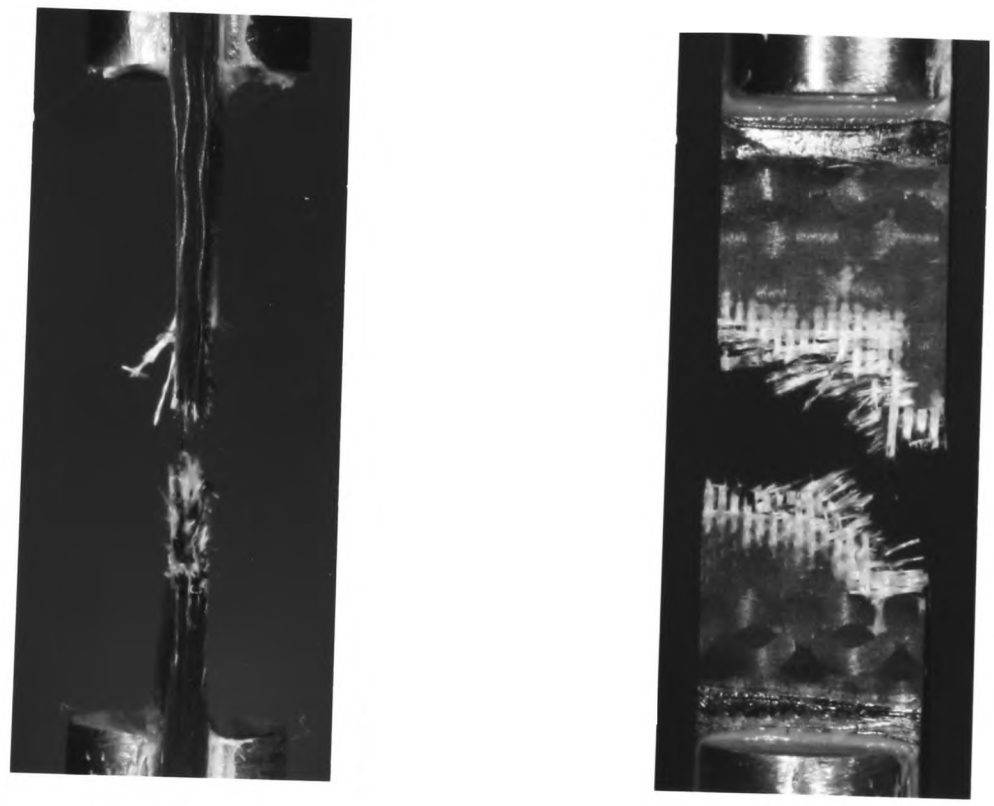

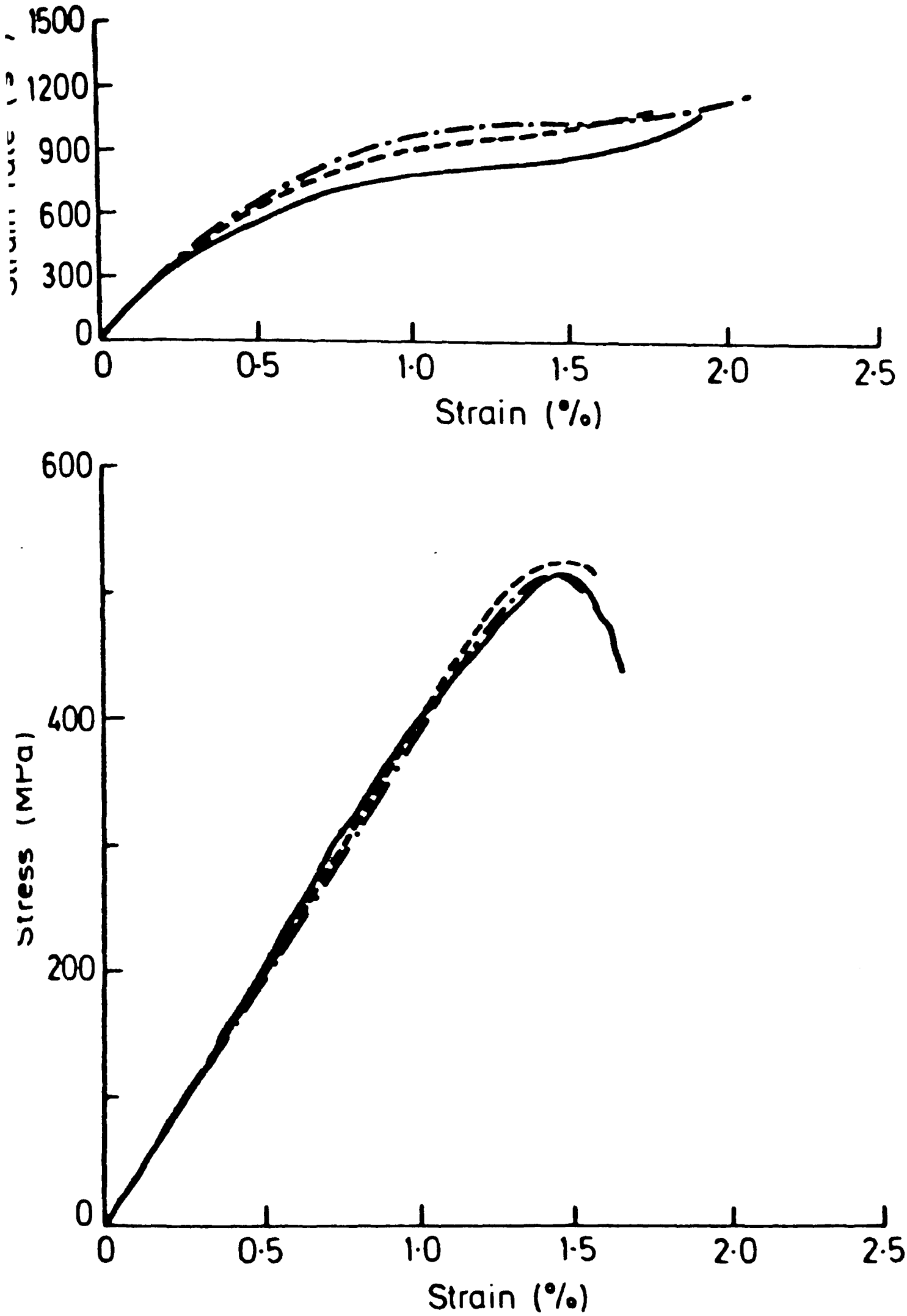

Fig.4.2 STRESS-STRAIN CURVES FOR TYPE 2b HYBRID SPECIMENS

response is essentially linear-elastic through to fracture. A similar linear-elastic response was also shown by the other two types of hybrid specimen, type 2a in Fig. 4.3 and type 1 in Fig. 4.4. The two tests on the former are in good agreement. Mean values of tensile modulus, tensile strength and fracture strain as obtained in the two sets of tests are: 32.2 GPa, 522 MPa, 1.78% and 34.4 GPa, 519 MPa, 1.87% respectively. The scatter in the latter is marginally greater with the measured tensile modulus lying between 30.4 and 33.0 GPa while the fracture strength varies from 448 to 470 MPa.

Results of tests on the all-carbon laminate are presented in Figs. 4.5 and 4.6 for specimens cut in the warp and weft directions respectively. As in the hybrid specimens, an essentially linear-elastic response was observed. Here, however, a much greater experimental scatter is apparent (see Table 4.1) especially in the measurement of modulus. In Table 4.1, E is the initial modulus in the loading direction, σ_{TS} is the maximum stress supported by the specimen, and ε_f the corresponding strain; σ_y and ε_y are estimates of the stress and strain at the limit of linear elastic response of the specimen.

Mean stress-strain curves for the two sets of tests are compared in Fig. 4.7. Although specimens cut in the warp direction show a greater strength and strain to failure no significant difference in the modulus for the two directions of loading was observed.

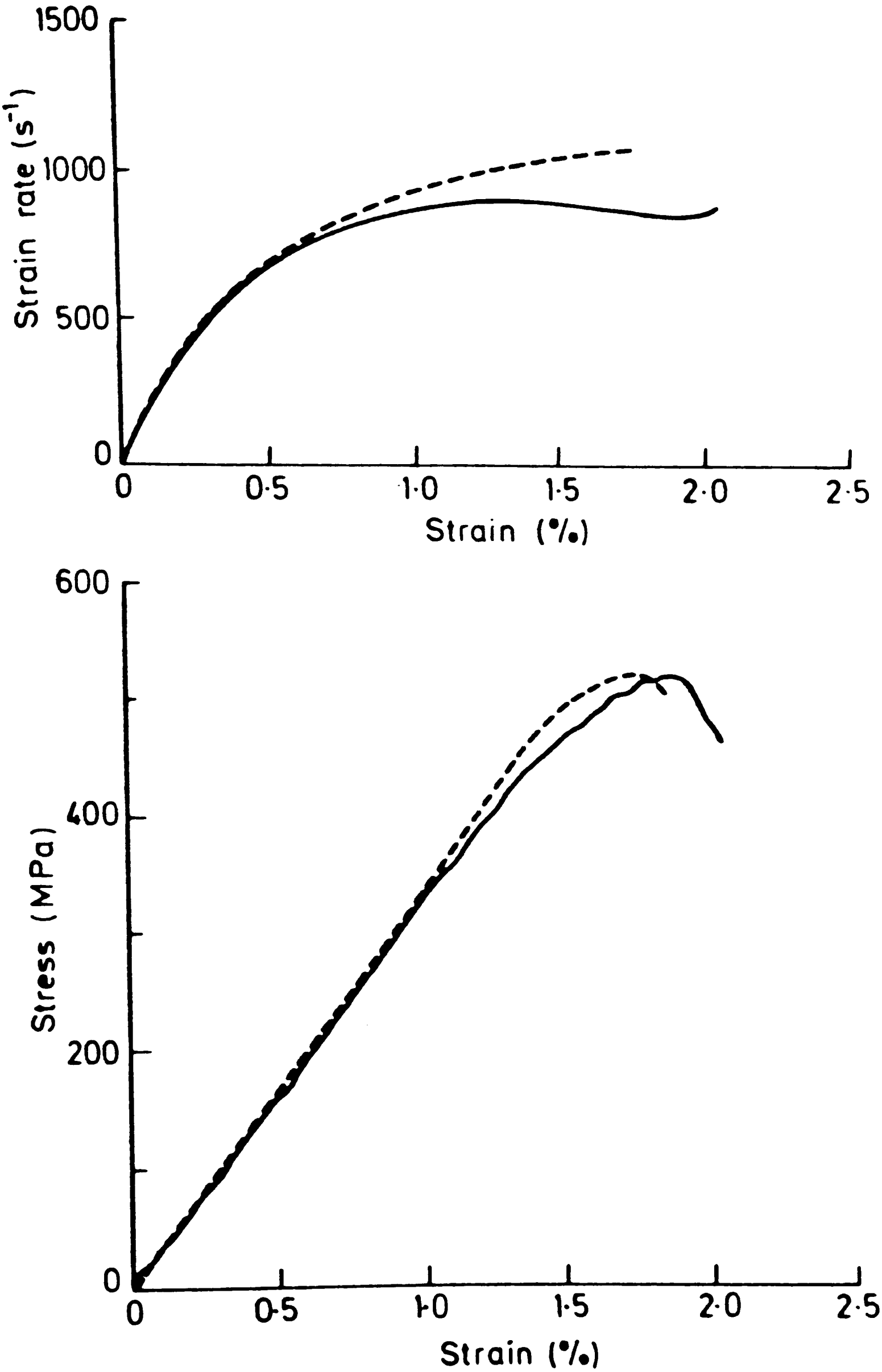

Fig.4.3 STRESS-STRAIN CURVES FOR TYPE 2a HYBRID SPECIMENS

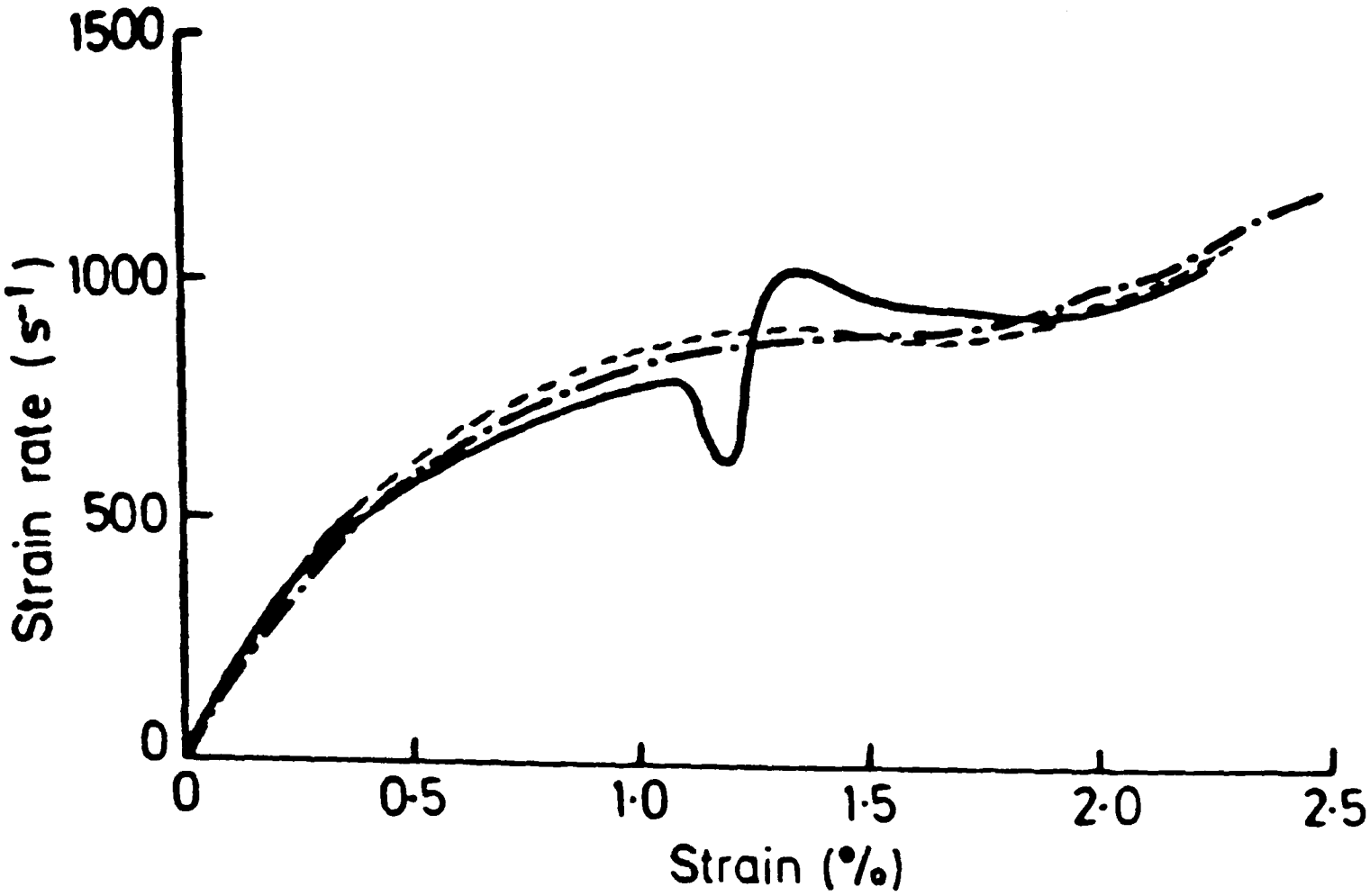

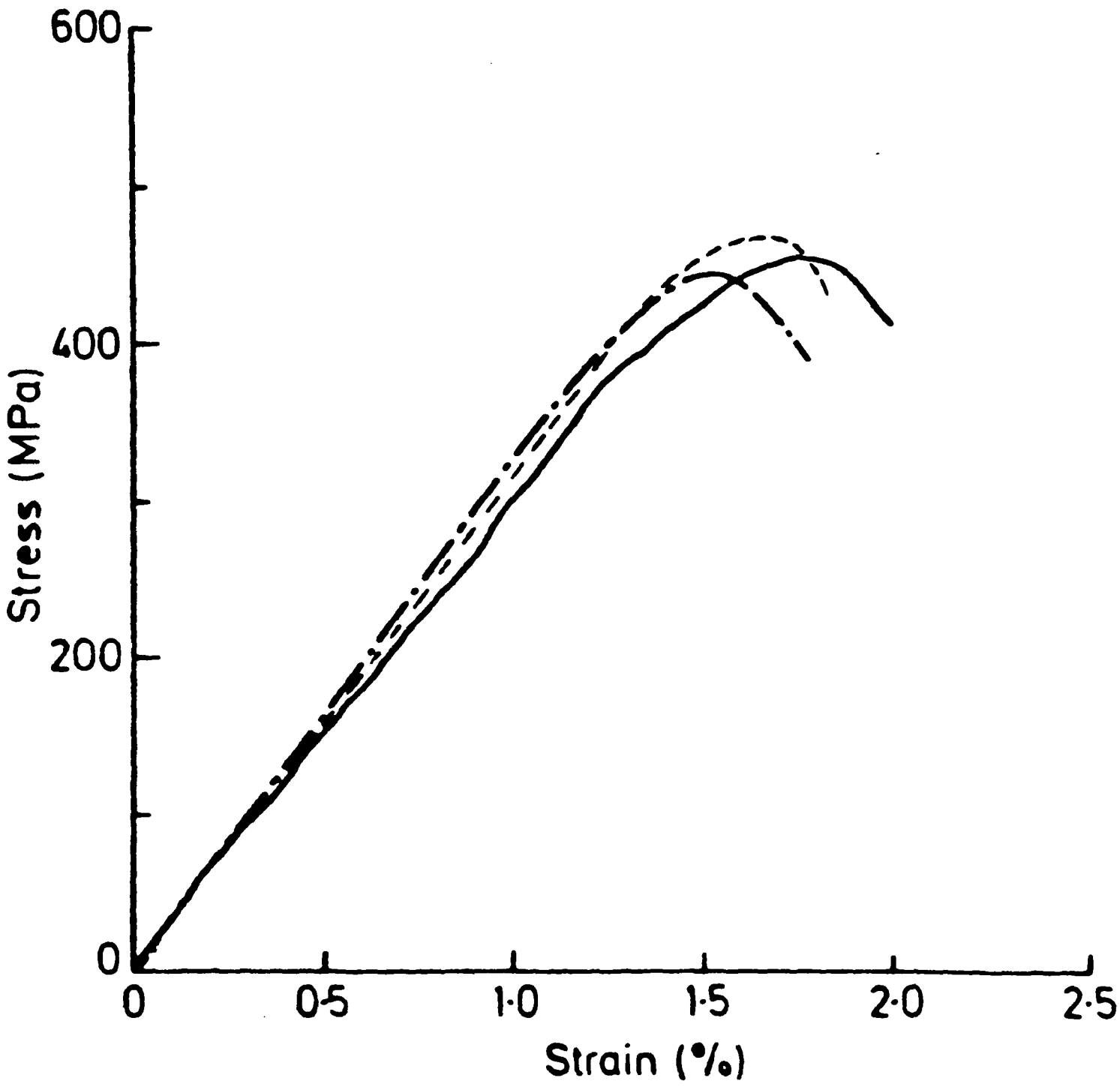

Fig.4.4 STRESS-STRAIN CURVES FOR TYPE I HYBRID SPECIMENS

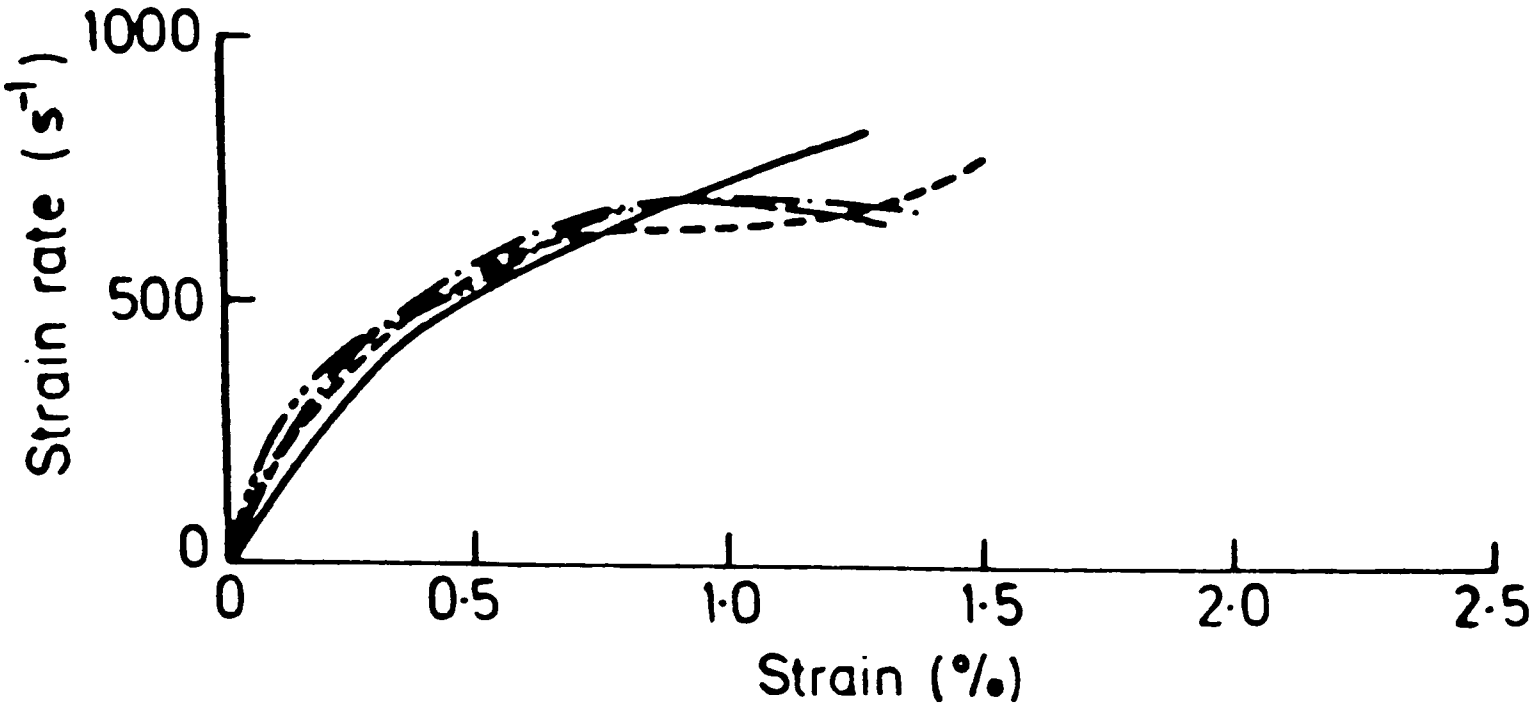

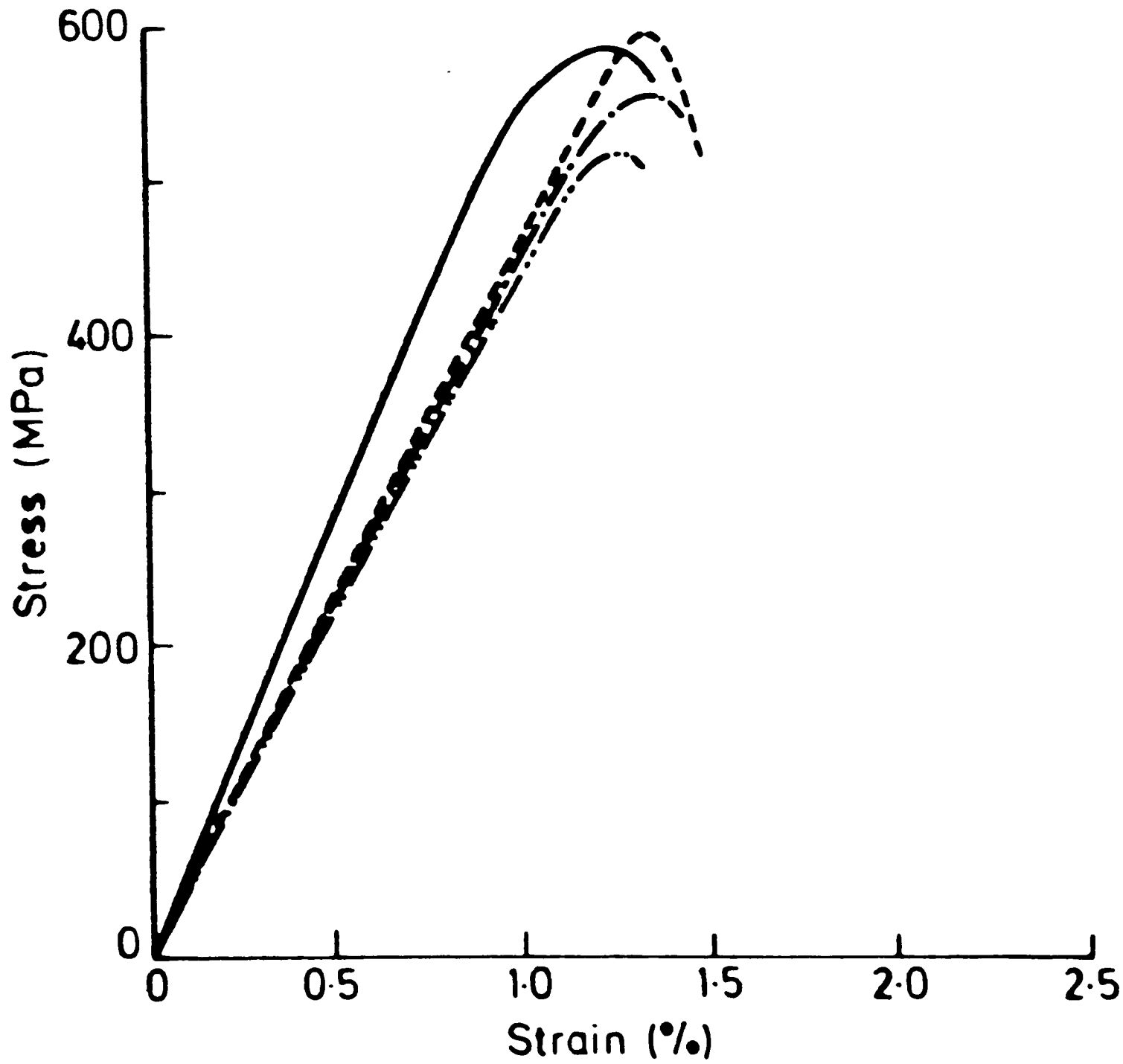

Fig.4.5 STRESS-STRAIN CURVES FOR ALL-CARBON SPECIMENS

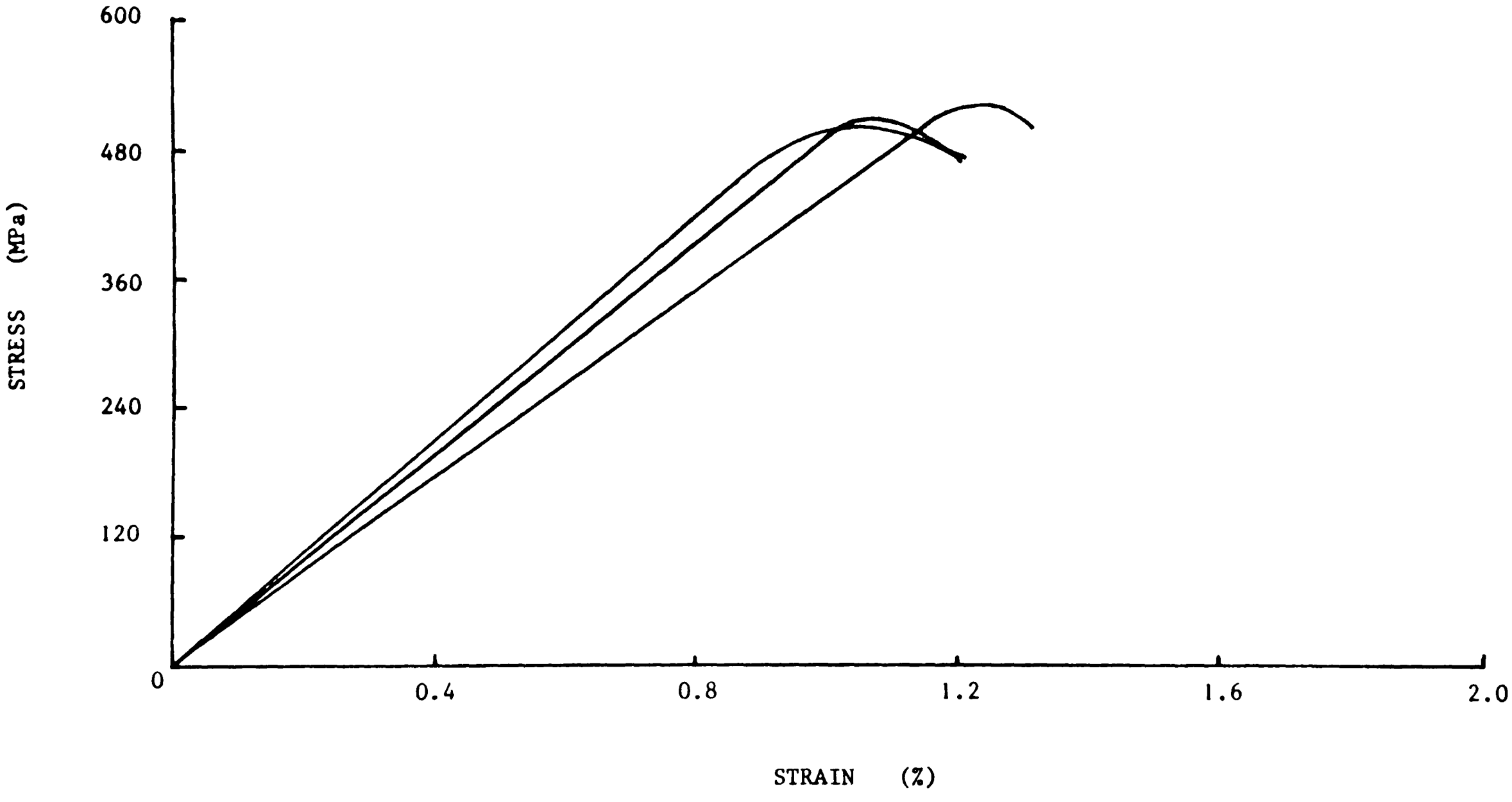

Fig. 4.6 IMPACT STRESS-STRAIN CURVES FOR ALL-CARBON SPECIMENS LOADED IN THE WEFT DIRECTION

Fig.4.7 COMPARISON OF IMPACT STRESS-STRAIN CURVES FOR ALL-CARBON SPECIMENS LOADED IN WARP AND WEFT DIRECTIONS

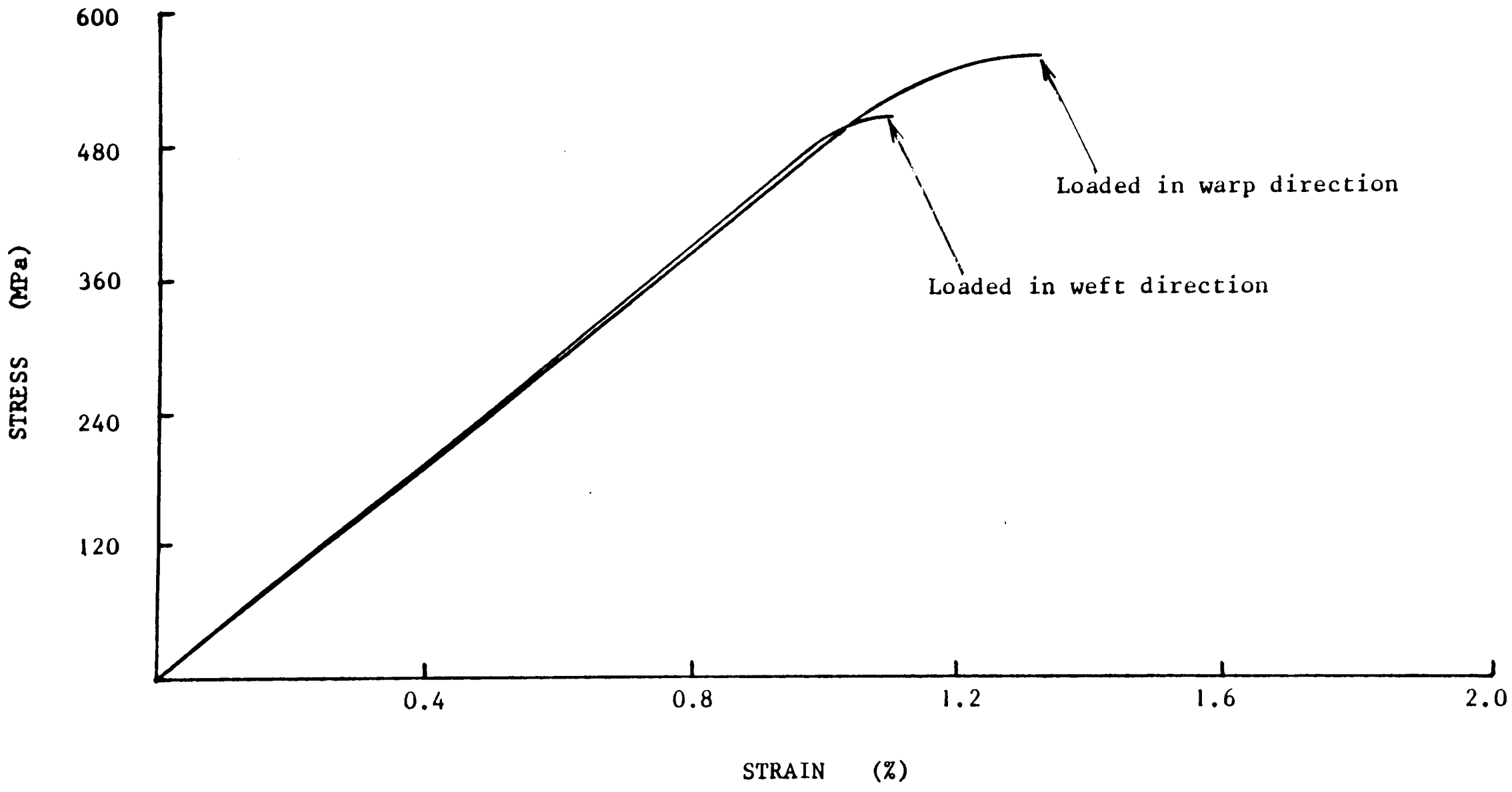

Table 4.1 Comparison of Mechanical Properties in Warp and Weft Directions for All-Carbon Specimens under Impact Loading

Direction of Loading	E (GPa)	σ_{TS} (MPa)	ε_f (%)	σ_y (MPa)	ε_y (%)
Warp	48.7 ± 7.0	562 ± 37	1.32 ± 0.08	501 ± 30	1.04 ± 0.14
Weft	49.0 ± 4.0	508 ± 9	1.10 ± 0.10	482 ± 24	1.00 ± 0.14

Unlike the hybrid and all-carbon specimens, a considerable amount of anelastic deformation was shown by the all-glass reinforced composite. Results from three tests on specimens loaded in the warp direction are plotted in Fig. 4.8 - these are in good agreement. Less good agreement was observed in tests on specimens loaded in the weft direction. Stress-strain curves for two such tests are shown in Fig. 4.9. Mean stress-strain curves for the warp and weft directions, taken from Figs. 4.8 and 4.9 are compared in Fig. 4.10. Here there is a significant reduction in both modulus and strength in the weft direction but a slight increase in the failure strain.

A summary of the impact test results for specimens loaded in the weft direction is given in Fig. 4.11 which compares the mean stress-strain curves in each case. Except for the all-glass specimens where the modified gas-gun loading system was utilized the same impact velocity was used in all tests. In spite of this the average strain rate as defined in section 2.6.3, decreased continuously from ~900/s for type 1 hybrid specimens to ~290/s for all-carbon specimens. Previous work on the rate sensitivity of FRP suggests that a 3:1 variation in strain rate is not sufficient to affect

Fig. 4.8 IMPACT STRESS-STRAIN CURVES FOR ALL-GLASS SPECIMENS LOADED IN THE WARP DIRECTION

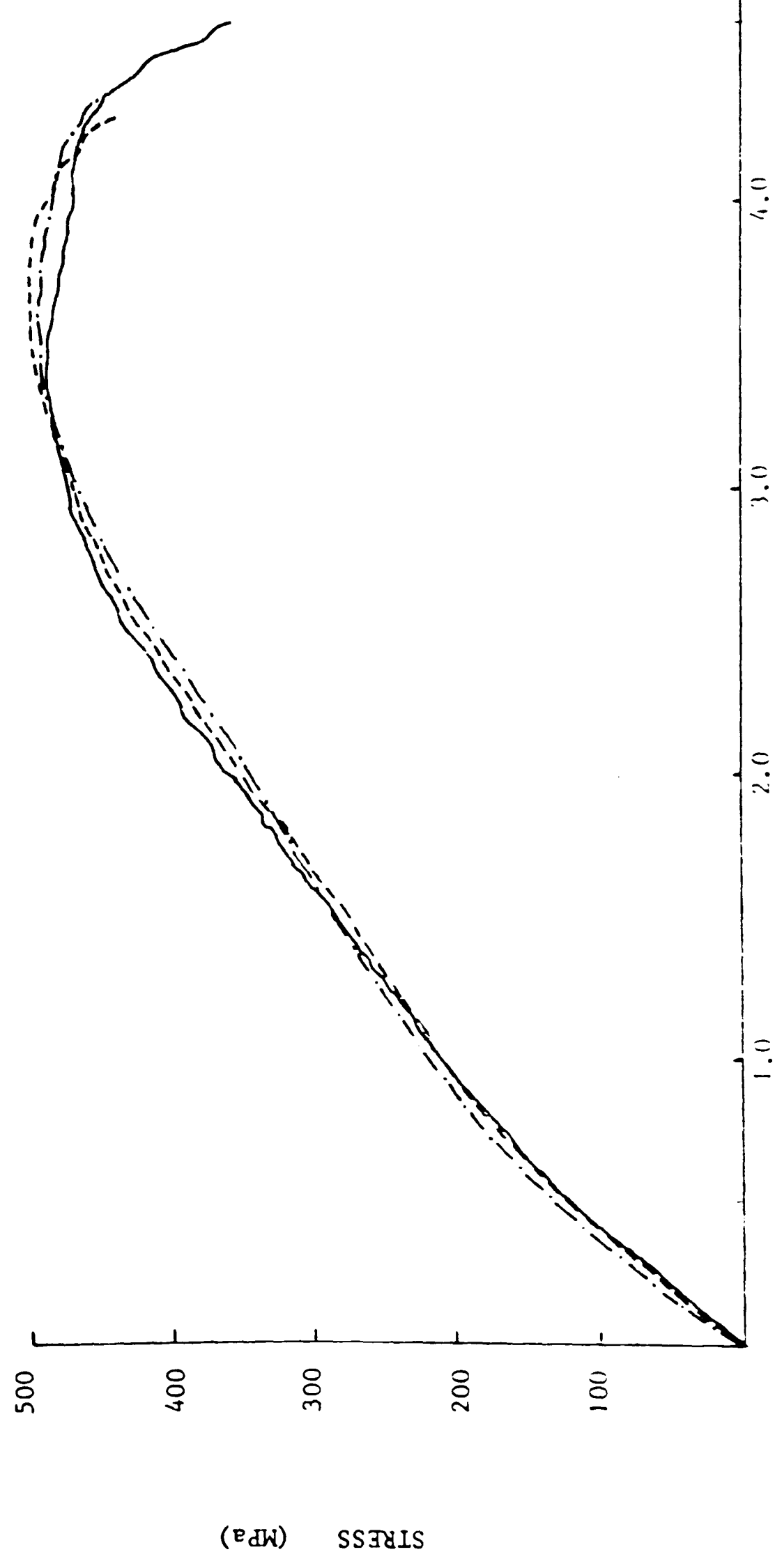

Fig.4.9 IMPACT STRESS-STRAIN CURVES FOR ALL-GLASS SPECIMENS LOADED IN THE WEFT DIRECTION

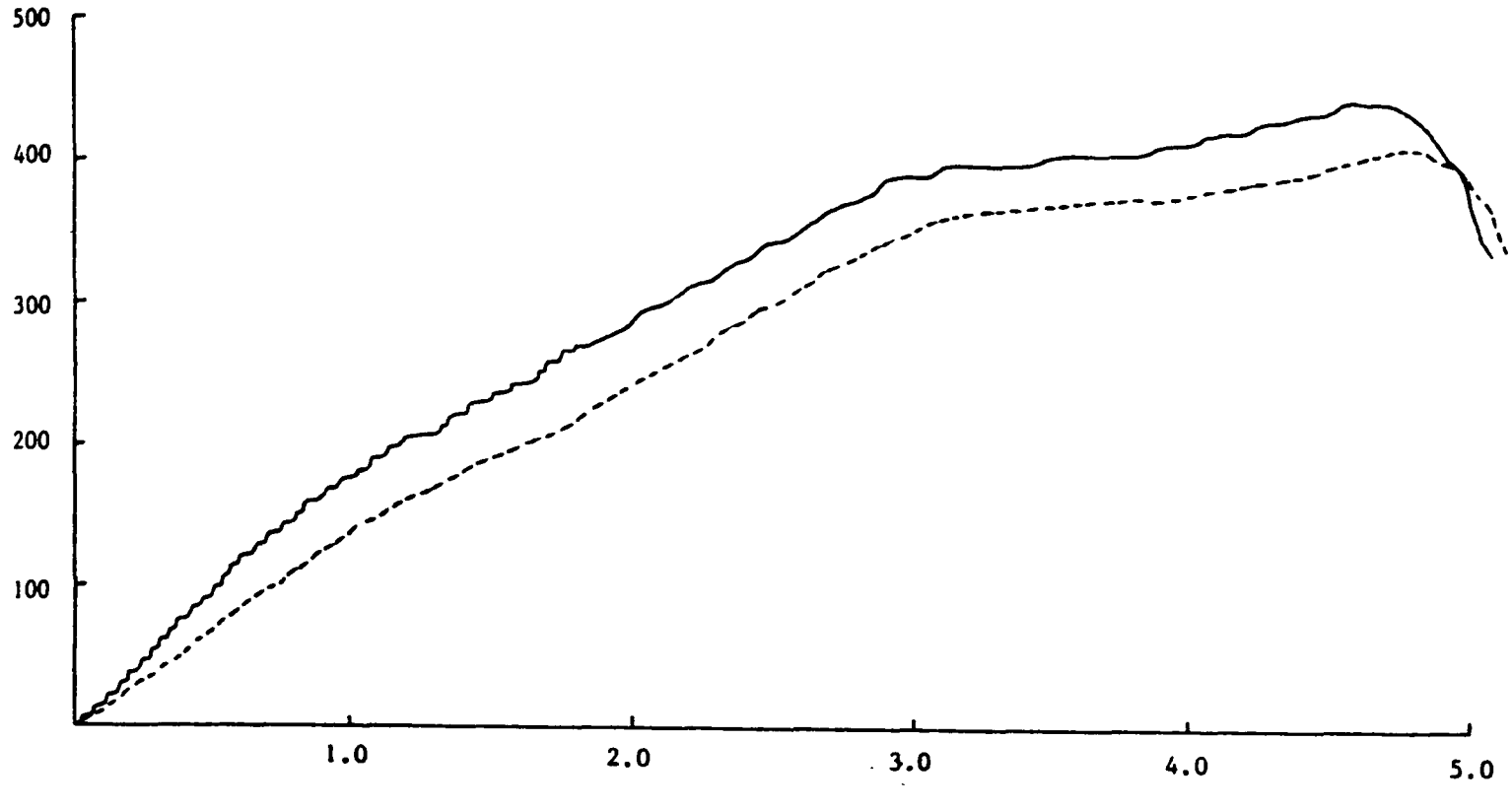

) COMPARISON OF IMPACT STRESS-STRAIN CURVES FOR ALL-GLASS SPECIMENS LOADED IN WARP AND WEFT DIRECTIONS

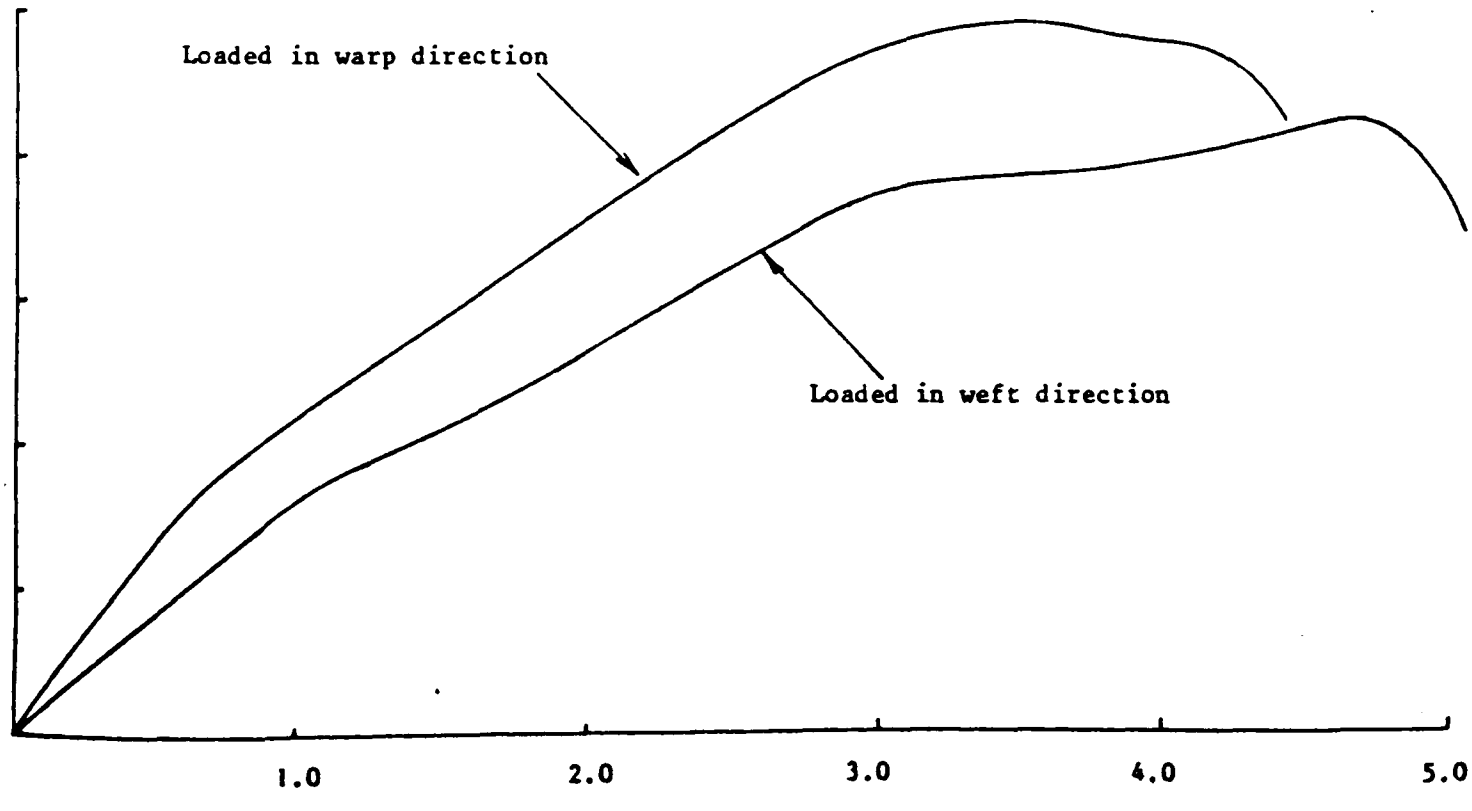

Fig. 4.11 EFFECT OF HYBRID COMPOSITION ON MEAN IMPACT STRESS-STRAIN CURVES

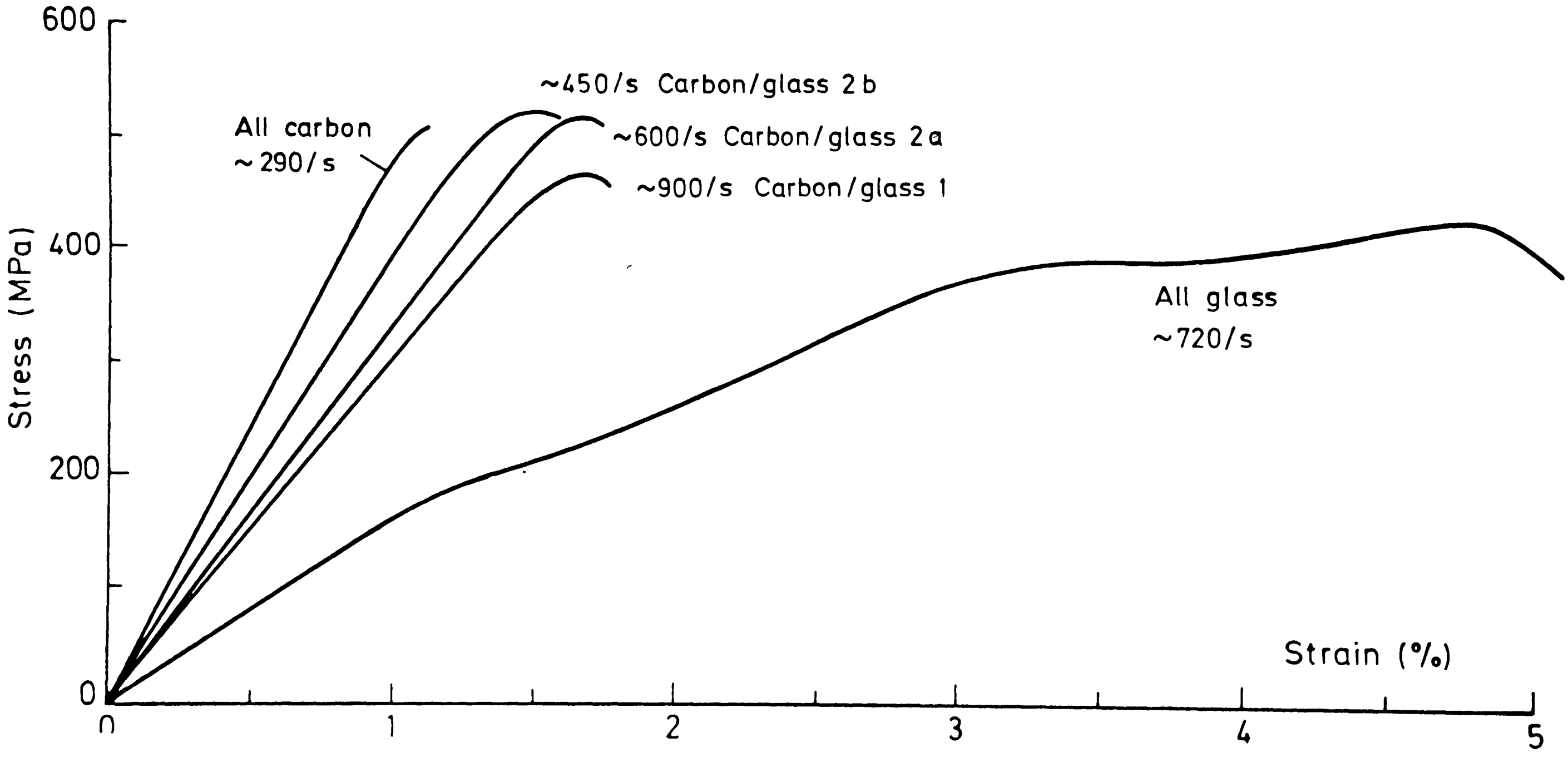

significantly the mechanical properties being measured i.e. to invalidate the comparison between the different tests in Fig. 4.11 [67,78].

4.2.2 Hydraulic Machine Tests

Several tests were performed on each of five types of specimen cut with the tensile axis in the weft direction, at a rate of deformation of ~10/s. Stress strain curves for two hybrid combinations (types 2b and 1) are presented in Figs. 4.12 and 4.13 respectively. Close agreement is found between the measured values of tensile modulus for each specimen type. In the region of anelastic deformation some scatter is apparent in the stress at a given strain and in the strain at fracture, of the order of ± 18 MPa and ± 0.2 % strain respectively, but for both specimen types the general behaviour is similar. The results from five tests on type 2a hybrid specimens are compared in Fig. 4.14. Here the scatter in the measured values of tensile strength 445 MPa ± 19 MPa and tensile modulus 34.8 GPa ± 2.8 GPa is a little greater while the observed values of fracture strain 1.89% ± 0.14% showed better agreement.

Stress-strain plots of the four tests on all-carbon specimens are given in Fig. 4.15 and may be seen to agree very closely. For the all-glass specimens, the principal features of the stress-strain curves, as at impact rates of strain, are the extended region of anelastic deformation and the high strain at failure, ~3.4% (see Fig. 4.16).

Mean stress-strain curves for the various specimens are compared in Fig. 4.17. The general behaviour shown is, almost in every respect, similar

Fig.4.13 INTERMEDIATE RATE STRESS-STRAIN CURVES FOR TYPE 1 HYBRID SPECIMENS

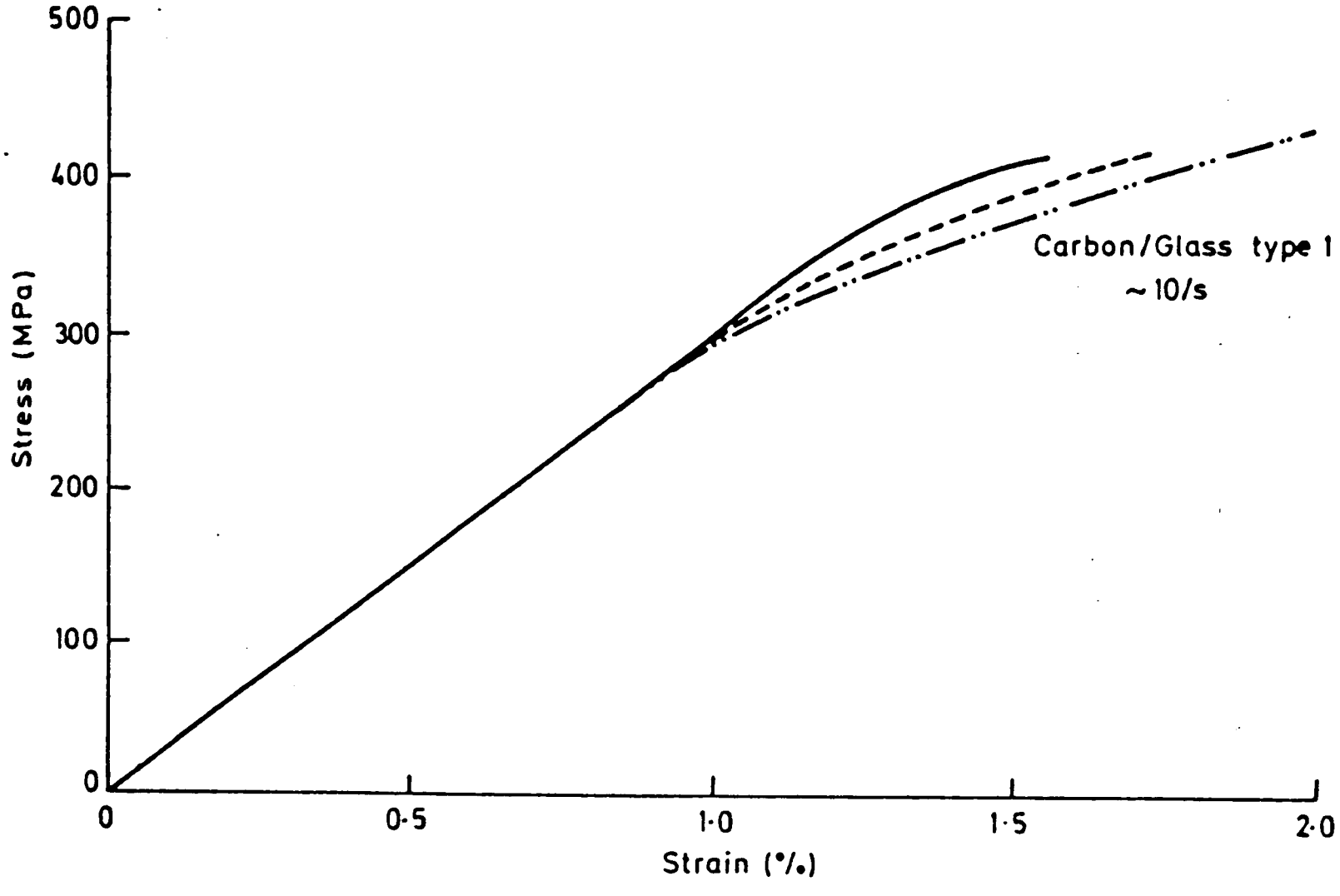

Fig.4.12 INTERMEDIATE RATE STRESS-STRAIN CURVES FOR TYPE 2b HYBRID SPECIMENS

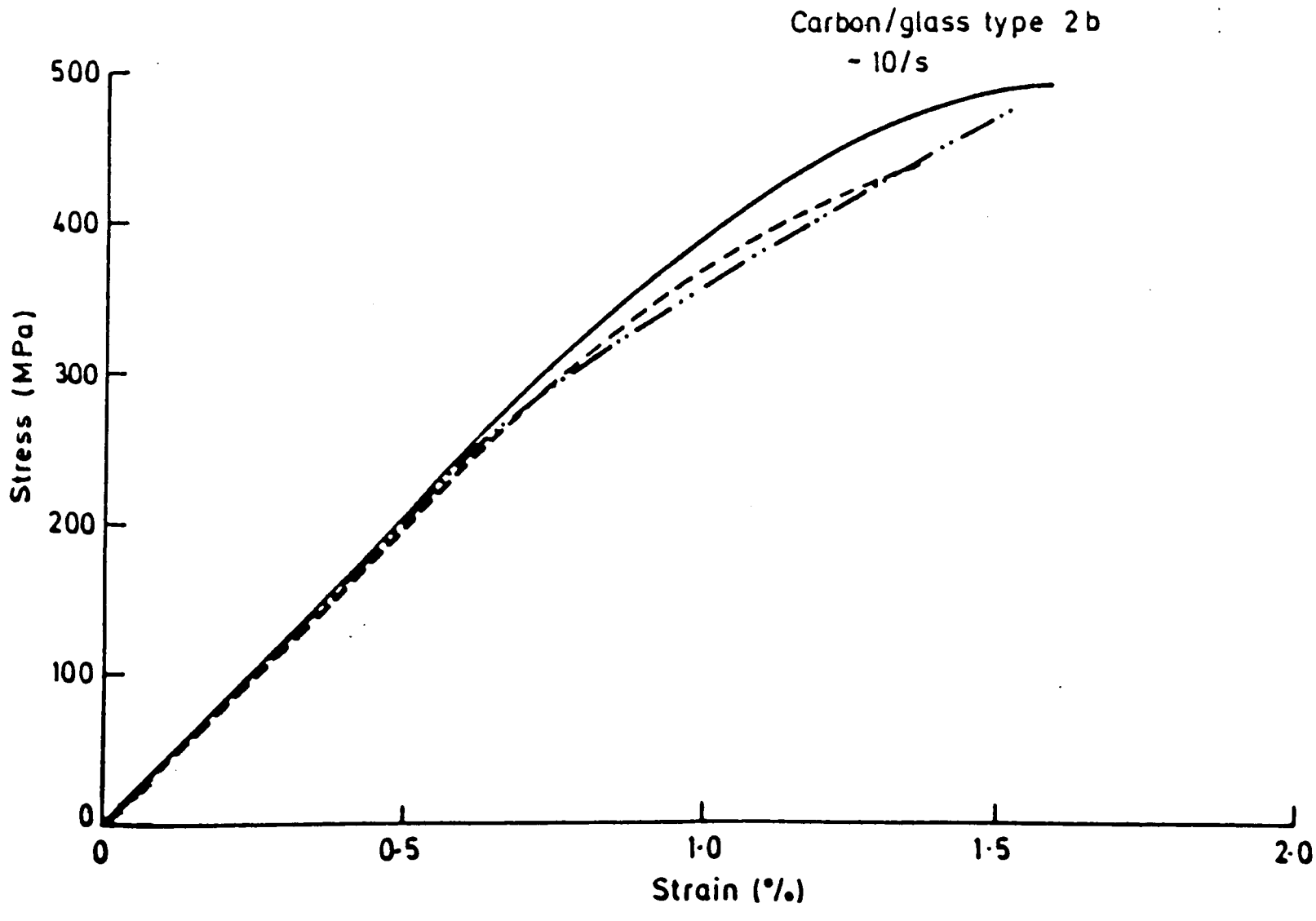

Fig. 4.14 INTERMEDIATE RATE STRESS-STRAIN CURVES FOR TYPE 2a HYBRID SPECIMENS

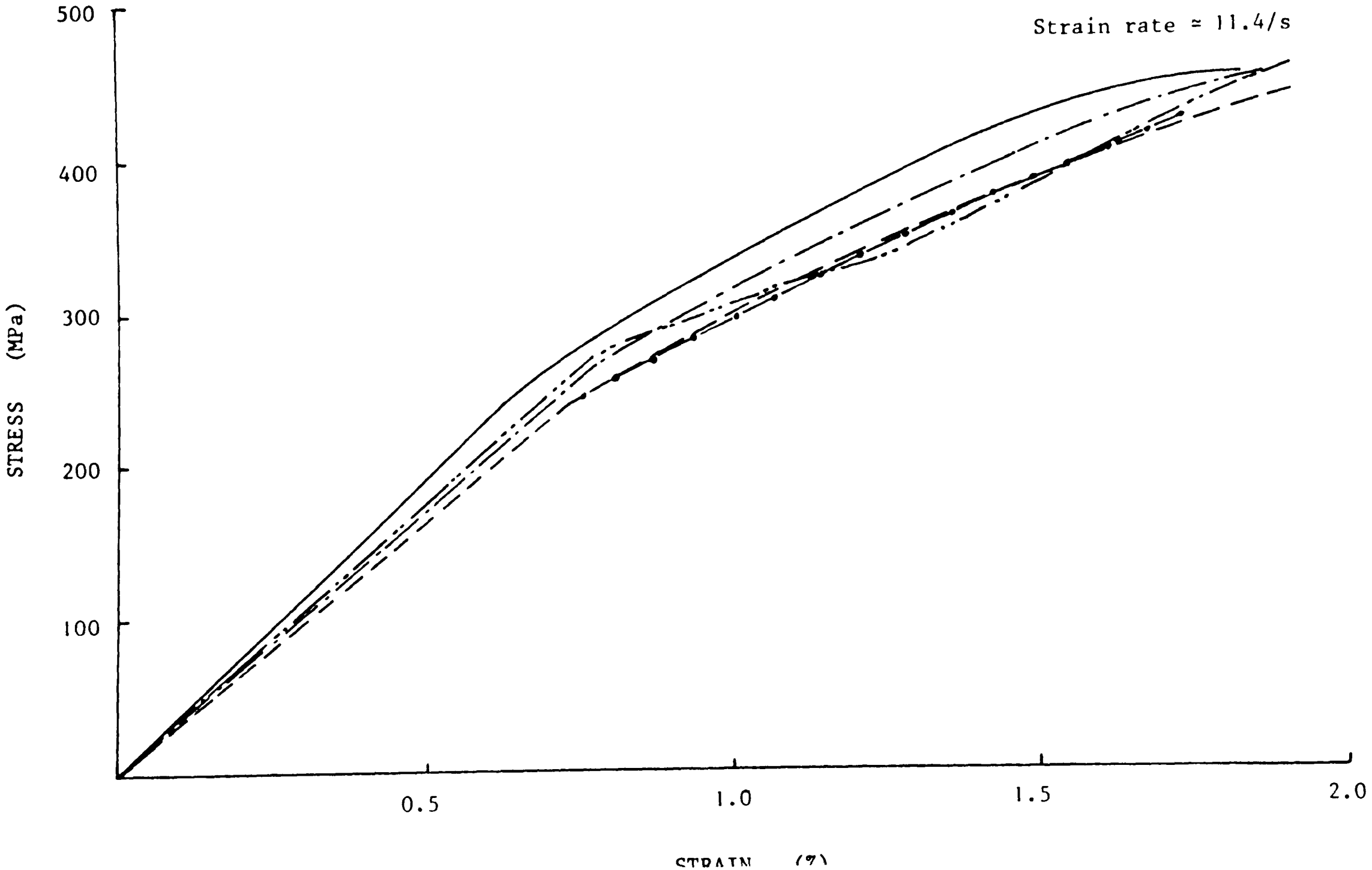

Fig. 4.15 INTERMEDIATE RATE STRESS-STRAIN CURVES FOR ALL-CARBON SPECIMENS

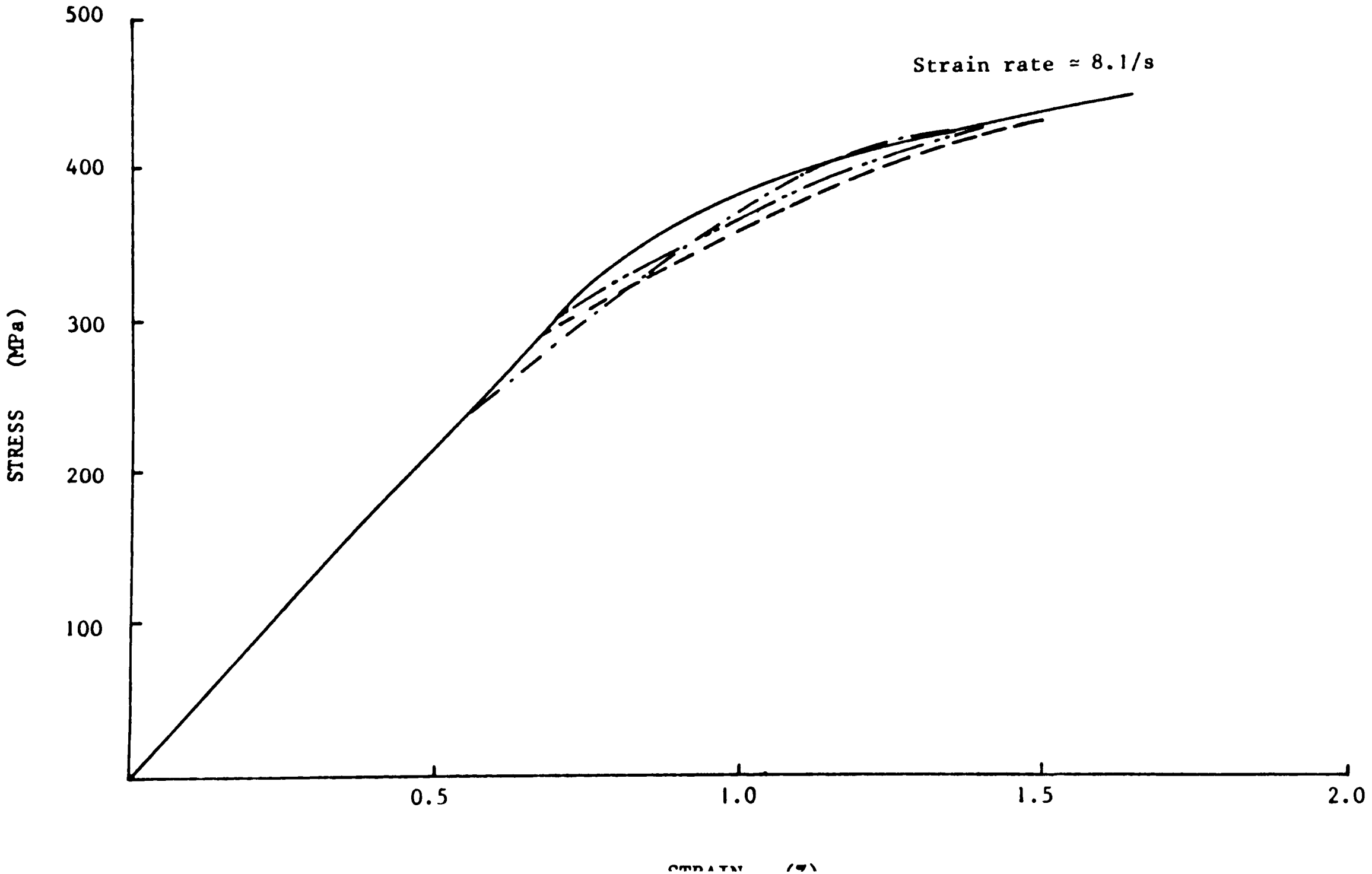

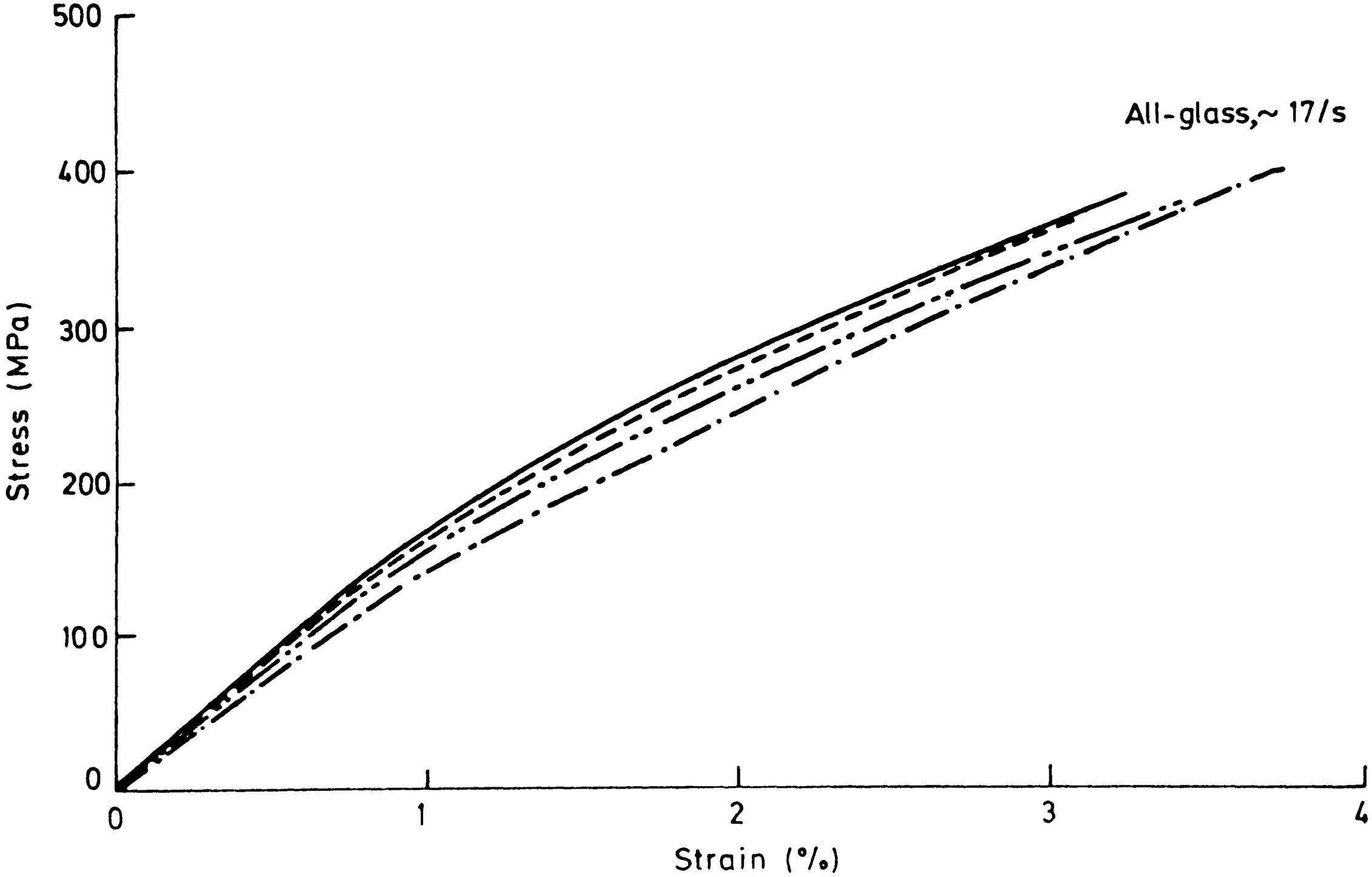

Fig. 4.16 INTERMEDIATE RATE STRESS-STRAIN CURVES FOR ALL-GLASS SPECIMENS

Fig. 4.17 EFFECT OF HYBRID COMPOSITION ON MEAN INTERMEDIATE RATE STRESS-STRAIN CURVES

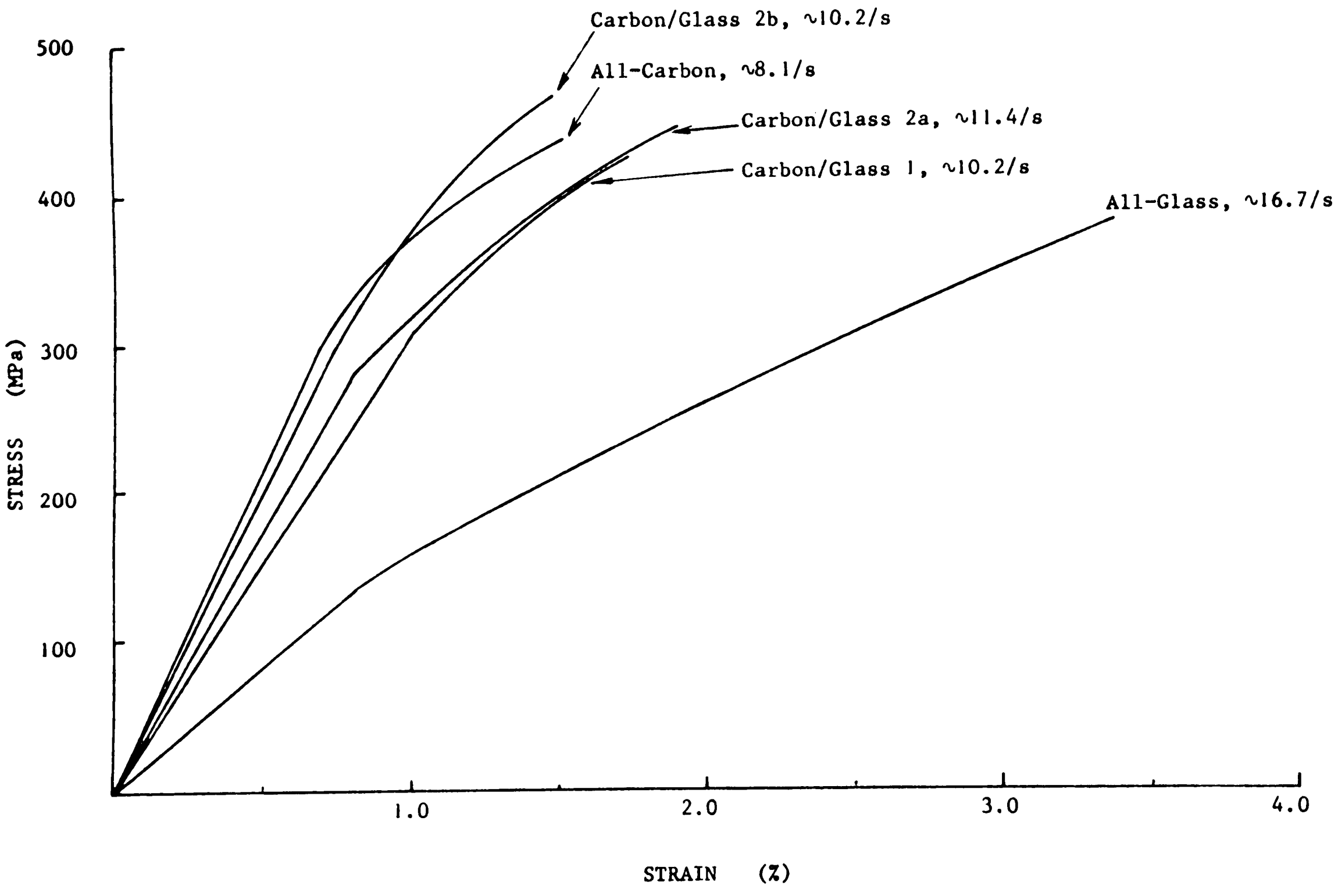

to that observed at impact rates with, for example, a continuously increasing initial modulus with carbon weight fraction and, in the main, a continuously reducing strain at failure. As at impact (see Fig. 4.11) and quasi-static rates of deformation (to be discussed in Section 4.2.3), the type 2b hybrid specimens with 0.75 weight fraction of carbon fibres exhibit a higher failure strength than the all-carbon composite specimens. The source of this anomalous behaviour is not clear but will be discussed in Chapter 6.

4.2.3 Quasi-static Tests

Stress-strain curves for quasi-static tests at a mean strain-rate of $\sim 10^{-3}$/s on carbon/glass type 2b, 2a and 1, the all-carbon and the all-glass specimens are shown in Figs. 4.18, 4.19, 4.20, 4.21 and 4.22 respectively. Results are presented for four tests on each hybrid material and three tests on the all-carbon or all-glass laminates. All specimens were loaded in the warp direction. For the type 1 and type 2b hybrids the scatter between individual results was very small. In the type 2a hybrid tests one specimen appeared significantly stronger than the other three.

For the all-carbon specimens the scatter in the measured tensile modulus, 43.3 GPa ± 2.7 GPa, tensile strength 428.3 MPa ± 18.5 MPa, and fracture strain, 1.35% ± 0.25% was much greater than in the all-glass composites and may be related to the coarser weave of the carbon reinforcement. Also shown in Figs. 4.23 and 4.24 are stress-strain plots of experimental results obtained in tests on the all-carbon and all-glass

Fig. 4.18 QUASI-STATIC STRESS-STRAIN CURVES FOR TYPE 2b HYBRID SPECIMENS

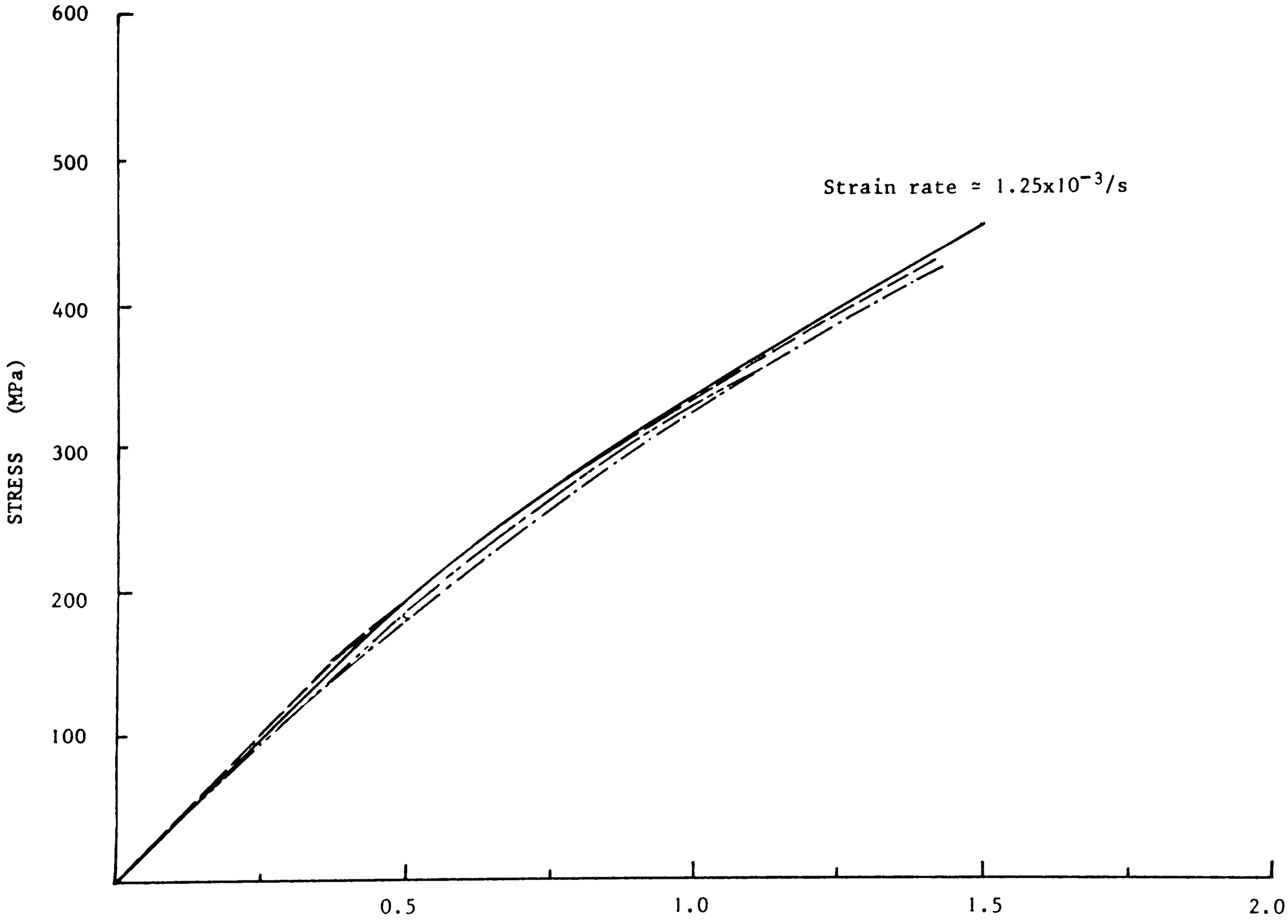

Fig. 4.19 QUASI-STATIC STRESS-STRAIN CURVES FOR TYPE 2a HYBRID SPECIMENS

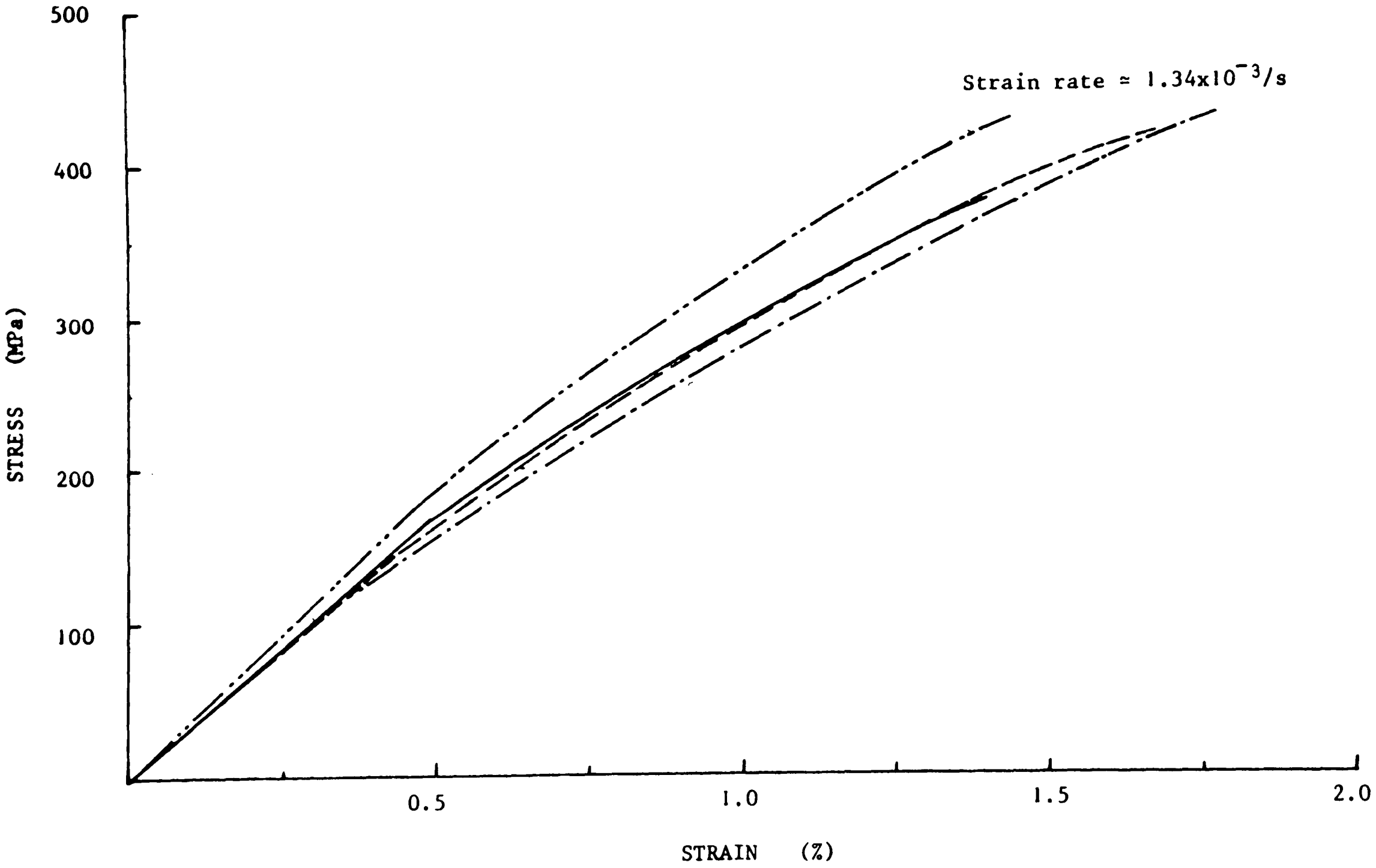

Fig. 4.20 QUASI-STATIC STRESS-STRAIN CURVES FOR TYPE 1 HYBRID SPECIMENS

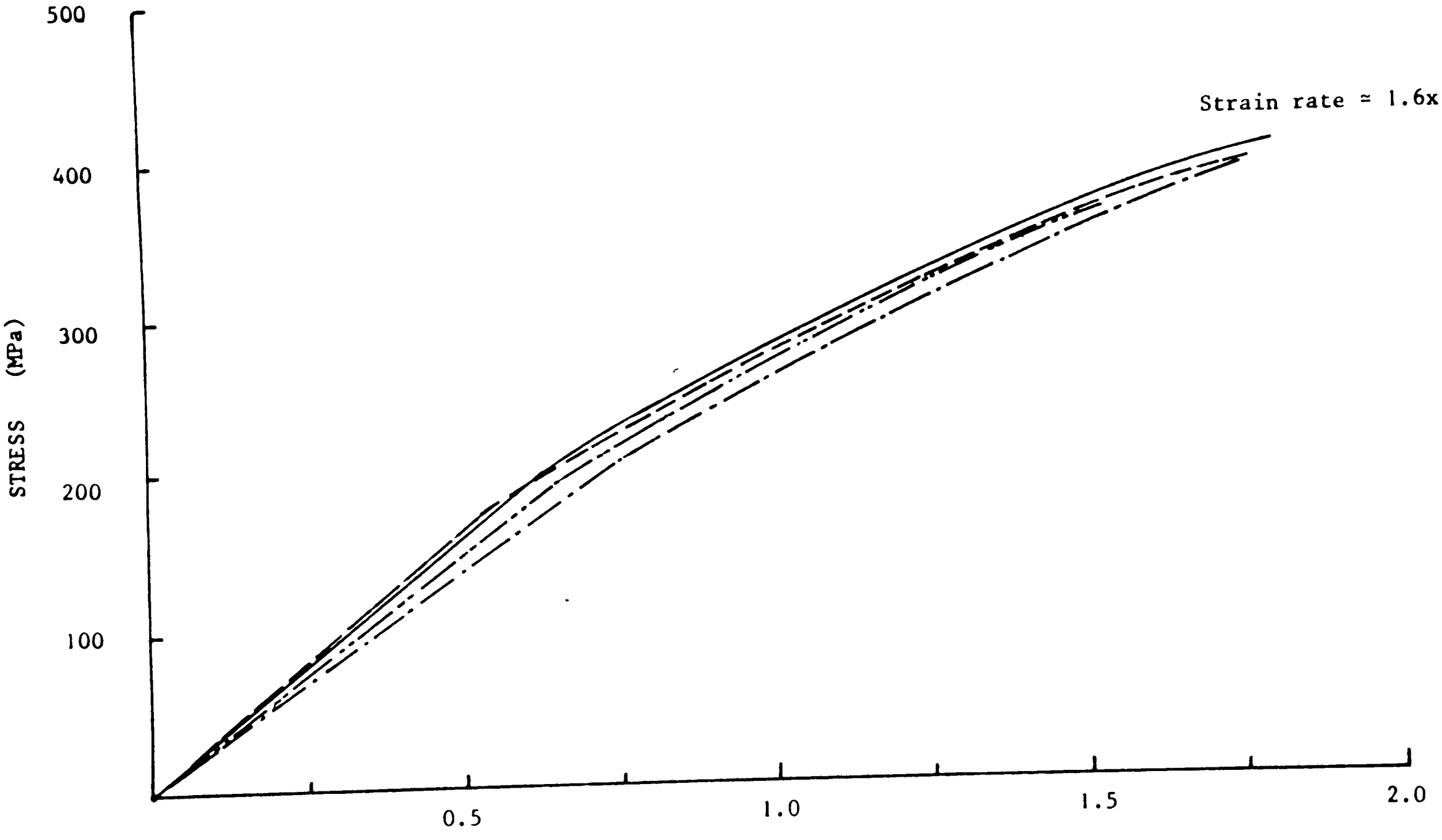

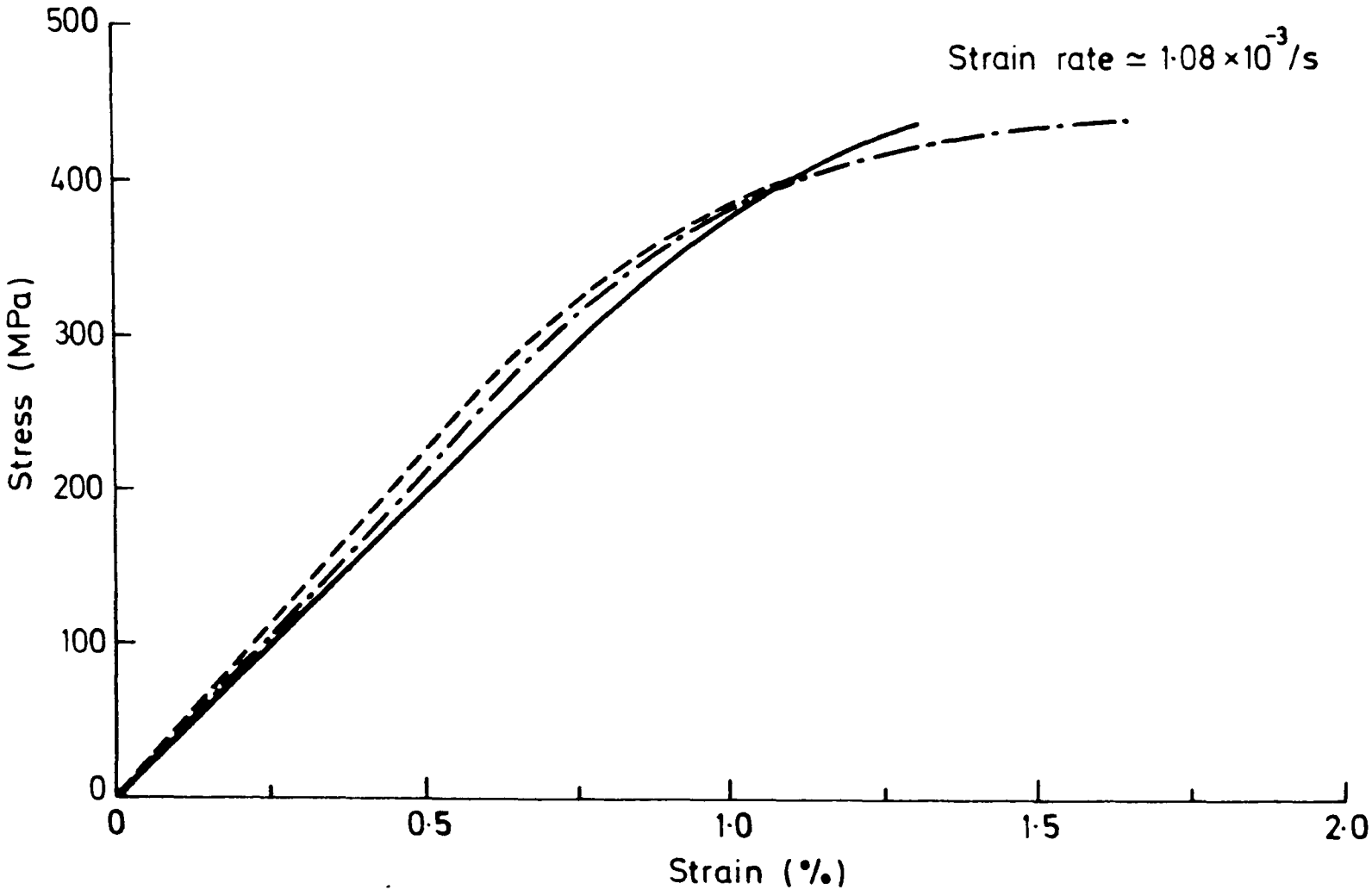

Fig. 4.21 Quasi-static stress-strain curves for all-carbon specimens.

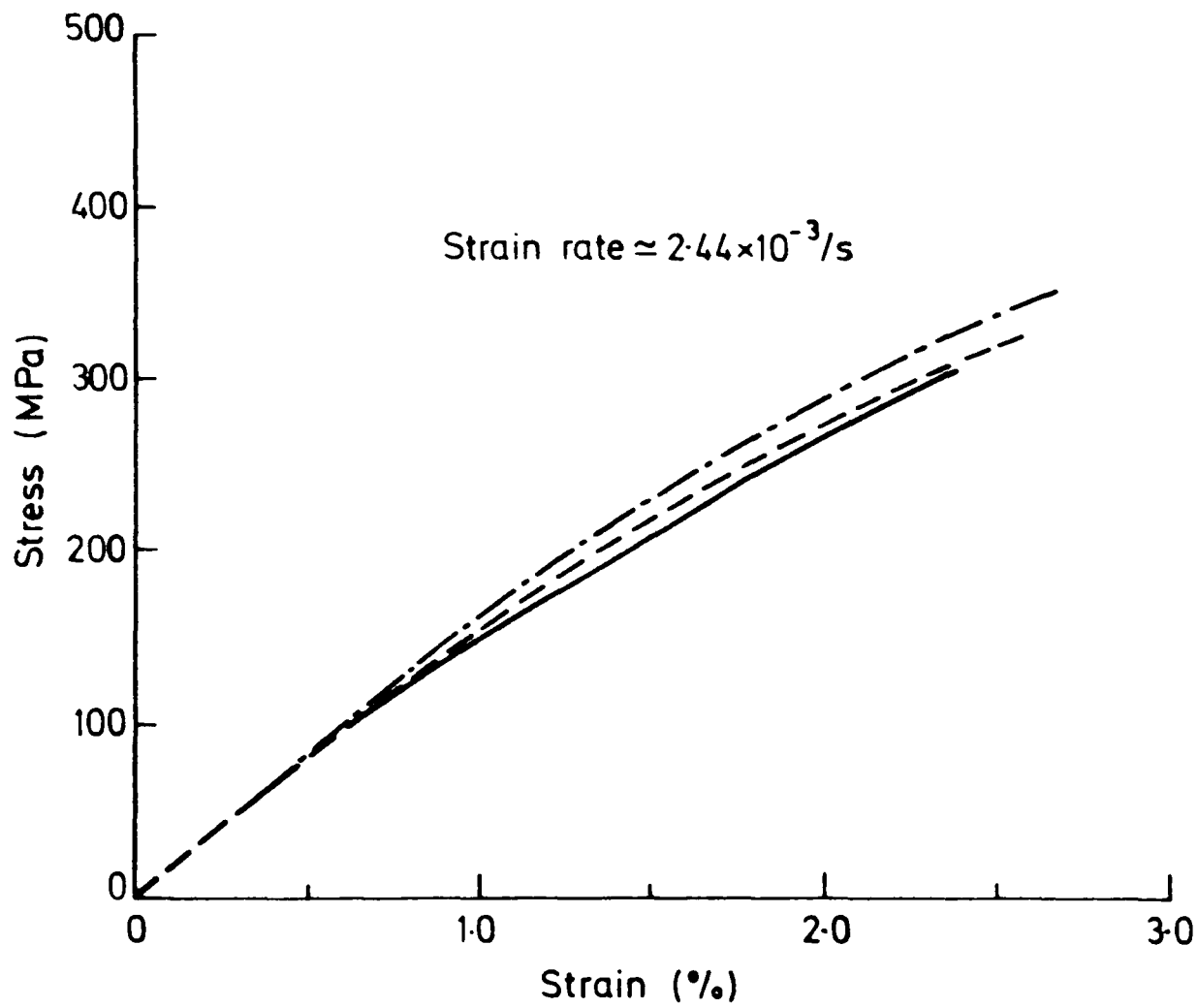

Fig. 4.22 Quasi-static stress-strain curves for all-glass specimens

Fig.4.23 QUASI-STATIC STRESS-STRAIN CURVES FOR ALL-CARBON SPECIMENS

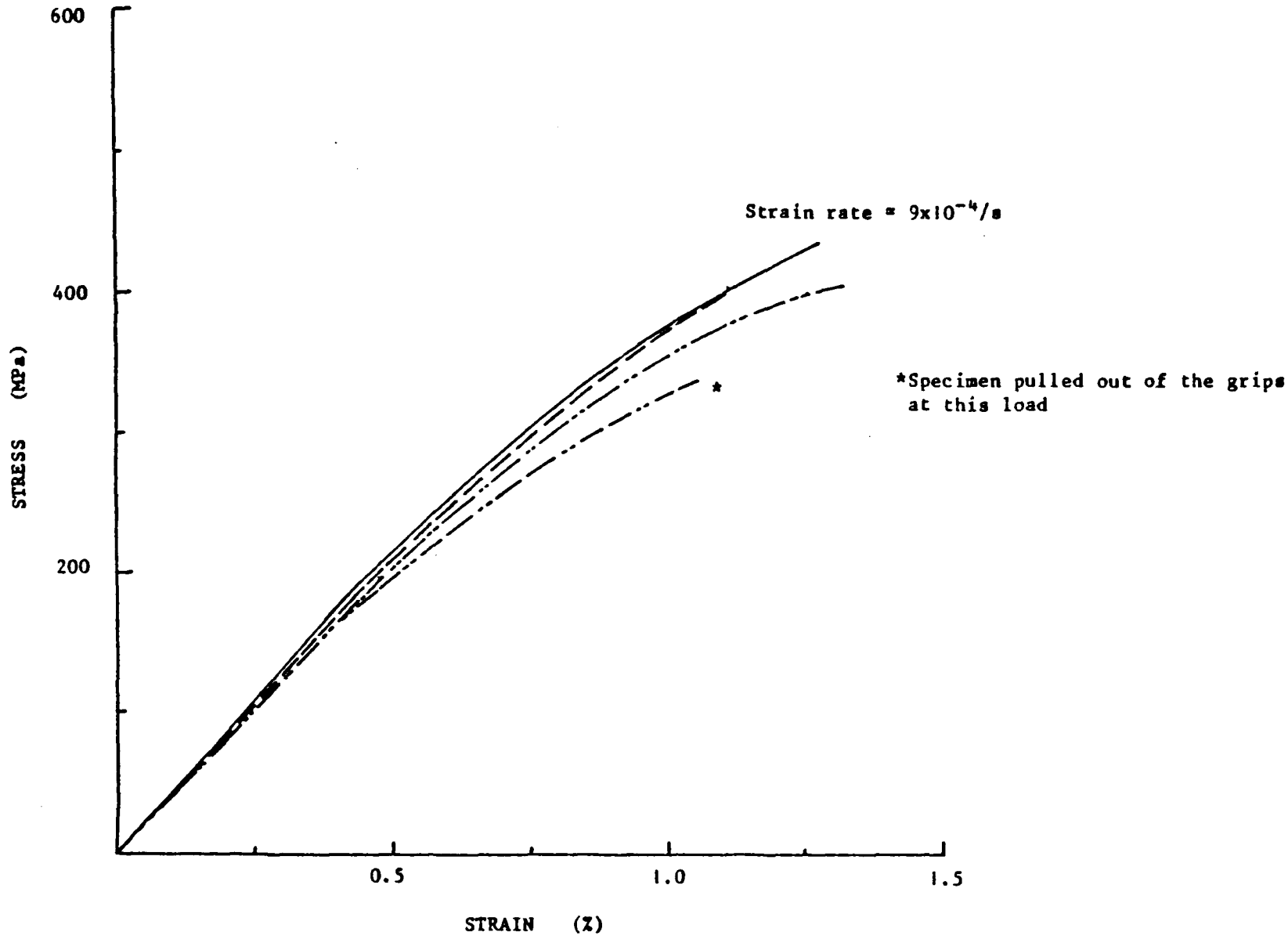

Fig.4.24 QUASI-STATIC STRESS-STRAIN CURVES FOR ALL-GLASS SPECIMENS

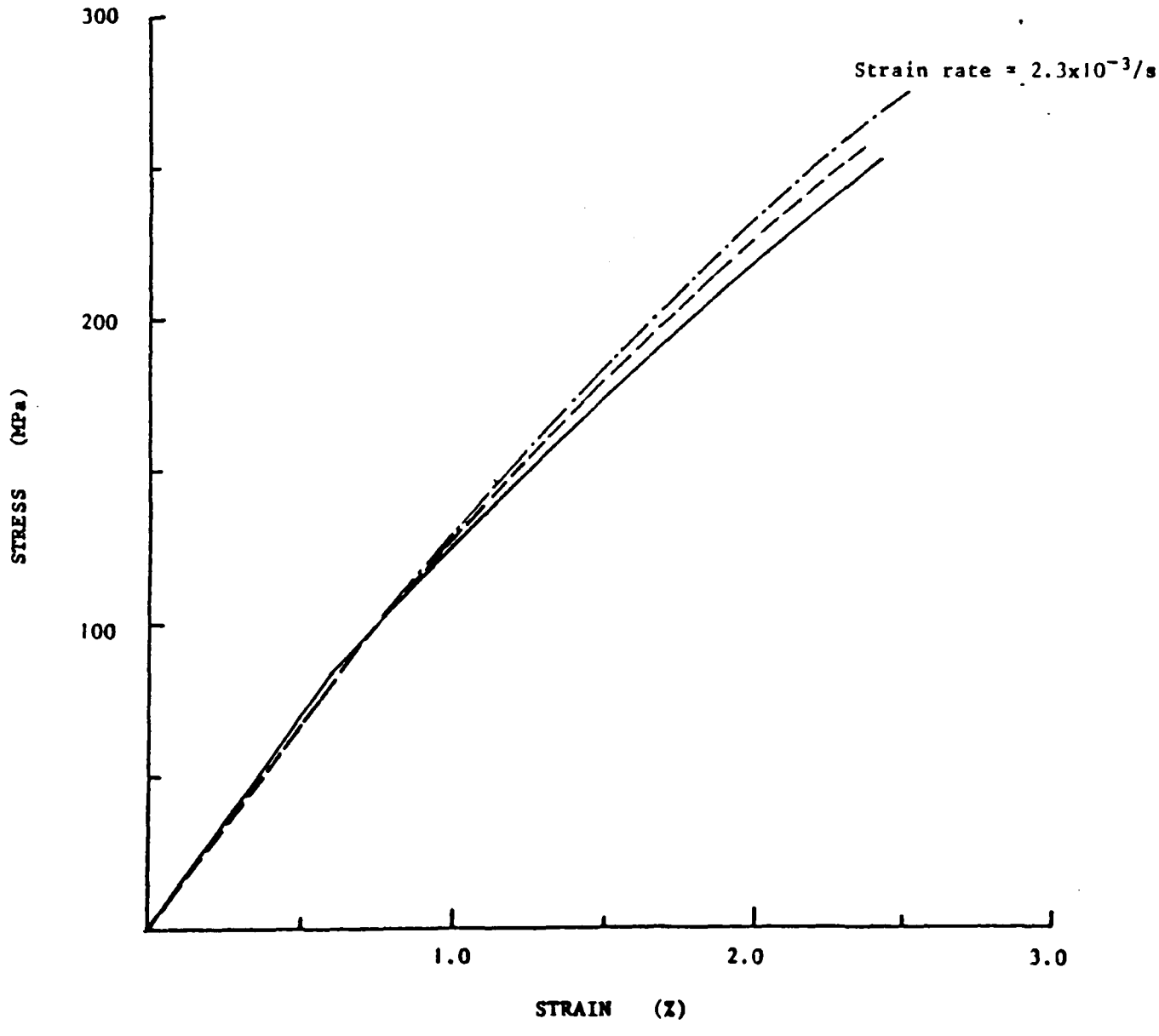

specimens cut with the tensile axis in the weft direction. One of the all-carbon specimens pulled out of the grips so a tensile failure load and a corresponding failure strain could not be determined, otherwise the individual tests showed better agreement than for the same material loaded in the warp direction. The results from three tests on the all-glass specimens were very close. Figures 4.25 and 4.26 compare the mean stress-strain curves from Figs. 4.21 and 4.22 respectively, with the corresponding curves of Figs. 4.23 and 4.24. A comparison of the mechanical properties in the two directions is given in Table 4.2 below. The definitions of the various symbols are as given

Table 4.2 Comparison of Mechanical Properties in Warp and Weft Directions for All-Glass and All-Carbon Specimens (Quasi-static tests).

Material	Orientation	E (GPa)	σ_{TS} (MPa)	ε_f (%)	σ_y (MPa)	ε_y (%)
All-glass	Warp	16.7	328	2.53	92	0.55
	Weft	13.7	262	2.45	87	0.63
All-carbon	Warp	43.3	428	1.35	240	0.55
	Weft	42.5	416	1.24	172	0.40

in section 4.2.1.

A small difference in properties for the two directions is apparent in the all-carbon specimens and a more significant difference in the all-glass specimens. This is not surprising since for the glass reinforcing mat there were more ends (252) than picks (173) per 10cm whereas for the much coarser carbon mat there was the same number (47) in each direction.

Fig.4.25 **COMPARISON OF QUASI-STATIC STRESS-STRAIN CURVES FOR ALL-CARBON SPECIMENS LOADED IN WARP AND WEFT DIRECTIONS**

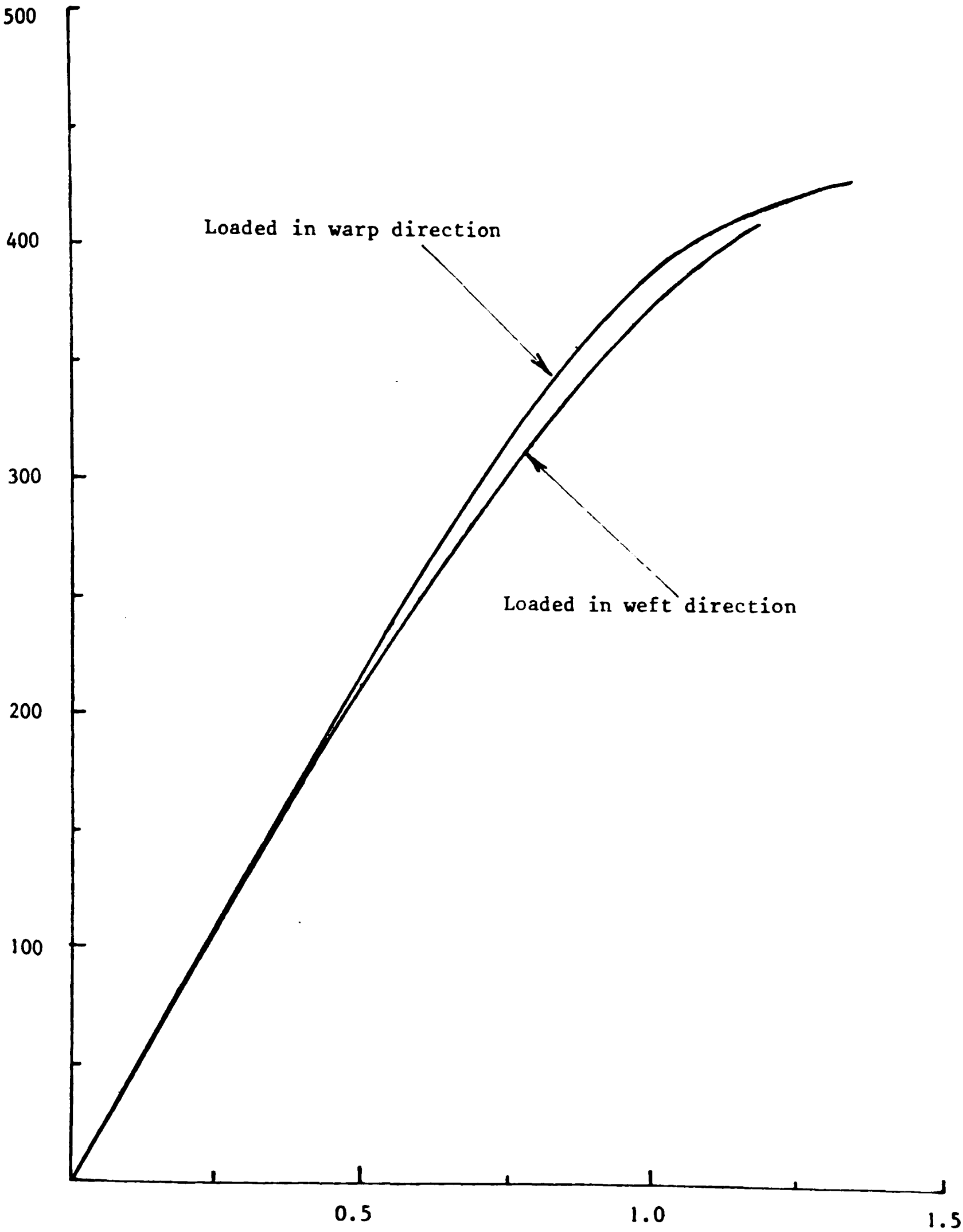

Fig.4.26 **COMPARISON OF QUASI-STATIC STRESS-STRAIN CURVES FOR ALL-GLASS SPECIMENS LOADED IN WARP AND WEFT DIRECTIONS**

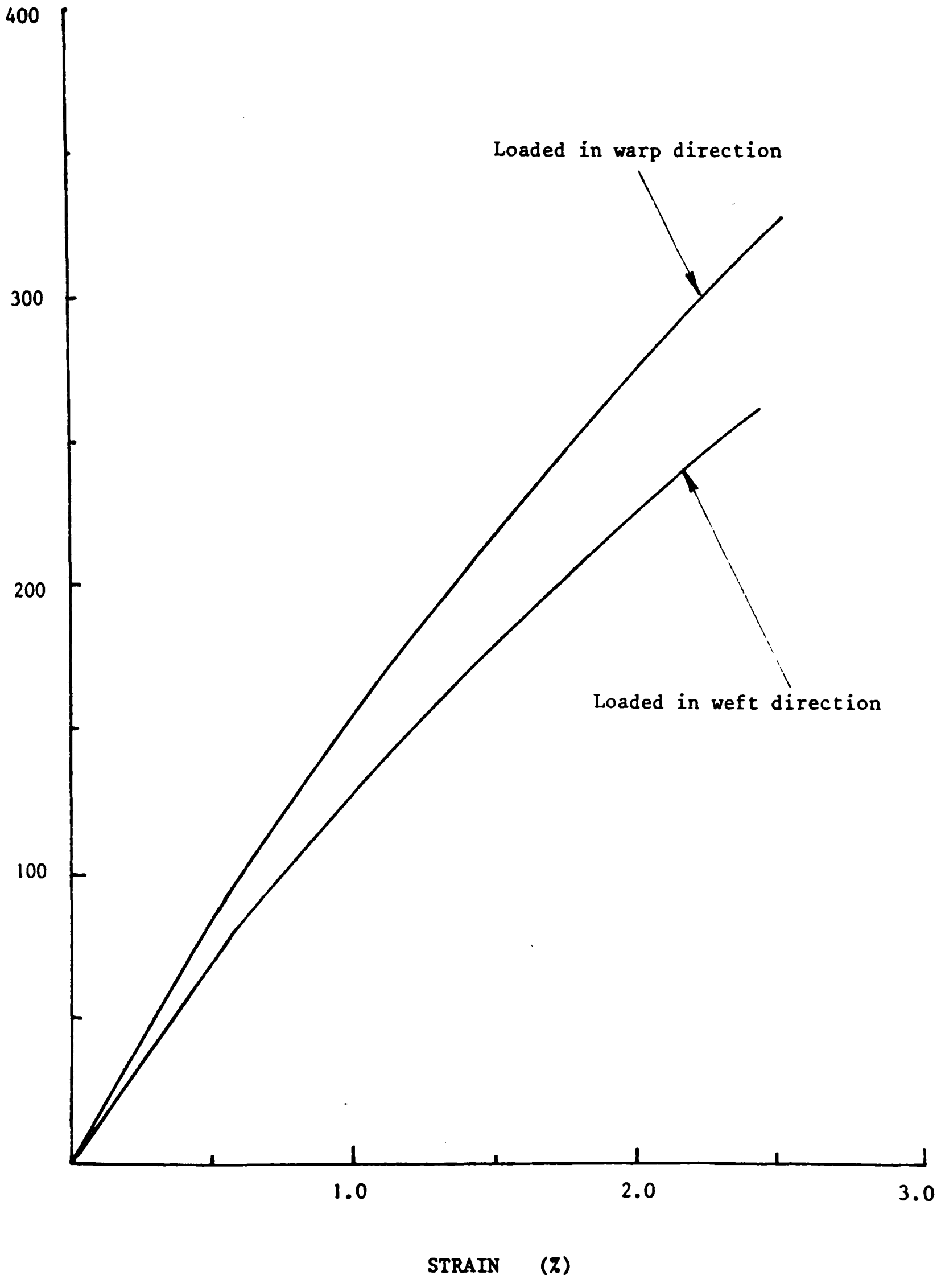

Mean stress-strain curves from each of five series of tests on specimens loaded in the warp direction are compared in Fig. 4.27. As at intermediate and impact loading rates the fracture strength of the type 2b hybrid exceeds that of the all-carbon specimens. The trend followed by the initial modulus and fracture strain corresponds with that observed at higher loading rates.

4.3 Elastic Properties and Compressive Strength Results

4.3.1 Elastic Property Tests

To allow a determination of the full two-dimensional stiffness matrix for the all-carbon and all-glass laminates, tests were performed on parallel-sided coupons cut from these materials with the loading axis along the warp (L) or the weft (T) directions or at 45^{o} to both warp and weft directions (x or 45^{o}). Strain gauges were attached to the specimens as shown earlier (see Fig. 2.37). Results are presented for quasi-static and impact tests.

Quasi-static tests

Each coupon was loaded and unloaded several times, remaining within the elastic range. Results obtained in this way for an all-glass coupon loaded in the warp direction are shown in Fig. 4.28, the scatter band indicated at each load being for six measurements, three during loading and three during unloading. The resulting modulus in the loading direction, E_L, was found to be 16.35 GPa, which compares with the value of 16.7 GPa given in Table 4.2.

Fig. 4.27 EFFECT OF HYBRID COMPOSITION ON MEAN QUASI-STATIC STRESS-STRAIN CURVES

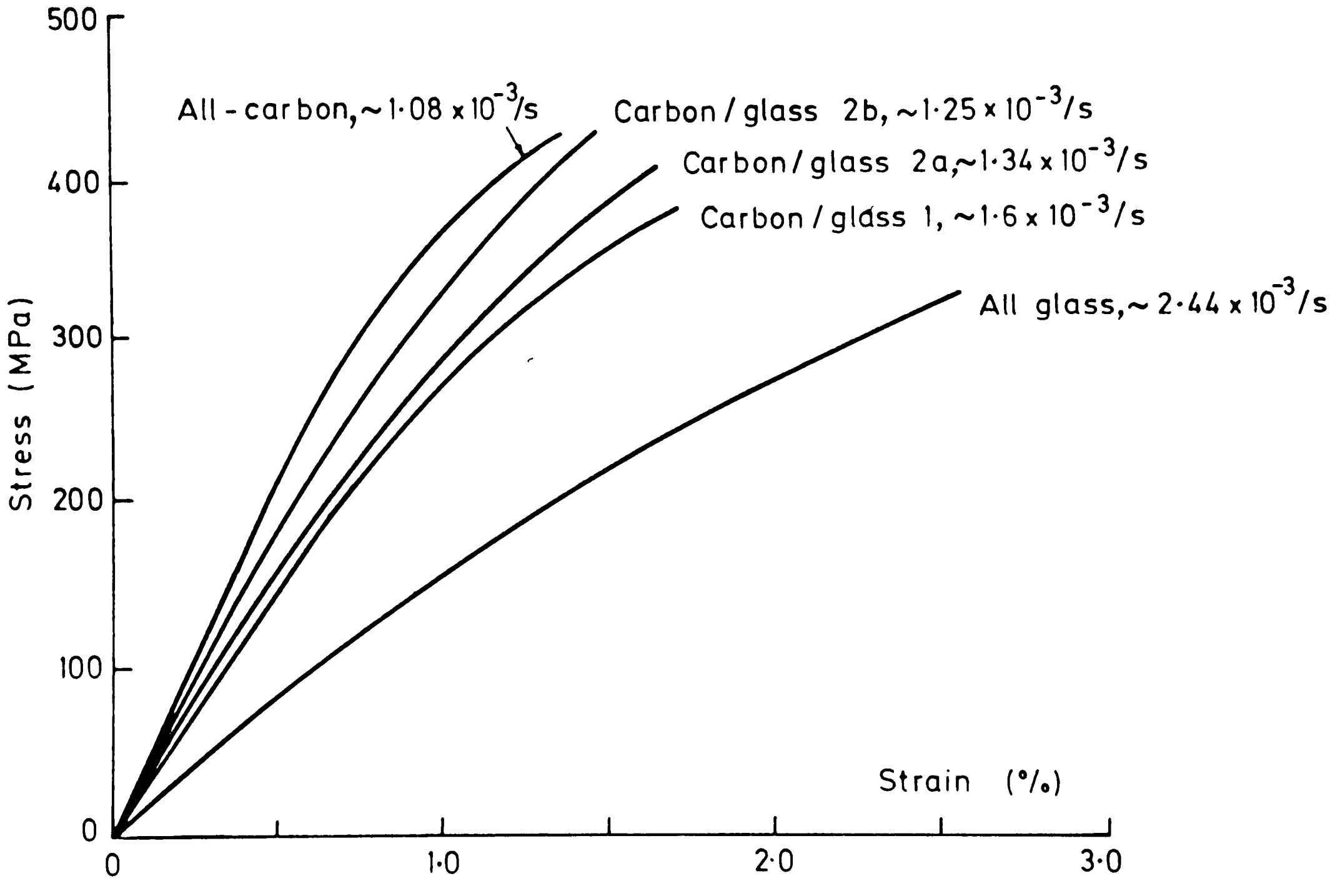

Fig.4.28 QUASI-STATIC 'ELASTIC' RELOADING TESTS FOR AN ALL-GLASS SPECIMEN LOADED IN THE WARP DIRECTION

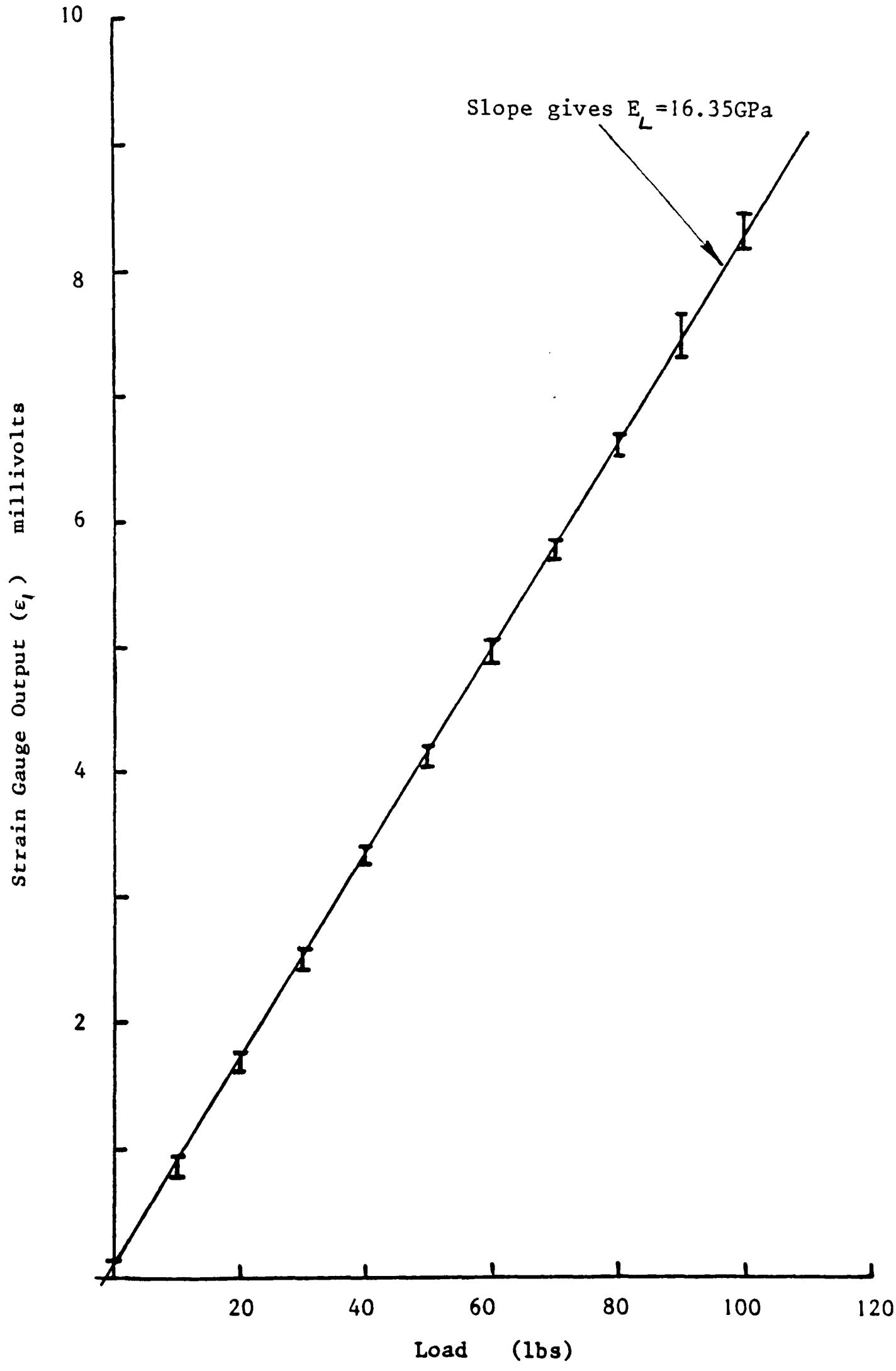

To obtain Poisson's ratio strain gauge signals in the loading and transverse directions (ε_1 and ε_2) are compared for the same three loading cycles, results obtained in this way for all-glass coupons loaded in the weft direction being shown in Fig. 4.29. The mean slope in Fig. 4.29 gives a Poisson's ratio, ν_{TL} of 0.141. Similar results for an all-glass coupon loaded in the warp direction gave $\nu_{LT} = 0.164$. The present results satisfies equation (3.22) i.e.

$$\nu_{LT} E_T = \nu_{TL} E_L$$

with an accuracy greater than $\pm 1\%$.

A similar series of tests was performed on coupons cut from the all-carbon laminate. Here, however, a difference in behaviour was observed between loading and unloading as may be seen from the results listed in Table 4.3. When fitted to equation (3.22) these show a discrepancy of $\pm 20\%$ when the loading results are used reducing to $\pm 5\%$ when the unloading line results are tested. In fact, failure of the symmetry hypothesis is not unusual and has been reported by many other investigators, for example Lempriere [139] and Bert, Mayberry and Ray [140]. A non-conservative behaviour of some constituent of the composite is usually postulated as the cause, possibly in this case the non-conservative microcracking of the epoxy resin during 'elastic' loading of the woven carbon fibre reinforced specimens. It is usual in such cases to define ν_{TL} in terms of equation (3.22) as $\nu_{LT}E_T$ / E_L.

Table 4.3 Elastic Constants for the All-Carbon Laminate (Quasi-static tests).

	E_L (GPa)	E_T (GPa)	ν_{LT}	ν_{TL}
Loading	46.4	43.6	0.144	0.088
Unloading	44.5	43.6	0.091	0.081

To determine the shear modulus similar reloading tests were performed on coupons cut at 45^o to the warp and weft directions. For the strain gauges aligned with the loading direction a discrepancy between the loading and unloading behaviour was again observed, more marked here for the all-glass than the all-carbon material and appearing as a lag in the strain gauge response on unloading, see Fig. 4.30. There was little difference however, between the slopes of the loading and unloading lines and an average result for the modulus in the 45^o direction, E_{45^o} of 5.39 GPa ($\pm 5\%$) is obtained. For the all-carbon specimens the corresponding result was 9.58 GPa ($\pm 0.5\%$). The required shear modulus, G_{LT}, may be obtained from equation (2.5) i.e.

$$G_{LT} = \left[\frac{4}{E_{45^o}} - \left(\frac{1}{E_L} + \frac{1}{E_T} - \frac{2\nu_{LT}}{E_L} \right) \right]^{-1}$$

Substituting $E_{45^o} = 5.39$ GPa, $E_L = 16.35$ GPa, $E_T = 13.77$ GPa and $\nu_{LT} = 0.164$ in equation (2.5) we obtain, for the all-glass laminate, a shear modulus $G_{LT} = 1.59$ GPa. A similar calculation for the all-carbon material, taking

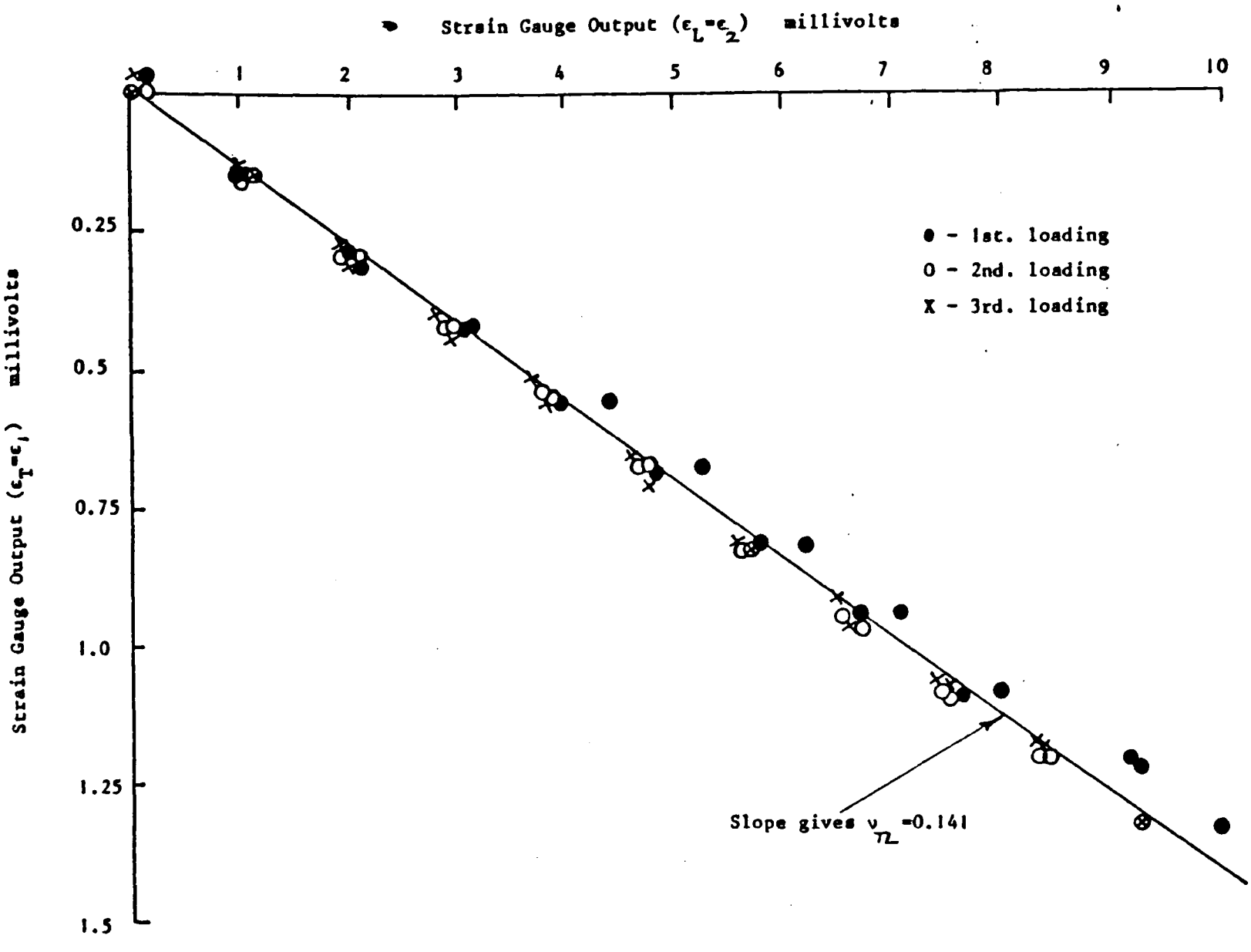

Fig.4.29 QUASI-STATIC 'ELASTIC' RELOADING TESTS FOR AN ALL-GLASS SPECIMEN LOADED IN THE WEFT DIRECTION

Fig.4.30 QUASI-STATIC 'ELASTIC' RELOADING TESTS FOR AN ALL-GLASS SPECIMEN LOADED IN THE 45° DIRECTION

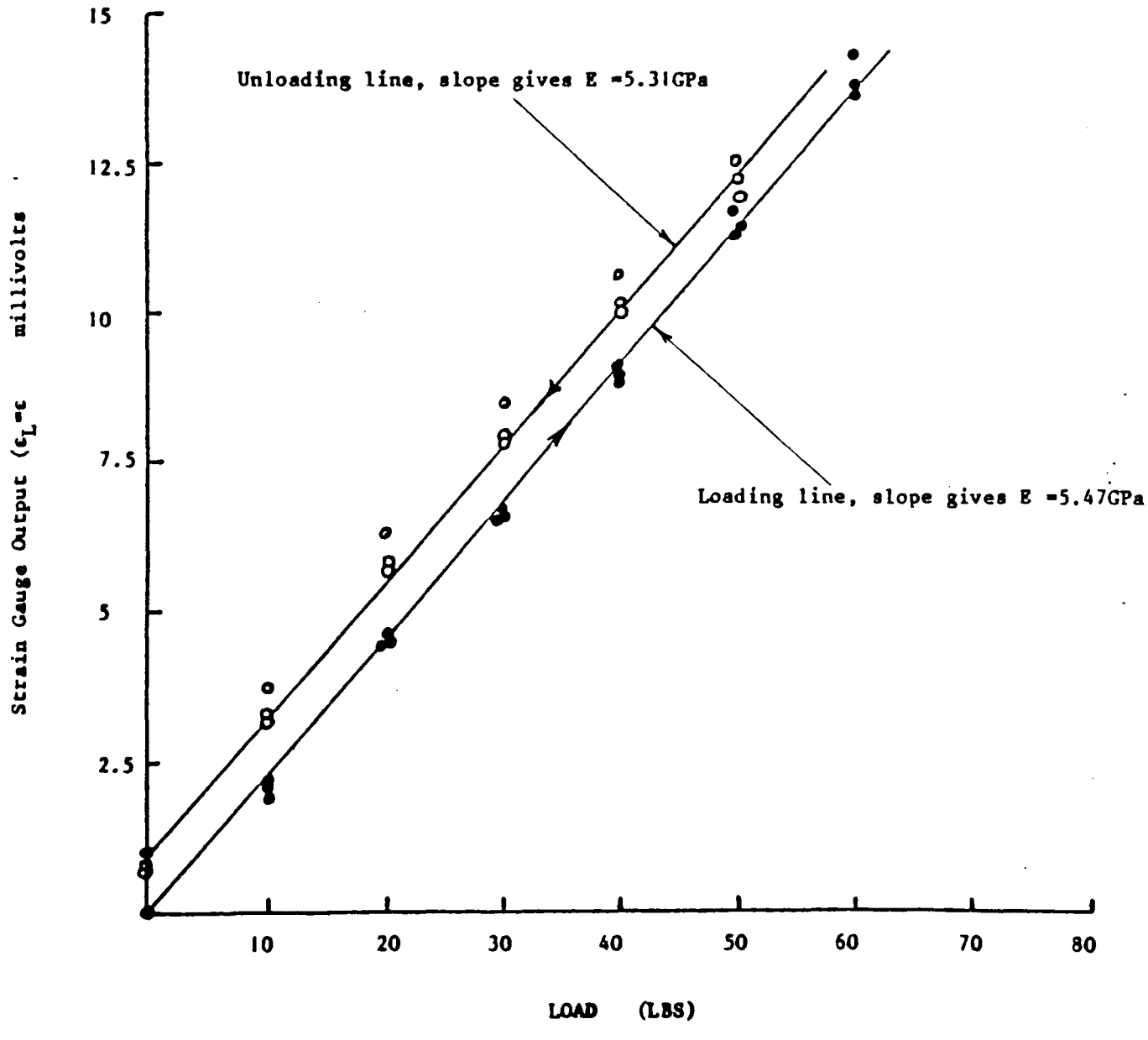

E_{45^o} = 9.58 GPa, E_L = 45.5 GPa, E_T = 43.6 GPa and either ν_{LT} = 0.144 (loading) or 0.091 (unloading) gives for the shear modulus values of either 2.64 GPa or 2.66 GPa respectively, a negligible difference.

Alternatively, the results from the 45^o test-piece may be substituted in equation (2.3) which gives the in-plane shear modulus as

$$G_{LT} = \sigma_x / 2\,(\varepsilon_x - \varepsilon_y)$$

In the present tests ε_y was not measured directly but may be determined, using the Mohr's circle for strain, from the strain gauge readings in the two reinforcing directions, ε_α and ε_β corresponding to ε_1 and ε_2 in Fig. 2.37, giving

$$\varepsilon_y = \varepsilon_\alpha + \varepsilon_\beta - \varepsilon_x$$

so that equation (2.3) becomes

$$G_{LT} = \sigma_x / \{\, 4\varepsilon_x - 2\,(\varepsilon_\alpha + \varepsilon_\beta)\} \qquad (4.1)$$

Defining the 'moduli' E_α and E_β as $\sigma_x / \varepsilon_\alpha$ and $\sigma_x / \varepsilon_\beta$, respectively, this gives

$$G_{LT} = \frac{1}{2} \left\{ \left(2/E_x\right) - \left(1/E_\alpha\right) - \left(1/E_\beta\right) \right\}^{-1} \qquad (4.2)$$

The variation of σ_x with both ε_α and ε_β was obtained from three elastic reloading tests on the 45^o all-carbon parallel-sided coupon. After an initial anomalous region a linear elastic response was obtained corresponding to mean values for E_α and E_β of 161.5 ± 13.5 GPa and 67.1 ± 4.8 GPa respectively. The same specimen was subsequently loaded to failure and curves of σ_x versus ε_α and ε_β obtained, as shown in the computer plots of Figs. 4.31 and 4.32, leading to further values of E_α and E_β of 162.7 GPa and 72.6 GPa respectively, in reasonable agreement with reloading tests. Corresponding results were obtained in similar tests on an all-glass coupon. Using the average values derived from these various results for E_x, E_α and E_β, the shear modulus was determined from equation (4.2) and found to be 2.74 GPa for the all-carbon and 1.61 GPa for the all-glass laminates, respectively, about 4% greater than the value previously determined from equation (2.5) for the all-carbon laminate and about 2% greater for the all-glass laminate.

From the three sets of results obtained in quasi-static tests (ie. standard tensile tests, 'elastic' reloading and tests to failure on parallel-sided coupons) on the all-carbon and all-glass laminates in the warp and weft directions, the mean values of the various elastic constants, see Table 4.4 are obtained,

Fig.4.31 QUASI-STATIC FAILURE TEST ON AN ALL-CARBON PARALLEL-SIDED COUPON LOADED IN THE 45° DIRECTION

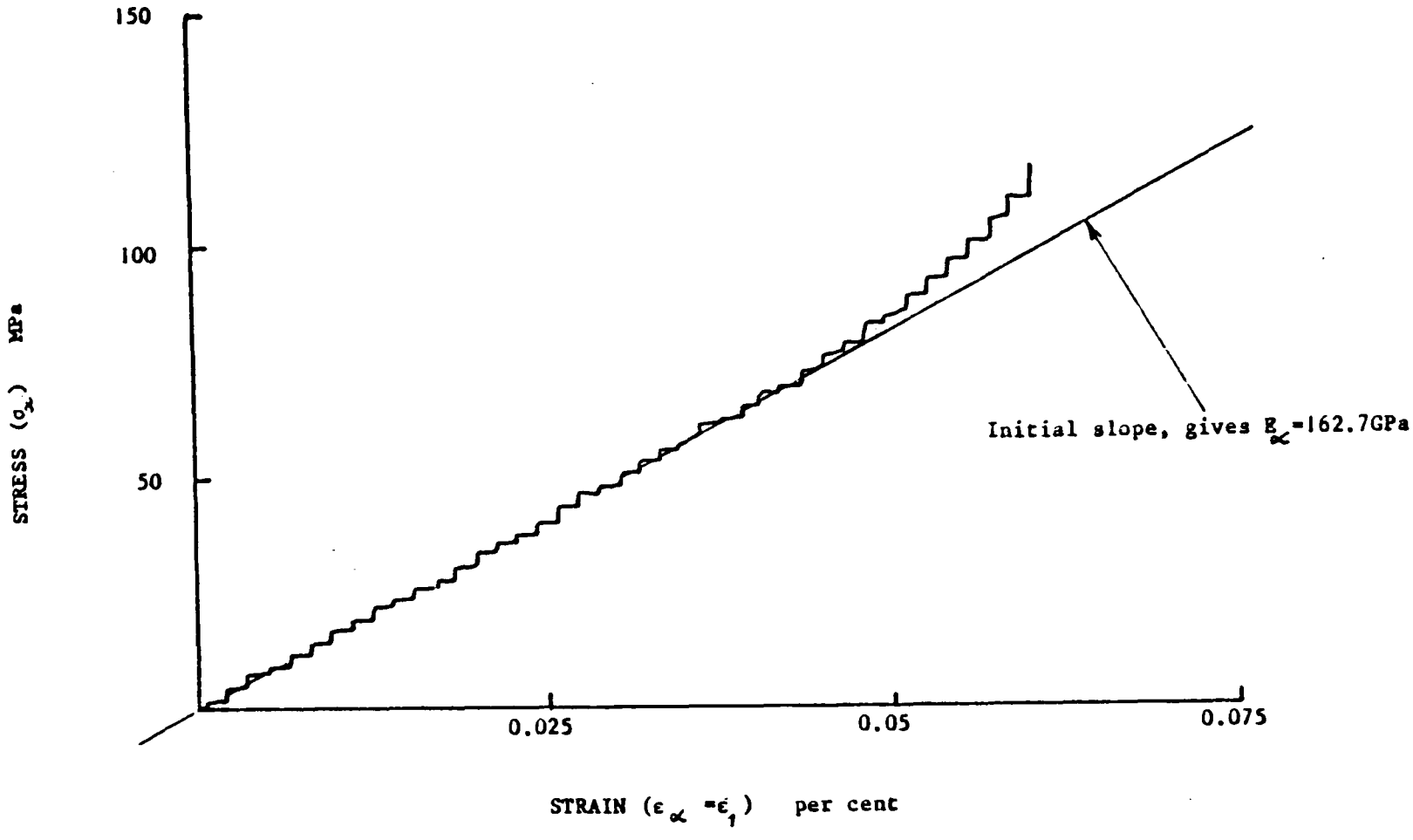

Fig.4.32 QUASI-STATIC FAILURE TEST ON AN ALL-CARBON PARALLEL-SIDED COUPON LOADED IN THE 45° DIRECTION

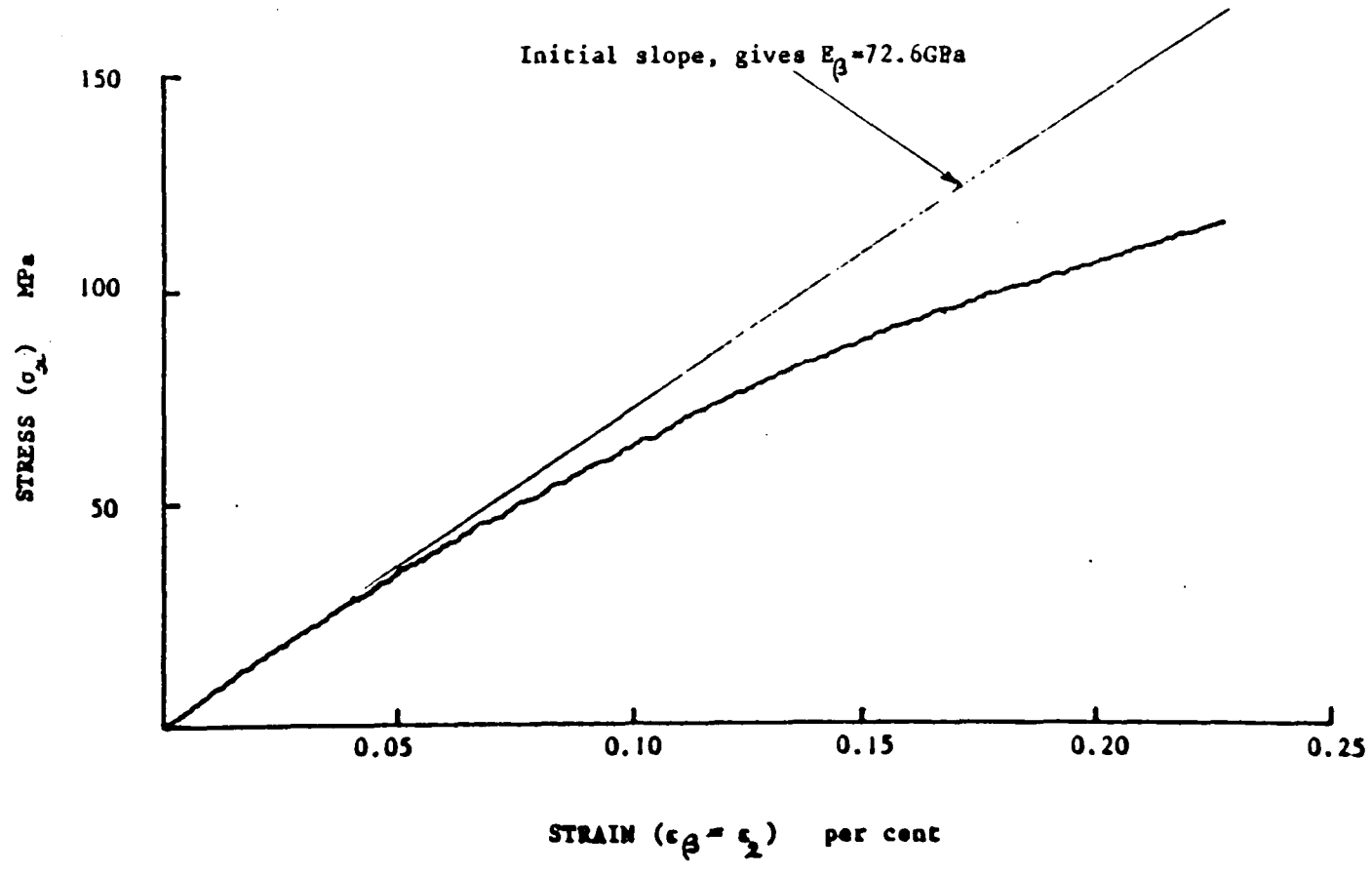

Table 4.4 Mean Quasi-Static Elastic Constants for Glass and Carbon Plies.

Material	E_L (GPa)	E_T (GPa)	E_x (GPa)	ν_{LT}	ν_{TL}	ν_{TL}^{*}	G_{LT}^{**} (GPa)
All-glass	16.6	13.75	5.65	0.165	0.138	0.137	1.69
All-carbon	45.3	43.3	9.86	0.139	0.089	0.133	2.73

where ν_{TL}^{*} is determined from equation (3.22) and G_{LT}^{**} from equation (2.5).

Using the mean values for E_L, E_T and ν_{LT}, the derived values for ν_{TL}^{*} and G_{LT}^{**} and assuming standard expressions for components of stiffness matrix as given by equation (3.21) the following stiffness matrices are obtained for the all-glass and the all-carbon plies under quasi-static loading:-

$$\left[Q_{ij} \right]_a = \left[Q_{ij} \right]_{CFRP} = \begin{bmatrix} 46.2 & 6.1 & 0 \\ 6.1 & 44.1 & 0 \\ 0 & 0 & 2.7 \end{bmatrix} \text{GPa} \qquad (4.3)$$

$$\left[Q_{ij} \right]_b = \left[Q_{ij} \right]_{GFRP} = \begin{bmatrix} 17.0 & 2.3 & 0 \\ 2.3 & 14.1 & 0 \\ 0 & 0 & 1.6 \end{bmatrix} \text{GPa} \qquad (4.4)$$

Impact tests.

Similar tests as for quasi-static elastic property measurements were performed at the impact rate. Here, however, the procedure of loading and reloading test-pieces within the elastic range was not feasible. Results of three tests on all-carbon parallel-sided coupons loaded in the weft direction are presented in Fig. 4.33. The measured modulus $E_T = 60.9 \pm 6.2$

GPa is significantly greater than the value obtained in standard tensile tests on similar material, see Table 4.1. Computer plots of warp (ε_1) versus weft (ε_2) strains in the tests of Fig. 4.33 are given in Fig. 4.34. The scatter in the measured Poisson's ratio, $\nu_{TL} = 0.079 \pm 0.015$, is appreciable. Results obtained from similar tests on all-carbon specimens cut with the loading axis in the warp direction and the all-glass laminate loaded in the warp or the weft directions showed a similar trend, the measured moduli being substantially greater than the corresponding values obtained in tests on waisted specimens, although the scatter in the measured Poisson's ratios of the all-glass composite was rather small. These results are presented in Table 4.5 where the elastic moduli obtained in standard tensile tests are included in parenthesis for comparison.

Table 4.5 Elastic Properties of the All-glass and All-carbon Composites under Tensile Impact.

Material	Orientation	E_L (GPa)	E_T (GPa)	ν_{LT}	ν_{TL}	ν^*_{TL}
All-glass	Warp	28.7 ± 1.2 (24.0 ± 1.2)	——	0.176 ± .007 (-)	——	0.125
	Weft	——	23.6 ± 0.6 (17.1 ± 1.7)	——	0.155 ± .005 (-)	
All-carbon	Warp	55.9 ± 2.6 (48.7 ± 7.0	——	0.061 ± .004 (-)	——	0.061
	Weft	——	60.9 ± 6.2 (49.0 ± 4.0)	——	0.079 ± .015 (-)	

* Based on figures in parenthesis, the measured ν_{LT} and the relationship

$$\nu_{TL} = \nu_{LT} E_T / E_L$$

Figures in parenthesis were obtained from standard tensile tests.

Fig.4.33 STRESS v. LONGITUDINAL STRAIN FOR IMPACT TEST ON A PARALLEL-SIDED ALL-CARBON SPECIMEN LOADED IN THE WEFT DIRECTION

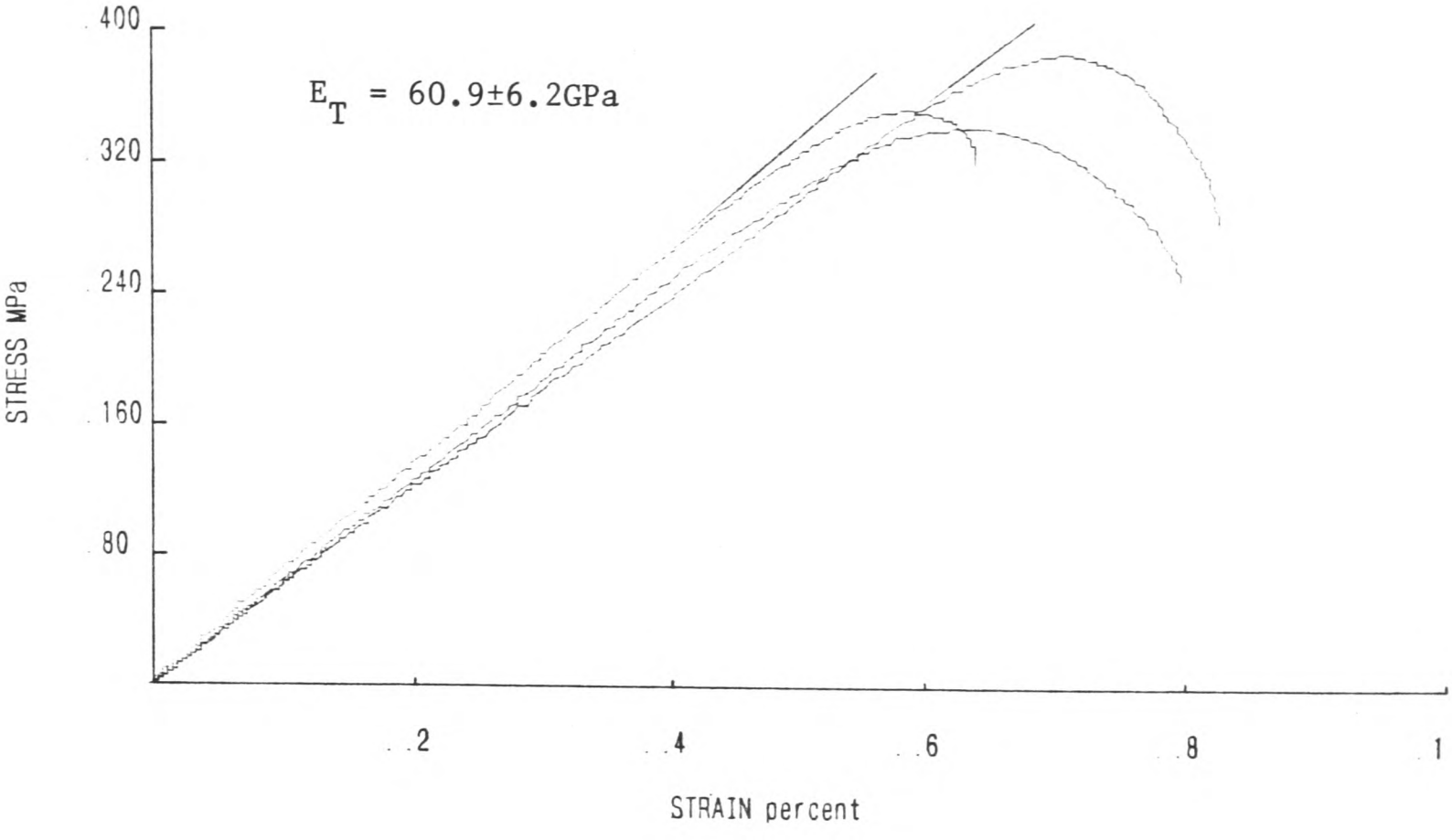

Fig.4.34 TRANSVERSE STRAIN v. LONGITUDINAL STRAIN FOR TEST OF Fig.4.33

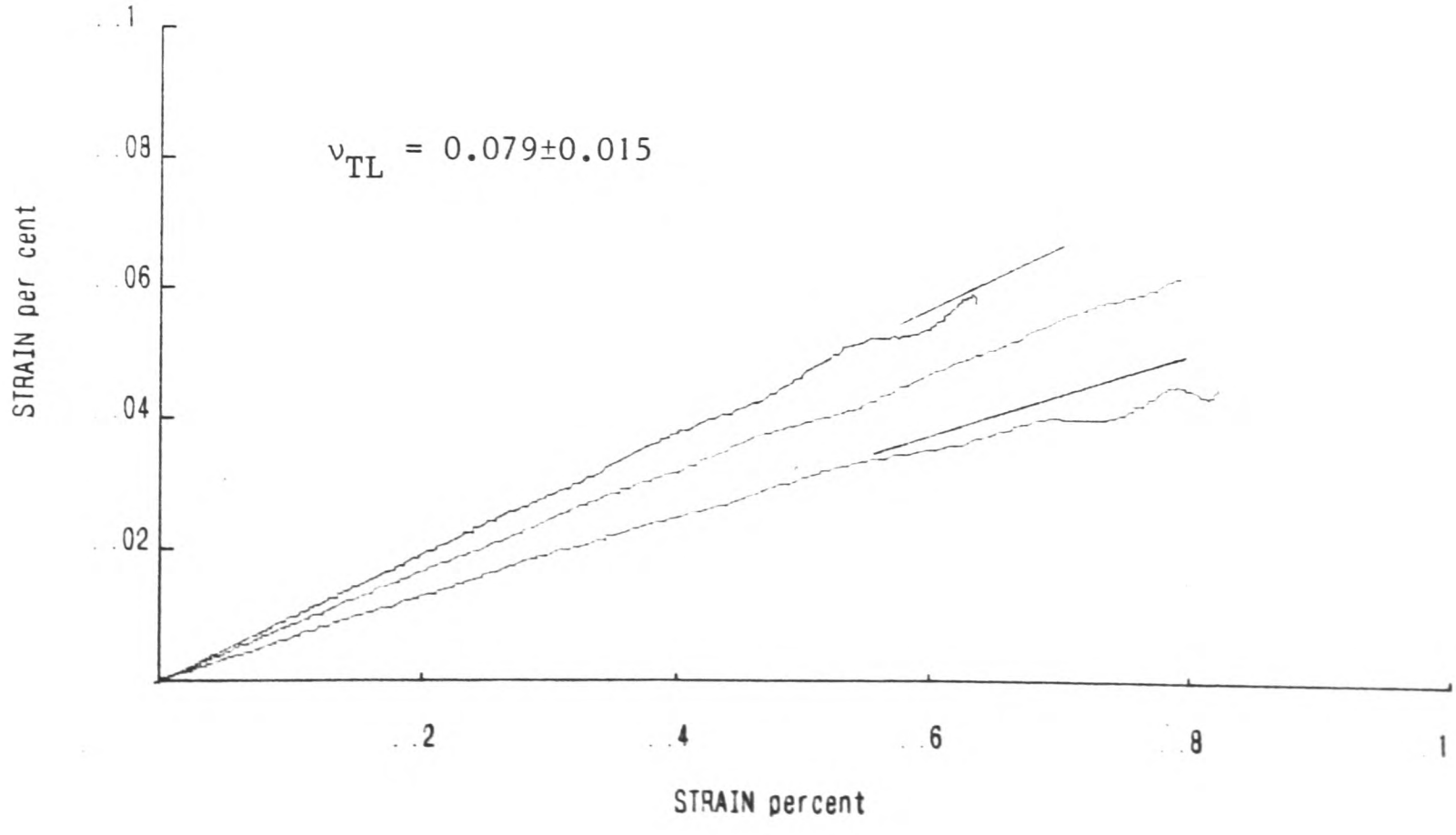

The disagreement between the observed elastic moduli arising from the difference in specimen design raises the question as to which of these are to be preferred in determining some components of the stiffness matrix for the all-glass or the all-carbon plies.

The requirement of predicting the properties of waisted hybrid composite specimens suggests that the elastic moduli as measured in standard tensile tests might be preferable even though the values derived from tests on parallel-sided coupons are more ~~in~~ consonant with the symmetry relation of equation (3.22), (within $\pm 3.5\%$ and $\pm 8.6\%$ for the all-glass and the all-carbon respectively) than are the results from standard tensile tests (within $\pm 10.6\%$ for the all-glass and ± 12.6 for the all-carbon plies).

In order to determine the in-plane shear moduli of the all-carbon and the all-glass laminates, parallel-sided coupons were again loaded at 45^{o} to both warp and weft directions. As yet, experimental data from these tests have only been partially processed and the results are not presented*. In fact, the in-plane shear modulus makes no contribution to the hybrid composite property predictions see equations (3.51) and (3.52) in section 3.4.1. The remaining components of the stiffness matrix for the all-carbon or the all-glass laminae are obtained by substituting the appropriate values of elastic moduli derived from standard tensile tests, the major Poisson's

---

* Data processing is now completed and the full two dimensional matrices are given in equations (4.3) and (4.4) for control materials.

ratio ν_{LT} and the minor Poisson's ratio ν^{*}_{TL} based on the symmetry hypothesis (Table 4.5) into the expressions in (3.21). Thus the stiffness matrices of the all-carbon and the all-glass plies under dynamic loading are respectively given by

$$\left[Q_{ij} \right]_a = \left[Q_{ij} \right]_{CFRP} = \begin{bmatrix} 48.9 & 3.0 & 0 \\ 3.0 & 49.2 & 0 \\ 0 & 0 & 4.0 \end{bmatrix} \text{GPa} \qquad (4.3)$$

$$\left[Q_{ij} \right]_b = \left[Q_{ij} \right]_{GFRP} = \begin{bmatrix} 24.5 & 3.1 & 0 \\ 3.1 & 17.5 & 0 \\ 0 & 0 & 3.8 \end{bmatrix} \text{GPa} \qquad (4.4)$$

4.3.2 Compressive Strength Tests.

The sole purpose of these tests was to determine the compressive strengths of the all-glass and the all-carbon laminates in both warp and weft directions as required by the Tsai-Wu criterion, see equation (3.53). Strain measurements were not made and no stress-strain curves are presented.

Quasi-static compression tests

Three tests on each material and in each of the two directions of reinforcement using standard (waisted) specimens were conducted. The compressive strength as derived from the load cell strain gauge output signal, was, for the all-carbon material slightly less than the tensile strength. In contrast the compressive strength of the all-glass laminate in either of the two orthogonal directions was about 40% of its strength in

tension. This observation is in line with that reported in the literature [4].

A comparison of the quasi-static tensile and compressive strengths of the all carbon and the all-glass laminates is given in Table 4.6.

Table 4.6 Comparison of Tensile and Compressive Strengths in Warp and Weft Directions for All-Glass and All-Carbon Specimens (Quasi-static tests).

Material	Orientation	Tensile Strength (MPa)	Compressive Strength (MPa)
All-glass	Warp Weft	328 ± 21 262 ± 18	128 ± 15 111 ± 5
All-carbon	Warp Weft	428 ± 19 416 ± 16	369 ± 17 394 ± 26

Impact Compression Tests

Tests were performed on similar sets of specimens as in the quasi-static compression tests at a projectile velocity of ~20m/s. In all tests, the output bar strain gauge signal from which the compressive strength was estimated showed a discernible peak load (see Fig. 4.35). The experimental scatter (see Table 4.7) was in general rather small and the difference between tensile and compressive strengths of the all-glass specimens is not as pronounced as at quasi-static loading rates. The all-carbon laminate especially in the weft direction exhibited a greater strength than in impact tension.

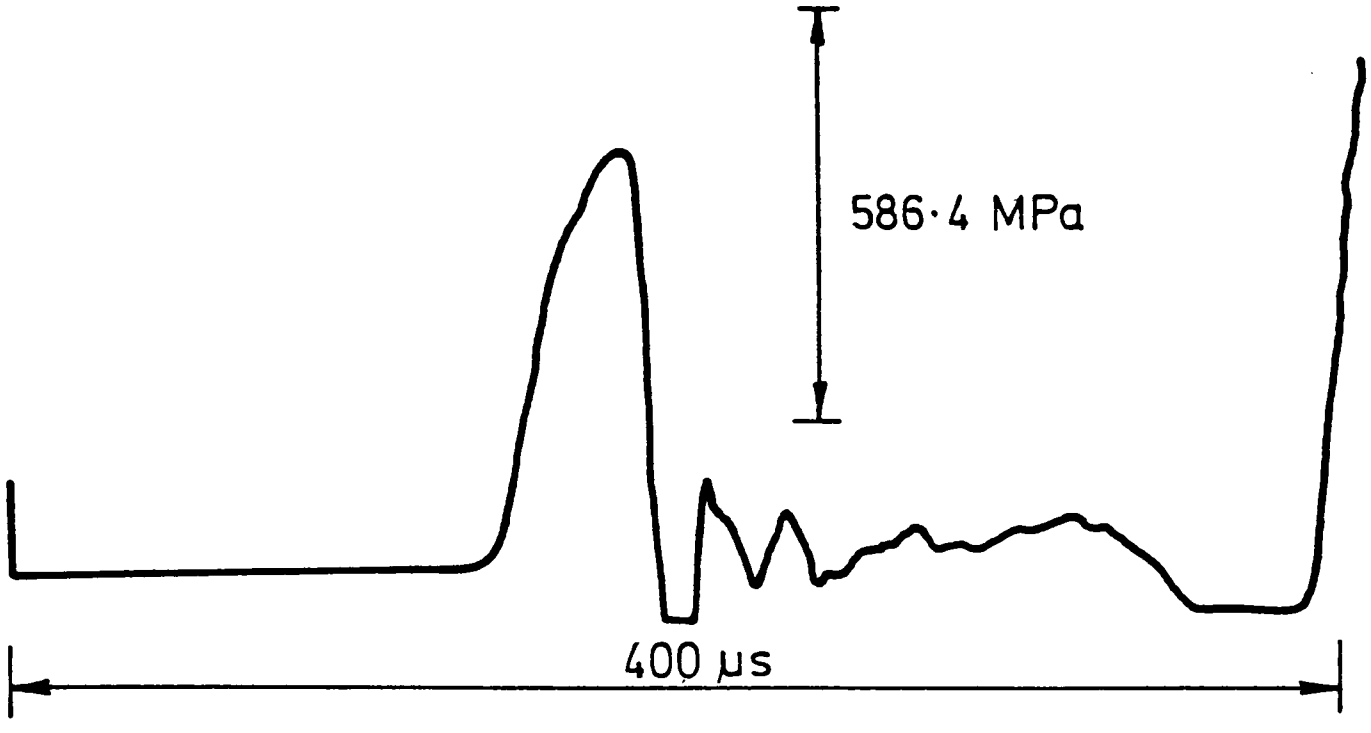

Fig. 4·35 Output bar strain-gauge signal for a typical impact compression test on an all-carbon specimen loaded in the warp direction

Table 4.7 Comparison of Tensile and Compressive Strengths in Warp and Weft Directions for All-Glass and All-Carbon Specimens (Impact Tests)

Material	Orientation	Tensile Strength (MPa)	Compressive Strength (MPa)
All-glass	Warp Weft	494 ± 6 427 ± 16	405 ± 4 385 ± 9
All-carbon	Warp Weft	562 ± 37 508 ± 9	572 ± 24 588 ± 11

A consideration of the results in Tables 4.6 and 4.7 reveals that the all-carbon and all-glass laminates are significantly more sensitive to strain rate in compression. In the all-glass specimens, for example, an increase of over 200% in compressive strength was observed in either the warp or the weft directions over six decades ($\sim 10^{-3}$/s to $\sim 10^{3}$/s); the corresponding increase in tensile strength was about 50 or 60%.

This observation supports the suggestion in section 1.7.4 that in uniaxial compression the rate sensitive resin matrix may be quite prominent.

4.4 Optical and SEM Studies of Fracture Surfaces

The mechanical response of a material is a reflection of the underlying micromechanisms controlling deformation. An understanding of the relation between the two is therefore essential for a judicious application of the material especially in the design of structures for impact resistance.

Various techniques are available for studying the micromechanisms of fracture in composite materials. Among the most common in current use are C-scan [49], X-ray radiography [141], acoustic emission [142-144]

fractography [145-148] and deplying of laminated composite specimens. But fractography is particularly suited to impact work [150,151]. In the present investigation an attempt was made to study the damage associated with failure in the various types of specimen at impact loading rates by optical and scanning electron microscopy. Some statically-loaded specimens were also examined for comparison. A Carl Zeiss Ultraphot IIC optical microscope was used for low magnification examination of fracture surfaces while at higher magnifications the JSM 35X scanning electron microscope was utilized. To reduce charging effects all specimens were coated with an Au/Pd alloy before being examined in the SEM.

Macrographs of the five types of specimen tested at the impact rate are shown in Figs. 4.36a to 4.36e from all-carbon to all-glass in a descending order of weight fraction of carbon from left to right. The comparison is partially obscured by the much coarser tow size and weave geometry in the carbon, in contrast to the glass, reinforcing mats. Nevertheless three modes of failure may be identified. A brittle failure in the all-carbon with fracture on planes perpendicular to the load and pull-out of fibre tows to about one half wavelength.

A much less planar fracture surface in the all-glass specimen with damage and fibre pull-out extending, relative to the wavelength of the weave, over a zone an order of magnitude greater than in the all-carbon composite, with separation between the orthogonally-aligned rovings in the fracture region playing a much greater part in the overall failure process. An intermediate response is exhibited by the three hybrid specimens. In

type 2a and type 1 specimens for example, separation of the othogonally-aligned rovings in the outermost glass mats and damage extending over

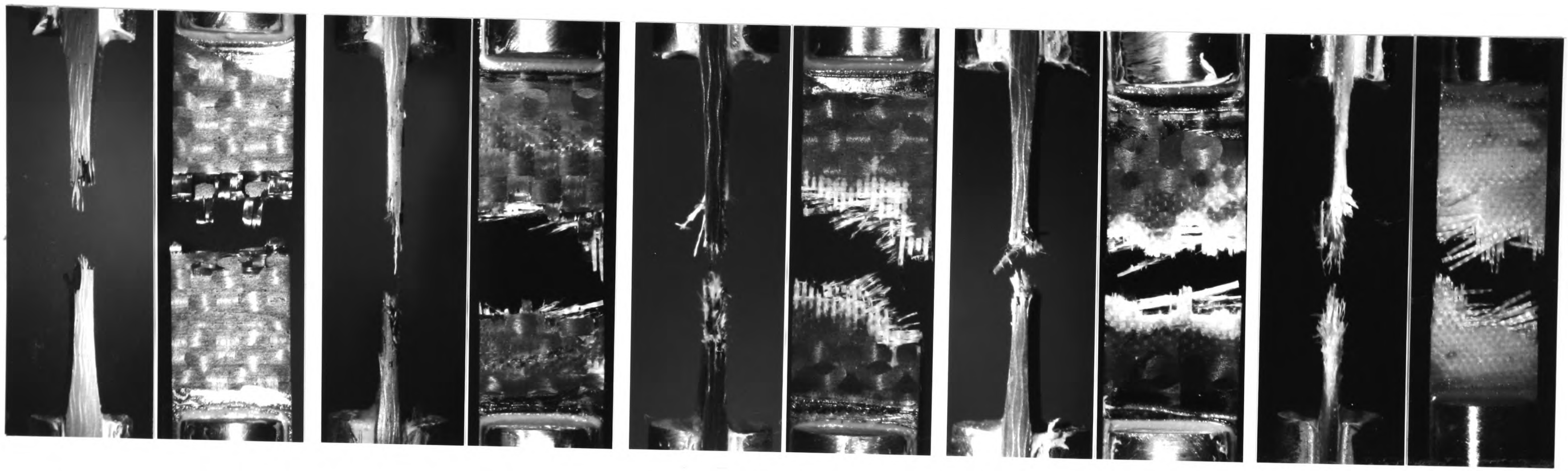

a) All-Carbon b) Carbon/Glass 2b c) Carbon/Glass Type 2a d) Carbon/Glass Type 1 e) All-Glass

Fig 4.36 EFFECT OF HYBRID COMPOSITION ON FAILURE MODE (x2)

(Impact tests)

several wavelengths of the glass weave may be observed. Although the fracture behaviour of the type 2b specimen is similar to that of the other two hybrid composites the extent of damage in the glass reinforced layers is more seriously limited by the adjoining carbon reinforced plies.

It is apparent that the clear distinction in mechanical response between the all-carbon and the three hybrid composites, on the one hand, and the all-glass composites, on the other, see Fig. 4.11, is not reflected in the fracture appearance where the clearest distinction is between the all-carbon composite on the one hand and the all-glass and the three hybrid composites on the other. Thus, while a carbon weight fraction of 0.4 or more leads to a near linear-elastic stress-strain response, the fine weave glass reinforcement dominates the fracture appearance for carbon weight fractions up to at least 0.6.

Macrographs of the various specimens obtained from quasi-static tests appear in Figs. 4.37a to 4.37e. When compared with those of Fig. 4.36 it is seen that the only significant difference in fracture appearance arising from the change in the rate of deformation occurred in the all-glass specimen which at the impact rate sustained much more extensive damage prior to failure and incidentally the greatest fracture strain in all tests.

As a first step to describing the fracture process in more detail the all-glass, all-carbon and type 1 hybrid specimens were examined in the SEM at a magnification of X20 (see Figs. 4.38, 4.39 and 4.40). Failure in the all-carbon specimen is characterised by a relatively flat fracture surface with only short pull-out lengths for the carbon fibre tows, see Fig. 4.38,

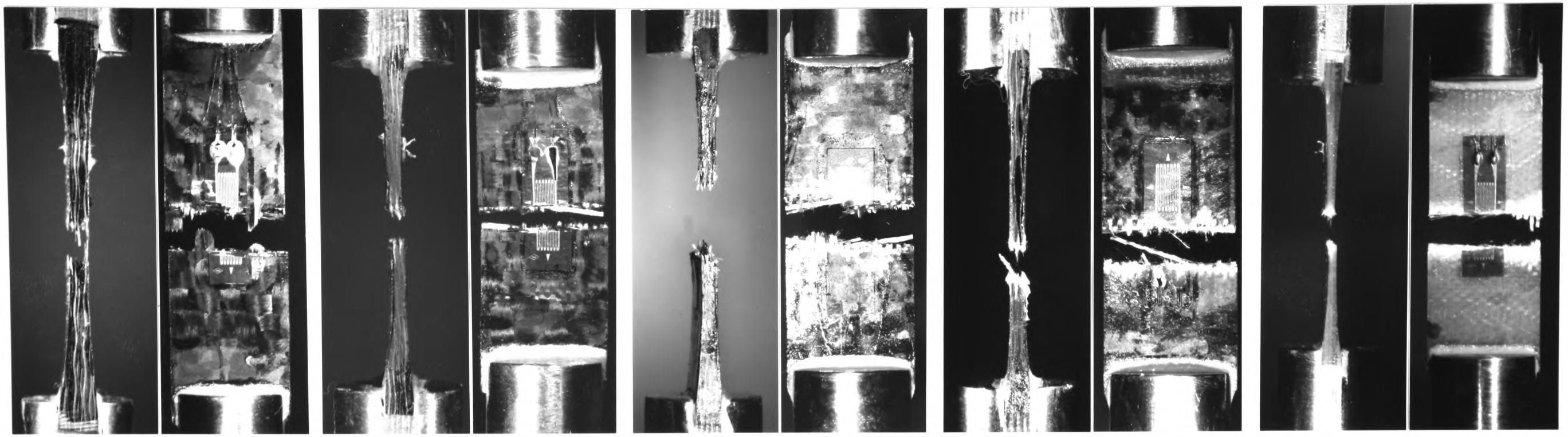

a) All-Carbon b) Carbon/Glass Type 2b c) Carbon/Glass Type 2a d) Carbon/Glass Type 1 e) All-Glass

Fig.4.37 EFFECT OF HYBRID COMPOSITION ON FAILURE MODE (x2)
(Quasi-static tests)

Fig.4.38 SCANNING ELECTRON MICROGRAPH OF FRACTURE REGION OF ALL-CARBON SPECIMEN (x20)

Approximate width of single carbon fibre tow

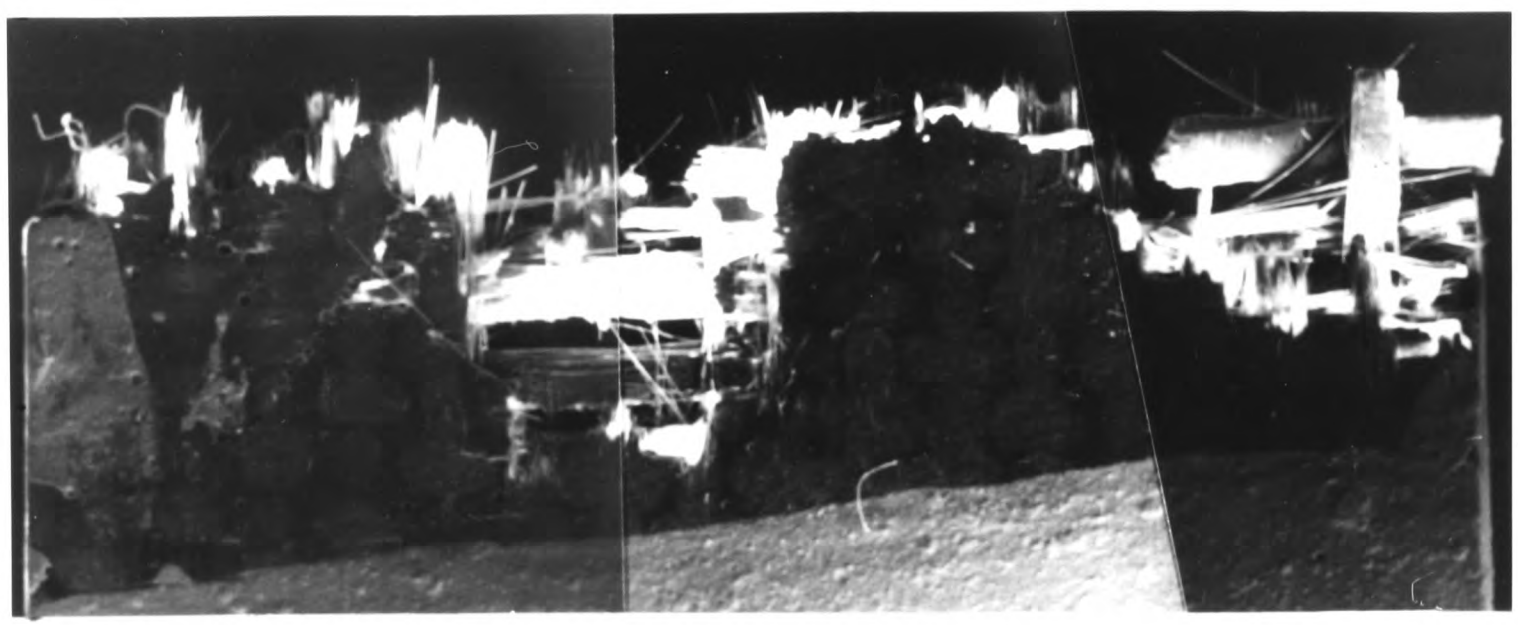

Approximately one half-wavelength of carbon fibre roving

Fig.4.39 SCANNING ELECTRON MICROGRAPH OF FARCTURE REGION OF TYPE 1 CARBON/GLASS HYBRID (x20)

Fig.4.40 SCANNING ELECTRON MICROGRAPH OF FRACTURE REGION OF ALL-GLASS SPECIMEN (x20)

but with quite extensive transverse cracking in a direction perpendicular to the applied load. In contrast, delamination and fibre pull-out is very marked in the failure of the all-glass specimen, see Fig. 4.40, with many transverse fibre tows involved. Delamination and fibre pull-out is also apparent in the glass reinforced plies of the hybrid specimen. Bearing in mind, however, that in type 1 hybrid the outermost two plies on both sides of the central parallel gauge section are glass reinforced, the damage in these regions apparent in Fig. 4.39 is much more limited than in the all-glass specimen of Fig. 4.40. The fracture surface is more clearly defined than in the all-glass specimen and where there is significant damage in the glass plies away from the fracture surface it appears to be limited to a region determined by failure in the carbon tows.

Representative features of the micrographs in Figs. 4.38, 4.39 and 4.40 were further examined in the SEM at higher magnifications. A region of fibre pull-out in the all-carbon specimen is shown in Fig. 4.41 at a magnification of X200. Both the broken ends of the pulled-out fibres and traces in the resin of regions from which fibres have pulled-out are readily visible. The pulled out lengths are short, indicative of a high interfacial shear strength. A micrograph of the pulled-out region of a similar specimen tested to failure at a quasi-static strain rate is included for comparison, see Fig. 4.42. As in Fig. 4.41, the magnification is X200 and the pull-out lengths are of the same magnitude as observed in Fig. 4.41 suggesting that the interfacial shear strength of the woven carbon/epoxy composite is insensitive to strain rate. This observation is in agreement with previous observations [64]. More scanning electron micrographs of typical failure modes in the impact loaded all-carbon specimen are given in Figs. 4.43 and

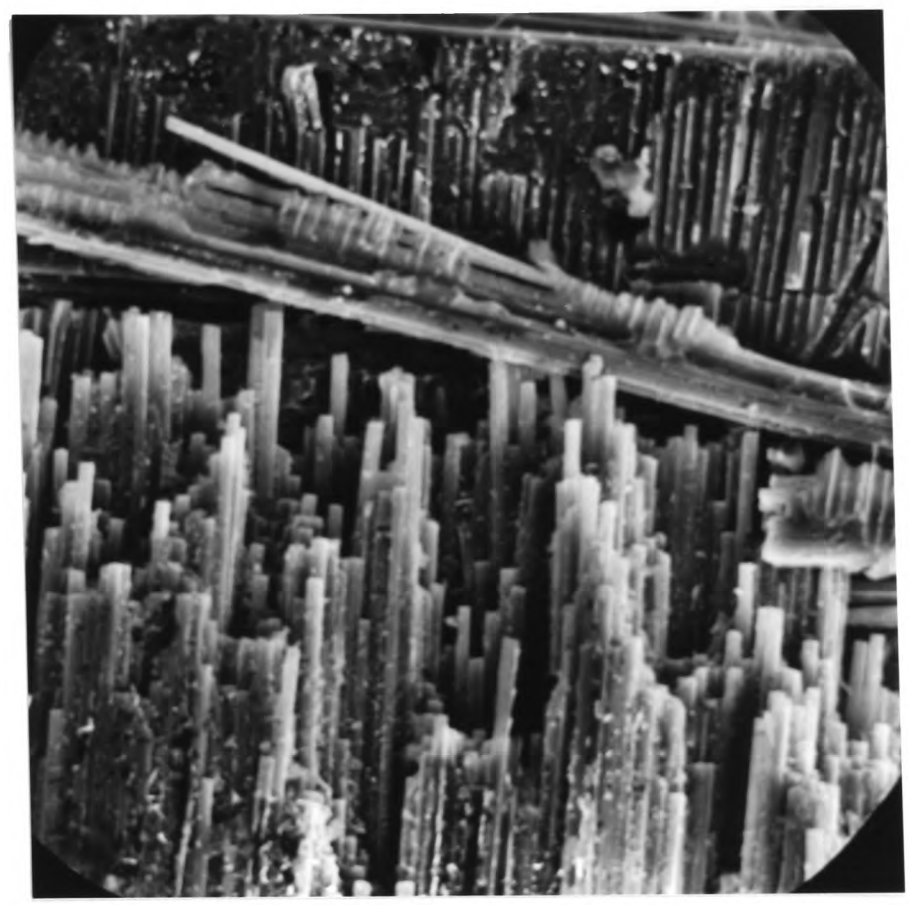

Fig.4.41 MATRIX CRACKING AND LIMITED FIBRE PULL-OUT IN AN IMPACT LOADED ALL-CARBON SPECIMEN (x200)

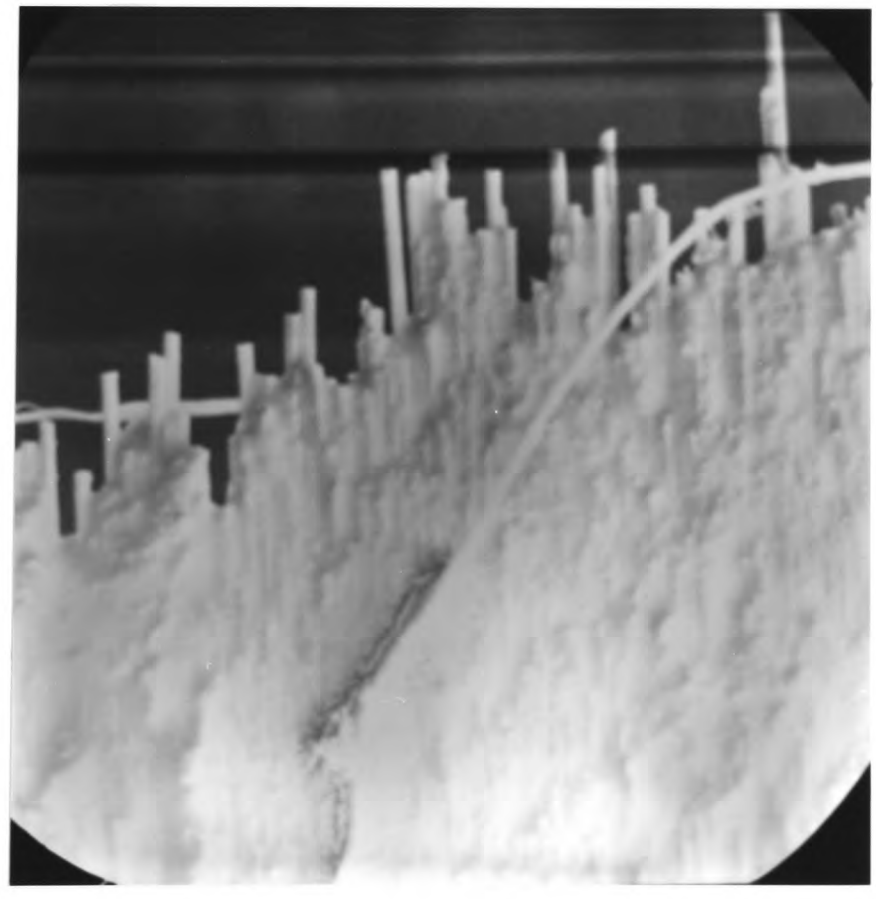

Fig.4.42 QUASI-STATIC FRACTURE APPEARANCE IN AN ALL-CARBON SPECIMEN (x200)

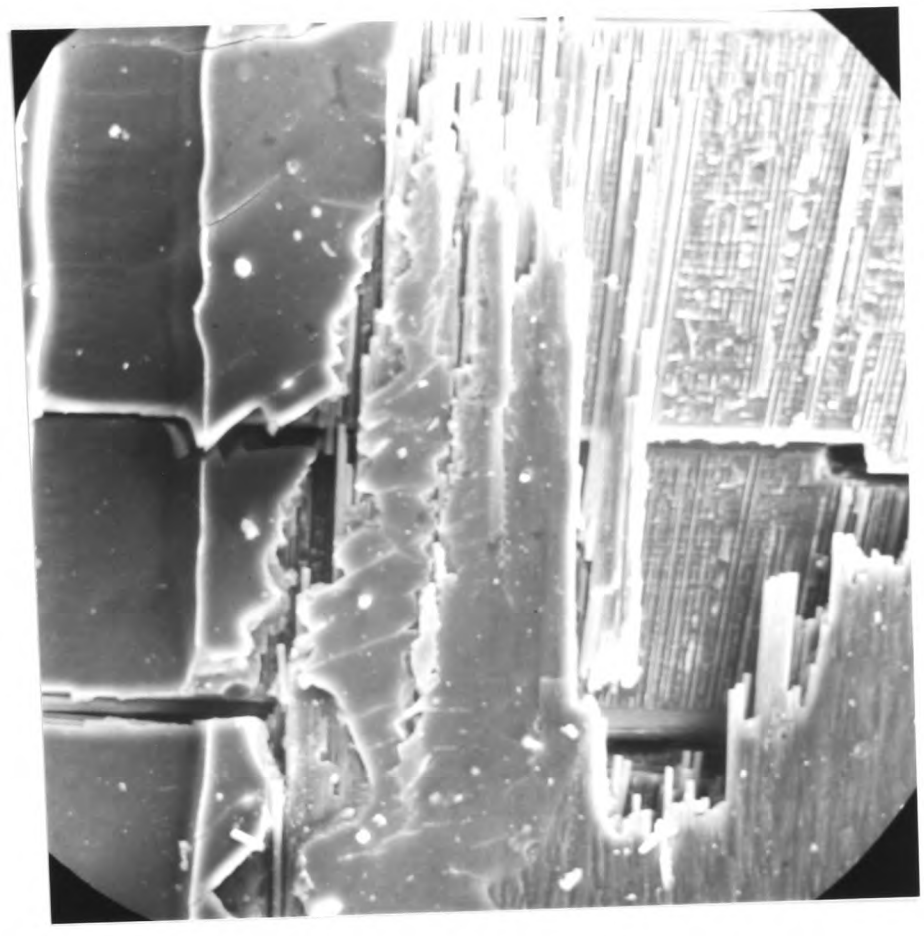

Fig.4.43 TRANSVERSE CRACKING AND CRACK DEFLECTION IN AN ALL-CARBON SPECIMEN (x100)

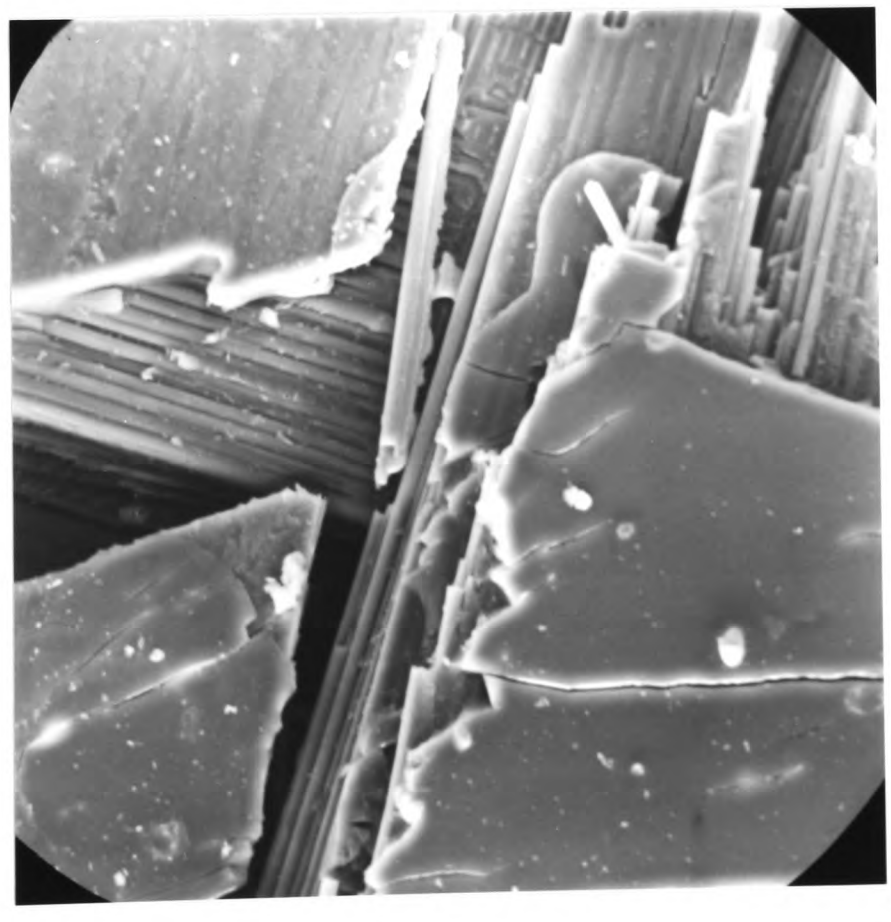

Fig.4.44 DELAMINATION AND FIBRE FRACTURE IN AN ALL-CARBON SPECIMEN (x200)

4.44. Fig. 4.43 at a magnification of X100 shows matrix cracks that are normal to the direction of loading. These cracks are deflected parallel to the axially-aligned fibre tows at the resin/reinforcement interface but only over a short distance, fracture across the fibre tows being closely related to the cracks in the resin. This is also clearly apparent at X200, see Fig. 4.44, where in addition delamination around orthogonally-aligned rovings may be observed. The occurrence of delamination within the resin rather than at the reinforcement/matrix interface, again signifies a strong interlaminar shear strength. At the same magnification as in Fig. 4.44 (x200) the all-glass specimen shows a very different behaviour, see Fig. 4.45, with extensive disintegration of the resin leaving long lengths of unbroken fibres in both axially-aligned and the orthogonal directions and with no clear fracture path. Extensive, evenly-spaced cracks normal to the direction of loading associated with what might be delamination, see Fig. 4.46, was a feature of the all-glass specimens. The micrograph was taken at a magnification of X500 and it is clear that delamination in this case was by failure of the reinforcement/matrix interface. No comparable features were observed in similar specimens tested at the quasi-static loading rate.

When individual carbon/glass hybrid specimens were observed in the SEM the failure characteristics of the all-carbon and the all-glass composites were reflected in the corresponding constituents but in a limited sense. Fig. 4.47 is a scanning electron micrograph of the damage zone in the glass reinforced outermost ply of the type 1 hybrid specimen of Fig. 4.39 at a magnification of X500. Several long bare fibres interspersed with fibre imprint and matrix cracks may be observed. A similar specimen tested in quasi-static tension, see Fig. 4.48, exhibited some similarity in fibre

Fig.4.45 LONG UNBROKEN DEBONDED FIBRES AND NO CLEAR FRACTURE PATH IN AN IMPACTED ALL-GLASS SPECIMEN

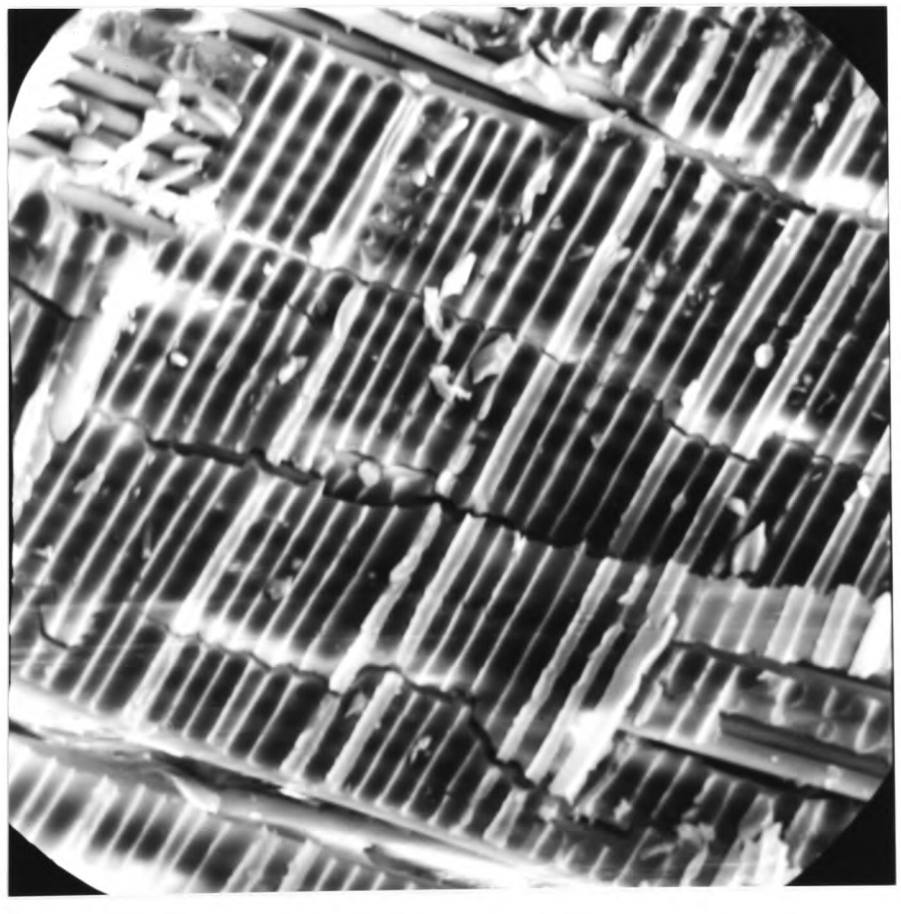

Fig.4.46 REGULARLY SPACED MATRIX CRACKS ASSOCIATED WITH DELAMINATION IN AN IMPACTED ALL-GLASS SPECIMEN

Fig.4.47 FIBRE/MATRIX DEBONDING AND MATRIX CRACKING IN THE GLASS PLIES OF AN IMPACTED TYPE 1 HYBRID SPECIMEN (x500)

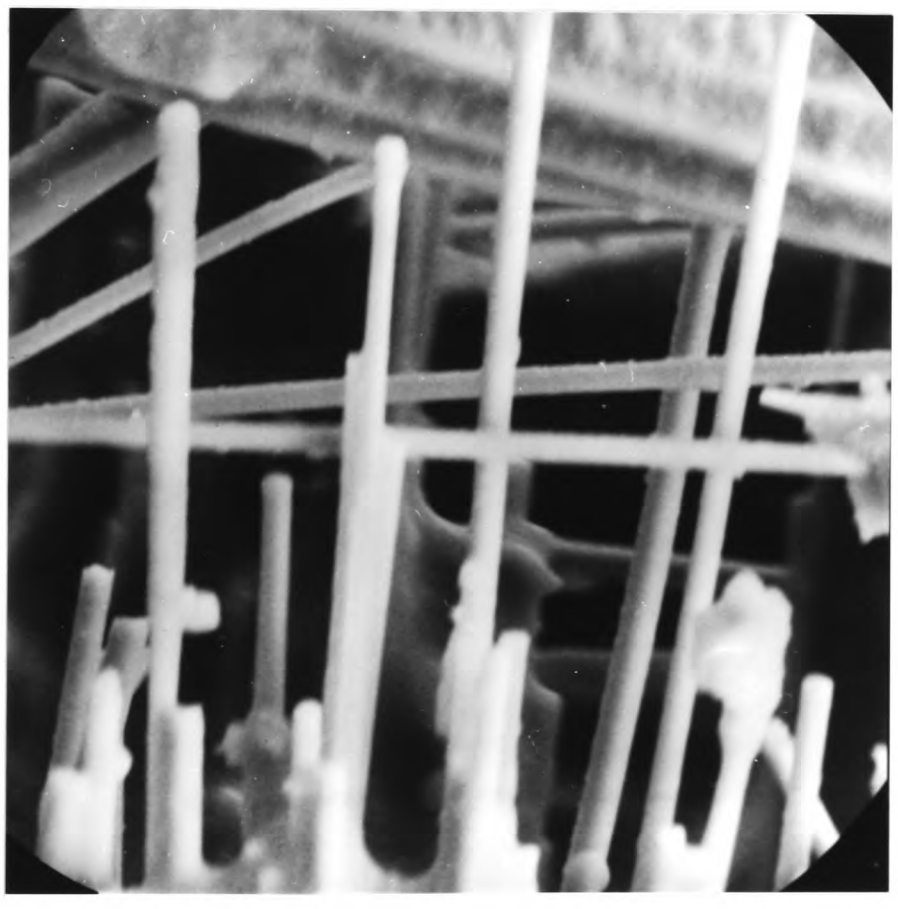

Fig.4.48 SIMILAR REGION TO Fig.4.47 UNDER QUASI-STATIC LOADING

structure with less damage to the resin matrix and no visible traces of regions from where fibres have been removed.

Some type 2b hybrid specimens tested at the impact rate were also studied in the SEM. Fig. 4.49a is part of the fracture surface of one such specimen as observed in the microscope at a magnification of X36. A schematic diagram of the micrograph is given in Fig. 4.49b, where the main features of the failure mode are identified. The outermost plies in the central parallel gauge section of the specimen are carbon reinforced and a contour of their fracture appearance is visible. Immediately below the carbon reinforced plies in the specimen are glass reinforced regions which can be seen to exhibit some of the features of a fractured all-glass material.

Micrographs of two locations indicated as 'D' and 'fibre pull-out' in the glass reinforced ply of the specimen, see Fig. 4.49b, are respectively given in Figs. 4.50 and 4.51 at a higher magnification of X200. These illustrate typical all-glass composite fracture appearance of long debonded unbroken fibres, fibre imprint and matrix cracks in the former and considerable fibre pull-out lengths in the latter. The point 'X', see Fig. 4.49b, within a crack in the outermost carbon reinforced ply is also shown in Fig. 4.52 at a magnification of X150. The characteristic all-carbon composite failure mechanism of limited fibre pull-out is visible.

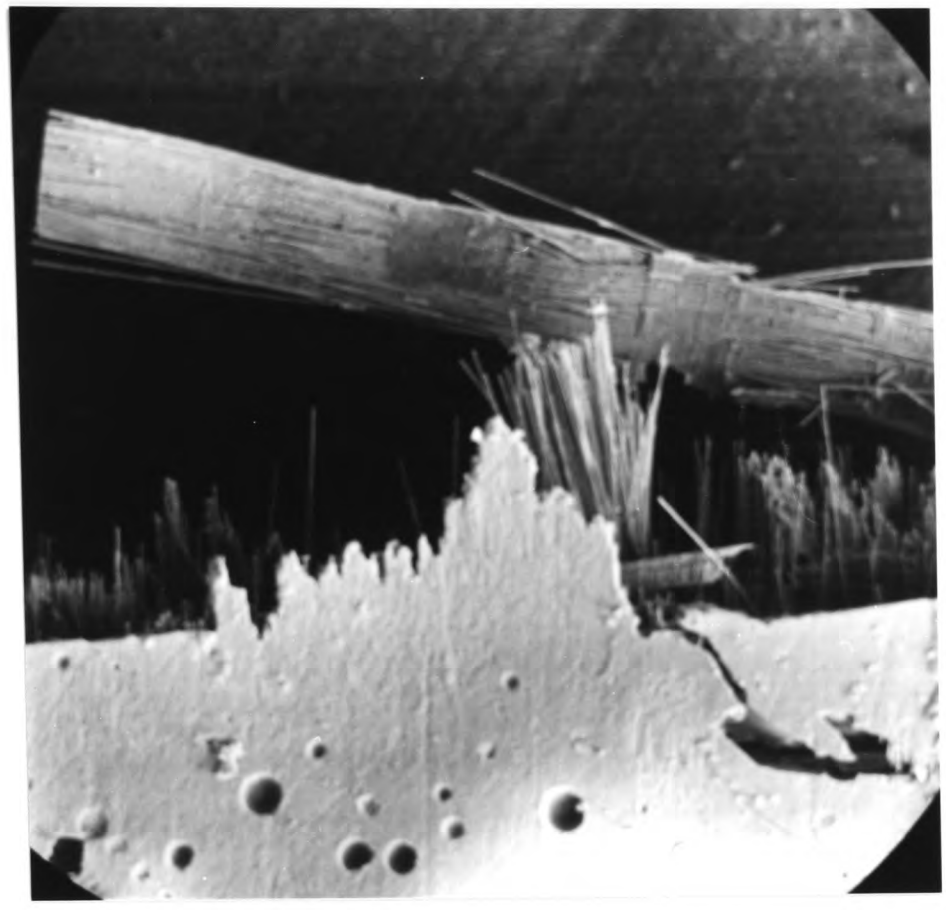

Fig.4.49a FRACTURE APPEARANCE OF IMPACTED TYPE 2b HYBRID SPECIMEN (x36)

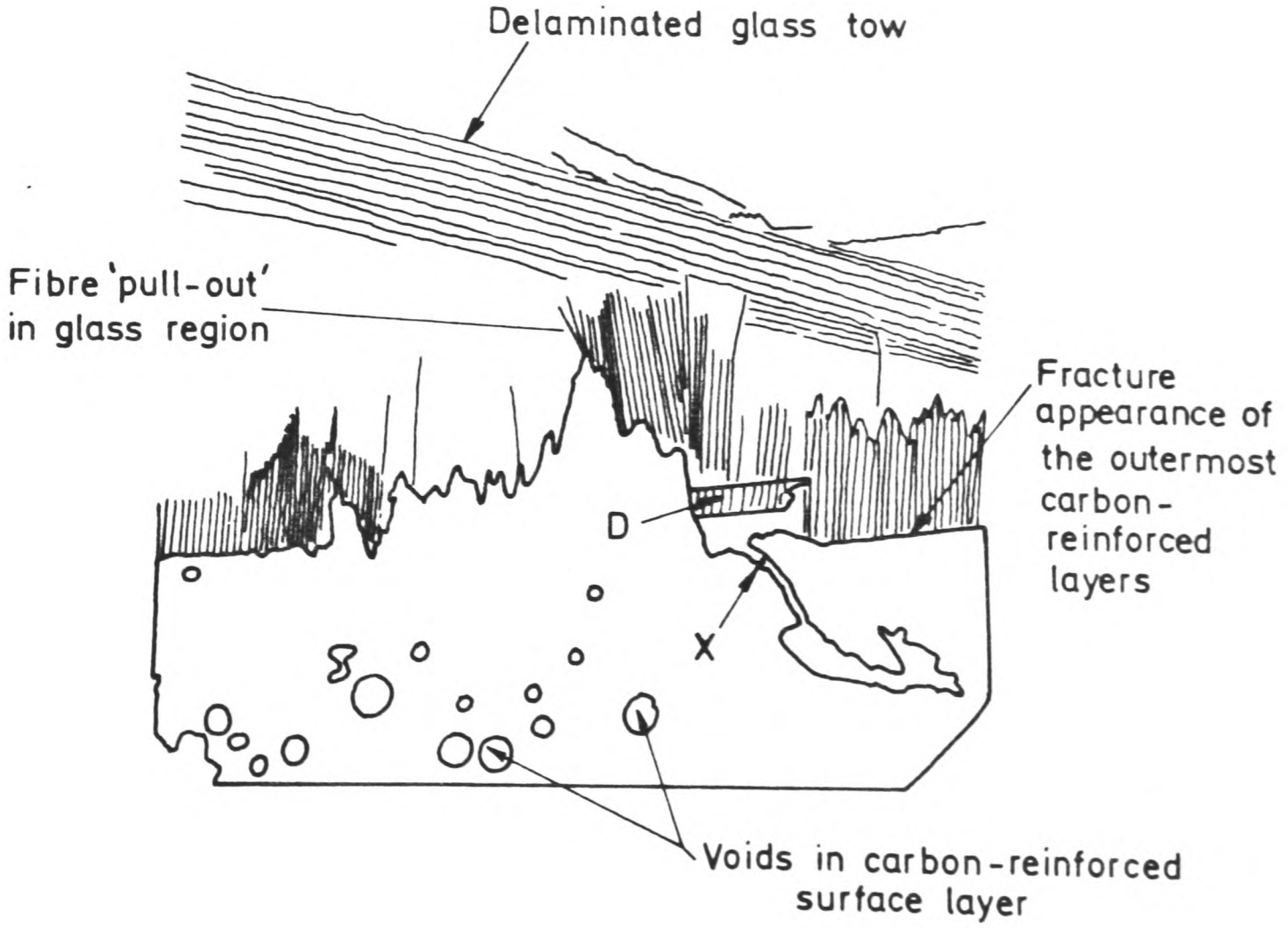

Fig.4.49b SCHEMATIC VIEW OF Fig.4.49a

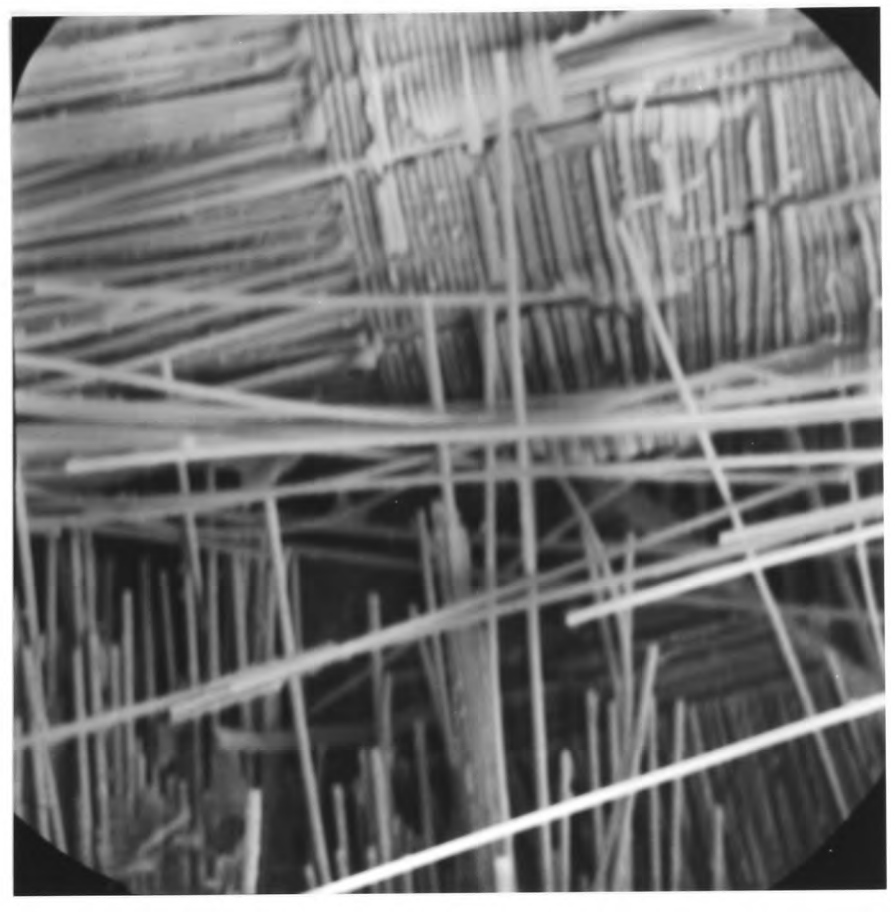

Fig.4.50 TYPICAL ALL-GLASS FRACTURE BEHAVIOUR IN GLASS PLIES OF TYPE 2b HYBRID AFTER IMPACT LOADING (x200)

Fig.4.51 EXTENSIVE FIBRE PULL-OUT IN GLASS PLIES OF IMPACTED TYPE 2b HYBRID SPECIMEN (x200)

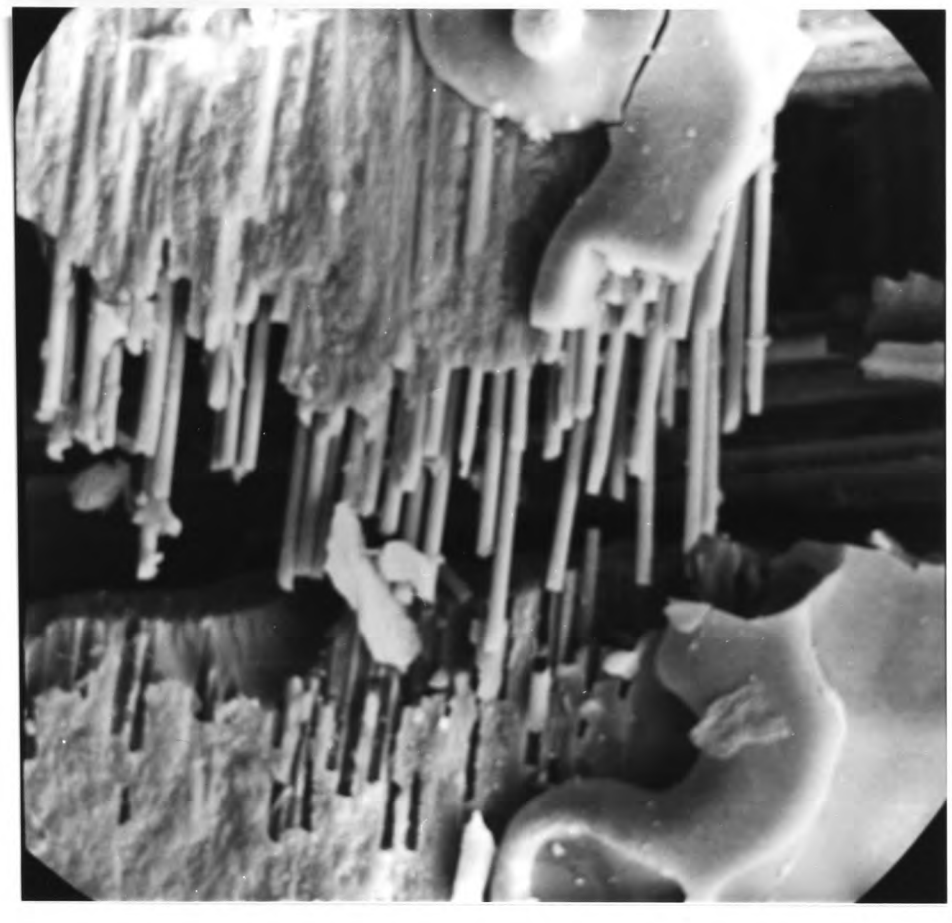

Fig.4.52 REGION 'X' OF Fig.4.49 AT HIGHER MAGNIFICATION x 150

CHAPTER 5

COMPARISON OF ANALYTICAL PREDICTIONS AND EXPERIMENTAL RESULTS

5.1 Introduction

In this chapter, the elastic and strength properties of the all-carbon and the all-glass specimens, see section 4.3, together with the Tsai-Wu criterion are used to predict the moduli and strengths, and hence the approximate stress-strain response of the hybrid composites. The predictions are then compared with the results in section 4.2. A discussion of the steps involved in the analysis may be found in section 3.4.2.

5.2 Prediction of Hybrid Moduli

5.2.1 Quasi-static Test Predictions

Using the matrices in equations (4.3) and (4.4), the various parameters β, μ, and λ, see equation (3.47), may be obtained from

$$\beta = (Q_{11})_b/(Q_{11})_a = 0.368$$

$$\mu = (Q_{22})_b/(Q_{22})_a = 0.320 \qquad (5.1)$$

$$\lambda = (Q_{12})_b/(Q_{12})_a = 0.377$$

For each of the three hybrid lay-ups the parameter α, see equation (3.47), and hence from equation (3.48) also the parameter ϕ, may be determined:

$$\begin{aligned} &\text{Hybrid type 1} \quad : \quad \alpha = 1.26 \; : \; \phi = 4104 \; (\text{GPa})^2 \\ &\text{Hybrid type 2a} \quad : \quad \alpha = 0.56 \; : \; \phi = 2843 \; (\text{GPa})^2 \\ &\text{Hybrid type 2b} \quad : \quad \alpha = 0.28 \; : \; \phi = 2404 \; (\text{GPa})^2 \end{aligned} \tag{5.2}$$

For uniaxial tensile loading in the warp direction the predicted values of the initial moduli are obtained from equation (3.56), giving values of 29.3 GPa, 35 GPa and 39.1 GPa, respectively, for type 1, type 2a and type 2b hybrids. A similar calculation for loading in the weft direction, for which α and ϕ remain unaltered but for which equation (3.56) now becomes

$$E^*_y = \phi / \{(1+\alpha)\ (1+\alpha\beta)(Q_{11})_a\} \tag{5.3}$$

gives reduced values for the predicted initial moduli of 26.9 GPa, 32.7 GPa and 36.8 GPa, respectively. As pointed out in section 4.2.3, for quasi-static tests on hybrid laminates the specimens were loaded in the warp direction and it is these results that are compared with the corresponding values predicted by laminate theory, see Table 5.1. A graphical comparison is also given in Fig. 5.1. It can be seen that the initial moduli as predicted by laminate theory are in excellent agreement with experimental measurements.

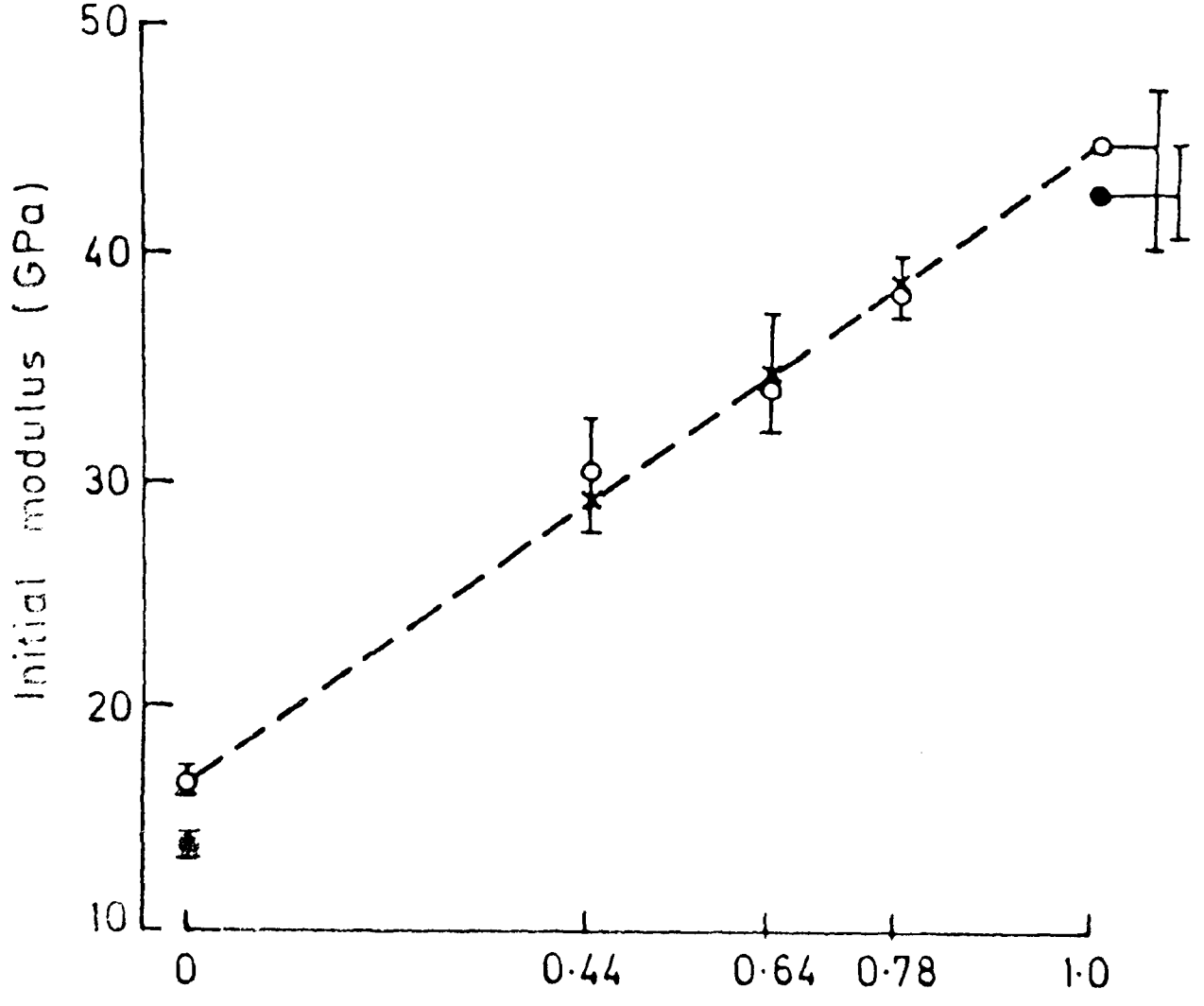

Fig. 5.1

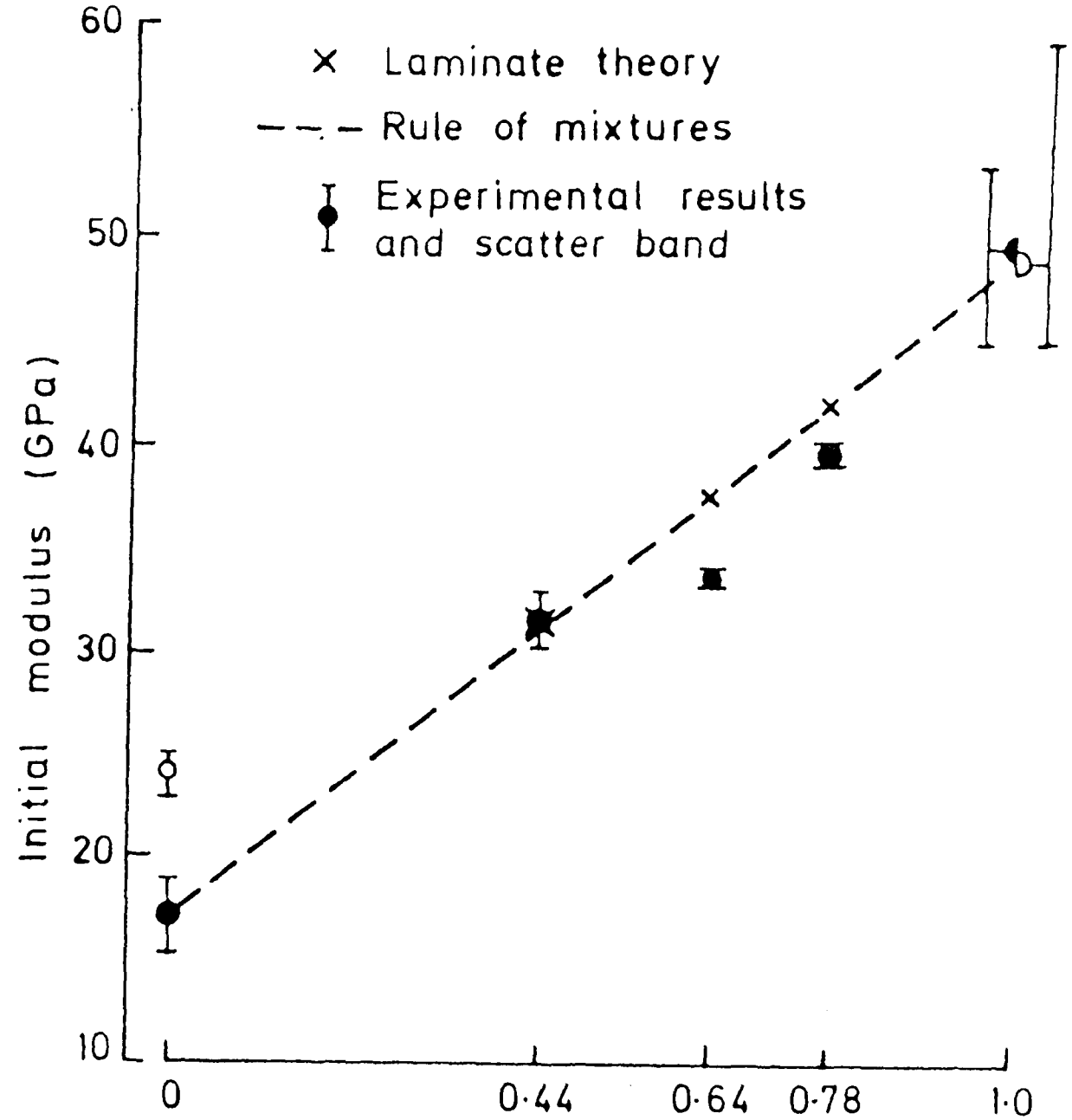

Fig. 5.2

Variation of initial modulus with volume fraction of carbon plies under quasi-static (Fig. 5.1) and impact (Fig. 5.2) loading conditions

Variation of initial modulus with volume fraction of carbon plies under quasi-

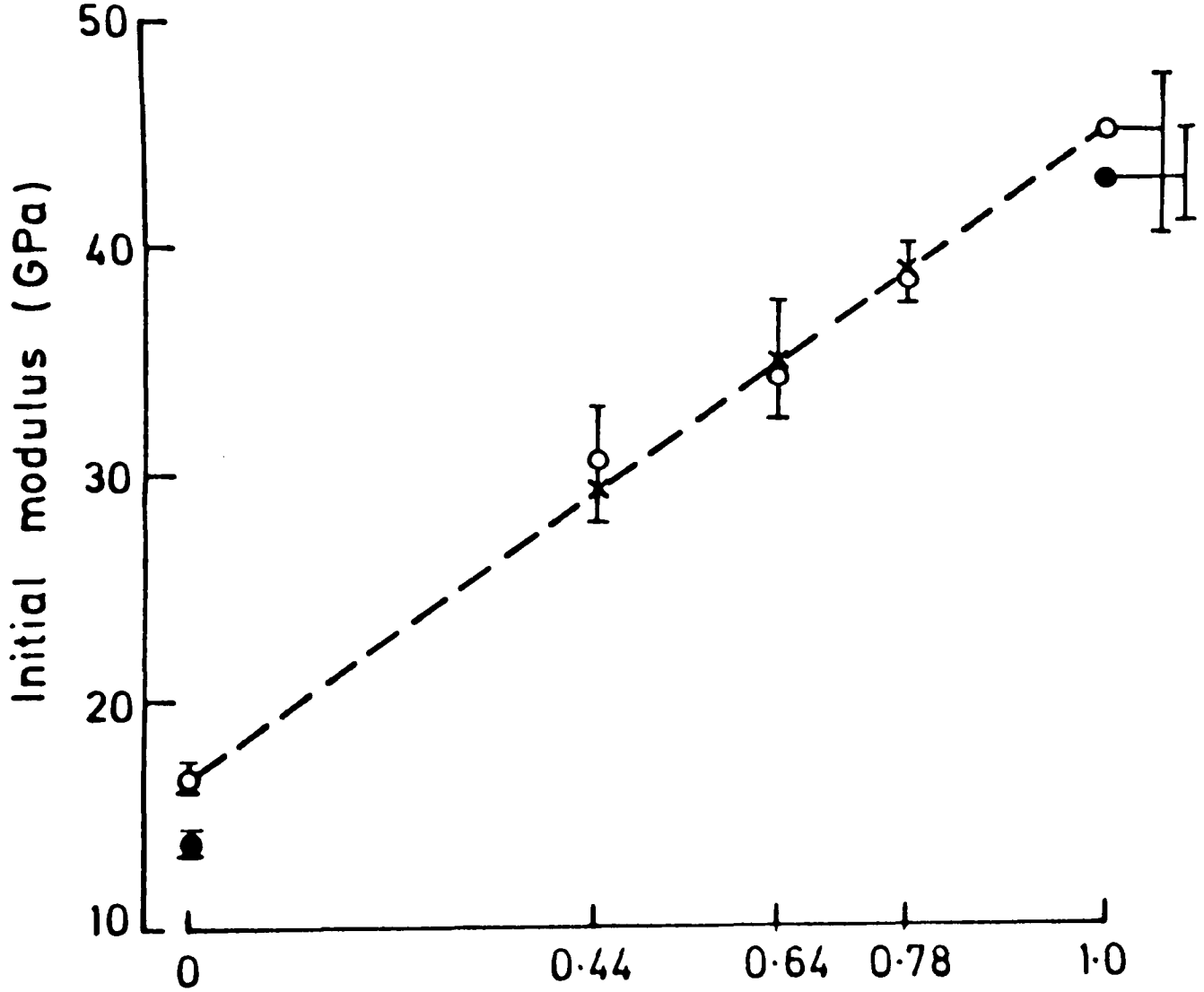

Fig. 5.1

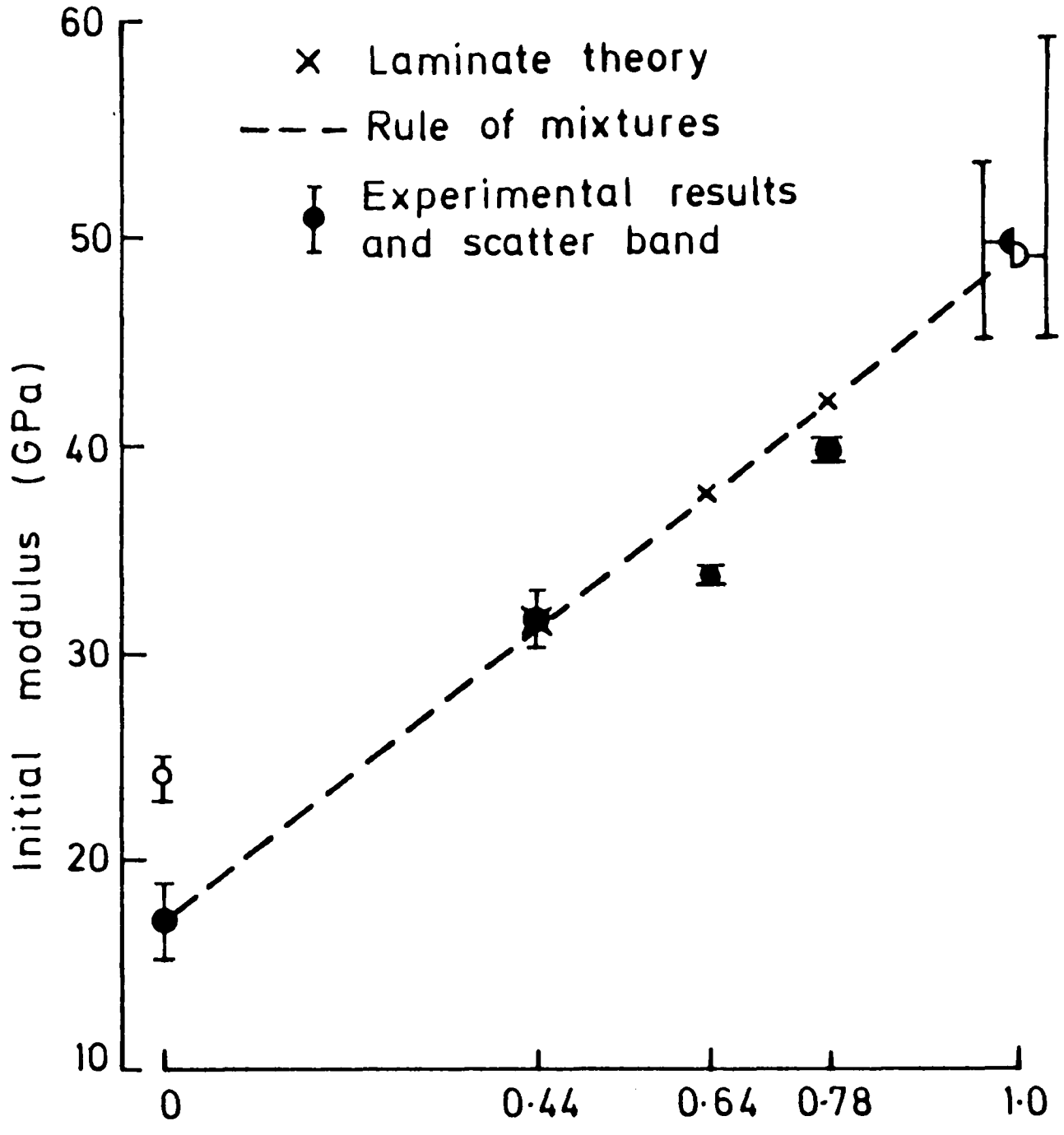

Fig. 5.2

Volume fraction of carbon reinforcing plies

Variation of initial modulus with volume fraction of carbon plies under quasi-static (Fig. 5.1) and impact (Fig. 5.2) loading conditions

Table 5.1 Comparison between Analytical Predictions and Experimentally Determined Values of Quasi-Static Hybrid Moduli (GPa) in the Warp Direction.

Hybrid	Analytical Prediction	Experimental Value
Type 1	29.3	30.1
Type 2a	35.0	34.4
Type 2b	39.1	38.9

5.2.2 Impact Test Predictions

Values of the various parameters β, μ and λ may be obtained from the impact stiffness matrices, see equations (4.5) and (4,6), and are:

$$\begin{aligned} \beta &= 0.501 \\ \mu &= 0.356 \\ \lambda &= 1.033 \end{aligned} \qquad (5.4)$$

For a given hybrid specimen the parameter α is the same at all rates of loading and for the three hybrid lay-ups are as given in equation (5.2). Substitution in equation (3.48) gives the various values of ϕ for these specimens:

$$\begin{aligned} &\text{Hybrid type 1} \quad : \alpha = 1.26 : \phi = 5638\ (\text{GPa})^2 \\ &\text{Hybrid type 2a} \quad : \alpha = 0.56 : \phi = 3673\ (\text{GPa})^2 \end{aligned} \qquad (5.5)$$

Hybrid type 2b : $\alpha = 0.28$: $\phi = 3002\ (GPa)^2$

The predicted values of moduli in both the warp and the weft directions are obtained from equations (3.56) and (5.3) respectively. Thus, for the type 1, type 2a and type 2b specimens loaded in the warp direction the predictions are, respectively, 35 GPa, 39.9 GPa and 43.3 GPa. The corresponding results for loading in the weft direction are 31.3 GPa, 37.6 GPa and 42.1 GPa. These latter values are compared with the experimental results in Table 5.2 and Fig. 5.2.

Table 5.2 Comparison between Analytical Predictions and Experimentally Determined Values of Hybrid Moduli (GPa) in the Weft Direction under Impact Loading.

Hybrid	Analytical Prediction	Experimental Value
Type 1	31.3	31.6
Type 2a	37.6	33.8
Type 2b	42.1	39.5

5.3 Prediction of Hybrid Strength

5.3.1 Quasi-static Test Predictions

For a uniaxially-loaded hybrid specimen cut with the tensile axis in the warp direction the stress distribution is given by equations (3.51) and

(3.52). The number of carbon plies in the central parallel gauge section of each specimen, (n-m) in these equations, is indicated in Fig. 2.9 and is, 2, for type 1, and 3, for both type 2a and type 2b specimens. Taking h_a = 0.287 mm and substituting for the various parameters in equations (3.51) and (3.52) from the quasi-static stiffness matrices [equations (4.3) and (4.4)], and equations (5.1) and 5.2), the results in Table 5.3 are obtained for the three hybrid specimens. A typical calculation for the prediction of failure in a type 1 hybrid specimen loaded in the warp direction is given below.

Table 5.3 Predicted Stress Distribution in Constituent Plies of Hybrid Specimens Loaded Quasi-Statically in the Warp Direction.*

HYBRID	CARBON PLY		GLASS PLY	
	σ_1/N_x (m^{-1})	σ_2/N_x (m^{-1})	σ_1/N_x (m^{-1})	σ_2/N_x (m^{-1})
Type 1	1190	-8.2	438	6.6
Type 2a	963	-3.5	354	6.3
Type 2b	1053	-2.1	387	7.5

* The units of N_x are MN/m

From Table 5.3, the stress distribution in a type 1 hybrid specimen loaded in the warp direction may be written

$$\sigma_1 = 1190\ N_x \qquad (5.6a)$$

$$\sigma_2 = -8.2\ N_x \qquad (5.6b)$$

for the carbon ply

and

$$\sigma_1 = 438\ N_x \tag{5.7a}$$

$$\sigma_2 = 6.6\ N_x \tag{5.7b}$$

for the glass ply; all symbols are as defined in Chapter 3. The strength parameters in the Tsai-Wu criterion, see equation (3.53), assumed to be the maximum stress before fracture for the all-carbon and the all-glass plies under quasi-static loading are given in Table 4.6, and are repeated here for convenience. The parameters (MPa) are, respectively,

$$X = 428,\ X' = 369,\ Y = 416,\ Y' = 394 \tag{5.8}$$

and

$$X = 328,\ X' = 128,\ Y = 262,\ Y' = 111 \tag{5.9}$$

for the carbon and glass plies. Substitution of equations (5.6a), (5.6b) and (5.8) or (5.7a), (5.7b) and (5.9) in the Tsai-Wu criterion produces a quadratic equation which when solved gives a critical traction

$$(N_x^*)_a = 0.36\ \text{MN/m} \tag{5.10}$$

for the carbon ply, or

$$(N_x^*) = 0.78\ \text{MN/m} \tag{5.11}$$

for the glass ply.

From equations (5.10) and (5.11) it is clear that the carbon plies are the first to fail. The stress and the strain in the hybrid specimen at the FPF point may be obtained from equations (3.54) and (3.55) respectively. Thus

$$\sigma_x^* = (N_x^*)_a / \{mh_b + (n-m)\, h_a\} = 277 \text{ MPa}$$

$$\varepsilon_x^* = (1+\alpha\mu)\, (Q_{22})_a\, (N_x^*)_a / \phi(n-m)h_a = 0.95\%$$

where $h_b = 0.121$ mm.

The axial stress (in the direction of the applied load) in the glass ply just before the FPF point is obtained by substituting $N_x = 0.36$ in equation (5.7a) and is approximately 158 MPa, i.e. less than half the failure strength of the all-glass composite specimen loaded in the warp direction. The problem now is what to do after FPF. The post FPF stress distribution in the carbon plies is likely to be very complex and may not be amenable to analytical techniques. This task is not addressed here, but we make a rough estimate of the damage in order to describe the post-FPF response of the degraded, glass-dominated hybrid composite.

Damage Quantification

The damage process in composite materials is very complex and is in general a combination of events such as cracking of the matrix, fibre failure and delamination in laminated composites. It is therefore difficult, if not impossible, to adequately quantify the effect of the various mechanisms on material mechanical properties. The usual practice is

to identify some mechanism as being dominant in a particular situation and then investigate its effects on some property e.g. stiffness. Probably the most widely studied mechanisms are delamination and transverse cracking [152-154]. Even in these cases, a scientific solution is yet to emerge [132].

The approach adopted here, is based on SEM observations and follows the work of Tsai and Azzi [130] later adapted to woven fabric composites based on glass or graphite reinforcements [107].

Scanning electron micrographs of the all-carbon and the outermost layers of the type 2b hybrid specimens, see section 4.4., indicate that failure of the plain-woven carbon fabric reinforced epoxy ply under tensile loading is essentially by cracking of the resin normal to the loading direction resulting in the fracturing and pulling out of fibres aligned with the load. We assume that this behaviour is typical of the carbon constituents in the hybrid composites employed in this investigation. For the carbon reinforced ply, therefore, the load-carrying ability in the direction of the applied load is considerably reduced after FPF. Indeed, except in the direction normal to the applied load, all components of $(Q_{ij})_a$ are significantly reduced giving a new value $(Q_{ij})_D$. Following Tsai and Azzi, therefore, we assume that despite FPF in the carbon plies they still continue to carry load but that as the traction increases to the point at which the glass plies also fail the increase in load in the carbon plies is very limited, corresponding to the much reduced stiffness matrix $(Q_{ij})_D$. The overall increase in traction following FPF must be that required to raise the stress in the glass plies from that at FPF to that at which they

also fail, i.e. 328 MPa, plus any corresponding (small) stress increase in the already 'failed' carbon plies. The increase in stress in the glass plies predominates and is given by

$$\sigma_A = 328 - 158 = 170 \text{ MPa} \qquad (5.12)$$

Let the corresponding additional traction required to produce failure in the glass plies be N_A and let the stiffness matrix of the carbon plies after FPF reduce to:

$$\left[Q_{ij} \right]_D = \begin{bmatrix} (Q_{11})_a / 100 & (Q_{12})_a / 100 & 0 \\ (Q_{12})_a / 100 & (Q_{22})_a & 0 \\ 0 & 0 & (Q_{66})_a / 100 \end{bmatrix} \qquad (5.13)$$

We now continue the analysis beyond FPF to obtain the new stress distribution in terms of $\left[Q_{ij}\right]_D$ and the original $\left[Q_{ij}\right]_b$ for the glass plies. From this we obtain a relation between σ_A and N_A. The various parameters β, λ, μ are modified to reflect the damage resulting from FPF. Thus, from equations (5.1) and (5.13)

$$\beta_D = (Q_{11})_b / (Q_{11})_D = 36.8$$

$$\lambda_D = (Q_{12})_b / (Q_{12})_D = 37.7 \qquad (5.14)$$

$$\mu_D = (Q_{22})_b / (Q_{22})_a = 0.32$$

Using equations (5.13) and (5.14) and the definition of ϕ in equation (3.48) the post-FPF equivalent of parameter ϕ, ϕ_D, is found to be 1346 GPa^2 for the

type 1 hybrid specimen. Remembering that for the type 1 hybrid specimen the parameter $\alpha = 1.26$, and assuming n, m and hence h_a to be unaffected by the failure of the carbon constituent, the stress distribution in the glass plies of the hybrid specimen may be obtained by substituting the post-FPF parameters for the pre-FPF equivalents in equations (3.52). This gives

$$\sigma_1 = \sigma_x = 1353\ N_x \qquad (5.15a)$$

$$\sigma_2 = \sigma_y = 130\ N_x \qquad (5.15b)$$

From equation (5.15a) we may write

$$N_A = {}^{\sigma_A}/_{1353}$$

where $\sigma_A = 170$ MPa, see equation (5.12). The additional traction required to produce failure in the glass constituent and by implication, the hybrid specimen, after FPF is ~ 0.13 MN/m. But the critical traction producing failure in the hybrid specimen is given by

$$N_{crit.} = (N_x^*)_a + N_A$$

where from equation (5.10), $(N_x^*)_a = 0.36$ MN/m.

Consequently the predicted fracture strength of the type 1 hybrid specimen is obtained from

$$\sigma_{TS} = N_{crit.} \,/\, \{ mh_b + (n-m)\, h_a \}$$

where the denominator is the specimen thickness, which based on the values of h_a, h_b previously given is 1.3 mm. The predicted fracture strength of approximately 377 MPa compares favourably with the experimental measurement of 381 MPa.

The additional strain in the specimen after FPF is given by the modified form of equation (3.55) i.e.

$$\varepsilon_A^* = (1 + \alpha\mu_D)\,(Q_{22})_D\,N_A \,/\, \phi_D\,(n-m)\,h_a$$

$$= 1.04\%$$

When added to the pre-FPF strain of 0.95% a fracture strain of ~2% is obtained. The experimental value is 1.7%.

With the same specimen loaded in the weft direction i.e. under a tensile traction N_y, it is easily shown that the initial stress distribution (before FPF) in the specimen is

$$\begin{Bmatrix} \sigma_x \\ \sigma_y \\ \tau_{xy} \end{Bmatrix}_a = {}^{N_y}/_{\phi\,(n-m)h_a} \begin{Bmatrix} \alpha\left[(\beta - \lambda)\,(Q_{11})_a(Q_{12})_a\right] \\ \left[(1 + \alpha\beta)(Q_{11})_a(Q_{22})_a - (1 + \alpha\lambda)(Q_{12}^2)_a\right] \\ 0 \end{Bmatrix} \tag{5.16}$$

$$\begin{Bmatrix} \sigma_x \\ \sigma_y \\ \tau_{xy} \end{Bmatrix}_b = N_y / (n-m)h_a \begin{Bmatrix} \left[(1 + \alpha\beta)(Q_{11})_a(Q_{12})_b - (1 + \alpha\lambda)(Q_{12})_a(Q_{11})_b\right] \\ \left[(1 + \alpha\beta)(Q_{11})_a(Q_{22})_b - (1 + \alpha\lambda)(Q_{12})_a(Q_{12})_b\right] \\ 0 \end{Bmatrix} \tag{5.17}$$

The stress and the strain at the 'knee' point, ε_y^* and σ_y^*, respectively, may be obtained from

$$\varepsilon_y^* = N_y^* (1 + \alpha\beta)(Q_{11})_a / \phi(n-m)h_a \tag{5.18}$$

$$\sigma_y^* = N_y^* / [mh_b + (n-m)h_a] \tag{5.19}$$

where N_y^* is the critical traction for the first ply to fail.

The procedure for predicting the fracture strength is the same as in the previous example except that, after the knee point the stiffness matrix of the carbon reinforced ply, see equation (5.13), becomes

$$\left[Q_{ij} \right]_D = \begin{bmatrix} (Q_{11})_a & (Q_{12})_a / 100 & 0 \\ (Q_{12})_a / 100 & (Q_{22})_a / 100 & 0 \\ 0 & 0 & (Q_{66})_a / 100 \end{bmatrix} \tag{5.20}$$

and is a consequence of the matrix cracks being normal to the weft tows. The state of stress as predicted for each hybrid lay-up under an applied tensile load in the weft direction is given in Table 5.4.

Table 5.4 Predicted Stress Distribution in Constituent Plies of Hybrid Specimens Loaded Quasi-statically in the Weft Direction.*

HYBRID	CARBON REINFORCED PLY		GLASS REINFORCED PLY	
	σ_1/N_y (m^{-1})	σ_2/N_y (m^{-1})	σ_1/N_y (m^{-1})	σ_2/N_y (m^{-1})
Type 1	- 1.36	1243	1.09	396
Type 2a	- 0.58	985	1.05	314
Type 2b	- 0.34	1066	1.23	340

* The units of N_x are MN/m

Predicted values of fracture strength for type 1, type 2a and type 2b hybrid specimens loaded in the warp direction are, respectively, 377 MPa, 401 MPa and 413 MPa. The corresponding predictions for specimens cut with the tensile axis in the weft direction are 331 MPa, 364 MPa and 381 MPa respectively. The former are compared with experimental measurements in Table 5.5 and Fig. 5.3. Also indicated in Fig. 5.3 are the rule of mixture predictions which are in less agreement with the experimental results. The present analysis predicts values of strength that lie between the mean values of the experimental measurements and the rule of mixture predictions. Analytical and experimental stress-strain plots for the three hybrid lay-ups are compared in Fig. 5.4.

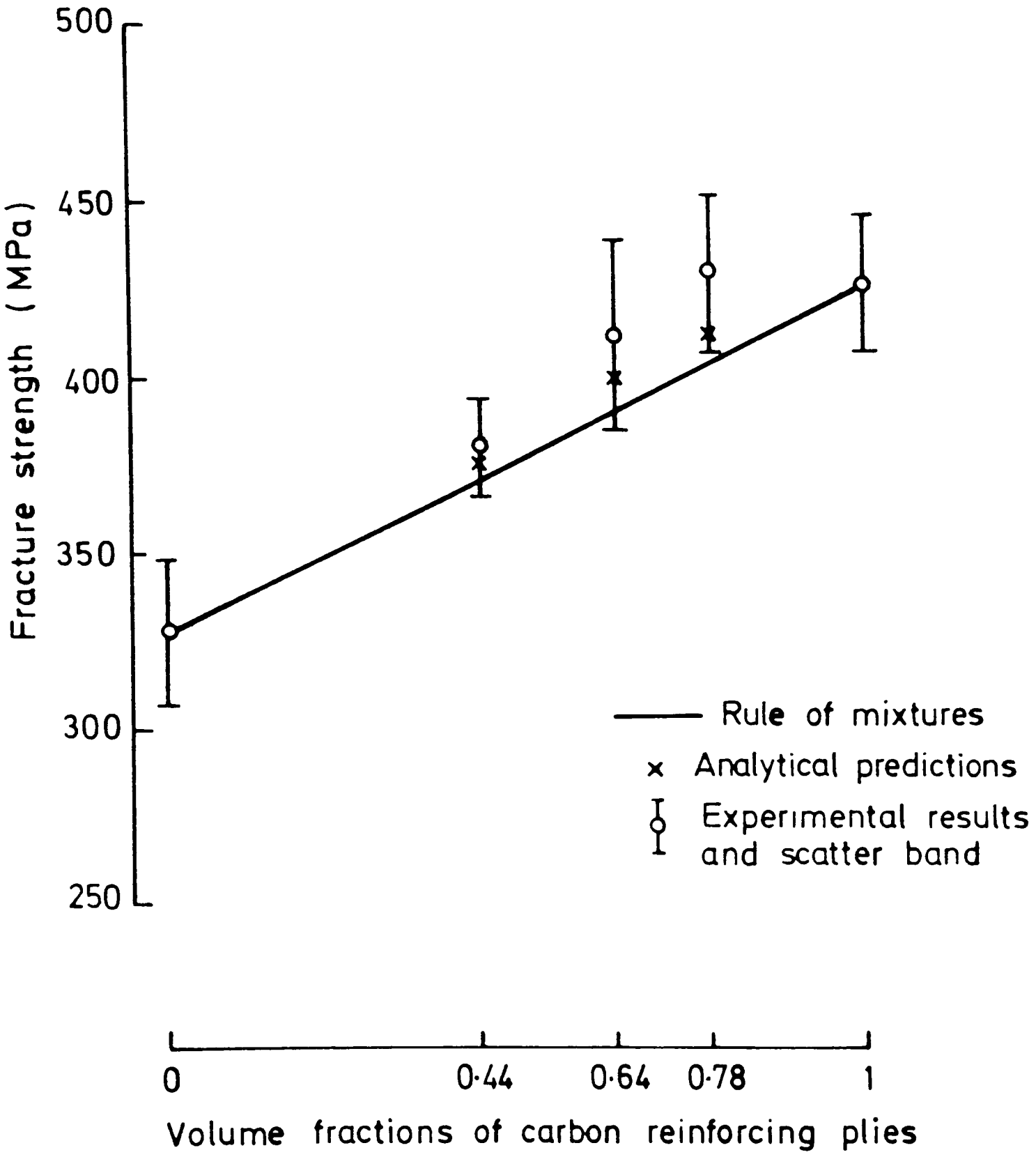

Fig. 5.3 Comparison between analytical predictions and experimentally determined values of quasi-static hybrid strengths

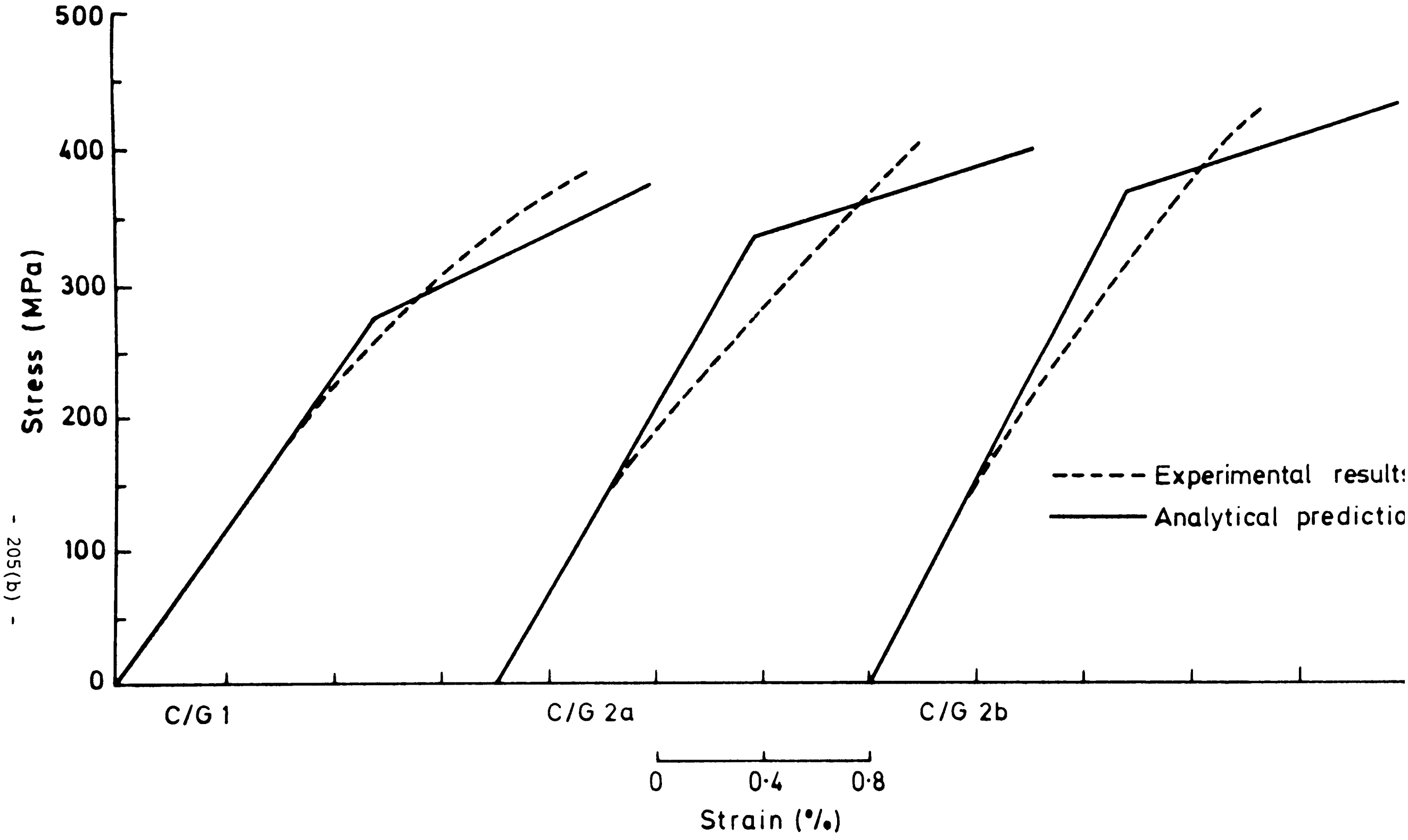

Fig. 5.4 Analytical and experimental stress-strain curves for quasi-static tests on hybrid composite specimens

Table 5.5 Comparison between Analytical Predictions and Experimentally Determined Values of Hybrid Strengths (MPa) in the Warp Direction under Quasi-Static Loading.

Hybrid	Analytical Prediction	Experimental Value
Type 1	377	381
Type 2a	401	413
Type 2b	413	431

5.3.2 Impact Test Predictions

A comparison of the quasi-static stress-strain curves for the all-carbon and the all-glass specimens in the two directions of reinforcement, see Figs. 4.25 and 4.26, shows some similarity in behaviour in the sense that no significant reduction in stiffness occurred in the early stages of deformation. Here, therefore, the definition of failure is a relatively simple matter and is synonymous with the attainment of maximum stress. The same is not true of the impact test results where, although for the all-carbon plies, see Fig. 4.7, the behaviour is again almost linear-elastic to failure and the estimated yield stress is about 90% of the maximum stress, for the all-glass specimen in each of the principal material directions a reduction to about 60% of the previous stiffness is seen at strains above ~1% strain, see Fig. 4.10. This would imply that the specimen experienced some damage at an early stage in the deformation process so, for FPF, it may be more meaningful to substitute the yield stress in place of the tensile strength for the all-glass material when applying the Tsai-Wu criterion.

However if FPF is found to be in the glass plies then the modified stiffness matrix for these plies should reflect the reduced stiffness shown in the stress-strain curve of Fig. 4.10. The following example on a type 2b hybrid specimen illustrates the approach.

Following the same procedure as in the quasi-static case, the stress distribution in a type 2b hybrid specimen prior to failure of the first ply may be obtained, respectively, as

$$\sigma_1 = -8N_y \qquad (5.21a)$$

$$\sigma_2 = 1057\ N_y$$

and

$$\sigma_1 = 30\ N_y \qquad (5.21b)$$

$$\sigma_2 = 373\ N_y$$

for the carbon and glass plies. The appropriate strength parameters (MPa) in the Tsai-Wu criterion at the impact rate are as given below.

for carbon plies, $X = 562$, $Y = 508$, $X' = 572$, $Y' = 588$ (5.22a)

for glass plies, $X_y = 151$, $Y_y = 165$, $X' = 405$, $Y' = 385$ (5.22b)

where X_y and Y_y are the 'yield' strengths in warp and weft directions respectively.

Substituting equations (5.21a) and (5.22b) or (5.21b) and (5.22b) into the Tsai-Wu equation and solving, the critical tractions for the constituent plies are obtained as follows:

Carbon plies: $(N_y^*)_a = 0.47$ MN/m (5.23)

Glass plies: $(N_y^*)_b = 0.44$ MN/m (5.24)

We therefore conclude that yielding in the glass plies preceded the failure of the carbon plies.

The impact stiffness matrix for the all-glass plies is then modified, each element being reduced to 75% of its previous value, corresponding, approximately, to the reduced stiffness following yield in the stress-strain curves of Fig. 4.10. The resulting stiffness matrix for the degraded glass plies becomes

$$\left[Q_{ij} \right]_{bD} = \begin{bmatrix} 18.4 & 2.33 & 0 \\ 2.33 & 13.1 & 0 \\ 0 & 0 & 2.85 \end{bmatrix} \text{GPa} \qquad (5.25)$$

The various parameters β_D, μ_D and λ_D, obtained from equations (4.5) and 5.25), are found to be $\beta_D = 0.376$, $\mu_D = 0.266$, $\lambda_D = 0.777$ and ϕ_D, the corresponding value of ϕ, see equation (3.48), is $2844(\text{GPa})^2$. The redistribution of stresses in the degraded hybrid composite is obtained in the usual manner. This gives:

for the carbon plies,

$$\sigma_1 = -6.7\ N_y \qquad (5.26a)$$

$$\sigma_2 = 1082\ N_y \qquad (5.26b)$$

and for the glass plies

$$\sigma_1 = 24\ N_y \qquad (5.27a)$$

$$\sigma_2 = 286\ N_y \qquad (5.27b)$$

At FPF in the glass plies, the stress in the glass, from $\sigma_2 = 373\ N_y$, see equations (5.21b), was 164 MPa i.e. the yield stress, and the stress in the carbon plies [using $\sigma_2 = 1057\ N_y$ in equations (5.21a)] was 465 MPa. Thus for failure of the carbon plies an increase in stress of 508 - 465 = 43 MPa is required. From equation (5.26b) this requires an additional traction of 43/1082 = 0.04 MN/m giving a total traction of 0.48 MN/m. The corresponding stress in the glass plies, from equation (5.27b) has increased by ~11 MPa to a value of 175 MPa. Since the failure strength of the glass plies is 427 MPa an additional stress of 252 MPa can be applied.

It may be observed that following FPF we resorted to a 'direct stress' approach as opposed to the Tsai-Wu criterion for evaluating the critical tractions of the constituent plies. In other words, we obtained the additional (post-FPF) stress required to produce failure in one constituent and from the prevailing stress distribution determined the corresponding additional traction. The other constituent is then subjected to the same increase in traction in order to be certain if the test continued or was terminated by failure of the composite as a whole.

The stiffness matrix of the 'failed' carbon plies is now modified as in equation (5.20). Using this matrix and that in equation (5.25) the various values of β_D^*, μ_D^* and λ_D^* are obtained. Thus

$$\beta_D^* = \beta_D = 0.376, \quad \mu_D^* = 26.6, \quad \lambda_D^* = 77.7$$

And adopting the usual approach ϕ_D^* is given as $224(\text{GPa})^2$. The state of stress in the glass plies is now

$$\sigma_1 = 588\ N_y \qquad (5.30a)$$

$$\sigma_2 = 3663\ N_y \qquad (5.30b)$$

From equation 5.30b an increase in the tensile stress on the glass plies of 252 MPa requires an increased traction of ~0.07 MN/m giving a final total traction of 0.55 MN/m. This corresponds to a composite fracture strength of ~500 MPa which compares with the average experimental value of 520 ± 8 MPa.

In the other two hybrid specimens (type 1 and type 2a) yielding of the glass plies again preceded the failure of the carbon plies. So the same somewhat lengthy analysis was performed. Values of the various parameters as well as the stress distribution as obtained at each stage of the analysis are presented in Tables 5.6 and 5.7 for type 1 and type 2a specimens respectively. Predicted hybrid strengths are 454 MPa for type 1 and 483 MPa for type 2a and may be compared with the experimental values of 458 MPa for the former and 521 MPa for the latter.

Table 5.6 Predicted Stress Distribution and Values of Various Parameters in Impact Tests on Type 1 Hybrid Specimens Loaded in the Weft Direction.*

STAGE	STRESS DISTRIBUTION				PARAMETERS			
	CARBON PLIES		GLASS PLIES					
	$\sigma_1/N_y^{(m-1)}$	$\sigma_2/N_y^{(m-1)}$	$\sigma_1/N_y^{(m-1)}$	$\sigma_2/N_y^{(m-1)}$	β	μ	λ	Φ $(GPa)^2$
PRE-FPF	-30	1206	24	425	0.501	0.356	1.033	5638
POST-FPF BUT BEFORE FAILURE OF CARBON PLIES	-27.5	1308	21.8	930	0.376	0.266	0.777	4699
AFTER FAILURE OF CARBON PLIES	--	--	162	1344	0.376	26.6	77.7	1215

* The units of Ny are MN/m .

Table 5.7 Predicted Stress Distribution and Values of Various Parameters in Impact Tests on Type 2a Hybrid Specimens Loaded in the Weft Direction*.

STAGE	STRESS DISTRIBUTION				PARAMETERS			
	CARBON PLIES		GLASS PLIES					
	$\sigma_1/N_y^{(m-1)}$	$\sigma_2/N_y^{(m-1)}$	$\sigma_1/N_y^{(m-1)}$	$\sigma_2/N_y^{(m-1)}$	β	μ	λ	Φ $(GPa)^2$
PRE-FPF	-14	970	25	342	0.501	0.356	1.033	3673
	-11.5	1012	20.5	267	0.376	0.266	0.777	3328
	--	--	286	1946	0.376	26.6	77.7	461

* The units of Ny are MN/m .

Lack of time has prevented the completion of the analysis i.e. prediction of strains and hence stress-strain 'curves' for the impact tests. However, the procedure is similar to that used for the quasi-static tests.

Although the technique appears to be reasonably successful several somewhat questionable assumptions are involved. Quantification of damage remains the main obstacle to a rational prediction of the failure strengths of composite materials especially at impact loading rates.

5.4 Effect of Transverse Sensitivity

The effect of transverse sensitivity on measured strains was discussed in section 2.10.3, where it was observed that the maximum error (~20%) in strain measurement occurred in impact tests on all-carbon parallel sided strips loaded in the warp direction. It was thought necessary, therefore, to estimate the effect of transverse sensitivity on predicted properties in this particular case.

The relation between the actual and measured strains along any two perpendicular axes are given by the following equations [see reference [98] for example],

$$\varepsilon_x = (1 - \nu_o k)(\varepsilon'_x - k\,\varepsilon'_y) \,/\, (1 - k^2) \qquad (5.31a)$$

$$\varepsilon_y = (1 - \nu_o k)(\varepsilon'_y - k\,\varepsilon'_x) \,/\, (1 - k^2) \qquad (5.31b)$$

where ε'_x = the measured (uncorrected) strain along the longitudinal gauge axis aligned with the applied load

ε'_y = the measured (uncorrected) strain along the longitudinal axis of the gauge which is perpendicular to the applied load

ε_x , ε_y are the corresponding corrected strains

ν_o = Poisson's ratio of the material on which the manufacturer's gauge factor was measured (usually 0.285)

K is the transverse sensitivity coefficient for the strain gauges

From equation (5.30) and (5.31) we have

$$\frac{\varepsilon_y}{\varepsilon_x} = \frac{\varepsilon'_y - K\varepsilon'_x}{\varepsilon'_x - K\varepsilon'_y} = \left(\frac{\varepsilon'_y}{\varepsilon'_x} - K\right) / \left(1 - K \frac{\varepsilon'_y}{\varepsilon'_x}\right)$$

Or

$$\nu_{LT} = (K + \nu'_{LT}) / (1 + K \nu'_{LT}) \qquad (5.32)$$

where ν_{LT} and ν'_{LT} are, respectively, the corrected and measured major Poisson's ratios. The transverse sensitivity coefficient of the strain gauges used in the present work was given by the manufacturers as +0.015. Using equation (5.32) the measured major Poisson's ratios, 0.061 for the all carbon and 0.176 in the all-glass specimens, when corrected become 0.076 and 0.190 respectively.

Based on the appropriate elastic moduli from Table 4.5 and the symmetry relation, see equation (3.22), the 'corrected' minor Poisson's ratios are found to be 0.076 for the all-carbon and 0.136 in the all-glass composites. From each pair of corrected Poisson's ratios and the relevant elastic moduli (i.e. in the warp and weft directions) the corrected components of the stiffness matrix which are required for the analytical prediction of stiffness and strength are obtained in each case and are for the all-carbon.

$$\left[Q_{ij} \right]_a = \begin{bmatrix} 49 & 3.7 & 0 \\ 3.7 & 49.3 & 0 \\ 0 & 0 & - \end{bmatrix} \text{GPa} \qquad (5.33)$$

and the all-glass:

$$\left[Q_{ij} \right]_b = \begin{bmatrix} 24.6 & 3.4 & 0 \\ 3.4 & 17.6 & 0 \\ 0 & 0 & - \end{bmatrix} \text{GPa} \qquad (5.34)$$

Equations (5.33) and (5.34) may, respectively, be compared with equations (4.5) and (4.6). Apart from the off-diagonal elements there is hardly any difference between each pair. The effect of this on the predicted moduli is insignificant. The effect on the predicted strengths has not been determined but is likely to be small.

CHAPTER 6

DISCUSSION

6.1 Effect of Hybrid Composition on Initial Modulus

Graphical plots of the variation of initial modulus with the volume fraction of carbon reinforcing plies at both quasi-static and impact rates were presented in Chapter 5 (Figs. 5.1 and 5.2 respectively). Under quasi-static loading the experimental results for the three hybrid lay-ups are seen to agree closely with the predictions of both the rule of mixtures and laminate theory. As said earlier, these specimens were cut with the tensile axis in the warp direction. Results from the impact tests show a slight deviation from analytical predictions. In this case, however, it is the weft, rather than the warp, direction which is being studied.

At the intermediate rate, see Fig. 6.1, where again specimens were loaded in the weft direction, the opposite response to that under impact loading can be seen, the experimentally measured moduli falling slightly above the predictions of the rule of mixtures.

6.2 Effect of Hybrid Composition on the Elastic Limit

The effect of an increasing volume fraction of carbon reinforcing plies on the initial yield stress and on the corresponding yield strain levels in

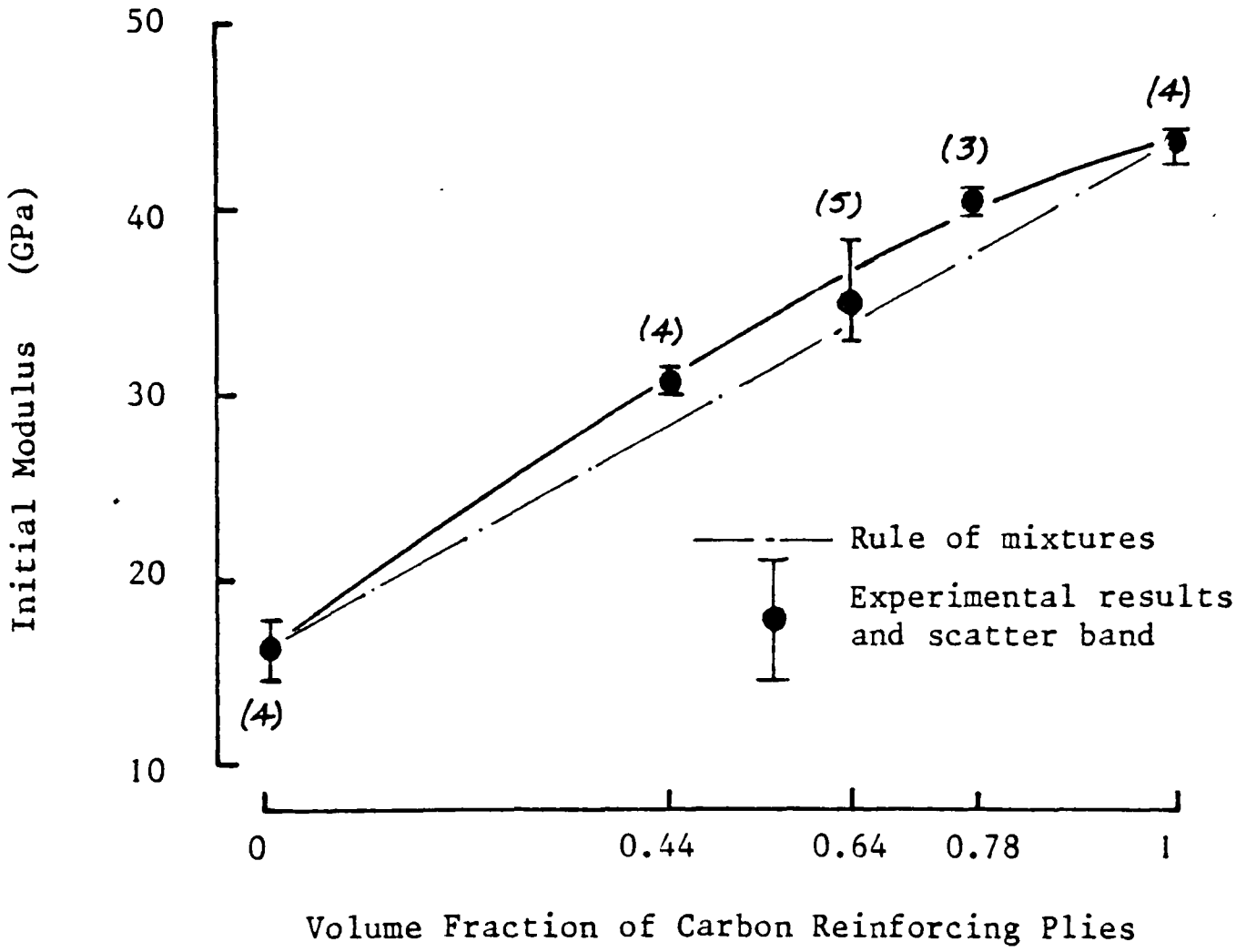

Fig. 6.1 Variation of Initial Modulus with Volume Fraction of Carbon Plies at Intermediate Rates of Loading

tests at all three rates of loading is shown in Figs. 6.2 and 6.3 respectively. Unlike the point of maximum stress, which is unambiguously indicated in each test, the 'yield' point, which corresponds to the limit of the intial linear elastic region, is much less clearly defined and the measured values given in Figs. 6.2 and 6.3 are somewhat subjective. They do, however, give a reasonably good indication of general trends in behaviour. In particular, Fig. 6.2 shows that the elastic stress range, at all three loading rates, is approximately doubled between the all-glass specimens and type 1 hybrids, where the volume fraction of carbon reinforcement is 0.44, but that a further increase in the proportion of carbon to glass reinforcement has very little effect.

It has been suggested [78] that the yield point, i.e. the limit of linear elastic response, in woven glass-reinforced composites corresponds to the situation where the axially-aligned fibre tows have sufficiently straightened under the applied load that, in regions of high local stress (or strain) concentration, the resin matrix develops cracks and breaks up. This is followed by a region of reduced stiffness, the 'knee' effect, until the onset of fibre fracture leads to final failure. For the woven carbon-reinforced composites the higher initial stiffness of the carbon fibre reinforcing mats leads to a higher yield point, assuming break up of the resin depends principally on a critical strain being reached. The region of reduced stiffness in the stress-strain response is correspondingly less marked, particularly as fracture of the first carbon fibre tow is more likely to lead to catastrophic failure.

Fig.6.2 EFFECT OF HYBRID VOLUME FRACTION ON STRESS AT LIMIT OF LINEAR ELASTIC RESPONSE

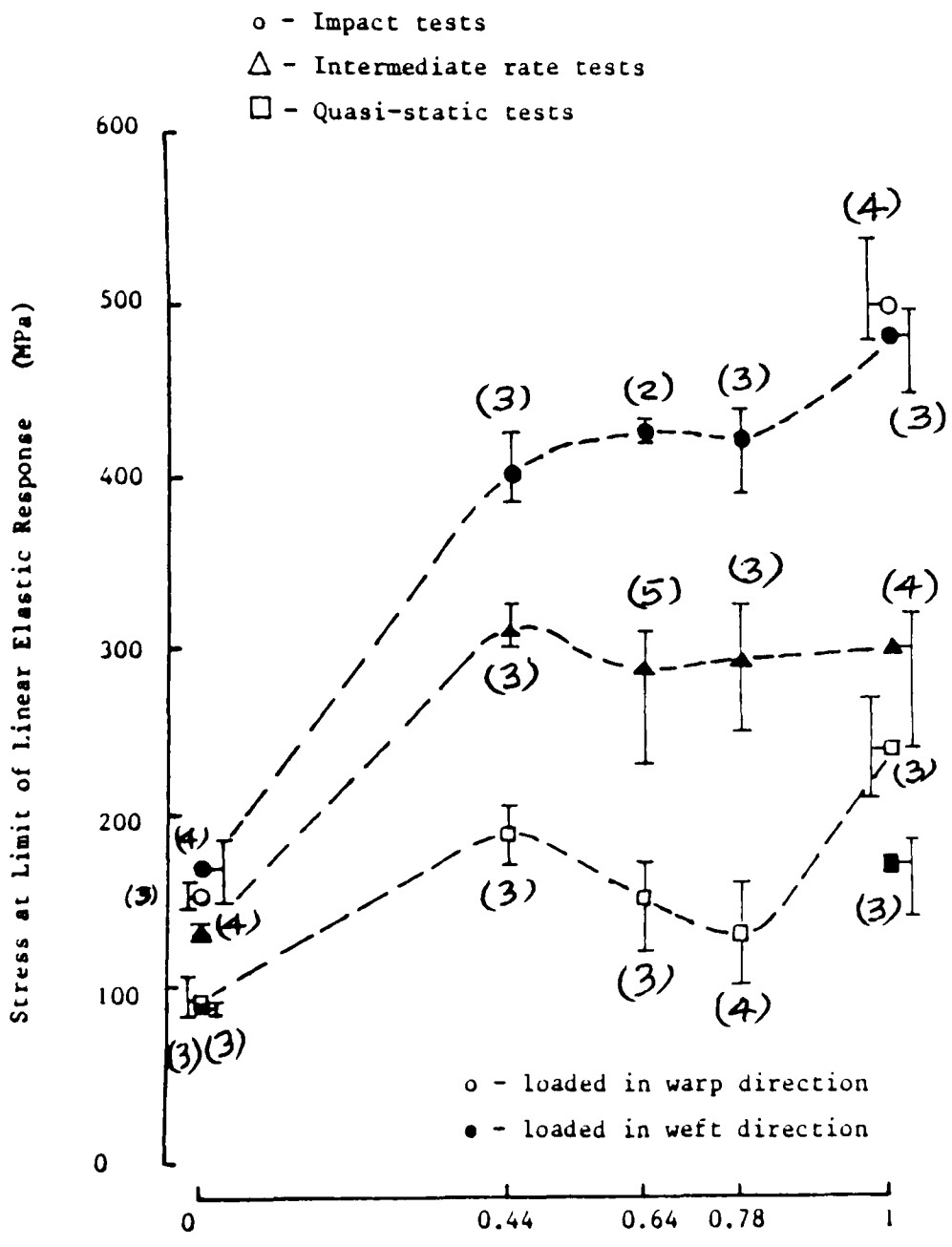

Fig.6.3 EFFECT OF HYBRID VOLUME FRACTION ON STRAIN AT LIMIT OF LINEAR ELASTIC RESPONSE

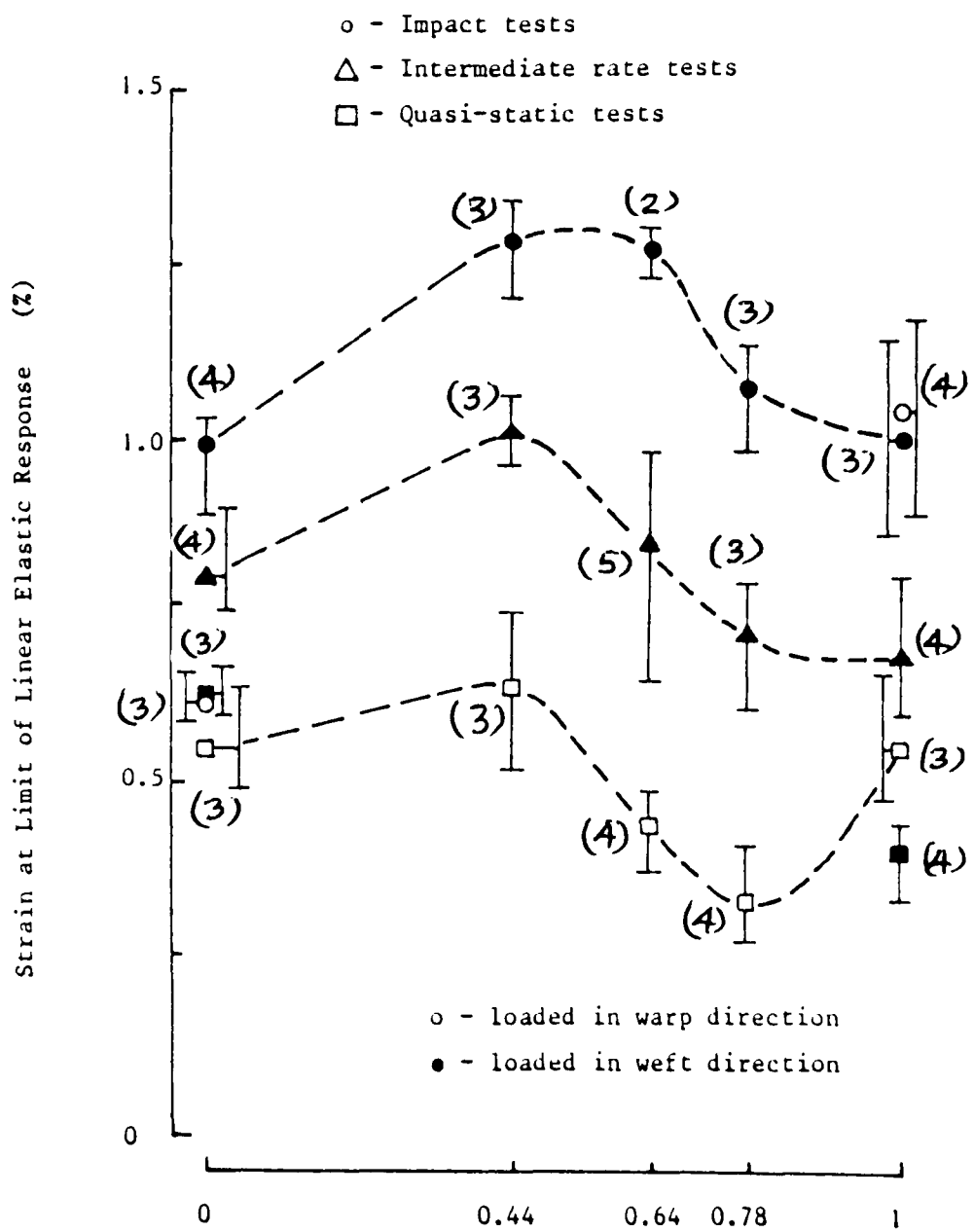

In the present results, if the yield point was controlled by the attainment of a critical strain in the matrix, then the stress levels in Fig. 6.2 should show the same general trends as the moduli in Figs. 5.1, 5.2 and 6.1. However, it is clear from Fig. 6.3 that, although the yield strain is approximately constant at any given loading rate there are considerable fluctuations about the mean value where the hybrid specimens are concerned, e.g. 0.5% ± 0.2% at the quasi-static rate, 1.1% ± 0.2% under impact loading, leading to corresponding fluctuations in the yield stress, see Fig. 6.2. This is not surprising in view of the different geometries of weave in the glass and the carbon reinforcement, the glass having a very fine and the carbon a much coarser weave configuration, suggesting that the critical strain at yield might be different for the two types of reinforcement. This is not borne out by the results of Fig. 6.3, however, which show the same yield strain for the all-glass and the all-carbon plies in quasi-static tests when loaded in the warp direction and impact tests when loaded in the weft direction and closely similar yield strains in medium rate tests also when loaded in the weft direction. The situation is confused, however, by conflicting results for quasi-static tests in the weft direction where the all-carbon plies yield at a significantly lower strain and for impact tests in the warp direction where the reverse is the case.

Despite these anomalies the general trends observed in Figs. 6.2 and 6.3 at all three rates of loading and in three different testing machines are sufficiently similar to suggest that some significance may be placed on them. It should perhaps be noted that in addition to the volume fraction of carbon reinforcing plies a further difference between the three hybrid lay-ups is in the type of interlaminar regions present, both carbon/glass and

glass/glass in type 1 hybrids, only carbon/glass in type 2a and type 2b hybrids. This could have an effect on local stress concentrations which lead to the matrix break up at yield.

6.3 Effect of Hybrid Composition on the Maximum Stress and Failure Strain

At all three loading rates the maximum stress preceding final failure increases with the carbon content, as shown in Fig. 6.4, up to a volume fraction of about 0.8, at which point the hybrid strength exceeds that of the all-carbon specimens loaded in the same direction at the same strain rate. As a consequence a clear hybrid effect is apparent in that the failure strengths of the hybrids with carbon volume fractions between, say, 0.5 and 0.9 exceed that which would be predicted from a simple rule of mixtures based on the failure strengths of the all-glass and the all-carbon plies. The maximum increase due to this effect is small, only about 10% of the rule of mixtures prediction, but the general trend is consistent at all three rates of loading.

Similar results for the effect of carbon volume fraction on the failure strain, defined as the strain corresponding to the point of maximum stress, are given in Fig. 6.5. A mean failure strain for the all-carbon specimens of 1.31 $\pm$ 0.3% is determined from the results of all tests on this material in both the warp and the weft directions and at all three loading rates. For each of the three hybrid lay-ups a small hybrid effect, defined as the enhancement of the failure strain of the low elongation phase, is observed, to ~1.5%, ~1.6% and ~1.7% for the type 2b, the type 2a and the type 1 hybrid

Fig.6.4 EFFECT OF HYBRID VOLUME FRACTION ON MAXIMUM STRESS

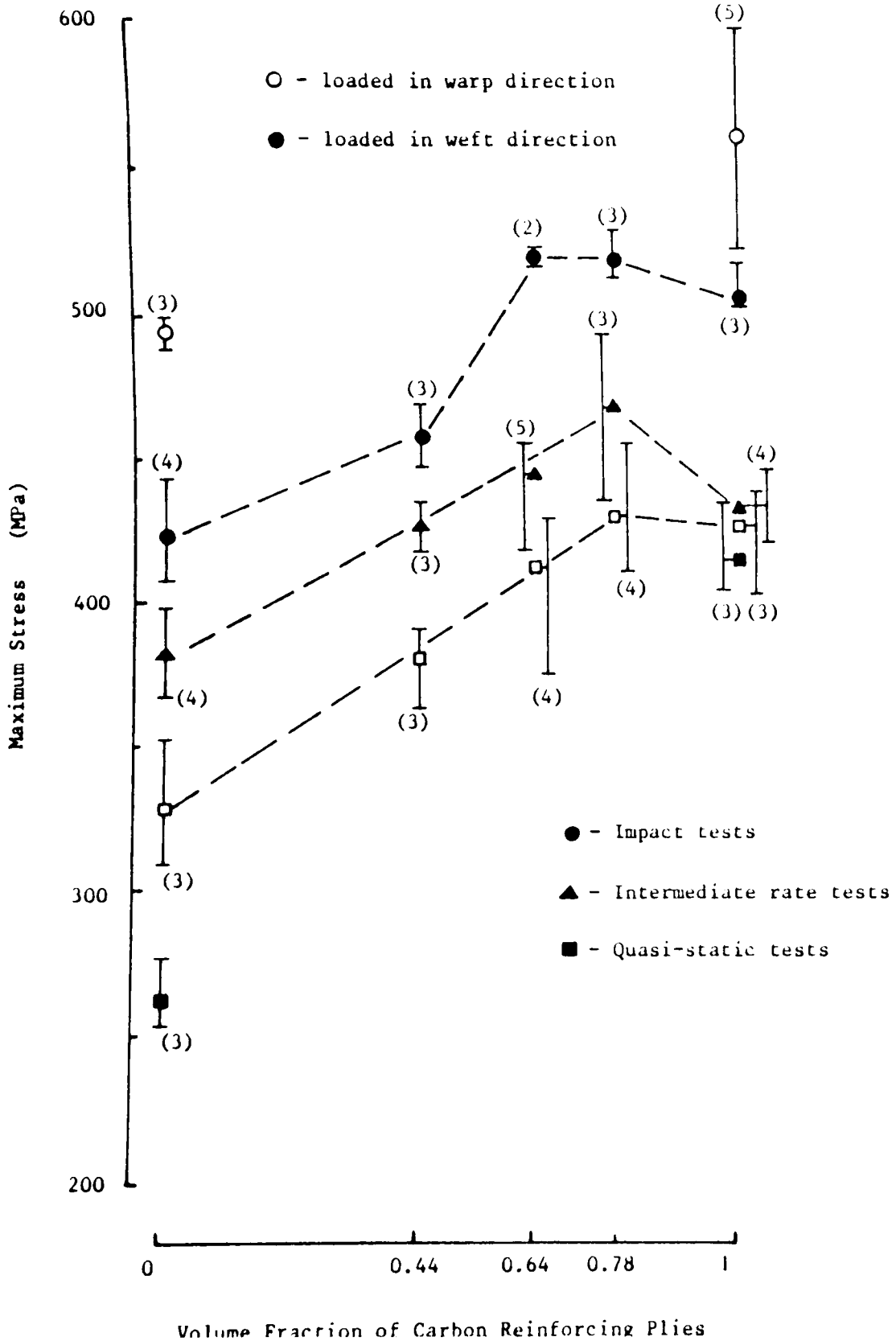

Fig.6.5 EFFECT OF HYBRID VOLUME FRACTION ON STRAIN AT FAILURE

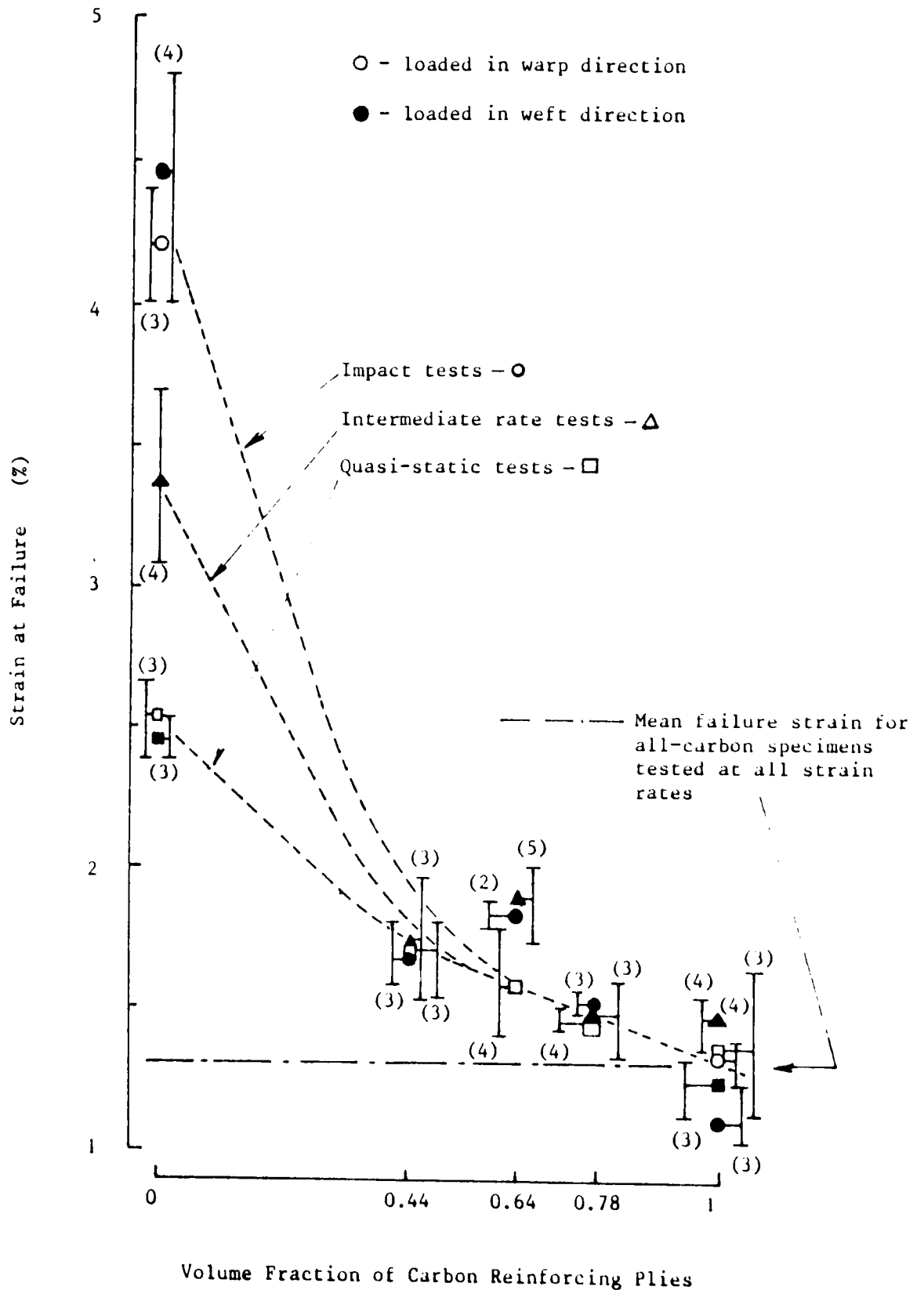

specimens respectively. A much more marked effect is seen in the all-glass specimens where the failure strain ranges from ~2.5% in the quasi-static tests to more than 4% under impact loading. SEM observations, see section 4.4, suggest that in impact tests on the hybrid specimens the relatively low overall strain was due to a restriction of the damage zone in the glass-reinforced plies by the limited elongation possible in the adjacent carbon-reinforced plies.

Taking the results of Figs. 6.4 and 6.5 together it may be seen that hybrid specimens with a carbon volume fraction of between, say, 0.6 and 0.7, at all rates of loading, show both an enhancement of the failure strain over that of the all-carbon plies and an increased failure strength over that predicted by the rule of mixtures.

6.4 Effect of Strain Rate on Hybrid Mechanical Properties

Stress-strain curves, in each case the mean of three tests, for the type 1 hybrid specimens at the three loading rates are compared in Fig. 6.6. The negligible effect of strain rate on the modulus and strain to failure and the marked increase in 'yield' stress and subsequent stress at failure at the higher strain rates were characteristic of all three hybrid lay-ups. Unfortunately the significance of the comparison in Fig. 6.6 is reduced in that the direction of loading (warp or weft) was different at the different loading rates. This was also true of the results for the other two hybrid lay-ups, but not of those for the all-glass and the all-carbon plies. Stress-strain curves for the all-glass composite loaded in the weft

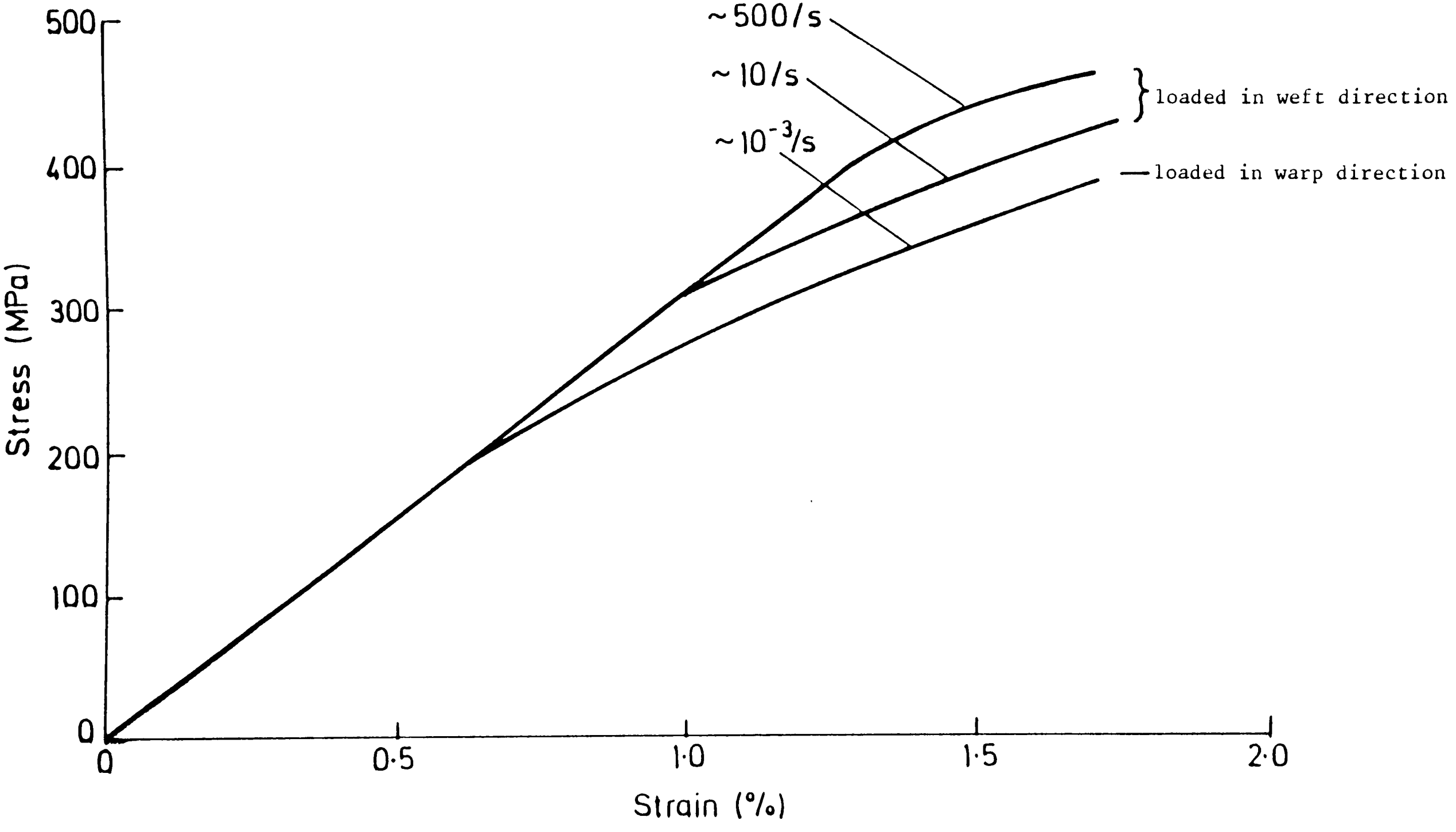

Fig.6.6 EFFECT OF STRAIN RATE ON STRESS-STRAIN CURVES FOR TYPE I HYBRID SPECIMENS

direction, are compared in Fig. 6.7 and here an effect of strain rate on the modulus and on the strain at failure is clearly observed. The general trends shown in Fig. 6.7 are similar to earlier results for plain-weave glass/epoxy composites [67] except that here the rate dependence of the failure strain is more marked and of the modulus and strength rather less marked.

A more detailed description of the effect of strain rate on the mechanical response of the various specimen types is given in Figs. 6.8 to 6.12. These show the variation of initial modulus, 'yield' and maximum stress and 'yield' and failure strain with the logarithm of the average strain rate for the all-glass and the all-carbon plies and the type 1, type 2a and type 2b hybrids respectively. The mean of each set of measurements, the scatter band and the number of test results obtained is indicated in each case.

For the all-glass specimens loaded in the weft direction the increase in modulus with strain rate is only a little greater than the experimental scatter. In the warp direction, however, the modulus is both greater and more clearly rate dependent. For the all-carbon specimens, Fig. 6.9a, the modulus is the same in the warp and weft directions and there is some indication of an increase in modulus under impact loading although the experimental scatter here is much greater. For each of the three hybrid lay-ups Figs. 6.10a, 6.11a and 6.12a, no significant effect of strain rate on modulus is observed, although the comparison is between specimens loaded in different directions at the various strain rates. Since the hybrid moduli obey the predictions of both the rule of mixtures and laminate theory

Fig.6.7 EFFECT OF STRAIN RATE ON STRESS-STRAIN CURVES FOR ALL-GLASS SPECIMENS LOADED IN WEFT DIRECTION

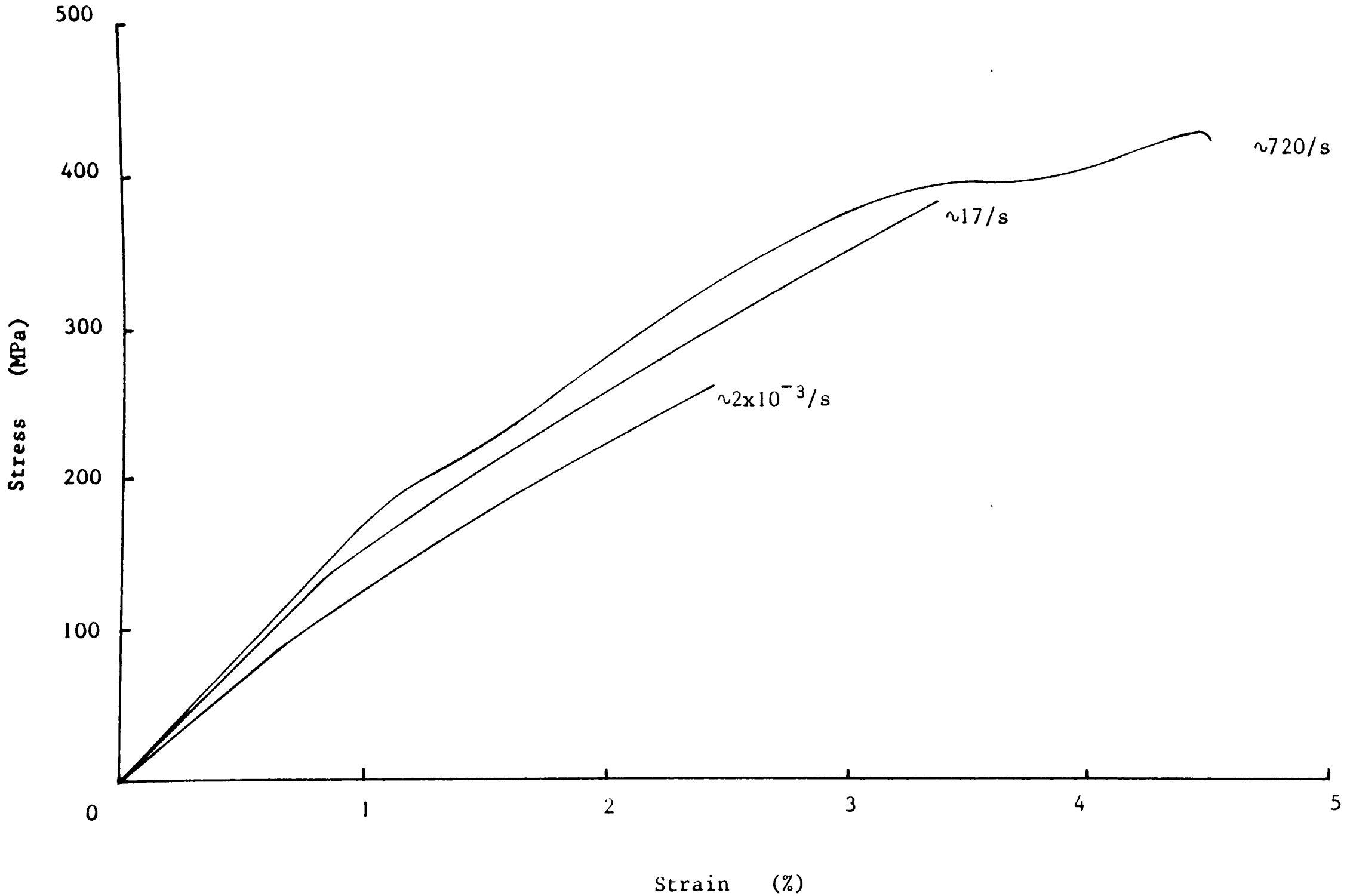

a) Initial Modulus

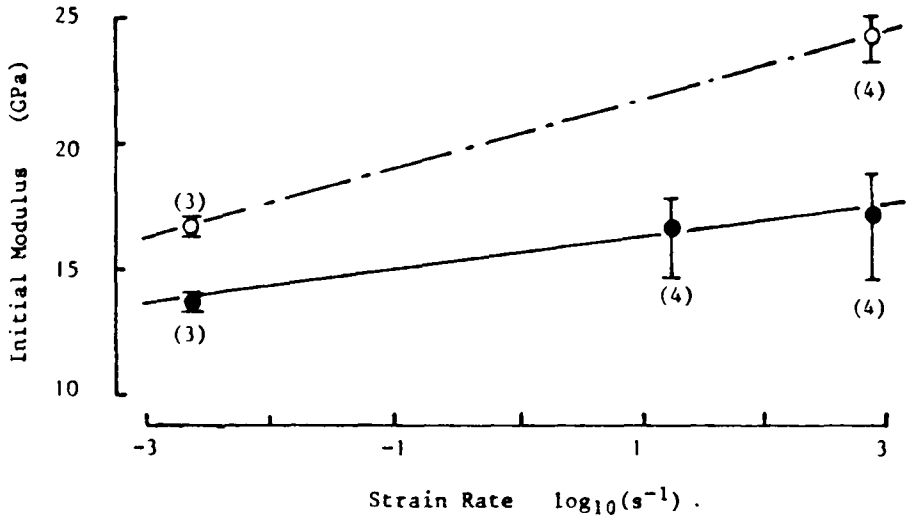

b) 'Yield' and Maximum Stress

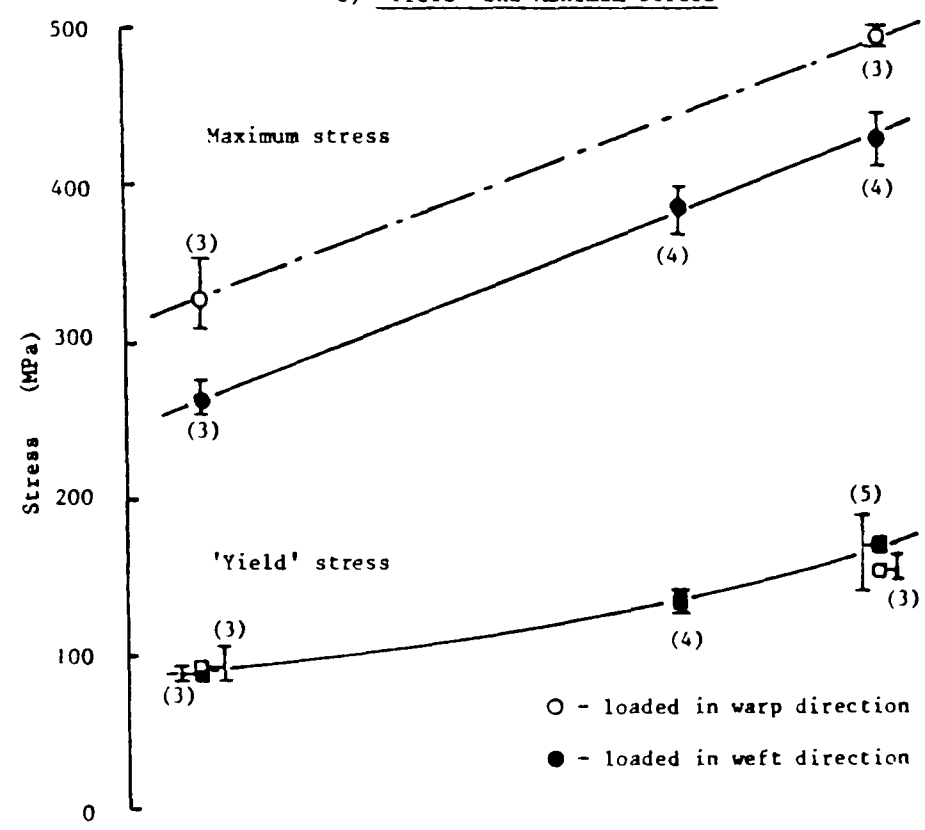

c) 'Yield' and Failure Strain

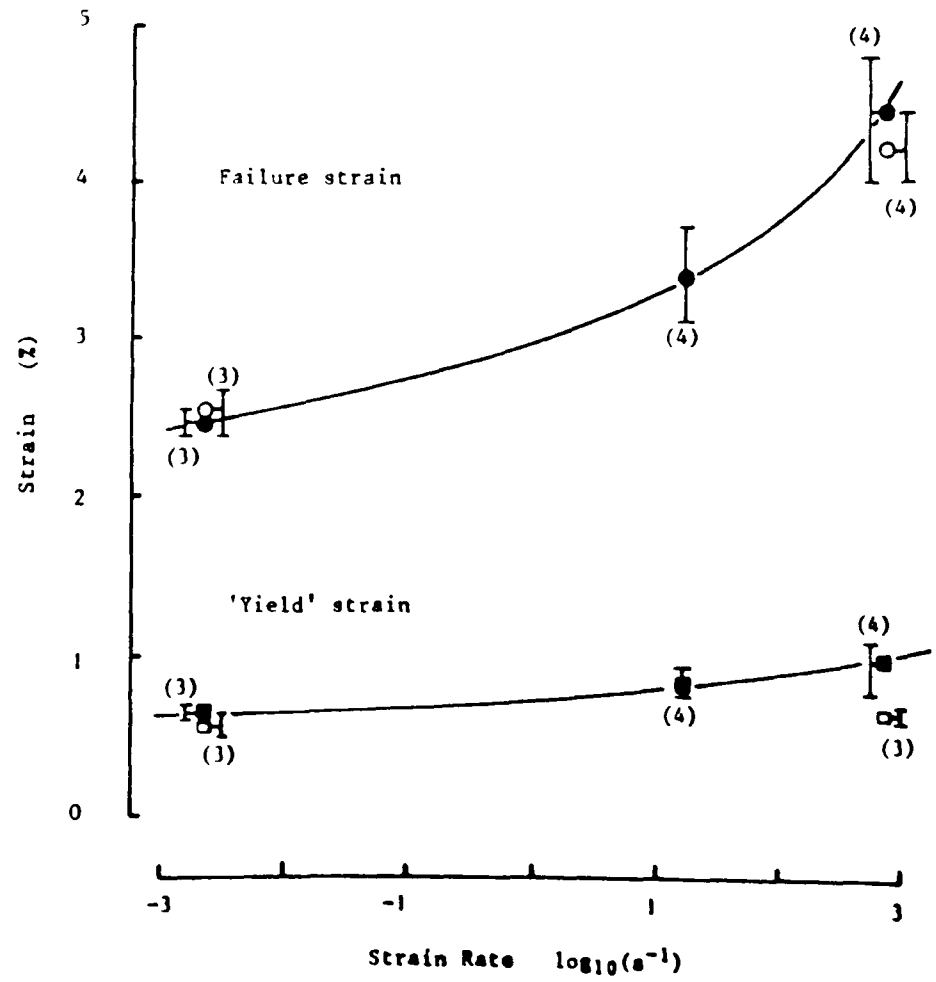

Fig.6.8 EFFECT OF STRAIN RATE ON TENSILE PROPERTIES OF ALL-GLASS SPECIMENS

a) Initial Modulus

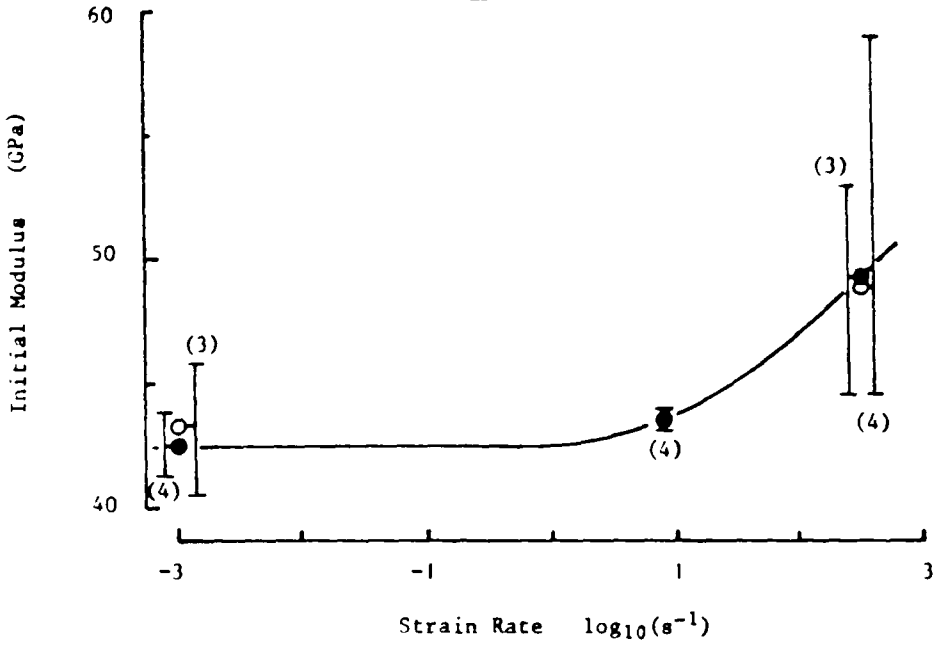

b) 'Yield' and Maximum Stress

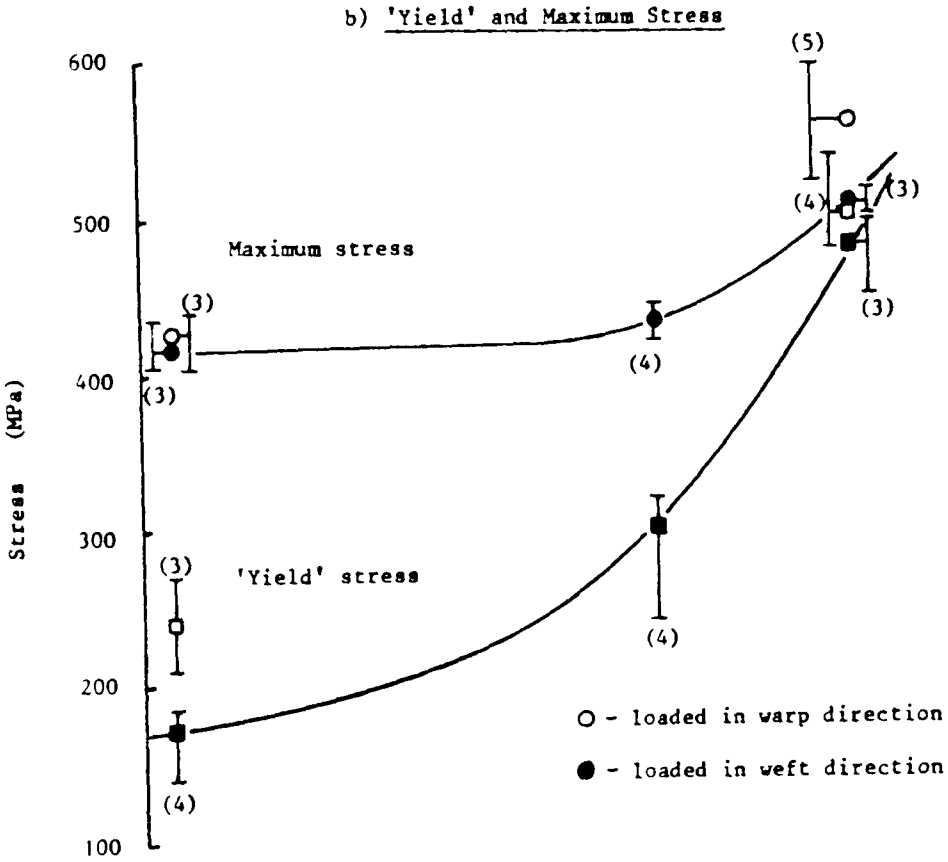

c) 'Yield' and Failure Strain

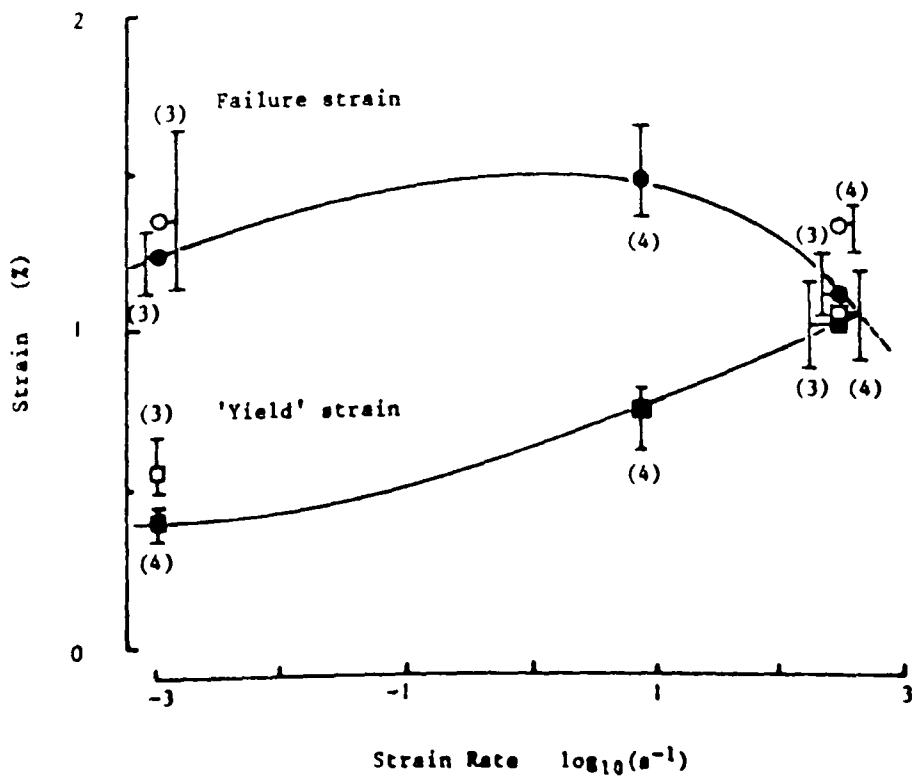

Fig.6.9 EFFECT OF STRAIN RATE ON TENSILE PROPERTIES OF ALL-CARBON SPECIMENS

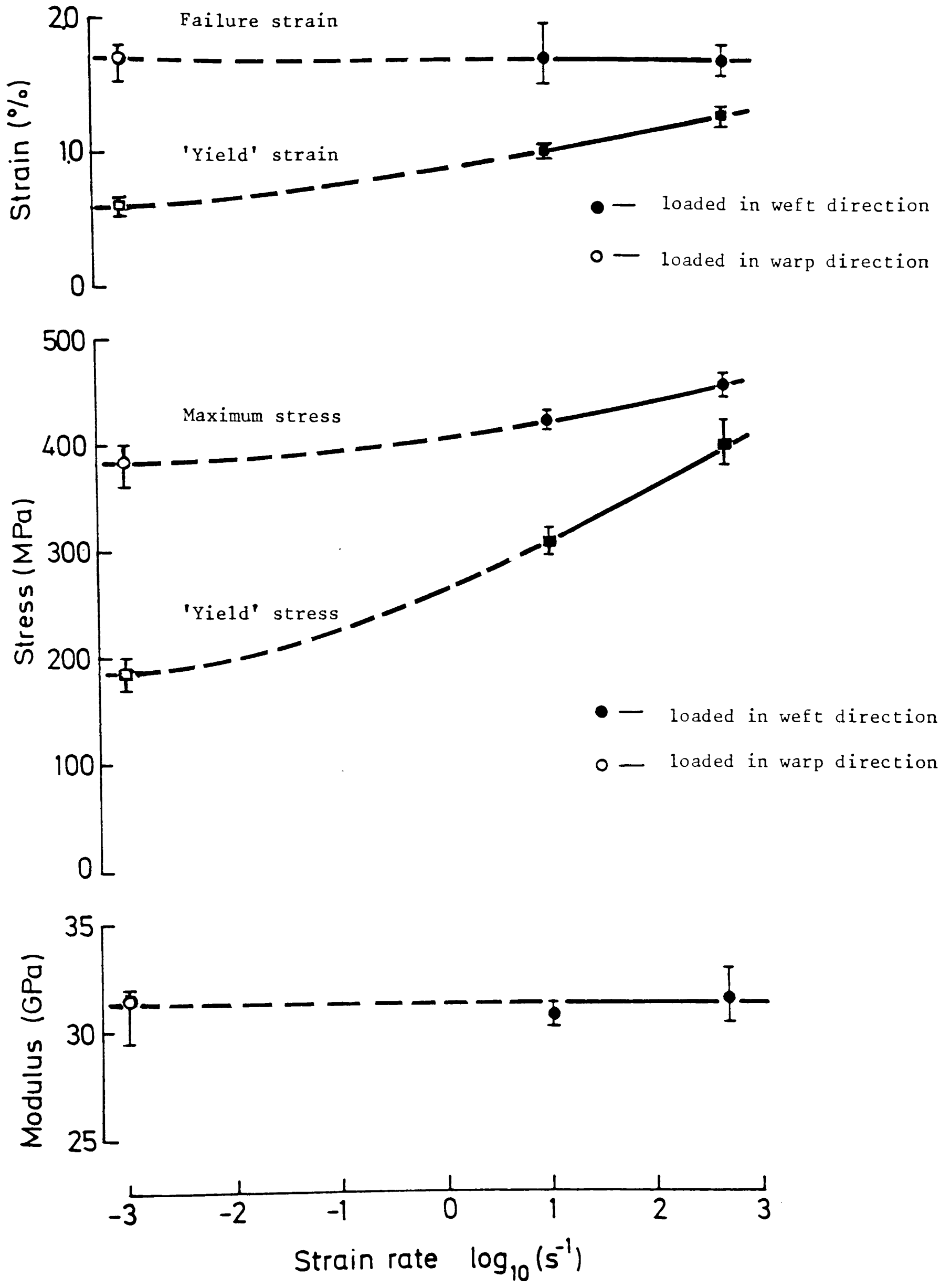

Fig.6.10 EFFECT OF STRAIN RATE ON TENSILE PROPERTIES OF TYPE 1 HYBRID SPECIMENS

a) Initial Modulus

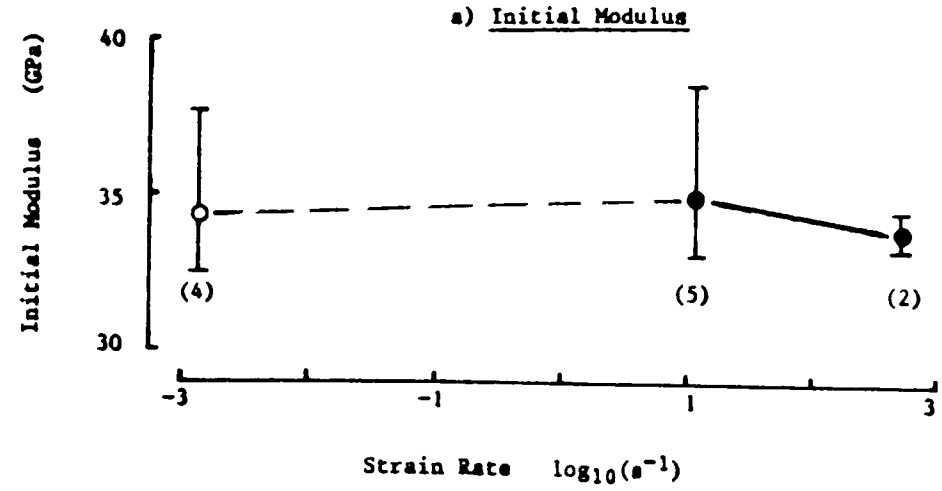

b) 'Yield' and Maximum Stress

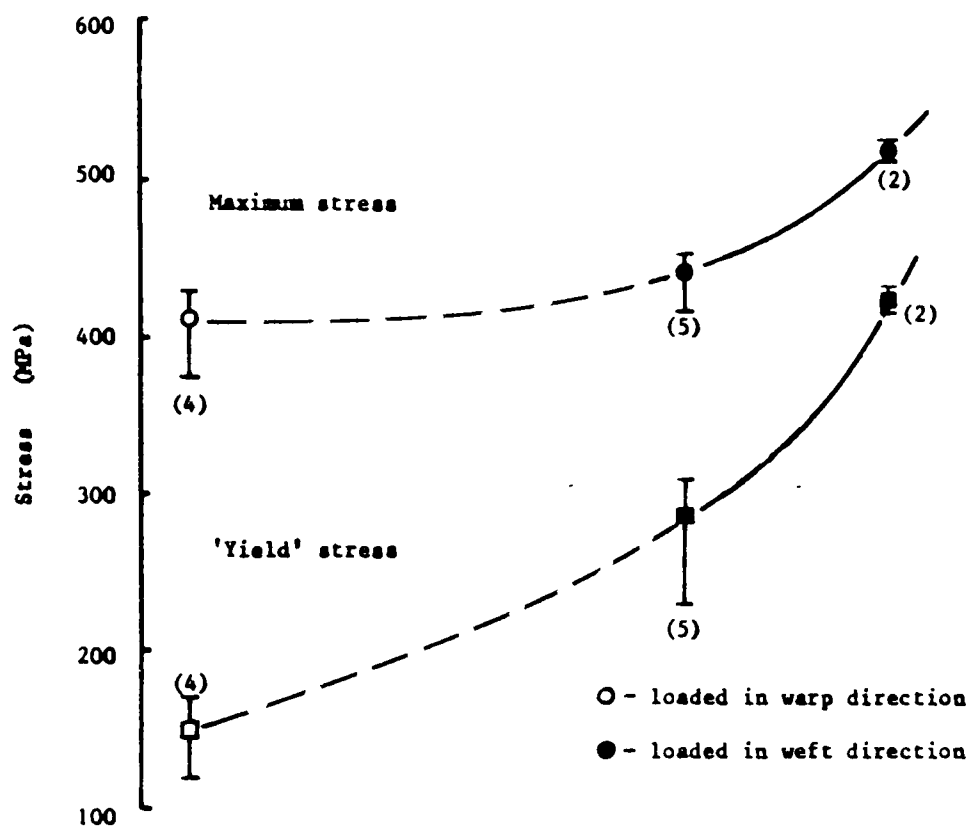

c) 'Yield' and Failure Strain

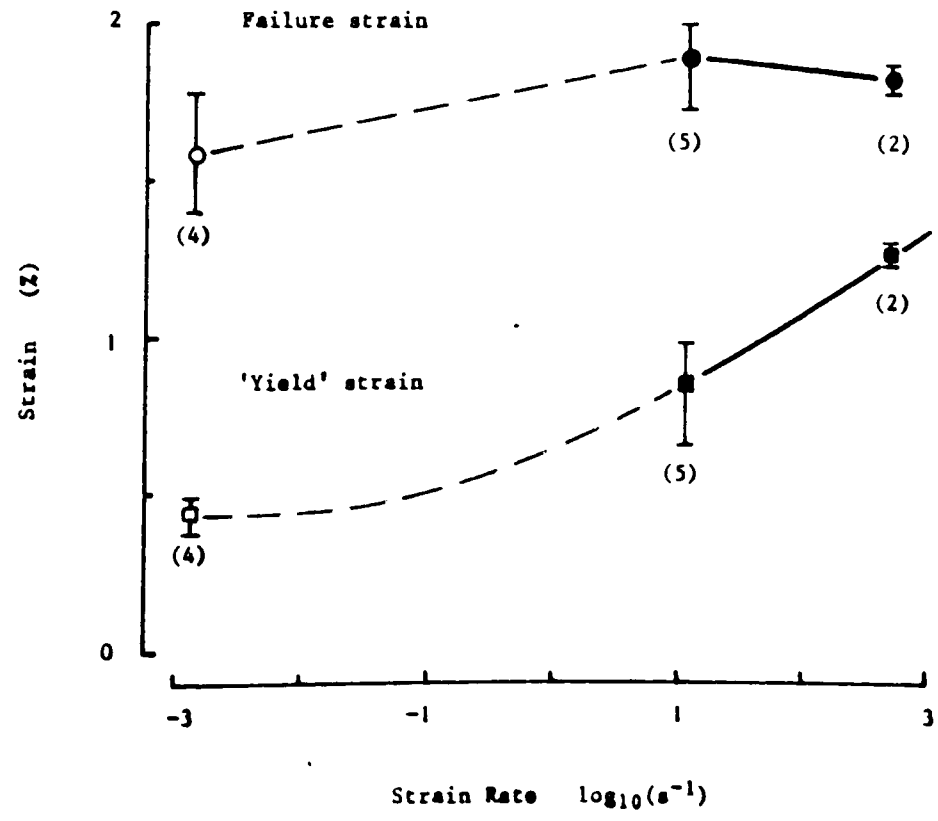

Fig.6.11 EFFECT OF STRAIN RATE ON TENSILE PROPERTIES OF TYPE 2a HYBRID SPECIMENS

a) Initial Modulus

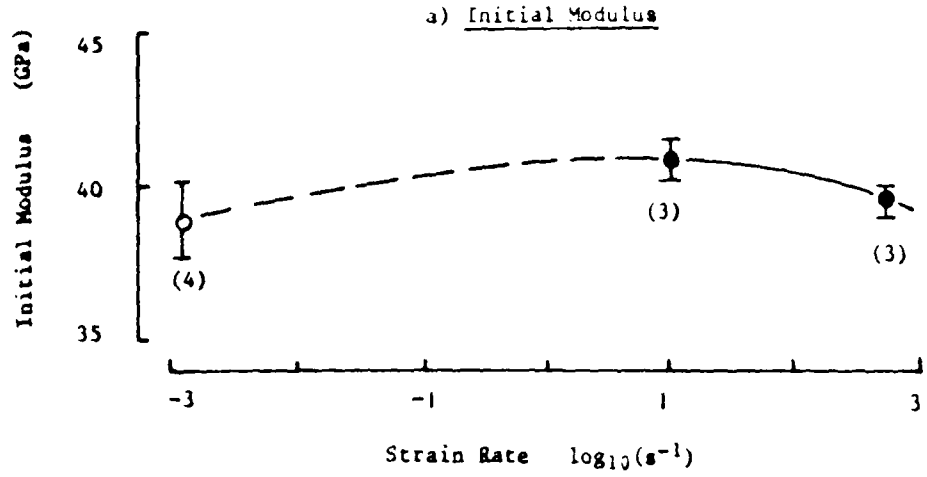

b) 'Yield' and Maximum Stress

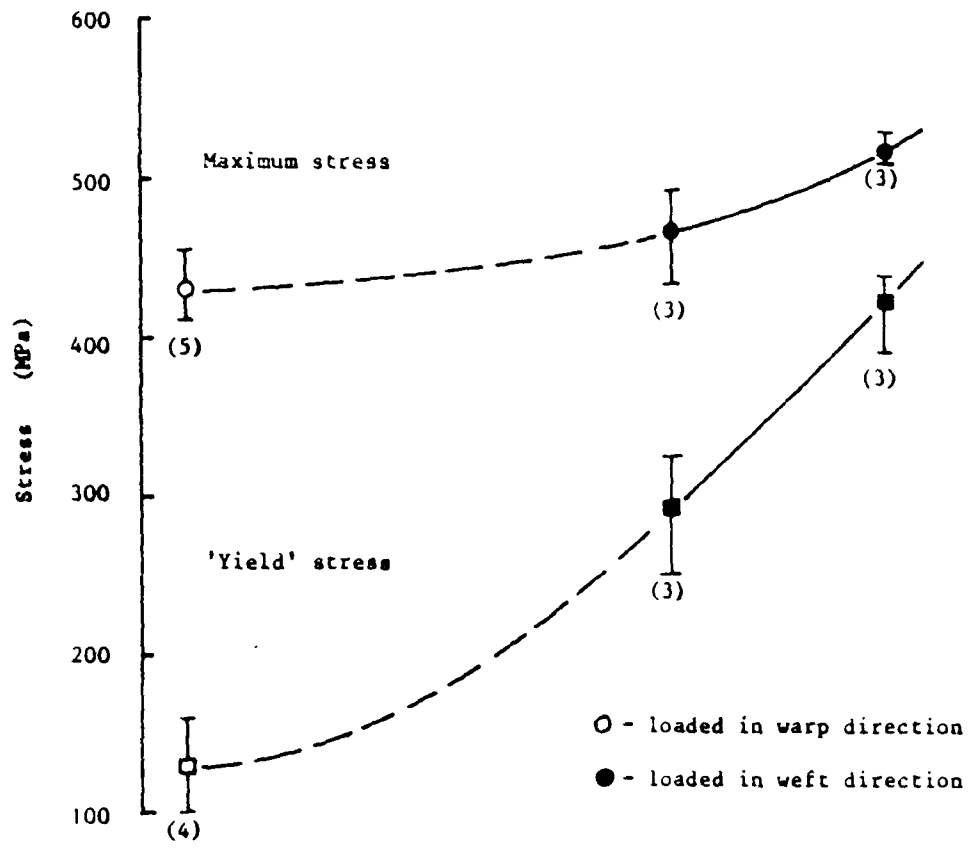

c) 'Yield' and Failure Strain

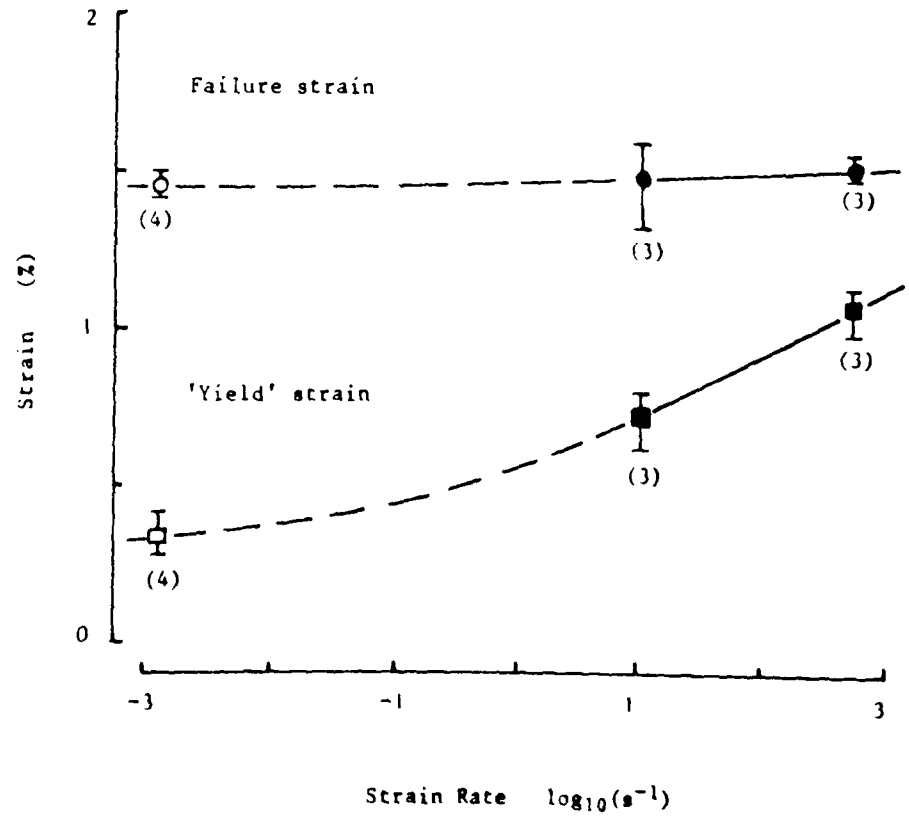

Fig.6.12 EFFECT OF STRAIN RATE ON TENSILE PROPERTIES OF TYPE 2b HYBRID SPECIMENS

in quasi-static tests, see Fig. 5.1, and both the all-glass and the all-carbon plies show an increased modulus with strain rate it would seem at first sight unlikely that the hybrid moduli would reach the rule of mixtures and laminate theory predictions in the impact tests. This is confirmed in Fig. 5.2 for the type 2a and type 2b hybrids which have moduli falling significantly below both the rule of mixtures and laminate theory predictions, by about 10% and 6% respectively, but not for type 1 hybrids where the experimentally determined modulus agrees well with both laminate and rule of mixture predictions.

For the all-glass specimens, Fig. 6.8b, both the yield stress and the maximum stress increase continuously with strain rate, there being no effect of loading direction on the former but a significant effect on the latter (this being, in fact, the indication of which are the warp and the weft directions). In contrast, for the all-carbon specimens, Fig. 6.9b, the maximum stress only begins to increase at the highest rate of strain while the yield stress shows a much more marked increase with strain rate at all rates. Thus, while for the all-glass specimens there is a modest increase in the elastic range and a much greater increase in the extent of the subsequent deformation as the strain rate is raised, the all-carbon specimens show the opposite effect with a markedly increased elastic range and a reduced anelastic deformation leading, at the highest strain rates, to a stress-strain curve which is linear elastic almost through to final failure. The hybrid specimens, as might be expected, showed a response intermediate between these two extremes but tending towards that of the all-carbon specimens. With increasing carbon content the yield stress becomes

more markedly strain rate dependent while the maximum stress only exhibits a significant rate dependence at high strain rates.

A similar contrast is apparent when considering the effect of strain rate on the strain at yield and at fracture. Thus, for all-glass specimens, Fig. 6.8c, the failure strain is almost doubled between the quasi-static and the impact tests, closely similar results being obtained for the warp and weft directions, while the yield strain increases only very slightly with strain rate. For the all-carbon specimens, however, Fig. 6.9c, it is the yield strain which is doubled while the failure strain shows a slight decrease at the highest strain rates, although the large experimental scatter prevents any great significance from being placed on this observation. Again all three hybrids, Figs. 6.10c, 6.11c and 6.12c, show a behaviour tending towards that of the all-carbon specimens with a significantly rate dependent yield strain but, apart from hybrid type 2a, no effect of strain rate on the failure strain. This reinforces the previous conclusion that, at least under uniaxial tensile loading, the failure strain in the hybrids is controlled by the same process as in the all-carbon specimens even though the presence of the glass-reinforced plies allows some increase in the absolute value of failure strain, see Fig. 6.5.

6.5 Impact Performance of Various Specimen Types

From the optical and scanning electron micrographs discussed in section 4.4 the following comments concerning the impact response of the various types of specimen may be made:

The woven-carbon/epoxy composite is brittle and absorbs relatively little energy compared to the woven-glass/epoxy composite.

The impact performance of the interlaminated hybrid composite based on woven reinforcements of differing geometries is controlled by the low elongation phase under tensile impact.

This conclusion is in accord with the general shape of the stress-strain curves in Fig. 4.11 and the variation of fracture strain with volume fraction of carbon reinforcing plies, Fig. 6.5.

The controlling effect of the low elongation (All-carbon composite) phase on the overall failure strain under impact tension agrees with the behaviour generally reported at quasi-static rates. Among other factors which have been found to affect the mechanical response at quasi-static rates are the lay-up configuration in dispersed fibre ply hybrids and intimacy of mixing of the constituent fibres in dispersed fibre hybrids. For the former a greater hybrid effect, defined as the enhancement of the failure strain of the low elongation phase, has been reported [155] when the outer surface is glass, rather than carbon, reinforced. Applied to the present impact tests this would imply a superior response for type 1 and type 2a hybrids over that for type 2b. While, on the average, this may be seen to be the case, the effect is small and may be due, in part, to the different carbon volume fractions for the three types of specimen.

As regards the intimacy of mixing in dispersed fibre hybrids it has generally been observed [156] that the more intimate the mixing of the

different fibre types the greater the hybrid effect. To test this for woven-reinforced materials would require the use of hybrid reinforcing mats where adjacent fibre tows are of alternating fibre types.

The present result, that under tensile impact the presence of the low elongation carbon reinforcing fibres prevents a full realisation of the energy absorbing potential of the glass reinforced plies, clearly follows from the specific combination of fine-weave glass and coarse-weave carbon reinforcement used and the application of a simple uniaxial tensile loading. Under this loading system both types of ply are constrained to extend by the same amount. The same constraint does not apply to other loading systems, e.g. to bending or to transverse impact loading. In such cases a greater hybrid effect might be expected if the glass plies were used in those regions of the specimen undergoing the higher elongations.

CHAPTER 7

CONCLUSIONS AND SUGGESTIONS FOR FURTHER WORK

The objectives of the research reported here were stated in section 1.8, and have in the main been accomplished. The following conclusions are drawn from the various aspects of the work.

The extended tensile impact machine in which the impact loading is applied through a projectile accelerated by a small gas gun is adequate for testing most FRP materials at strain rates of the order of $\sim 10^3$/s without recourse to a supplementary elastic test.

Analysis based on elementary one dimensional wave theory has shown that for a relatively thick specimen of a low-modulus glass-reinforced composite, ie. the worst case, the effect of stress-wave reflections in the grip regions on the tensile stress-strain response is negligibly small.

Reasonably good agreement between the stress levels determined at the specimen input and output interfaces is obtained, confirming that a uniform stress state in the specimen is attained early in the course of the test.

Using strain gauges attached directly to the parallel gauge section of the specimen an independent check of the specimen strain during elastic deformation has been made and the validity of the Hopkinson-bar strain measurement technique used in these tests, and hence of the computed modulus has been confirmed.

A modification to the gas gun loading system provides access to the specimen in the course of the test and facilitates other studies like temperature effects and in-situ fracture behaviour through high speed photography.

Room temperature stress-strain curves at three strain rates from quasi-static ($\sim 10^{-3}$/s) to impact ($\sim 10^{3}$/s) have been obtained for epoxy specimens reinforced with plain-weave fabrics of either carbon or glass or with several hybrid combinations of the two in various lay-ups, giving five different weight fractions of reinforcement from all-carbon to all-glass. An increase in initial modulus with hybrid composition (volume fraction of carbon reinforced plies) is observed at all strain rates. Also at the three strain rates, specimens with volume fractions in the approximate range 0.6 to 0.7 exhibit the so-called hybrid effect ie. an enhancement of failure strain over that for the all-carbon plies and an increased failure strength, especially under tensile impact, over that predicted by the rule of mixtures.

In interlaminated woven-reinforced carbon/glass/epoxy hybrid composites, the full energy absorbing potential of the glass constituent under dynamic loading conditions may not be achieved because of the early failure of the low elongation carbon plies.

The classical laminated plate theory and the rule of mixtures give accurate predictions of the initial modulus of hybrid specimens under uniaxial tension at both quasi-static and impact loading rates. Used in conjunction with Tsai-Wu strength criterion the laminate theory is useful in

predicting hybrid composite failure strengths in quasi-static or dynamic tension.

Suggestion for Further Work

Providing fundamental information on the impact response of composite materials is not an easy task because of the conflicting requirements reviewed in Chapter 1. In composite work, however, it is necessary to study independently a wide range of variables (ie. fibre volume fraction, stacking sequence, reinforcement geometry etc.). Specimen configurations and reinforcement lay-ups which would make this possible need to be developed. In particular it would be useful to be able to determine the effect of strain rate on the interlaminar failure strength both under shear and normal stress systems for use in numerical modelling of composite impact response.

All the work reported on here has dealt with woven material. However, analytical techniques are more simply applied to unidirectionally reinforced material. Assuming that a suitable specimen design can be evolved to obtain a tensile failure in such materials, laminated hybrid composites based on unidirectionally reinforced plies could be used in the impact tests. The classical laminated plate theory is more easily applied to such materials, and lay-ups of the angle ply or the cross-ply types are widely used in practice and should therefore be studied under impact loading.

The stiffness matrices determined in this work suitably transformed, could be applied to other situations in which there are relative orientations between the plies.

On the experimental side attempts should be made to reduce the stress fluctuations which appear on the initial part of the tensile loading wave in the modified gas gun and which appears to be related to the design of the fixing at the loading block/loading bar interface.

REFERENCES

1. Hancock, P. and Hockenhull, B.S., "Metals for Aerospace Applications", JBIS, 25, 125-152 (1972).

2. Gordon, J.E., "The new science of strong materials", Chap.8, Penguin Books, Middlesex, (1968).

3. Hull, D., "An introduction to composite materials", Chap.1, Cambridge University Press, Cambridge (1981).

4. Hancox, N.L., "High Performance Composites with Resin Matrices", in Handbook of Composites, 4, Chap.1, Kelly, A. and Mileiko, S.T. eds., Elsevier Science Publishers, Amsterdam (1983).

5. Cottrell, A.H., Contemp. Phys. 8, 1-3 (1967).

6. Kelly, A., "Strong Solids", Chap.5, Clarendon Press, Oxford (1973).

7. Holister, G.S. and Thomas, C., "Fibre Reinforced Materials", Chap.2, Elsevier Publishing Co., London (1966).

8. McGeehin, P., "Composites in Transportation", Materials in Engineering, 3, 378-387 (1982).

9. Hughes, J.D.H., "Composite Materials" - Part 2: Fibres for reinforcement, Metals and Materials, 2, 365-368 (1986).

10. Calcote, L.R., "The Analysis of Laminated Composite Structures", Chap.1, Van Nostrand Reinhold Co., New York (1969).

11. Sridhar, M.K., Basavarappa, G., Kasturi, S.G. and Balasubramanian, N., "Mechanical Properties of Jute-Polyester Composites", Indian J. Tech., 22, 213-215 (1984).

12. Seigel, H.J. and Juergens, R.J., "Composite materials and the challenge of business renewal", in Proc. Materials in Aerospace, 2, R. Aero. Soc., London, 424-439 (1986).

13. Knox, C.E., "Fiberglass Reinforcement", in Handbook of Composites, Chap.8, Lubin, G. ed., Van Nostrand Reinhold Co., New York (1982).

14. Schwartz, M.M., "Composite Materials Handboook", Chap.2, McGraw-Hill Book Co., New York (1984).

15. McCrum, N.G., "A review of the science of Fibre Reinforced Plastics", Chap.2, H.M.S.O., London (1971).

16. Watt, W. and Phillips, L.N., "Carbon fibres for engineering applications", Proc. I. Mech. E., 185, 52/71, 783-806 (1970-71).

17. Thomas, D.K., "Materials in Aerospace - A General Review", in Proc. Materials in Aerospace, 1, R. Aero. Soc., London, 1-16 (1986).

18. Ward, I.M., "Ultra-high modulus polyolefins", Phil. Trans. R.Soc. Lond., A294, 473-482 (1980).

19. Magat, E.E., "Fibres from extended chain aromatic polyamides", ibid, A294, 463-472 (1980).

20. Harris, B., "Engineering Composite Materials", Chap.1, The Inst. of Metals (1986).

21. Hancox, N.L., "Composite Materials" - Part 3: Matrices for composite materials, Metals and Materials, 2, 435-437 (1986).

22. Belbin, G.R., "Thermoplastic structural composites - a challenging opportunity", Proc. I. Mech. E., 198B, 71-81 (1984).

23. Cogswell, F.N. and Leach, D.C., "Thermoplastic Composites", in Proc. Materials in Aerospace, 1, R. Aero. Soc., London, 75-87 (1986).

24. Weatherhead, R.G., "FRP Technology", Chapters 9-13, Applied Science Publishers, London (1980).

25. Cooper, G.A. and Kelly, A., "Role of the Interface in the Fracture of Fiber-Composite Materials", ASTM STP 452, 90-106 (1969).

26. Curtis, P.T. and Morton, J., "The Effect of Fibre Surface Treatment on the compressive strength of CFRP Laminates", in Progress in Science and Engineering of Composites, Hayashi, T., Kawata, K. and Umekawa, S. eds., ICCM-IV, 219-226 (1982).

27. Broutman, L.J., "Measurement of the Fiber-Polymer Matrix interfacial strength", Interfaces in Composites, ASTM STP 452, 27-41 (1969).

28. Plueddemann, E.P., "Silane Coupling Agents", Chap.1, Plenum Press, New York (1982).

29. Varma, D.S., Needles, H.L., Kourtides, D.A. and Fish, R.H., "Interlaminar shear properties of Graphite Fiber, High-Performance Resin Composites", Polymer Composites, 4, 98-103 (1983).

30. Goan, J.C. and Prosen, S.P., "Interfacial Bonding in Graphite Fiber-Resin Composites", Interfaces in Composites, ASTM STP 452, 3-26 (1969).

31. Green, A.K. and Phillips, L.N., "Non-aerospace applications of carbon and other high-performance fibre materials and their hybrids", Materials in Engineering Applications, 1, 59-65 (1978).

32. Powell, P.C., "Engineering with Polymers", Chap.7, Chapman and Hall, London (1983).

33. "Reinforced Composites compete with metals as engineering materials", Plastics World, 33, No.5, p.43 (1975).

34. Smith, C.S., "Applications of fibre reinforced composites in marine technology", N.P.L. Conf., Composite standards, testing and design, 54-69 (1974).

35. Dorey, G., "Fracture Behaviour and Residual Strength of Carbon Fibre Composites Subjected to Impact Loads", AGARD, Conf. Proc. No. 163, 8-1 to 8-6, Munich (1974).

36. Daniel, I.M., LaBedz, R.H. and Liber, T., "New Method for Testing Composites at Very High Strain Rates", Exptl. Mech., 21, 71-77 (1981).

37. Davies, R.G. and Magee, C.L., "The Effect of Strain-Rate Upon the Tensile Deformation of Materials", J. Eng. Mater. Tech., Trans ASME, Series H, 97, 151-155 (1975).

38. Raymond, J.A., "Carbon Fibre Reinforcing", Plastics, design engineering series, 1, 121-129, Morgan-Grampian Publishers (1970).

39. Knight, B.W., "Glass Reinforced Plastics", ibid, 1, 103-119 (1970).

40. Ellis, C.D. and Harris, B., "The Effect of Specimen and Testing Variables on the Fracture of Some Fibre Reinforced Epoxy Resins", J. Composite Materials, 7, 76-88 (1972).

41. Novak, R.C. and Decrescente, M.A., "Impact Behavior of Unidirectional Resin Matrix Composites Tested in the Fiber Direction", ASTM STP 497, 311-323 (1972).

42. Hancox, N.L. and Wells, H., "Izod impact properties of carbon fibre / glass-fibre sandwich structures", Composites, 4, 26-30 (1973).

43. Adams, D.F. and Perry, J.L., "Static and Impact Behaivor of Graphite/Epoxy Composite Laminates Containing Third-Phase Reinforcement Materials", J. Testing and Evaluation, 5, 114-123 (1977).

44. Bucknall, C.B., "Toughened Plastics", Chap.10, Applied Science Publishers, London (1977).

45. Nicholas, T., "Instrumented Impact Testing Using a Hopkinson Bar Apparatus", Technical Report No. AFML-TR-75-54, United States Air Force, (1975).

46. Ireland, D.R., "Procedures and Problems Associated with Reliable Control of the Instrumented Impact Test", ASTM STP 563, 3-29 (1974).

47. Ruiz, C., "Inertial analysis of the Charpy test", Oxford University Engineering Laboratory Report No. 1571/85 (1985).

48. Dorey, G., Sidey, G.R. and Hutchings, J., "Impact properties of Carbon fibre/Kevlar 49 fibre hybrid composites", Composites, 9, 25-32 (1978).

49. Winkel, J.D. and Adams, D.F., "Instrumented Drop Weight Impact Testing of Composite Materials", University of Wyoming, Mech. Eng. Dept., Report No. UWME-DR-301-108-0 (1983).

50. Johnson, A.E., Moore, D.R., Prediger, R.S., Reed, P.E. and Turner, S., "The falling weight impact test applied to some glass-fibre reinforced nylons", J. Mater. Sci., 21, 3153-3161 (1986).

51. Ewins, P.D., "Tensile and Compressive Test Specimens for Unidirectional Carbon Fibre Reinforced Plastics", RAE Technical Report No. 71217 (1971).

52. Dootson, M., "The design of specimens for the measurement of the mechanical properties required to characterise a unidirectional CFRP material under static short term loading", B.A.C. Report No. S.O.N. (P) 86 (1972).

53. Klepaczko, J.R., Bassim, M.N. and Hsu, T.R., "Fracture toughness of coal under quasi-static and impact loading", Engineering Fracture Mechanics, 19, 305-316 (1984).

54. Bhargava, J. and Rehnstrom, A, "Dynamic Strenth of Polymer Modified and Fiber-Reinforced Concretes", Cement and Concrete Research, 7, 199-208 (1977).

55. Griffiths, L.J. and Martin, D.J., "A study of the behaviour of a carbon fibre composite using the split Hopkinson pressure bar", J. Phys. D. Appl. Phys., 7, 2329-2341 (1974).

56. Hauser, F.E., "Techniques for Measuring Stress-Strain Relations at High Strain Rates", Exptl. Mech., 6, 395-402 (1966).

57. Lindholm, U.S. and Yeakley, L.M., "High Strain-rate Testing: Tension and Compression", Exptl. Mech., 8, 1-9 (1968).

58. Sierakowski, R.L., Nevill, G.E., Ross, C.A. and Jones, E.R., "Dynamic Compresive Strength and Failure of Steel Reinforced Epoxy Composites", J. Composite Materials, 5, 362-377 (1971).

59. Daniel, I.M. and Liber, T., "Testing of Fiber Composites at high strain rates", Proc. ICCM 2, Norton, B., Signorelli, R., Street, K. and Phillips, L. eds., 1003-1018, Toronto (1978).

60. Bai, Y. and Harding, J., "Fracture initiaton in glass-reinforced plastics under impact compression", Proc. Int. Conf. on Structural Impact and Crash-worthiness, Imperial College, London, 2, 482-493 (1984).

61. Parry, T., Oxford University Engineering Laboratory (unpublished work).

62. Harding, J., "The effect of dynamic loading on the mechanical properties of glass-reinforced platics", Oxford University Engineering Laboratory Report No. 1042/72 (1972).

63. Parry, T. and Harding, J., "The failure of glass-reinforced composites under dynamic torsional loading", Oxford University Engineering Laboratory Report No. 1365/81 (1981).

64. Werner, S.M. and Dharan, C.K.H., "The Dynamic Response of Graphite Fiber-Epoxy Laminates at High Shear Strain Rates", J. Composite Materials, 20, 365-374 (1986).

65. Kawata, K., Hondo, A., Hashimoto, S., Takeda, N. and Chung, H.L., "Dynamic Behaviour Analysis of Composite Materials", Proc. Japan-US Conf. on Composite Materials, Kawata, K. and Akasaka, T. eds., 2-11, Japan Soc. for Composite Materials, Tokyo (1981).

66. Harding, J. and Welsh, L.M., "Impact Testing of Fibre-Reinforced Composite Materials", in Progress in Science and Engineering of Composites, Hayashi, T., Kawata, K. and Umekawa, S. eds., ICCM-IV, 845-852, Tokyo (1982).

67. Harding, J. and Welsh, L.M., "A tensile testing technique for fibre-reinforced composites at impact rates of strain", J. Mater, Sci., 18, 1810-1826 (1983).

68. Harding, J., Wood, E.O. and Campbell, J.D., "Tensile testing of materials at impact rates of strain", J. Mech. Engng. Sci., 2, 88-96 (1960).

69. Kokoshvili, S.M. and Kalnin, P.P., "Construction of the Stress-Strain Dependence for Glass-Reinforced Plastics from an Experimental Study of Impact-Wave Processes", Polymer Mechanics, 10, 602-606 (1974).

70. Rotem, A. and Lifshitz, J.M., "Longitudinal strength of unidirectional fibrous composite under high rate of loading", Proc. 26th Annual Tech. Conf. of the S.P.I., Reinforced Plastics/Composites Divison, Paper 10-G, 1-10, New York (1971).

71. Fujii, T. and Miki, M., "A study on impact behavior of unidirectional fiber reinforced plastics", Proc. Symposium on Mechanical Behaivour of Materials, 83-91, Kyoto (1973).

72. Harding, J., "The effect of high strain rate on material properties", Oxford University Engineering Laboratory Report No. 1627/86 (1986).

73. Back, P.A.A. and Campbell, J.D., "The behaviour of a reiforced plastic material under dynamic compression", Proc. Conf. Prop. Mater. at High Rates of Strain, 221-228, I. Mech. E., London (1957).

74. Lindholm, U.S., "Some Experiments with the split Hopkinson Pressure Bar", J. Mech. Phys. Solids, 12, 317-335 (1964).

75. Billington, E.W. and Brissenden, C., "Dynamic stress-strain curves for various plastics and fibre-reinforced plastics", J. Phys. D: Appl. Phys., 4, 272-286 (1971).

76. Welsh, L.M. and Harding, J., "Dynamic Tensile Response of Unidirectionally Reinforced Carbon Epoxy and Glass Epoxy Composites", Proc. 5th Int. Conf. on Composite Materials, 1517-1531, ICCM-V, TMS-AIME, San Diego (1985).

77. Harris, B., "The Strength of Fibre Composites", Composites, 3, 152-167 (1972).

78. Welsh, L.M. and Harding, J., "Effect of strain rate on the tensile failure of woven reinforced polyester resin composites", Proc. DYMAT 85, Int. Conf. on Mech. and Physical Behaviour of Materials under Dynamic Loading, Jour. de Physique, Colloque C5, 405-414 (1985).

79. Armenakas, A.E. and Sciammarella, C.A., "Response of glass-fiber reinorced epoxy specimens to high rates of tensile loading", Exptl. Mech., 13, 433-440 (1973).

80. Dew-Hughes, D and Way, J.L., "Fatigue of fibre reinforced plastics: a reivew", Composties, 4, 167-173 (1973).

81. Harris, B. and Bunsell, A.R., "Impact properties of glass fibre/carbon fibre hybrid composites", Composites, 6, 197-201 (1975).

82. Adams, D.F. and Perry, J.L., "Low Level Charpy Impact Response of Graphite/Epoxy Hybrid Composties", J. Engng. Mater. Tech., 99, 257-263 (1977).

83. Kawata, K., Hashimoto, S., Takeda, N. and Sekino, S., "On High-Velocity Brittleness and Ductility of Dual-Phase Steel and Some Hybrid Fiber Reinforced Plastics", ASTM STP 864, 700-711 (1985).

84. Harding, J., "The effect of the rate of loading on the deformaton of some metals", D.Phil. Thesis, Department of Engineering Science, Oxford University (1960).

85. Cooper, R.H. and Campbell, J.D., "Testing of Materials at Medium Rates of Strain", J. Mech. Eng. Sci., 9, 278-284 (1967).

86. Cilley, E., Roylance, D. and Schneider, N., "Methods of Fiber and Void Measurement in Graphite/Epoxy Composites", ASTM STP 546, 237-249 (1974).

87. Agarwal, B.D. and Broutman, L.J., "Analysis and Performance of Fiber Composites", Chap.2, John Wiley and Sons, New York (1980).

88. Purslow, D., "On the optical assessment of the void content in composite materials", Composites, 15, 207-210 (1984).

89. Jones, M.L.C. and Hull, D., "Microscopy of failure mechanisms in filament wound pipe", J. Mater. Sci., 14, 165-174 (1979).

90. Tuttle, M.E. and Brinson, H.F., "Resistance Strain-gage Technology as Applied to Composite Materials", Exptl. Mech., 24, 54-65 (1984).

91. Pink, E. and Campbell, J.D., "Deformation characteristics of reinforced epoxy resin", Part 1: The mechanical properties, J. Mater. Sci., 9, 658-664 (1974).

92. Sims, D.F., "In-Plane Shear Stress-Strain Response of Unidirectional Composite Materials", J. Compos. Mater., 7, 124-128 (1973).

93. Yeow, Y.T. and Brinson, H.F., "A comparison of simple shear characterization methods for composite laminates", Composites, 9, 49-55 (1978).

94. Van Gemert, D., "Direct Shear Compliance Measurement for Fibre Reinforced Composites", Colloquium on Mechanical Characterisation of Load Bearing Fibre Composite Laminates, A.H. Cardon and G. Verchery eds., 191-198, Brussels (1984).

95. Pindera, M.J. and Herakovich, C.T., "Shear Characterization of Unidirectional Composites with the Off-Axis Tension Test", Exptl. Mech., 26, 103-112 (1986).

96. Fowser, S.W., Pipes, R.B. and Wilson, D.W., "On the Determination of Laminate and Lamina Shear Response by Tension Tests," Comp. Sci. Tech., 26, 31-36 (1986).

97. Rosen, B.W., "A simple procedure for experimental determination of the longitudinal shear modulus of unidirectional composites", J. Compos. Mater., 6, 552-554 (1972).

98. Contributed by Measurements Group, Inc., Raleigh, NC., "Errors due to transverse sensitivity in strain gages", Exptl. Techniques, 30-35, SESA Publicaton (1983).

99. Woolstencroft, D.H., Curtis, A.R. and Haresceugh, R.I., "A comparison of test techniques used for the evaluation of the unidirectional compressive strength of carbon fibre-reinforced plastic", Composites, 12, 275-280. (1981).

100. Kolsky, H., "An investigation of the Mechanical Properties of Materials at very High Rates of Loading", Proc. Physical Soc., London, B62, 676-700 (1949).

101. Smith, C.B., "Some New Types of Orthotropic Plates Laminated of Orthotropic Material", J. Appl. Mech., 20, 286-288 (1953).

102. Lekhnitskii, S.G., "Anisotropic Plates", Chap.9, Gordon and Breach, New York (1968).

103. Reissner, E. and Stavsky, Y., "Bending and Stretching of Certain Types of Heterogeneous Aeolotropic Elastic Plates", J. Appl. Mech., 28, 402-408 (1961).

104. Whitney, J.M. and Leissa, A.W., "Analysis of Heterogeneous Anisotropic Plates", J. Appl. Mech., 36, 261-266 (1969).

105. Azzi, V.D. and Tsai, S.W., "Elastic Moduli of Laminated Anisotropic Composites", Exptl. Mech., 9, 177-185 (1965).

106. Kikukawa, H. and Takaki, J., "Experimental Investigation of Anisotropic Laminate Structural Behaviour", in Progress in Science and Engineering of Composites, Hayashi, T., Kawata, K. and Umekawa, S. eds., ICCM-IV, 405-412, Tokyo (1982).

107. Ishikawa, T. and Chou, T.-W., "Stiffness and Strength Behaviour of Woven Fabric Composites:, J. Mater. Sci., 17, 3211-3220 (1982).

108. Curtis, P.T. and Bishop, S.M., "An Assessment of the potential of Woven-Carbon Fibre-Reinforced Plastics for High Performance Applications", Composites, 15, 259-265 (1984).

109. Tsai, S.W. and Wu, E.M., "A General Theory of Strength for Anisotropic Materials", J. Composite Materials, 5, 58-80 (1971).

110. Hearmon, R.F.S., "An Introduction to Applied Anisotropic Elasticity", Chap.1, Oxford University Press, Oxford (1961).

111. Love, A.E.H., "A Treatise on the Mathematical Theory of Elasticity", Chap.III, Dover Publications, New York (1944).

112. Jones, R.M., "Mechanics of Composite Materials", Chap.2, Scripta Book Co., New York (1975).

113. Christensen, R.M., "Mechanics of Composite Materials", Chap.5, Wiley-Interscience, New York (1979).

114. Norris, C.B., "The Elastic Theory of Wood Failure", Trans. Am. Soc. Mech. Engrs., 61, 251-261 (1939).

115. Hill, R., "A Theory of the Yielding and Plastic Flow of Anisotropic Metals", Proc. Roy. Soc. (London), Ser.A, 193, 281-297 (1948).

116. Azzi, V.D. and Tsai, S.W., "Anisotropic Strength of Composites", Exptl. Mech., 15, 283-288 (1965).

117. Marin, J., "Theories of Strength for Combined Stresses and Non-Isotropic Materials", J. Aeronautical Sciences, 24, 265-268 and 274 (1957).

118. Hoffman, O., "The Brittle Strength of Orthotropic Materials", J. Composite Materials, 1, 200-206 (1967).

119. Zakharov, K.V., "Strength Criteria for Laminated Plastics", Soviet Plastics, No.8, 51-53 (1961).

120. Gol'denblat, I.I. and Kopnov, V.A., "Strength of Glass Reinforced Plastics in the Complex Stress Rate", Polymer Mechanics, 1, No.2, 54-59 (1965).

121. Huang, C.-L. and Kirmser, P.G., "A Criterion of Strength for Orthotropic Materials", Fibre Science and Technology, 8, 103-112 (1975).

122. Protasov, V.D. and Kopnov, V.A., "Study of the Strength of Glass Reinforced Plastics in the Plane State of Stress", Polymer Mechanics, 1, No.5, 26-28 (1965).

123. Owen, M.J. and Rice, D.J., "Biaxial Strength Behaviour of Glass Fabric Reinforced Polyester Resins", Composites, 12, 13-25 (1981).

124. Sendeckj, G.P., "A Brief Survey of Empirical Multiaxial Strength Criteria for Composites", Composite Materials: Testing and Design (Second Conference), ASTM STP 497, 41-51 (1972).

125. Narayanaswami, R. and Adelman, H.M., "Evaluation of the Tensor Polynomial and Hoffman Strength Theories for Composite Materials", J. Composite Materials, 11, 366-377 (1977).

126. Liu, J.Y., "Evaluation of the Tensor Polynomial Strength Theory for Wood", ibid, 18, 216-226 (1984).

127. Collins, B.R. and Crane, R.L., "A Graphical Representation of the Failure Surface of a Composite", ibid, 5, 408-413 (1971).

128. Tsai, S.W. and Hahn, H.T., "Introduction to Composite Materials", Chap.7, Technomic Publishing Co., Westport Conn. (1980).

129. Kim, R.Y., "In-Plane Tensile Strength of Multidirectional Composite Laminates", in Progress in Science and Engineering of Composites, Hayashi, T., Kawata, K. and Umekawa, S. eds., ICCM-IV, 455-464, Tokyo (1982).

130. Tsai, S.W. and Azzi, V.D., "Strength of Laminated Composite Materials", A.I.A.A. Journal, 4, 296-301 (1966).

131. Yeow, Y.T. and Brinson, H.F., "An Experimental Investigation on the Tensile Moduli and Strengths of Graphite/Epoxy Laminates", Exptl, Mech., 17, 401-408 (1977).

132. Talreja, R., "Transverse Cracking and Stiffness Reduction in Composite Lamiantes", J. Composite Materials, 19, 355-375 (1985).

133. Kimpara, I., Takehana, M. and Hamamoto, A., "Analysis of Internal Failure Mechanism of Woven-Roving Composites", ICM-II, 1340-1344, Boston (1976).

134. Ishikawa, T., Matsushima, M. and Hayashi, Y., "Experimental Confirmation of the Theory of Elastic Moduli of Fabric Composites", J. Composite Materials, 19, 443-458 (1985).

135. Bunsell, A.R. and Harris, B., "Hybrid carbon and glass fibre composites", Composites, 5, 157-164 (1974).

136. Aveston, J. and Kelly, A., "Tensile first cracking strain and strength of hybrid composites and laminates", Phil. Trans. R. Soc. Lond. A294, 519-534 (1980).

137. Manders, P.W. and Bader, M.G., "The strength of hybrid glass/carbon fibre composites", J. Mater. Sci. 16, 2233-2245 (1981).

138. Kiselev, M.R., Zubov, P.I., Sukhareva, L.A., Zaborovskaya, E.E. and Dontsova, E.P., "Investigation of Internal Stresses in Glass-Reinforced Plastics", Polymer Mechanics, 1, No.1, 60-64 (1965).

139. Lempriere, B.M., "Uniaxial Loading of Orthotropic Materials", AIAA Journal, 6, 365-368 (1968).

140. Bert, C.W., Mayberry, B.L. and Ray, J.D., "Behavior of Fiber-Reinforced Plastic Laminates under Biaxial Loading", ASTM STP 460, 362-380 (1969).

141. Ratwani, M.M. and Kan, H.P., "Effect of Stacking Sequence on Damage Propagation and Failure Modes in Composite Laminates", ASTM STP 775, 211-228 (1982).

142. Mehan, R.L. and Mullin, J.V., "Analysis of Composite Failure Mechanisms Using Acousitc Emissions", J. Composite Materials, 5, 226-269 (1971).

143. Guild, F.J., Walton, D., Adams, R.D. and Short, D.", The application of acoustic emission to fibre-reinforced composite materials", Composites, 7, 173-179 (1976).

144. Garg, A. and Ishai, O, "Characterisation of damage initiation and propagation in graphite/epoxy laminates by acoustic emission", Eng. Fract. Mech., 22, 595-608 (1985).

145. Bessell, T.J. and Shortall, J.B., "The mechanical properties and fracture behaviour of unidirectionally reinforced nylon 6", J. Mater. Sci., 12, 365-372 (1977).

146. Smith, P.A., Gilbert, D.G. and Poursartip, A., "Matrix cracking of composites inside a scanning electron microscope", J. Mater. Sci. Lett., 4, 845-847 (1985).

147. Sato, N., Kurauchi, T. and Kamigaito, O., "In situ SEM observation of fracture process of carbon-fibre-reinforced epoxy resin compsite", ibid, 4, 1095-1098 (1985).

148. Purslow, D., "Matrix fractography of fibre-reinforced epoxy composites", Composites, 17, 289-303 (1986).

149. Elber, W., "Failure Mechanics in Low-Velocity Impacts on Thin Composite Plates", NASA Technical Paper 2152 (1983).

150. Adams, D.F., "A scanning electron microscopic study of hybrid composite impact response", J. Mater. Sci., 10, 1591-1602 (1975).

151. Hayes, S.V. and Adams, D.F., "Rate sensitive tensile impact properties of fully and partially loaded unidirectional composites", J. Testing and Evaluation, 10,61-68 (1982).

152. Saghizadeh, H. and Dharan, C.K.H., "Delamination Fracture Toughness of Graphite and Aramid Epoxy Composites", J. Eng. Mater. Tech., Trans ASME, Series H, 108, 291-295 (1986).

153. Bader, M.G., Bailey, J.E., Curtis, P.T. and Parvizi, A., "The Mechanisms of Initiation and Development of Damage in Multi-Axial

Fibre-Reinforced Plastics Laminates", ICM 3, 3, Miller, K.J. and Smith, R.F. eds., 227-239, Pergamon Press, Oxford (1979).

154. Altus, E. and Ishai, O., "Transverse Cracking and Delamination in the Failure Process of Composite Laminates", Comp. Sci. Tech., 26, 59-77 (1986).

155. Kretsis, G., Matthews, F.L., Morton, J. and Davies, G.A.O., "Basic Technology of Hybrid Composites", 1st Progress Report, May 1984, Department of Aeronautics, Imperial College, London.

156. Phillips, M.G., "Fracture and Fatigue of Hybrid Composites", in Fibre Composite Hybrid Materials, Hancox, N.L. ed., Applied Science Publishers, London, p 150 (1981).

APPENDIX 1 - Specification of the Electronic Instrumentation

SPECIFICATION	TRANSIENT	RECORDER	
	DL 902	DL 912	DL 922
SIGNAL INPUT:-			
Frequency Response	DC to o.4 MHz	DC to 6 MHz	DC to 6 MHz
Input range	100mV to 5V	100mV to 20V	100mV to 50V
A/D CONVERTER:-			
Resolution	8 bits (1 part in 256)	8 bits (1 part in 256)	8 bits (1 part in 256)
Conversion rate	1MHz maximum (40 µs/word)	20MHz maximum 30 ps/word)	20MHz maximum (50 ns/word)
MEMORY:-			
Memory size	2048 x 8 bit words	4096 x 8 bit words	2048 x 8 bit words
TIMEBASE:-			
Sweeptime	~ 2ms to 102.4s	~ 205µs to 8.2s	100µs to 4s

Fylde FE - 351 - UA Universal Amplifier

Input : ± 15V

Output: ± 10V

Gain x 20 to x 1000

Frequency Response : D.C. to 50KHz (-3dB), D.C. to 10 KHz (2%)

Slewing Rate : Full output up to 25 KHz

Common Mode Rejection : Greater than 100 dB, DC to 1 KHz

APPENDIX 2

Wave Analysis for Grip Regions

The loading-bar/specimen/output-bar assembly is shown in Fig. A2.1 divided into five regions of different effective acoustic impedance. If the change in impedance between regions 1 and 2 and between regions 4 and 5 is sufficiently great, stress waves may be reflected at these interfaces, giving the wave propagation pattern shown schematically in the figure. Both the input and the output bars have a diameter of 3/8 in (9.525 mm) and both are centreless ground, the former from an annealed IMI318 titanium alloy and the latter from an annealed phosphor bronze alloy. The corresponding values of density, ρ, Youngs modulus, E, longitudinal elastic wave speed, c, acoustic impedance, ρc, and driving point impedance, ρcA (where A is the cross-sectional area), are listed in Table A2 below. Also included in the Table are similar data for a woven-glass reinforced epoxy composite specimen loaded in the 45^{o} orientation taken from earlier work [67]. In the grip regions, i.e. regions 2 and 4, effective values of density and modulus are derived using the rule of mixtures and the relative areas of cross-section of the bar and the specimen. The effective wave speed is then taken as $\sqrt{E/\rho}$ in the normal way.

Table A2 Estimated Impedances for Loading-Bar/Specimen Assembly

Region		1	2	3	4	5
ρ	(kg/m^3)	4431	3260	1885	5676	8906
c	(m/s)	5106	4660	3116	3554	3627
E	(GPa)	115.5	70.8	18.3	71.7	117.2
ρc	($kg/m^2\mu s$)	22.62	15.19	5.87	20.17	32.30
ρcA	(kg/s)	1612	1083	192.5	1437	2302

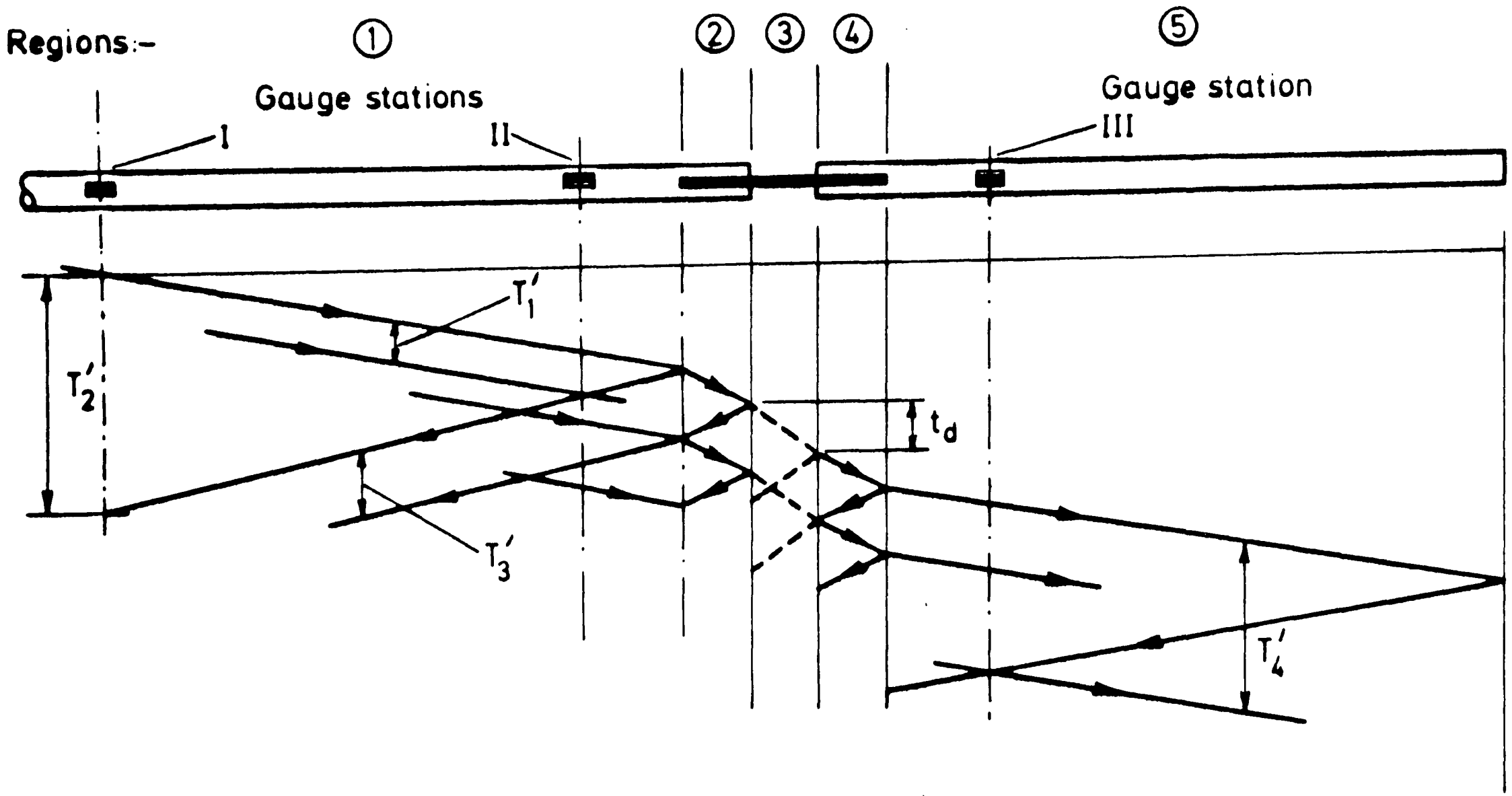

Fig. A2.1 LOADING-BAR/SPECIMEN/OUTPUT-BAR ASSEMBLY AND LAGRANGE DIAGRAM FOR WAVE REFLECTIONS IN SPECIMEN GRIP REGIONS

To analyse for the effect of reflected waves in the grip region of the input bar the method of characteristics is used, as illustrated in Fig. A2.2. Referring to this figure, for all points between A and C, corresponding to the position of gauge station II, the input wave at times $<T_1'$ is given by

$$\alpha_1 = E\varepsilon_I = E\varepsilon_{II} \qquad \text{(A2.1)}$$

while for all points along ACC_1C_2 ...., to the limiting time T_2', the relation

$$\alpha_1 = E\varepsilon_I \qquad \text{(A2.2)}$$

still holds.

At the interface between the loading-bar and the grip region, i.e. for points along BDD_1... in Fig. A2.2 for times $<T_3'$ elementary one-dimensional longitudinal elastic wave theory gives the relations

$$\alpha_2 = \{2Z_2/(Z_2 + Z_1)\}\ (A_1/A_2)\alpha_1 \qquad \text{(A2.3)}$$

$$\beta_1 = \{(Z_2 - Z_1)/(Z_2 + Z_1)\}\alpha_1 \qquad \text{(A2.4)}$$

where $Z = \rho cA$ is the effective driving point impedance in the given region. Since α_1, Z_1 and Z_2 are known, α_2 and β_1 may be calculated.

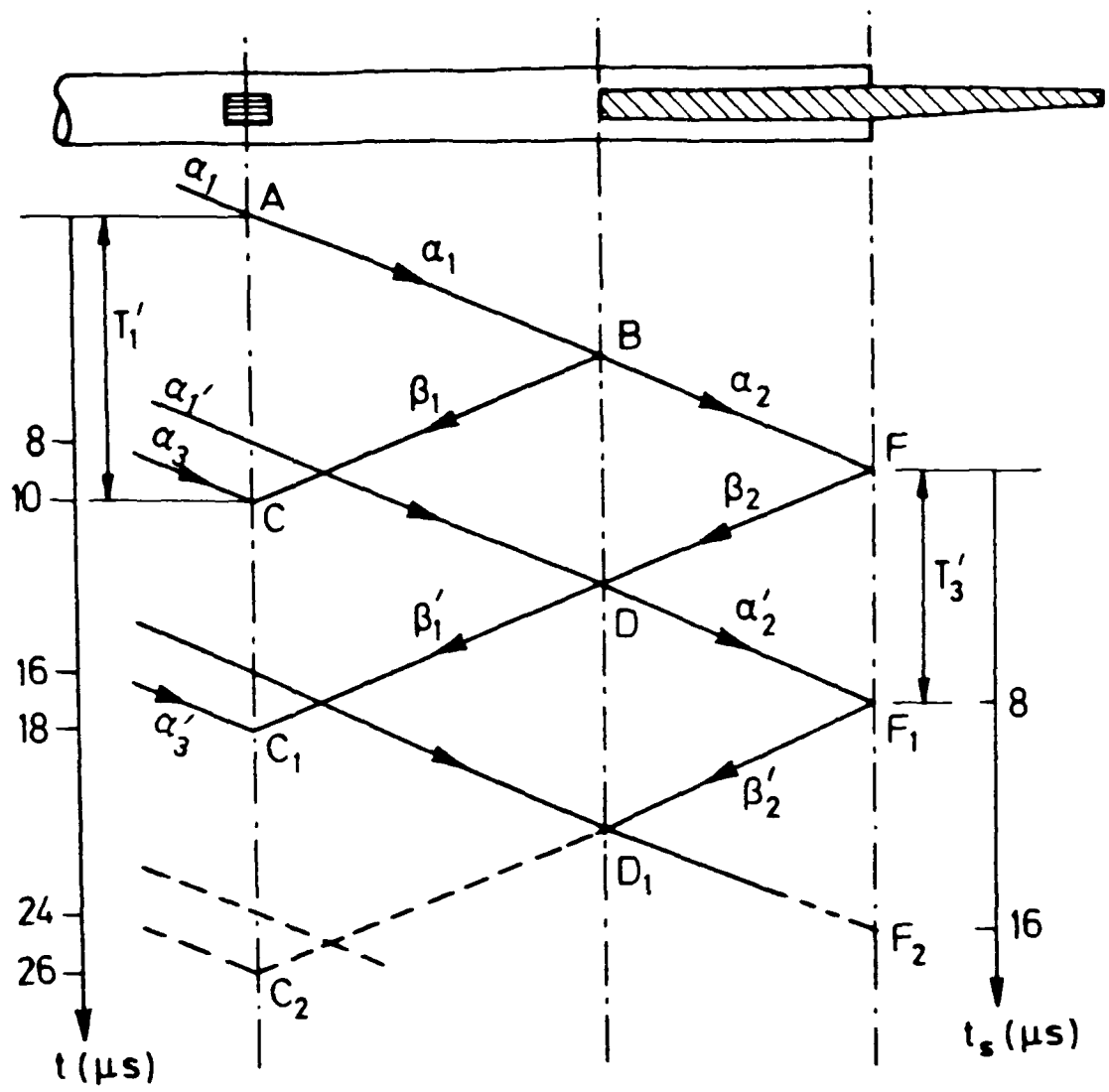

Fig. A2.2 WAVE ANALYSIS FOR GRIP REGION OF INPUT BAR

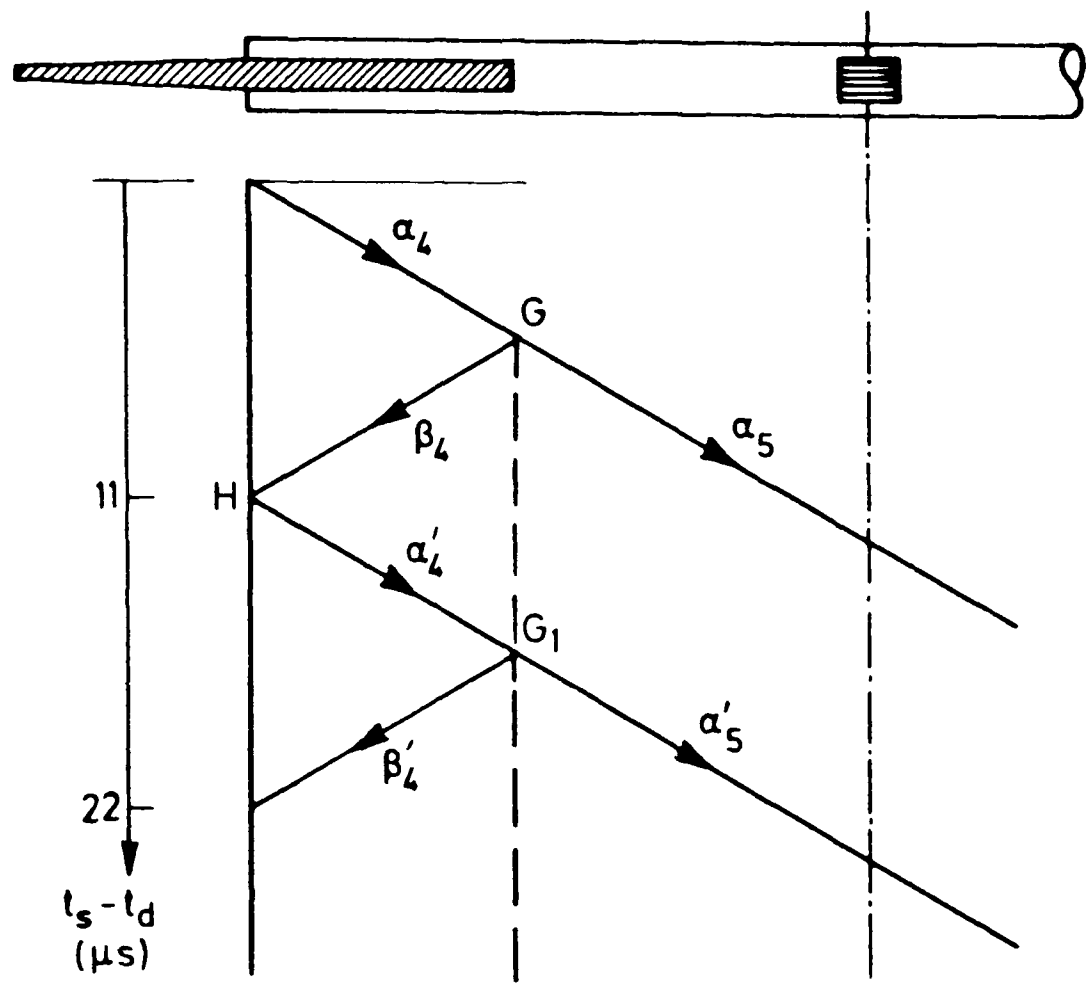

Fig. A2.3 WAVE ANALYSIS FOR GRIP REGION OF OUTPUT BAR

The reflected β wave from the interface represented by $BDD_1...$ interacts with the incident α wave at gauge station II represented by $CC_1C_2...$ such that at a point such as C_1, for example, for which the time is given by $T_1' < t < T_2'$, the relations

$$\alpha_3' = E\varepsilon_I \qquad \text{(A2.5)}$$

$$\beta_1' + \alpha_3' = E\varepsilon_{II} \qquad \text{(A2.6)}$$

hold, allowing the determination of β_1'. At the interface $BDD_1...$ for points from D onwards, i.e. for times given by $T_3' < t < T_2'$, the relations (A2.3) and (A2.4) are modified to become

$$\alpha_2' = \{(Z_1 - Z_2)/(Z_1 + Z_2)\}\beta_2 + \{2Z_2/(Z_1 + Z_2)\}(A_1/A_2)\alpha_1' \qquad \text{(A2.7)}$$

$$\beta_1' = \{(Z_2 - Z_1)/(Z_2 + Z_1)\}\alpha_1' + \{2Z_1/(Z_1 + Z_2)\}(A_2/A_1)\beta_2 \qquad \text{(A2.8)}$$

Since β_1' has been obtained from (A2.5) and (A2.6) and α_1' is given by (A2.2) at the appropriate time, t, equations (A2.7) and (A2.8) may be solved to give β_2 and α_2'. Finally the stress and particle velocity at, for example, point F on the loading-bar/specimen interface may be obtained from the relations.

$$\sigma = \beta_2 + \alpha_2 \qquad \text{(A2.9)}$$

and $$v = (\beta_2 - \alpha_2)/\{(\rho c)_2\} \qquad \text{(A2.10)}$$

where $(\rho c)_2$ is the acoustic impedance in region 2, the grip region of the input bar. The calculation proceeds in a stepwise manner up to the limit at $t = T_2'$.

The analysis of wave reflections in the grip region of the output bar, see Fig. A2.3 is rather simpler. For times, $t < T_4'$, where T_4' is defined in Fig. A2.1, we have

$$\alpha_5 = E\varepsilon_{III} \tag{A2.11}$$

while for points along GG_1 ... the relations

$$\alpha_4 = \{(Z_5 + Z_4)/2Z_5\}(A_5/A_4)\alpha_5 \tag{A2.12}$$

$$\beta_4 = \{(Z_5 - Z_4)/2Z_5\}(A_5/A_4)\alpha_5 \tag{A2.13}$$

hold. Thus β_4, determined at point G, and α_4', determined at point G_1, may be combined to give the stress and particle velocity at point H, on the specimen/output-bar interface, using the relations

$$\sigma = \beta_4 + \alpha_4' \tag{A2.14}$$

and $$v = (\beta_4 - \alpha_4')/\{(\rho c)_4\} \tag{A2.15}$$

APPENDIX 3

PUBLICATIONS ASSOCIATED WITH THE THESIS

1. Saka, K. and Harding, J., "Behaviour of Fibre-Reinforced Composites under Dynamic Tension", Oxford University Engineering Laboratory Report No. OUEL 1543/84.

2. Saka, K. and Harding, J., "The Deformation and Fracture of Hybrid-Reinforced Composites under Tensile Impact", Proc. International Union of Theoretical and Applied Mechanics (IUTAM) Symposium on Macro and Micro-Mechanics of High Velocity Deformation and Fracture, Tokyo, 1985 (in press).

3. Saka, K. and Harding, J., "Behaviour of Fibre-Refinforced Composites under Dynamic Tension", Second Progress Report, Oxford University Engineering Laboratory Report No. OUEL 1602/85.

4. Saka, K. and Harding, J., "Behaviour of Fibre-Reinforced Composites under Dynamic Tension", Interim Report, 1st May 1985 - 30th April 1986, Grant No. AFOSR-85-0218, October, 1986.

5. Harding, J., Saka, K. and Taylor, M.E.C., "The Effect of Strain Rate on the Tensile Failure of Woven-Reinforced Carbon/Glass Hybrid Composites", (to be presented at "IMPACT '87" W. Germany).